Universität der Bundeswehr München
Fakultät für Luft- und Raumfahrttechnik
Institut für Thermodynamik

The Stochastic Fields Method in Large Eddy Simulation of Turbulent Partially Premixed Combustion
- A Quantitative Analysis -

Maximilian Hansinger, M.Sc.

Vollständiger Abdruck der von der
Fakultät für Luft- und Raumfahrttechnik
der Universität der Bundeswehr München
zur Erlangung des akademischen Grades eines

Doktor-Ingenieurs (Dr.-Ing.)

genehmigten Dissertation

1. Gutachter: Prof. Dr. rer. nat. Michael Pfitzner
2. Gutachter: Prof. Dr.-Ing. Johannes Janicka

Die Dissertation wurde am 28.09.2020 bei der Universität der Bundeswehr München eingereicht und durch die Fakultät für Luft- und Raumfahrttechnik am 25.03.2021 angenommen.

Tag der Prüfung: 29.03.2021

Abstract

The combustion of fuels, whether they are fossil or synthetic, is and will remain an important source for the primary energy production. In order to support the design process of novel combustion devices engineers need reliable and efficient simulation tools. The flames in industrial combustors are usually affected by turbulence and lots of applications operate in a partially premixed mode, including extinction and re-ignition effects and mixed flame modes. These flame configurations are difficult to model. In the past, it has been shown that especially the Flamelet/Progress variable (FPV) approach and the Eulerian Stochastic fields (ESF) method, which belongs to the family of transported PDF methods, are suitable to model partially premixed flames. The FPV approach is computationally relatively cheap, as it uses tabulated chemistry and a presumed sub–grid probability density function (PDF). On the contrary, the ESF method is assumed to be more accurate, but also more expensive, as it uses finite-rate chemistry and directly solves the sub–grid PDF with additional stochastic transport equations.

The objective of this work is to analyze and quantitatively compare the ESF method with the FPV approach in simulations of turbulent partially premixed flames within the context of time resolving Large Eddy Simulations (LES). The focus is on the ESF method and it is investigated how the choice of the specific ESF formulation, the chemical mechanism, the number of stochastic fields, the turbulence model, and the computational grid affect the overall prediction quality of the simulation. These results are then directly compared to simulations conducted with the FPV approach using both premixed and non–premixed manifolds. In addition, a quantitative analysis is carried out using the Wasserstein metric to measure the dissimilarity between experimental and numerical data sets.

In the present work, three relatively new turbulent methane/air flame configurations that show partial premixing are investigated. The first case is a flame with inhomogeneous fuel inlet, which exhibits a mixed flame mode and shows a moderate degree of extinction. The second flame is a piloted non–premixed diffusion flame that is close to blow-off and shows a strong degree of local extinction. Finally, an oxy–fuel jet flame is investigated, which has a high proportion of hydrogen in the fuel stream. In order to model differential diffusion effects properly, the ESF method has been extended in this work to account for detailed molecular transport.

The analysis suggests that the ESF method should be the preferred combustion model in the simulation of all three flame configurations, in order to obtain the most accurate results for all analyzed quantities of interest. It is shown, however, that the method is relatively insensitive to the selected number of stochastic fields and that other parameters, such as the choice of the chemical mechanism are more relevant for the accuracy of the results. This indicates that in LES the sub–grid turbulence chemistry interaction may be deliberately neglected, given a finite rate mechanism is used. In addition, it is shown that

the FPV approach also provides satisfying results for some quantities of interest, which are compatible to the ESF results. Finally, the simulations of the oxy–fuel flame indicate that, given the high content of hydrogen, differential diffusion effects need to be incorporated to obtain reasonable results.

Kurzfassung

Die Verbrennung von Kraftstoffen, ungeachtet ob fossiler oder synthetischer Natur, ist und bleibt eine wichtige Quelle für die Primärenergieerzeugung. Um den Entwurfsprozess neuartiger Brenner zu unterstützen, benötigen Ingenieure zuverlässige und effiziente Simulationswerkzeuge. Die Flammen in industriellen Brennern werden in der Regel durch die Interaktion mit Turbulenz beeinflusst und befinden sich in einem teilweise vorgemischten Zustand, einschließlich Lösch- und Wiederzündungseffekten und mixed-mode Zuständen. Diese Flammenkonfigurationen sind in der Regel schwer zu modellieren. In der Vergangenheit hat sich gezeigt, dass insbesondere der Flamelet/Progress variable (FPV) Ansatz und die Methode der Eulerian Stochastic Fields (ESF), die zur Familie der transportierten PDF-Verfahren gehört, zur Modellierung teilweise vorgemischter Flammen geeignet sind. Der FPV-Ansatz ist vom Rechenaufwand her relativ günstig, da er tabellierte Chemie und eine 'presumed sub–grid' Wahrscheinlichkeitsdichtefunktion (PDF) verwendet. Im Gegensatz dazu wird die ESF-Methode als genauer, aber auch teurer betrachtet, da sie chemische Reaktionsraten direkt berechnet und die sub–grid PDF mit zusätzlichen stochastischen Transportgleichungen löst.

Das Ziel dieser Arbeit ist die Analyse und der quantitative Vergleich der ESF-Methode mit dem FPV-Ansatz in Simulationen turbulenter, teilweise vorgemischter Flammen im Rahmen von zeitauflösenden Large Eddy Simulationen (LES). Der Schwerpunkt liegt dabei auf der ESF-Methode und es wird untersucht, wie sich die Wahl der spezifischen ESF-Formulierung, des chemischen Mechanismus, der Anzahl der stochastischen Felder, des Turbulenzmodells und des Rechengitters auf die gesamte Vorhersagegüte der Simulation auswirkt. Diese Ergebnisse werden mit Simulationen verglichen, die mit dem FPV-Ansatz, unter Verwendung vorgemischter und nicht-vorgemischter Tabellen durchgeführt wurden. Darüber hinaus wird eine quantitative Analyse unter Verwendung der Wasserstein-Metrik durchgeführt.

In der vorliegenden Arbeit werden drei relativ neue turbulente Methan/Luft Flammenkonfigurationen untersucht, die eine partielle Vormischung zeigen. Im ersten Fall handelt es sich um eine Flamme mit einem Einlass mit inhomogenem Brennstoff-Luft-Gemisch, die einen gemischten Flammenmodus mit einen mäßigen Verlöschungsgrad aufweist. Bei der zweiten Flamme handelt es sich um eine pilotierte, nicht vorgemischte Diffusionsflamme, die nahe des Ausblasens ist und starkes Verlöschen aufweist. Anschließend wird eine oxy–fuel Freistrahl-Flamme untersucht, die einen hohen Anteil an Wasserstoff im Brennstoffstrom aufweist. Um die Effekte differentieller Diffusion richtig zu modellieren, wurde die ESF-Methode in dieser Arbeit erweitert um den detaillierten molekularen Transport zu berücksichtigen.

Die Analyse legt nahe, dass die ESF-Methode das bevorzugte Verbrennungsmodell bei der Simulation aller drei Flammenkonfigurationen sein sollte, um für alle relevanten Größen

die genauesten Ergebnisse zu erhalten. Es zeigt sich jedoch, dass die Methode in LES relativ unempfindlich gegenüber der gewählten Anzahl stochastischer Felder ist und dass andere Parameter, wie z.B. die Wahl des chemischen Mechanismus, für die Genauigkeit der Ergebnisse ausschlaggebender sind. Dies deutet darauf hin, dass bei der LES die chemische Wechselwirkung der sub–grid Turbulenz bewusst vernachlässigt werden kann, sofern ein chemischer Reaktionsmechanismus verwendet wird. Darüber hinaus wird gezeigt, dass der FPV-Ansatz für einige ausgwählte Größen zufriedenstellende Ergebnisse liefert, welche mit den ESF-Ergebnissen kompatibel sind. Auch wird gezeigt, dass für die Simulationen der oxy–fuel Flamme, differentielle Diffusionseffekte miteinbezogen werden müssen, um akzeptable Ergebnisse zu erhalten und die Flammenstruktur korrekt wiederzugeben.

Vorwort

Die vorliegende Arbeit ist im Rahmen meiner Tätigkeit als wissenschaftlicher Mitarbeiter am Institut für Thermodynamik der Universität der Bundeswehr München entstanden.

Meinem Doktorvater Prof. Dr. rer. nat. Michael Pfitzner möchte ich dafür danken mir diese Arbeit ermöglicht zu haben. Der stetige Austausch und die zahlreichen interessanten Diskussionen haben wesentlich zum erfolgreichen Abschluss beigetragen. Des weiteren möchte ich mich bedanken bei Thorsten Zirwes vom KIT und Prof. Dr.-Ing. habil. Markus Klein für die erfolgreiche Zusammenarbeit im Rahmen verschiedener Publikationen; letzterem gebührt zusätzlicher Dank für die Übernahme des Prüfungsvorsitzes. Herrn Prof. Dr.-Ing. Johannes Janicka danke ich für die Übernahme des Koreferates und die gründliche Prüfung der Dissertation.

Ganz herzlich möchte ich mich bei allen Kollegen am Institut für die Zusammenarbeit und die gute Arbeitsatmosphäre bedanken. Insbesondere Danke ich Paola Breda, Arne Lampmann, Christoph Traxinger, Prof. Dr.-Ing. habil. Tobias Sander, Prof. Dr.-Ing. Christian Mundt, Sigi Bayer, Annett Sturm, Dr.-Ing. Julian Zips, Dr. Edison Ge und Dr. Junsu Shin für die abwechslungsreichen Diskussionen, die erfolgreiche Zusammenarbeit bei verschiedenen Forschungsvorhaben und das allgemein positive Klima am Institut, welches zum Gelingen dieser Arbeit beigetragen hat. Dank gebührt auch Dr.-Ing. Hagen Müller, meinem Vorgänger, für die tolle Vorarbeit und die Einarbeitung zu Beginn meiner Zeit am Institut.

Ein ganz besonderer Dank geht an dieser Stelle an meine Familie, meine Freunde, sowie meine Freundin Tinta, für die uneingeschränkte Unterstützung während allen Phasen der Promotion.

München, 8. April, 2021   Maximilian Hansinger

Publications

Throughout the time at the institute, several contributions were published in scientific journals and at conferences in cooperation with other researchers. The present dissertation is partly based on the publications listed below.

Publications in peer reviewed journals

Klein, M., Nachtigal, H., Hansinger, M., Pfitzner, M., and Chakraborty, N. "Flame Curvature Distribution in High Pressure Turbulent Bunsen Premixed Flames". *Flow, Turbulence and Combustion* 101.4 (2018), pp. 1173–1187. DOI: `10.1007/s10494-018-9951-1`

Zirwes, T., Zhang, F., Habisreuther, P., Hansinger, M., Bockhorn, H., Pfitzner, M., and Trimis, D. "Quasi-DNS Dataset of a Piloted Flame with Inhomogeneous Inlet Conditions". *Flow, Turbulence and Combustion* 104.4 (2020), pp. 997–1027. DOI: `10.1007/s10494-019-00081-5`

Hansinger, M., Zirwes, T., Zips, J., Pfitzner, M., Zhang, F., Habisreuther, P., and Bockhorn, H. "The Eulerian Stochastic Fields Method Applied to Large Eddy Simulations of a Piloted Flame with Inhomogeneous Inlet". *Flow, Turbulence and Combustion* 105.3 (2020), pp. 837–867. DOI: `10.1007/s10494-020-00159-5`

Hansinger, M., Pfitzner, M., and Klein, M. "Statistical Analysis and Verification of a New Premixed Combustion Model with DNS Data". *Combustion Science and Technology* (2020), pp. 1–22. DOI: `10.1080/00102202.2020.1781833`

Breda, P., Hansinger, M., and Pfitzner, M. "Chemistry computation without a sub-grid PDF model in LES of turbulent non-premixed flames showing moderate local extinction". *Proceedings of the Combustion Institute* (2020). DOI: `10.1016/j.proci.2020.06.161`

Hansinger, M., Pfitzner, M., and Sabelnikov, V. "LES of oxy–fuel jet flames using the Eulerian Stochastic Fields method with differential diffusion". *Proceedings of the Combustion Institute* (2020). DOI: `10.1016/j.proci.2020.06.206`

Hansinger, M., Ge, Y., and Pfitzner, M. "Deep residual networks for flamelet/progress variable tabulation with application to a piloted flame with inhomogeneous inlet". *Combustion Science and Technology* (2020). DOI: `10.1080/00102202.2020.1822826`

Conference contributions

Hansinger, M., Müller, H., and Pfitzner, M. "Comparison of Premixed and Non-Premixed Manifold Representations in the LES of a Piloted Jet Flame with Inhomogeneous Inlets". *8th European Combustion Meeting*. Dubrovnik, Croatia, 2017

Müller, H., Hansinger, M., and Pfitzner, M. "Large Eddy Simulation einer turbulenten LOx/GCH 4 Flamme unter Verwendung der Eulerian Stochastic Fields Methode Large eddy simulation of a turbulent LOx/GCH 4 flame using the Eulerian stochastic field method". *28. Deutscher Flammentag*. Darmstadt, 2017

Ge, Y., Hansinger, M., Traxinger, C., and Pfitzner, M. "Deep residual learning applied to real-gas thermodynamics". *International Conference of Computational Methods in Sciences and Engineering 2018*. Thessaloniki, Greece, 2018, p. 150004. DOI: 10.1063/1.5079207

Hansinger, M., Zips, J., and Pfitzner, M. "Eulerian Stochastic Fields method and model free finite rate chemistry applied to Sydney partially premixed flame". *9th European Combustion Meeting*. Lisbon, Portugal, 2019

Lampmann, A., Hansinger, M., and Pfitzner, M. "Comparison of LES combustion models for turbulent premixed flames at atmospheric pressures". *9th European Combustion Meeting*. Lisbon, Portugal, 2019

Breda, P., Hansinger, M., and Pfitzner, M. "Low dimensional chemistry manifolds applied to premixed methane/air flames under atmospheric conditions". *9th European Combustion Meeting*. Lisbon, Portugal, 2019

Hansinger, M., Ge, Y., and Pfitzner, M. "Deep residual networks for flamelet/progress variable tabulation method in combustion LES". *29. Deutscher Flammentag*. Bochum, 2019

Lampmann, A., Hansinger, M., and Pfitzner, M. "Artificially thickened flame vs. Eulerian stochastic fields combustion models applied to a turbulent partially-premixed flame". *29. Deutscher Flammentag*. Bochum, 2019

Contents

List of Figures

List of Tables

Nomenclature

Acronyms

ANN	Artificial neural network
ATF	Artificially thickened flame
BFER	Global methane mechanism with 6 species
CFD	Computational Fluid Dynamics
CFL	Courant-Friedrichs-Lewy
CMC	Conditional moment closure
CPU	Central processing unit
DNS	Direct numerical simulation
EMST	Euclidean minimum spanning tree
ESF	Eulerian Stochastic Fields
GPU	Graphic processor unit
GRI	Gas Research Institute
GRI-3.0	Methane mechanism version 3.0 by Gas Research Institute
FGM	Flamelet generated manifold
FPI	Flame prolongation of ILDM
FPV	Flamelet/progress variable
IEM	Interaction by exchange with the mean
ILDM	Intrinsic low dimensional manifold
ISAT	In-situ adaptive tabulation
JL-R	Extended Jones-Lindstedt methane mechanism
KIT	Karlsruhe Institute for Technology
LES	Large Eddy simulation
LFA	Laminar flamelet assumption
LMST	Linear mean-square estimate
Lu13	Methane mechanism with 13 species
Lu19	Methane mechanism with 19 species
Lu30	Methane mechanism with 30 species
MMC	Multiple mapping conditioning
MPI	Message Passing Interface
ODE	Ordinary differential equation
PDF	Probability density function
PISO	Pressure implicit with time splitting of operators
PSP	Parameterized scalar profile
qDNS	quasi-DNS
RANS	Reynolds averaged Navier-Stokes simulation

REDIM	Reaction-Diffusion-Manifold
RMS	Root mean squares
SGS	Sub–grid scale
SPDE	Stochastic partial differential equation
SPMM	Shadow positioning mixing model
TCI	Turbulence–chemistry interaction
TKE	Turbulence kinetic energy
TNF	Turbulent non–premixed flames
tPDF	Transported probability density function
UniBW	Bundeswehr University Munich
WALE	Wall-adapting local eddy viscosity

Roman Symbols

a_N	Coefficient of the pressure matrix	-
a_P	Coefficient of the pressure matrix	-
A	Pre-exponential factor	-
A_S	Model constant	Pa s
$\mathcal{A}$	Drift term	-
B_β	Vreman model parameter	-
BI_T	Burning index	-
c	Progress variable	-
c	Concentration	mol/L
C_k	Kolmogorov constant	-
c_p	Specific heat capacity at constant pressure	mol/L
c_v	Specific heat capacity at constant volume	mol/L
C_D	ESF mixing constant	-
C_V	Vreman model constant	-
C_w	WALE model constant	-
C_χ	FPV mixing constant	-
dW	Stochastic Wiener increment	$s^{1/2}$
D	Diameter	m
D_P	Pilot diameter	m
D	Diffusion coefficient	m^2/s
D^T	Thermal diffusion coefficient	m^2/s
$\mathcal{D}$	Multi component diffusion coefficient	m^2/s
E	Activation energy	J
$\mathcal{E}$	Turbulent energy spectrum	m^3/s^2
$\mathcal{F}$	Joint probability density function	-
$\mathcal{G}$	Filter kernel	-
h	Enthalpy	J
h_S	Sensible enthalpy	J
h^0	Enthalpy of formation	J
$\mathcal{H}$	Heaviside step function	-
J	Diffusive species flux	$kg/(m^2s)$
J_S	Diffusive enthalpy flux	$kg/(m^2s)$
k	Wave number	1/m

k	Species reaction velocity	l/(mol s)
l	Length scale	m
l_{I}	Integral length scale	m
l_{η}	Kolmogorov length scale	m
L_{r}	Recess length	m
$\mathcal{L}$	Geometric length scale	m
m	Mass	kg
m_{tot}	Total mass of the mixture	kg
M	Molar mass	kg/mol
M	Pope criteria	-
$\mathcal{M}$	Mixture averaged molar mass	kg/mol
$\mathcal{M}$	Chemical symbol	-
$\mathcal{M}_{sgs}$	Micro mixing term	-
n	Specific mole number	-
N	Number of scalars or species	-
N_r	Number of elementary reactions	-
N_s	Number of stochastic fields	-
$\mathcal{N}$	Normal distribution	-
p	Pressure	Pa
p_{d}	Hydrodynamic pressure	Pa
p^0	Thermodynamic pressure	Pa
PV	Progress variable	-
PV_n	Normalized progress variable	-
$\mathcal{P}$	Marginal probability density function	-
$\mathcal{P}_{sgs}$	Joint sub–grid probability density function	-
r	Rate of species production	mol/(m^{3}s)
R	Gas constant	J/(kg K)
$R_{\phi_1\phi_2}$	Correlation coefficient between scalar ϕ_1 and ϕ_2	-
$\mathcal{R}$	Universal gas constant	J/(K mol)
u	Velocity	m/s
u^c	Correction velocity	m/s
U_{J}	Pipe flow velocity	m/s
U_{P}	Pilot velocity	m/s
U_{Co}	Co-flow velocity	m/s
$\mathcal{U}$	Bulk flow velocity	m/s
s	Stoichiometric oxygen-to-fuel ratio	-
s_{L}	Laminar flame speed	m/s
s^d	WALE model parameter	1/m^2
S	Strain rate tensor	-
S	Stochastic variable	-
T	Temperature	K
T_{b}	Burnt temperature	K
T_{u}	Unburnt temperature	K
T_{Co}	Co-flow temperature	K
T_{F}	Fuel temperature	K
T_{P}	Pilot temperature	K
T_{st}	Temperature at stoichiometry	K

T_{S}	Sutherland model constant	K
T_0	Reference temperature	K
t	Time	s
$\mathcal{T}$	Time interval	s
x	Cartesian coordinate	m
X	Mole fraction	-
y	Cartesian coordinate	m
Y	Mole fraction	-
z	Cartesian coordinate	m
Z	Mixture fraction	-

Greek Symbols

α	Scalar	-
χ	Scalar dissipation rate	1/s
χ_{st}	Scalar dissipation rate at stoichiometry	1/s
δ	Flame thickness	m
δ_{th}	Thermal flame thickness	m
Δ	Filter width	m
ϵ	Turbulent Dissipation rate	$\mathrm{m}^2/\mathrm{s}^3$
γ	Random vector	-
λ	Thermal conductivity	W/(K m)
μ	Laminar molecular viscosity	Pa s
μ_t	Turbulent molecular viscosity	Pa s
ν	Laminar kinematic viscosity	m^2/s
ν_t	Turbulent kinematic viscosity	m^2/s
ν	Stoichiometric coefficient	-
ρ	Density	kg/m^3
ϕ	Equivalence ratio	-
ϕ	Scalar value	-
ψ	Phase space	-
σ	Prandtl or Schmidt number	-
σ_t	Turbulent Prandtl or Schmidt number	-
τ	Stress tensor	-
τ_c	Chemical time scale	s
τ_{sgs}	Sub–grid mixing time scale	s
$\dot{\omega}$	Chemical source term	1/s
ζ	Scalar field	-
ζ	Unmixedness	-

Non–dimensional Numbers

Da	DAMKÖHLER number
Ka	KARLOVITZ number
Le	LEWIS number
Ma	MACH number
Pr	PRANDTL number
Pr_t	TURBULENT PRANDTL number
Re	REYNOLDS number
Re_t	TURBULENT REYNOLDS number
Re_η	KOLOMOGOROV REYNOLDS number
Sc	SCHMIDT number
Sc_t	TURBULENT SCHMIDT number

Sub- and Superscripts

α	Species index
b	Backward reaction
ext	Extintion
f	Forward reaction
fl	Flame
F	Fuel
i	i-direction
i	Index of time step
ij	Einstein notation
i,j,k	Vector component
l	Reaction index
l	Species index
k	Species index
n	Index of stochastic field
O	Oxidizer
res	Resolved contribution
sgs	Sub–grid scale contribution
st	Stoichiometry
t	Turbulent
T	Temperature
Z	Mixture fraction

Chapter 1

Introduction

1.1 Motivation

In the year 2019 the combustion of fossil fuels, such as gas, oil, or coal, supplied up to 80 % of the world's energy demand [28]. With a constantly growing world population and additional economic growth, total energy consumption is expected to increase by about 20-30 % in 2040, as forecasted by the International Energy Agency [101]. Depending on the socio-economic development and political decisions and regulations, the combustion of fossils still will contribute to about 70-80 % of the primary energy production [27]. Although such predictions are prone to uncertainties, there is certainty that the demand for fossil fuels on the global scale will be increasing in the near future. There may be multiple reasons for such a development. One of them is the fact that hydrocarbon fuels have a very high energy density. Nowadays, they are technically easy to extract, store, and distribute, which makes them the ideal source of energy in the transportation sector (mainly for vehicles, ships, and aircrafts), the electricity sector, or space heating. Despite the efforts to gradually substitute the share of oil, coal, and natural gas with renewable sources of energy in the electricity production, there remain many industrial processes, such as the production of metals, cement, or asphalt concrete, which rely on high temperatures generated by combustion.

Burning fossil fuels as a source of energy had a significant contribution to the technical and economic progress over the past two centuries. However, this development does come with a downside, which is air pollution through the emission of soot, nitrogen dioxide (NO_2), sulfur dioxide (SO_2), carbon monoxide (CO), and the man made climate change as a result of the emission of greenhouse gases. Only for the year 2016, the World Health Organization [283] estimates that air pollution indirectly caused about 4.2 million premature deaths through stroke, heart disease, lung cancer, and asthma. Compared to the pre-industrial era the average temperature has risen about 1 °C on the global scale. There is strong scientific consensus that greenhouse gas emissions have caused climate change [196, 249]. Based on technological, economical and regulatory developments different scenarios are possible, with a predicted temperature increase between 1.5 °C and, in the worst case, 3 °C for the year 2050, compared to the pre-industrial era [108]. The effects could be severe: desertification, sea level rise, heat waves, ocean acidification, changing precipitation patterns and droughts, as well as the implications of dealing with socio-economical damages related to climate change and its mitigation.

As a countermeasure to the impending consequences through climate change and pol-

1

lution, policy makers already agreed at the first Kyoto protocol in 1997 to take action and reduce greenhouse gas and pollutant emissions. In 2016 a new agreement, the Paris agreement, was signed by 194 states and the European Union. The agreement aims to limit the increase in temperature to not more than 1.5 °C on average. For each signing country specific actions are formulated how this goal should be achieved. For example, Germany has committed itself to increasing the share of renewable energies and reducing its greenhouse gas emissions by 40 % in 2020 and by 55 % in 2030, compared to the emissions of 1990. As mentioned, there remain some sectors that will rely on combustion as primary source of energy also in the future. The only possible way to comply with the emission goals is to make the combustion processes more efficient and cleaner. The limited supply of fossil fuels and its associated market price is another driving force to reduce the fuel consumption in many industrial sectors.

In order to improve the efficiency of aero-engines, gas turbines, internal combustion engines, or industrial furnaces, first, the complex physical combustion processes in these devices need to be understood sufficiently well. Second, engineers need reliable tools at hand to improve existing, or invent new combustion devices. With the increasing computational power over the last decades, numerical simulations in the field of *Computational Fluid Dynamics* (CFD) have established themselves as an indispensable tool in the digital design process where they substitute or support costly physical experiments. The CFD based design allows the engineers to vary the geometry, fuel composition, or general operating conditions with ease and at relatively low cost. However, for the results to be accurate, the employed numerical models need to be reliable and universally applicable.

1.2   Research objectives

Industrial combustion processes usually occur at highly turbulent conditions [205] where the interaction of the flow field with the chemical reactions in the flame have an impact on the overall combustion efficiency. Turbulence may also quench or blow-off the flame and enhance pollutant formation. From the perspective of CFD simulations the *Large Eddy Simulation* (LES) approach has emerged as a valuable tool to compute time resolved, unsteady, turbulent flows that allow to gain insights into the three dimensional flow structure (see Section 1.3.1). In order to compute the flame physics (temperature, heat release, species), a combustion model is needed.

From an academic perspective, combustion is roughly classified into premixed and non–premixed combustion regimes, which both feature different characteristics. In the premixed regime, fuel and oxidizer are initially homogeneously mixed and the flame propagates freely through the unburnt mixture. On the contrary, in the non–premixed regime, fuel and oxidizer are initially separated and they need to mix before they burn. Based on these phenomenological assumptions a multitude of turbulent combustion models have been devised , which are bound to a specific combustion regime (see Section 1.3.2).

However, in practice, many combustion devices operate in a partially premixed regime, a mode where both premixed and non–premixed regimes may appear. Additionally, strong turbulence may lead to localized extinction and re-ignition events, which enhances partial premixing. There are not many combustion models that are able to cope with these effects. Two of them are the Eulerian Stochastic Fields (ESF) method, which belongs to the class of transported probability density function (PDF) methods, and the flamelet/progress variable (FPV) model (see Section 4).

The ESF method has already proven to cope well with partially premixed combustion in the LES context [228] and also the FPV method showed good results for flames with a mild degree of localized extinction [102]. However, both models are fundamentally different and differ a lot in their computational costs[1]. Moreover, there are many parameters in the ESF method that, presumably, may change its prediction accuracy and computational cost, such as the underlying chemical mechanism, the number of stochastic fields, or the resolution of the computational grid. As these aspects have found little consideration so far in the literature, it is the objective of this work to quantitatively evaluate the impact of different parameter settings on the overall simulation accuracy of the ESF method. Moreover, a systematic comparison against simulation results with the FPV combustion model will be carried out. For consistency, all simulations have been conducted on the same meshes and with identical numerical schemes. Recently, Johnson, Wu, and Ihme [115] attempted to quantitatively assess different LES combustion models based on simulations from different research groups, using probabilistic evaluation tools. The work provides the foundation towards a detailed comparison of combustion models and the methodology will be applied in the present work, too.

For the evaluation and model comparison three different flame setups have been selected, which have a certain relevance for industrial applications. The first case is a piloted flame with inhomogeneous fuel inlet where the combustion mode transits from a premixed state at the fuel exit to a non–premixed state further downstream [9, 173]. Such flows are technically interesting as they feature improved stability and favorable levels of emissions. The second flame is Flame F from the Sandia flame series [7]. It is close to blow-off and resembles well the strong turbulence effects in industrial combustion devices. The third configuration is an oxy–fuel flame [250] that exhibit also a strong degree of localized extinction. Additionally, differential diffusion effects play a role as the fuel is premixed with hydrogen (H_2). To incorporate these effects, the ESF method has been modified to account for differential diffusion. The flame is burnt in an oxygen/carbon dioxide (O_2/CO_2) environment, which makes it especially interesting for the carbon capture and storage techniques, where such configurations are applied.

1.3 State of research

1.3.1 Trends in turbulent simulations

Turbulent flows can be found frequently in nature and technological applications, and its description has been a subject of study for several decades. Although turbulent flows are three dimensional, vary in time, and appear to be of a chaotic nature their motion can be fully described with mathematical transport equations, the so called *Navier-Stokes* equations. However, except for extremely simplified assumptions[2], there is no universal way that allows to solve these equations in an analytical manner. Instead, numerical methods are needed to solve the transport equations and iteratively predict the spatio–temporal flow dynamics. Turbulent flows comprise a wide bandwidth of time and length scales, which manifest themselves in the form of swirls and eddies. The largest ones are imposed through the geometry of the flow configuration and transfer the kinetic energy down to the smallest, energy dissipating scales which are of universal, isotropic character and depend on the fluid's

---

[1]The computational resources needed to carry out the numerical simulation.
[2]For example, some laminar flow configurations can be solved analytically.

viscosity μ [225]. Reynolds [237] introduced already in 1895 the non–dimensional *Reynolds number* Re, which is meant to quantify the degree of turbulence in flows.

Numerical simulations, which accurately resolve all time and length scales of turbulence are referred to as *Direct Numerical Simulation* (DNS). In academia, DNS is a valuable method to gain fundamental insights towards understanding the nature of turbulence and to validate turbulence closure models. The governing equations are discretized directly and solved numerically. As, by definition, the mesh is fine enough to resolve the smallest eddies, one can obtain an accurate three-dimensional, time-dependent solution of the governing equations completely free of modeling assumptions. The only errors are those introduced by the numerical approximation.

DNS makes it possible to compute and visualize any flow quantity of interest, including some that are difficult or impossible to measure in experiments. It allows to study the spatial relationships between flow variables and to obtain insight into the detailed kinematics and dynamics of turbulent structures. To resolve all the scales of motion, one requires a number of grid points proportional to the 9/4 power of the Reynolds number Re, so the cost of the computation scales with increasing Reynolds number, according to $\mathrm{Re}^{9/4}$ [65]. For this reason, DNS have largely been limited to low or moderate Reynolds numbers, and their widespread application to engineering–type problems within the next decade appears unlikely.

A different approach is given through the numerical solution of the *Reynolds Averaged Navier-Stokes* (RANS) equations. In RANS, the flow field is decomposed into a mean and fluctuating part, hence, temporal averaging is performed. Only the temporal mean values of the flow quantities are computed directly, whereas all turbulent fluctuations around the mean are modeled in Reynolds-stress terms. RANS simulations are computationally very efficient as the numerical grid can be fairly coarse. Therefore, it is a widely used tool in engineering applications, as parameter studies can be carried out rather quickly. However, the RANS approach suffers from one principal shortcoming: the fact that the turbulence model must represent a very wide range of scales. While the small scales tend to be somewhat universal, the large ones are affected very strongly by the boundary conditions and the geometry of the flow configuration. As it does not seem possible to model the effect of the large scales of turbulence in the same way in flows that are very different, RANS simulations do require a lot of calibration and tuning of the model constants for a given flow configuration. Moreover, RANS has also limitations when it is applied to highly unsteady, complex, three dimensional flow problems.

LES is a technique intermediate between the direct simulation of turbulent flows in DNS and the solution of the RANS equations. In LES, the contribution of the large, energy-carrying structures to momentum and energy transfer is computed exactly. Only the effect of the smallest scales of turbulence is modeled. Since the small scales tend to be more homo-geneous and universal and less affected by the boundary conditions than the large ones, there is hope that their modeling can be simpler and require fewer calibrations and adjustments when applied to different flow configurations. LES are similar to DNS in the way that they provide a three-dimensional, time dependent solution of the Navier-Stokes equations. Thus, they still require fairly fine meshes. However, they can be used at higher Reynolds numbers than DNS at much lower computational costs. With increasing computational power LES will continue its transition from the academic environment towards industrial applications, when a deeper physical understanding of the flow problem is needed. However, there is still a wide variety of LES turbulence models available, which all have their benefits and

disadvantages. All have been calibrated and validated based on generic, non–reactive flows at ambient pressures. So far there is no turbulence model that explicitly takes into account the steep temperature and viscosity gradients in reactive flows, high pressure conditions, or incorporates the effects of differential diffusion. Moreover, with the transition to LES new problems arise from the numerical discretization schemes, the optimal choice of grid resolution, or the need for high quality transient inlet boundary conditions.

1.3.2 Turbulent combustion models

Another central aspect in the numerical simulation of reactive flow systems is the description of turbulent combustion. It is a complex physical process involving a large number of length and time scales that include non-linear interactions between the chemical reactions and turbulent fluctuations, which makes it difficult to represent these phenomena in the form of a generalized model. Although there have been made a lot of efforts over the past 50 years to understand the turbulent combustion physics, yet not all processes are fully understood [16]. Instead of having one universally applicable combustion model that is valid for all kinds of combustion problems a multitude of specialized models have been developed that are suitable for specific flame configurations and setups. For an extensive overview on the different kinds of combustion models the reader is referred to the review papers by Pitsch [215], Veynante and Vervisch [271], and Bilger et al. [16], as well as the books by Echekki [49] and Poinsot and Veynante [217].

The following subsection presents recent developments in combustion modeling with relevance to the simulation of partially premixed flames.

General requirements

In reacting flows, mass and momentum equations alone are not sufficient to describe the variations of species and temperature due to chemical reactions. Therefore, a combustion model is needed. Such a model has to fulfill two requirements in LES: describe the thermo–chemical evolution of the reactive system, and account for unresolved sub-grid turbulence–chemistry (TCI) interaction. Both aspects will be outlined in more detail below.

1. **Thermo–chemical relation**
   The combustion model has to provide the necessary information on the thermo–chemical state. If species and enthalpy transport equations are solved directly in the flow solver then the model has to provide the integrated reaction source terms for all involved reactive scalars in the reaction system. This is the case if a detailed, reduced, or global chemical reaction mechanism is used. A different approach is pursued by chemistry reduction techniques, which aim to reduce the dimensionality of the combustion manifold. The thermo–chemical state space is precomputed and then mapped according to one or more controlling variables. In non–premixed combustion, this variable may be the mixture fraction that represents the local fuel share in the mixture. In premixed combustion, it may be the reaction progress variable that allows an attribution of the species composition and temperature as a function of the reaction's progress. In the flow solver, apart from the momentum equation, only a transport equation for the controlling variable(s) need to be solved. Since the species composition and the temperature are unique functions of these variable(s) they can be retrieved during run time from the precomputed data base.

2. **TCI model**
   The high frequency fluctuations of the turbulent flow may impede or increase chemical reactions and can generally alter the flame structure locally. However, these fluctuations are not known in LES due to the low pass filtering. For an accurate prediction of the filtered source terms the sub-grid distribution of the species, in the form of a sub–grid *Probability Density Function* (PDF), has to be known, modeled, or presumed.

Model overview

Tabulated chemistry models: In non–premixed combustion one of the most prominent model is the steady laminar *flamelet* model, introduced by Peters [201, 203]. The general idea of the flamelet model is that, in the case of fast chemistry and high Damköhler numbers (this assumes that chemical reactions are not or only weakly perturbed by turbulence), the inner flame structure of turbulent diffusion flames is locally the same as in a laminar diffusion flame. Hence, the turbulent flame can be described as a superposition of laminar *flamelets* which can be computed from generic one-dimensional configurations. For non–premixed combustion the counter-flow diffusion flame configuration is used to compute flamelets in mixture fraction space as a function of the scalar dissipation rate. Based on different laminar flamelet computations the thermo–chemical state space (containing temperature and the species composition) can be pre-computed at constant pressure and stored in structured tables. The high dimensional space is then reduced to a two-dimensional manifold. As the flamelets are computed in the absence of turbulence, TCI is accounted for by integrating the laminar flame solution on a presumed joint PDF of mixture fraction and scalar dissipation rate. During the simulation the thermo–chemical state is then retrieved as a function of the table access parameters, which has the advantage that only two additional transport equations need to be solved in the flow solver. The temperature and species composition can be received ad-hoc via linear table interpolation. This comes along with a tremendous speed up compared to the ordinary differential equation (ODE) integration of the stiff chemical reaction system to obtain species production and heat release rates. Due to its efficiency and straight forward implementation in numerical codes it has been widely used for the simulation of turbulent non–premixed flames, both in the LES and RANS context. For example Pitsch and Steiner [213] used it to simulate the Sandia D flame, Müller et al. [183] applied it successfully in the simulation of a small scale rocket combustion chamber.

The major drawback of this model is its range of validity, which is restricted to the high Damköhler regime [16]. So, the prediction quality decreases when partial premixing and localized extinction play a role. To overcome this deficit Pierce and Moin [209] and Pierce [210] proposed the *flamelet/progress variable* (FPV) concept where the thermo–chemical data base is parameterized by a progress variable, instead of the scalar dissipation rate. This progress variable explicitly traces the reaction's progress and is meant to cope with re-ignition and extinction events, which is an effect of partial premixing between fuel and oxidizer. The FPV model has been successfully used by Ihme, Cha, and Pitsch [102] to predict local extinction and re-ignition effects in non-premixed turbulent combustion. Ihme and Pitsch [103, 104] applied the FPV model to the Sandia Flames D and E, which feature a low to moderate degree of localized extinction and re-ignition, and achieved good results. The FPV model is also suitable for the prediction of autoignition in a lifted methane/air flame as demonstrated by Ihme and See [106]. Over the last decade it became a prominent model to simulate unsteady effects and partially premixed combustion in the LES

context [106, 145, 163, 166, 199, 200, 229, 248, 281].

Others extended and applied the flamelet concept to account for real-gas effects in trans critical combustion [291], differential diffusion [212], radiation effects [177], the formation of soot [129, 180], or included enthalpy as an additional table access parameter [162, 289] to model wall heat transfer in combustion chambers.

Another chemistry tabulation technique is the *intrinsic low dimensional manifold* (ILDM) methodology, developed by Maas and Pope [164, 165]. It is based on a direct mathematical analysis of the dynamic behavior of the non-linear response of the chemical system. As it does not assume any type of underlying flame structure to construct the thermo–chemical database, it is, in theory, suitable to simulate any type of combustion regime. However, in practice, for the simulation of hydrocarbon combustion in air at least five or more chemical coordinates (table dimensions) are needed to reproduce accurate results [55] and it often has difficulties at low temperatures and with the description of ignition phenomena [217]. To overcome deficits in the ILDM method, Bykov and Maas [33] proposed the Reaction-Diffusion-Manifold (REDIM) approach where the chemical reactions are coupled to a diffusion process.

Also to be mentioned is the *in-situ adaptive tabulation* (ISAT) technique proposed by Pope [218] and Yang and Pope [285]. ISAT is an unstructured tabulation method where at the beginning of the simulation no subspace of the composition space is tabulated. During the reactive flow simulation the table is generated and gradually updated from the direct solving of the time evolution of species mass fraction compositions. So to say, it is a combination of the table look up technique with direct chemical integration. During the flow simulation the table grows and the probability increases that eventually the whole composition space accessed by the particular flame configuration is tabulated. The thermo–chemical information can then be queried from the table rather than it needs to be computed with direct integration of the chemical reaction mechanism.

It has to be noted that both ILDM and ISAT are reduction methods to establish the thermo–chemical relation. When they are used in the simulation of turbulent flames within the LES context a model to account for TCI is still required. ILDM and ISAT are often used together with PDF methods.

In premixed combustion tabulated chemistry is applied in the form of the *flame prolongation of ILDM* (FPI), proposed by Gicquel, Darabiha, and Thevenin [78] and Fiorina et al. [57], and the *flamelet generated manifold* (FGM) method, proposed by Oijen and Goey [193] and Oijen et al. [194]. FPI and FGM have in common that the look up tables are generated from simulations of one dimensional laminar premixed flames using complex chemical schemes (as in the flamelet model for non–premixed flames). Species mass fractions and reaction rates are then tabulated as a function of a set of reaction coordinates. In its initial formulation the FGM tables were parameterized by a progress variable and the enthalpy that allows the modeling of premixed non–adiabatic flames while the tables generated with FPI were parameterized by a progress variable and the mixture fraction that allows the simulation of premixed flames with varying mixture fraction, i.e. stratified and partially premixed flames. However, recently the FGM manifold has also been extended to account for heat losses showing good prediction quality in the simulation of stratified swirled flames within gas turbine combustors [46]. To close the unresolved terms in LES, the table values have to be coupled with a TCI model. Common methods include the use

of presumed β-PDFs [274] or flame surface density (FSD) concepts [19].

Based on the FPI tabulation Fiorina et al. [56] proposed the *filtered tabulated chemistry for LES* (F-TACLES) methodology. The main idea is to tabulate all filtered quantities, including the reaction source term, based on one dimensional premixed flamelets as a function of a progress variable, the LES filter width, and the mixture fraction. The model can also be extended to account for differential diffusion and achieved good results in the simulation of a stratified turbulent jet flame [176].

A comprehensive review on the different chemistry tabulation techniques can be found in [58].

So far, all these models have in common that the accessible thermo–chemical state space is precomputed and stored in tables. In the case of sophisticated chemistry models with several hundred species involved or multi-physics applications where an increased number of table access parameters leads to high dimensional tables, the database can have enormous memory requirements during the simulation. In some cases the database may even be larger then the available RAM on the high-performance system. Moreover, with interpolation schemes of higher order the table interpolation times can increase drastically for high dimensional tables. To overcome these issues Weise and Hasse [280] used dynamic memory and MPI extensions to reduce memory requirements, Liang, Pope, and Pepiot [154] considered spline fits, whereas Shunn [254] considered binary trees, both as an alterative to structured tables. With the advent of machine learning in combustion research a different data reduction strategy is pursued by the usage of *Artificial Neural Networks* (ANN) [245]. In a supervised learning process the ANN regressor is trained to predict the data from the tables given the controlling variables. The advantage is that the memory footprint of the network is independent of the dimensionality or discretization of the tables only depends on the network's complexity which is determined by the number of employed neurons. This approach has first been used by Flemming, Sadiki, and Janicka [59] for the flamelet model and by Ihme, Schmitt, and Pitsch [105] for the FPV model. Both achieve good results but report long training and inference times[3]. However, given the advancements in the machine learning community this issue can be overcome as shown recently by [234], who used self-organizing maps to reduce the network's complexity. Hansinger, Ge, and Pfitzner [91] employed deep residual network structures [96] and graphics cards (GPU) accelerated inference, thereby reducing the memory footprint by a factor of 60 while keeping the inference time in the range of the FPV table interpolation.

Conditional Moment Closure: The *Conditional Moment Closure* (CMC) method has been formulated individually by Klimenko [134] and Bilger [15]. The general idea of CMC is that reactive scalar fluctuations are conditioned on the mixture fraction. As the fluctuations of reactive scalars are mainly associated with fluctuations of the mixture fraction, a turbulent non–premixed flame may be described by the conditional values of reactive scalars on mixture fraction rather than by their conventional means. Additional transport equations for the conditional moments of the reactive scalars are then solved along with the momentum equations to achieve the turbulence-chemistry closure. Initially developed for RANS [133] it has been successfully adopted to LES [190] and shows good results in the simulation of turbulent bluff-body flames [188], lifted flames [189], partially premixed flames [138, 139], and localized extinction in the Sandia Flame F [70]. The chemistry is

---

[3]The time needed by the network to predict the output.

usually represented with a reduced mechanism, however, a coupling of CMC with tabulated chemistry has also shown to be possible [267].

Thickened flame model: One of the challenges in RANS and LES of premixed combustion lies in the numerical underresolution of the flame front. As the thickness of a premixed flame front is usually much smaller than the grid spacing the flame front cannot be resolved in the computation. This leads to numerical problems and inaccuracies. To overcome this aspect an attractive solution has been proposed by Butler and O'Rourke [31], the *artificially thickened flame* (ATF) model. Instead of refining the computational grid so that the flame becomes resolvable, they propose to thicken the flame front and therewith make it resolvable on coarse grids. In the balance equation of the species mass fractions and the enthalpy the diffusivity is increased by a factor and the chemical source term is scaled down by the same factor. To account for flame wrinkling on the sub-grid scale Colin et al. [41] proposed an efficiency function in the LES context that increases both diffusivity and the reaction rate. Initially it has been developed for premixed combustion modes, but it also shows good results for partially premixed applications [21]. As an alternative to direct chemical integration Kuenne, Ketelheun, and Janicka [141] coupled the ATF model with an FGM table which showed overall good simulation results for premixed [141] and stratified flames [142].

PDF methods: *Transported probability density function* methods are an attractive modeling approach to the closure problems that arise from averaging or filtering chemical source terms in RANS and LES. The idea is to solve a transport equation that describes the joint PDF of the set of reactive scalars, i.e. the species mass fractions and the enthalpy. It is a one-point, one-time PDF that contains statistical information about the joint sub-grid scalar distribution at a given point in space and time (so the PDF does neither inform about the temporal evolution, nor about the spatial distribution of the scalars).

The idea has been formulated first by Dopazo and O'Brien [48] and was adopted by Pope [222] who then contributed significantly to the advancement of PDF methods in turbulent combustion simulation. The PDF transport equation provides a mathematically exact description of the sub-grid scalar distribution. However, it contains unclosed terms that require modeling and the construction of high-dimensional analytical joint PDFs is computationally infeasible. It was Pope [220, 221] who then devised a method to solve the PDF transport equation with Monte Carlo methods and thereby set the foundation for the *Lagrangian particle* method [219]. In this approach the PDF is represented by an ensemble of stochastic (Lagrangian) particles. This method is grid free, since the particles have their spatial position as a stochastic variable, which changes according to the spatial transport and diffusive terms in the PDF equation. Each particle contains the composition of the reactive scalars and the reaction rates are solved for each particle composition. The filtered chemical source term is then obtained from the ensemble of particles encountered within the respective grid cell. As with many combustion models the particle method was initially devised for RANS but has been extended for the application as an LES combustion model in the form of the filtered density function method. Important contributions were made by Colucci et al. [42], Gao and O'Brien [67], Givi [80], Jaberi et al. [110], and Pope [224].

A drawback of this method is the high number of particles that are needed to describe the PDF [75] and the numerical coupling of the finite-volume flow solver and the Lagrangian particles is not straight forward and requires several numerical aspects to be considered [186]. An improvement, that allows to reduce the number of particles was given by [40] with the

Multiple Mapping Conditioning (MMC) model. Another approach is given by Valiño [268], who proposed a fully Eulerian formulation of the PDF transport equation, known as the *Eulerian Stochastic Fields* (ESF) method. The idea is to construct the joint PDF from an ensemble of scalar fields which are continuous over the filter width. The fields evolve according to stochastic transport equations, which are a stochastic equivalent to the PDF transport equation. Decorrelation of the individual fields is achieved via a Wiener process. Sabel'nikov and Soulard [240, 241] and Soulard and Sabel'nikov [258] came up with the same idea of continuous stochastic fields. However, the difference is they formulated the stochastic transport equation according to the rules of Stratonovic calculus, while Valiño [268] used Itô calculus. Both have to be treated differently in the numerical implementation, but they can be transformed into each other [68]. Recently, Valiño, Mustata, and Letaief [269] provided a revised version of the original ESF formulation. Wang, Zhang, and Pant [278] presented a thorough mathematical examination of the two ESF formulations by Valiño. He found inconsistencies regarding the sub-grid variance production of scalar fluctuations and provides correction terms. However, his findings apply to the PDF of a single scalar at low Reynolds numbers in the RANS context.

As mentioned previously, the actual PDF transport equation contains unclosed terms that require modeling, both in the particle, and the ESF method. The most difficult part is the closure of the micro-mixing term, which accounts for the molecular transport processes on the sub-grid scale. Several models have been proposed to solve this problem. The most prominent ones are the *Interaction by Exchange with the Mean* (IEM) [272] or *Linear Mean-Square Estimation* (LMST) [48], the *Modified Curl's* model (MC) [112], and the *Euclidean Minimum Spanning Tree* (EMST) model [262]. More recent models include the *Shadow Positioning Mixing Model* (SPMM) [223], and the *Parameterized Scalar Profile* (PSP) model [178]. Richardson and Chen [238] proposed an approach to account for differential mixing rates for PDF simulations with pairwise-exchange mixing models such as IEM and EMST. Zhou, Yang, and Ren [288] used the MC model in conjunction with a differential scalar mixing timescale model to account for detailed molecular transport. Kuron et al. [144] devised a hybrid mixing rate model, based on EMST, that is meant for the simulation of premixed combustion. As most of these models have been explicitly devised for application within the Lagrangian particle method, up to now only the IEM model has been used in the ESF context. Although it is the least complex one and has known modeling deficits Raman and Pitsch [233] demonstrated that in LES the IEM model provides sufficiently accurate results. A detailed overview and comparison on different mixing models can be found in [36, 37, 179, 235].

The particle method has been successfully employed in the simulation of non–premixed combustion [111, 233, 252, 276, 286], lifted flames [35, 87], bluff-body flames [185], stratified flames [266], partially premixed [97, 232], and premixed combustion [155, 260]. With similar success the ESF method was applied to the simulation of non–premixed flames [122, 187], stratified flames [5, 23, 100], lifted flames [2], mixed mode combustion [94], partially premixed swirl flames [29, 64], spark ignition [123], or premixed combustion [119, 227]. However, despite good simulation results the application of the ESF method to premixed combustion should be evaluated with care. Picciani, Richardson, and Navarro-Martinez [208] argue that a highly resolved mesh, with grid spacing in the order of magnitude of the flame thickness, is needed for accurate results with the ESF method in premixed combustion simulation. In order to overcome this Picciani, Richardson, and Navarro-Martinez [207] proposed a coupling of the ESF method with the ATF model for premixed flame simula-

tion. Simulation results of turbulent premixed combustion are also shown in the Appendix C. Nevertheless, the transported PDF method is a very promising modeling approach for the simulation of flames covering a wide variety of combustion modes [170]. The interested reader is also referred to the review paper by Haworth [95] for more information about the transported PDF methods.

1.3.3 Experimental test cases and numerical simulations

For the development and the validation of combustion models generic laboratory scale flame configurations are used which can be operated at well-defined (and reproducible) conditions and allow detailed time resolved measurements of velocity and scalar fields. Herein, the most significant database is managed by the *International workshop on measurements and computation of turbulent non–premixed flames* (TNF) [265]. The aim of the workshop is to establish a series of well-defined laboratory flames with a detailed database of experimental measurements, which may serve for the calibration and validation of different combustion modeling approaches. Initially, mainly non–premixed flames were addressed, e.g. the well known piloted Sandia Flames D-F, which feature different degrees of localized extinction. However, in the recent years the database has been expanded towards partially premixed, mixed mode, and stratified flames. In this work, some of the newer flames from three different configurations out of the TNF database are analyzed with different combustion modeling approaches. The setups are briefly introduced hereafter and an overview on different modeling approaches by other research groups is provided.

Piloted flame with inhomogeneous inlet

This piloted methane/air flame has recently been investigated by Barlow et al. [9] at Sandia Livermore National Laboratories, and Meares et al. [173] and Meares and Masri [174] at the University of Sydney. The mixture fraction profile at the burner inlet is inhomogeneous and unsteady. This is achieved by adding a small, retractable central tube within the main tube of the burner and separately supplying fuel and air for partial premixing. Both tubes are located within the pilot annulus. The burner is operated at different inlet velocities (maximum Re = 66,500) and at different degrees of partial premixing. For modelers the most interesting setups are the flames which have a recess distance of the inner fuel pipe of 75 mm. This leads to an inhomogeneous mixture fraction distribution over the burner inlet resulting in a dominantly premixed combustion mode close to the jet exit and a non–premixed mode further downstream. The respective setups are the FJ200-5GP-Lr75-57 and the FJ200-5GP-Lr75-80 flames, which have a bulk inlet velocity of the main jet of 57 m/s, and 80 m/s, respectively. From now on only the abbreviation version will be used, i.e. Lr75-57 and Lr75-80.

Due to their mixed-mode characteristics these flames have been featured at the 13th and 14th TNF workshop. Combustion modeling groups around the world were encouraged to simulate these flames with their modeling approaches and compare their results at the workshops. Up to now some of these results have been published and are summarized hereafter.

The group from Princeton University did LES of case Lr75-57 with the FPV model on a computational grid with 2 million cells. In their first publication Perry, Mueller, and Masri [200] used a two mixture fraction model to overcome the limitations of single mixture fraction FPV models that presume a single, compositionally uniform fuel stream. The flame

structure, in terms of temperature scatter plots, is matched very well with this model. Perry and Mueller [199] investigated also the effect of multi-scalar subfilter PDF models for the two mixture fraction FPV approach and found that the choice of the presumed subfilter PDF has a significant impact on the results of the flame structure. Moreover, the Princeton group also provided transient inlet boundary conditions for the combustion simulation which they obtained from LES of the mixing process between fuel and air in the main burner pipe.

Maio et al. [168] from Laboratoire EM2C at Université Paris-Saclay simulated case Lr75-80 with F-TACLES and the ATF model on a tetrahedral mesh with 72 million cells, in both cases FPI was used to represent the chemistry. The inlet boundary conditions are taken from the Princeton group. The general flame structure characteristics are reproduced with both models equally well. However, radial temperature profiles are only matched close to the burner inlet and differ from the experimental results further downstream.

Galindo et al. [66] from the University of Sydney used a sparse-Lagrangian MMC combustion model with a reduced 22 species chemical mechanism to simulate case Lr75-80 on a LES mesh that consists of 1.4 million cells. They use their own inlet boundary conditions. As it was shown, the model has difficulties to reproduce the premixed flame structure in the near field but captures well the non–premixed flame structure further downstream.

The group around Wang and Zhang [277] from Purdue University did LES of case Lr75-57 and Lr75-80 with the Lagrangian particle (transported PDF) method and the EMST mixing model on a mesh with 2.3 million cells. Their simulation includes the inert mixing process in the main fuel pipe. The chemical scheme is not explicitly mentioned in this publication, however, from the reference to [276] it is assumed that the GRI-2.11 mechanism with 49 species has been employed. The general premixed and non–premixed flame structures are well captured. Differences can be observed in the radial distribution of the temperature and mixture fraction.

Kleinheinz et al. [132] from RWTH Aachen investigated case Lr75-80 on a structured LES mesh with 3.1 million cells. They used a FPV based multi-regime combustion model where the progress variable source term is composed from the individual contributions of the premixed and non–premixed combustion regimes. The general flame characteristics could be reproduced reasonably well.

Tian and Lindstedt [264] from Imperial College London simulated case Lr75-57 and Lr57-80 with a RANS based transported PDF approach and investigated the effect of the EMST, modified Curl's model, and extended modified Curl's model. For the chemical scheme a reduced 20 species mechanism is used. The modified Curl's model was found to be the most suitable mixing model for these cases. The general flame characteristics in terms of temperature scatter plots are in very good agreement with the experiments.

Zirwes et al. [293] from Karlsruhe Institute of Technology (KIT) conducted a model free quasi-DNS (qDNS) of case Lr75-57. The block structured mesh consisted of 150 million cells. The computational mesh achieves DNS-like resolution quality only in the upstream region near the nozzle exit where results from experiments are available. This is why the term quasi-DNS is used. However, no sub–grid turbulence or combustion model has been used. The chemistry is represented by an analytically reduced 19 species mechanism (Lu19). Inlet boundary conditions have been created from a separate non-reactive highly resolved pipe flow simulation. The results are in very good agreement with the experimental data in terms of scalar radial distribution and scatter plots.

Johnson, Wu, and Ihme [115] from Stanford University did LES of case Lr75-57 with the FPV combustion model. They also did a quantitative comparison of the anonymized LES

calculations, which were presented at the 13th TNF workshop, using the Wasserstein metric as a probabilistic method to enable quantitative evaluations of LES combustion models. The previous overview on simulations of the Sydney burner is summarized in Table 1.1 and showed that there are many groups investigating the same test case, but use different numerical codes, meshes, turbulence models, chemical schemes, and boundary conditions. This introduces additional uncertainties with respect to the evaluation of different combustion modeling approaches. The Wasserstein metric can directly be evaluated from scatter data or statistical results through probabilistic reconstruction. Johnson, Wu, and Ihme [115] show that the Wasserstein metric is an effective validation tool that provides an objective and quantitative evaluation of model deficiencies. Therefore, it will also be used in this work.

The stochastic fields LES results by Hansinger et al. [94] will be discussed in detail in Section 6.1, as they are part of the research presented in this work.

Group	Case	Cells	TCI	Chemistry	Ref.
Princeton Univ.	Lr75-57	2 mio.	presumed PDF	FPV table	[199, 200]
EM2C	Lr75-80	73 mio.	ATF F-TACLES	FPI table	[168]
Univ. of Sydney	Lr75-80	1.4 mio.	MMC	22 species	[66]
Purdue Univ.	Lr75-57 Lr75-80	2.3 mio.	particle PDF	49 species	[277]
RWTH Aachen	Lr75-80	3.1 mio.	presumed PDF	FPV table	[132]
Imperial College	Lr75-57 Lr75-80	30,000 (RANS)	particle PDF	20 species	[264]
KIT	Lr75-57	150 mio.	qDNS	19 species	[293]
Stanford Univ.	Lr75-57	1.6 mio.	presumed PDF	FPV table	[115]
UniBW	Lr75-57	4.5 mio.	ESF	19 species	[94]

Table 1.1: Simulations of the Sydney piloted flames with inhomogeneous inlet.

Sandia Flame F

The Sandia Flame Series, namely flames D, E and F, are non-premixed piloted jet flames with increasing levels of extinction. They were investigated by Barlow and Frank [7], Barlow and Karpetis [10], Karpetis and Barlow [124], and Schneider et al. [246], and are extensively used in the combustion community as a reference benchmark for the validation of turbulent combustion models.

Flames D-F have all the same geometric setup, with the only difference being the varying fuel jet and pilot operating velocities. Species composition and temperatures are kept identical, with the exception for Flame F where the pilot temperature is reduced from 1880 K to 1860 K. Flame D can be considered as a diffusion flame and has been successfully simulated with the steady laminar flamelet model [213]. In this work Flame F will be analyzed and used for a quantitative comparison of combustion models. It exhibits a strong degree of localized extinction and is difficult to model with standard models for non–premixed combustion (e.g. the steady laminar flamelet model). The flame is operated at a jet Reynolds number of Re = 44,800, the fuel consists of a mixture of methane (25 vol-%) and air (75 vol-%). The flame can be considered partially premixed in the sense that localized extinction allows for a partial premixing between fuel and oxidizer. As a result of the high scalar dis-

sipation rates and turbulent fluctuations the chemical processes are unable to balance the strong heat losses and the flame quenches. Once the strain reduces, the partially premixed composition may re-ignite again. These effects of extinction and re-ignition are usually difficult to model. The following paragraphs give an overview on previous simulations of Flame F by other research groups.

Xu and Pope [284] from Cornell University were among the first to simulate the Sandia Flame Series, including Flame F. They used a RANS based transported PDF approach with EMST mixing model and ISAT with a 16 species mechanism for the representation of the chemical state. Overall they achieve very good agreement with the experimental data. The degree of localized extinction is well matched. Cao and Pope [34] (Cornell University) investigated the influence of chemical mechanisms in transported RANS-PDF simulations using the Sandia Flame Series. When a full or analytically reduced mechanism is used they obtain good results for Flame F, whereas global extinction is observed for skeletal mechanisms. Kronenburg and Kostka [140] and Straub et al. [261] used the Conditional Moment Closure (CMC) and the Multiple Mapping Condition (MMC) for their RANS calculations.

Vreman et al. [275] from TU Eindhoven applied premixed and non–premixed FGM with a presumed β-PDF approach to LES of Flame D and F. The results obtained for flame D are satisfactory, but despite the transient nature of the LES, the extinction in Flame F was not found to be properly captured. They argued that extinction in Flame F mainly occurs on scales smaller than the resolved ones in the simulation. By replacing the β-PDF approach with a thickened flame model the prediction of localized extinction could be improved to some extent.

Flame F has already been simulated with the ESF method by Jones and Prasad [122] from Imperial College London within their LES investigations of the flame series D-F. The results are generally in good agreement with the experiments. However, extinction in Flame F was underpredicted in the downstream region, presumably due to a simplified 15-step chemical mechanism.

Garmory and Mastorakos [70] from Cambridge University simulated Flame D and F with a LES-CMC approach. They obtained good results for Flame D and adequately predicted localized extinction in the front region of the flame.

Ge, Cleary, and Klimenko [73] from the University of Queensland did LES of the Sandia Flame series using the Sparse-Lagrangian MMC model. The results were in good agreement with the experiments. However, localized extinction in Flame F is found to be difficult to model.

Ferraro et al. [53] from Bundeswehr University Munich (UniBW) developed a hybrid RANS/LES conditional transported PDF approach and simulated Flames D-F with the GRI-3.0 mechanism. The mixture fraction conditional mean values of the temperature are in good agreement with the experiments for all flames with this method.

Recently, Yu et al. [287] and Breda, Yu, and Pfitzner [26] from KIT and UniBW simulated the Sanida Flame series including Flame F with RANS and LES and a hybrid ESF-REDIM approach. Using the REDIM tabulated chemistry, they could considerably reduce the computational time, compared to a detailed chemical mechanism, and achieved accurate results.

Table 1.2 gives an overview on the mentioned works that include the simulation of Sandia Flame F.

Group	Flames	Cells	TCI	Chemistry	Ref.
Cornell Univ.	D-F	3,600 (RANS)	particle PDF	16 species	[284]
Cornell Univ.	D-F	9,216 (RANS)	particle PDF	GRI-3.0 GRI-2.1 skeletal	[34]
Imperial College	D-F	RANS	CMC	48 species	[140]
Univ. of Stuttgart	D-F	10,000 (RANS)	MMC	19 species	[261]
TU Eindhoven	D & F	10,000 (RANS)	presumed PDF	FGM	[275]
Imperial College	D-F	1 mio.	ESF	19 species	[122]
Cambridge Univ.	D & F	1.3 mio.	CMC	19 species	[70]
Univ. of Queensland	D-F	0.9 mio.	MMC	34 species	[73]
UniBW	D-F	13,000 (RANS)	particle PDF	16 species GRI-3.0	[53]
KIT	E-F	RANS	ESF	REDIM	[287]
UniBW	D-F	2.3 mio.	ESF	REDIM	[26]

Table 1.2: Simulations of Sandia Flame F.

Oxy–fuel flame

Another test case that is analyzed in this work is the non–premixed turbulent oxy–fuel jet flame series, which was investigated by Sevault et al. [250] at NTNU Trondheim. The measurement data of the six flames (named A1-A3 and B1-B3) is also available from the TNF database [265]. The fuel is composed of CH_4 and H_2 which is burnt in an O_2/CO_2 environment, so no air is used and N_2 is completely excluded from the combustion process. Depending on the H_2 content in the fuel and the jet Reynolds number (maximum Re = 18,000) the flames show a strong degree of localized extinction (which also causes partial premixing of unburnt fuel and oxidizer). Furthermore, given the high vol.-% of H_2 in the fuel stream differential diffusion effects play a role and have an impact on the flame structure.

So far, only a few research groups have investigated these flames in numerical simulations. The first one were Garmory and Mastorakos [71] from the University of Cambridge. They did LES of flame A1 and A3 using the CMC combustion model with a reduced 16 species chemical mechanism. Detailed molecular transport was not accounted for. They reproduced well the spatial location of localized extinction and the trend of increasing extinction with decreasing H_2 content in the jet, but mispredict radial species profiles. They attribute this discrepancy to the effect of differential diffusion, which is neglected in their unity Lewis number diffusion model.

Mahmoud et al. [166, 167] from the institute of Energy and Power Plant Technology (EKT) at Technical University Darmstadt did RANS and LES of flame A1, A3, and B3 with a hybrid ESF-FPV approach where the chemistry is pre-tabulated in a FPV database and the sub-grid scalar distribution is constructed from the joint PDF of mixture fraction and progress variable which is transported with the stochastic fields method. The presented results for species and temperature profiles differ from the experimental data. They ex-

plain the discrepancies with the absence of detailed molecular transport in their modeling approach.

Gierth et al. [79] from the institute for Simulation of Reactive Thermo-Fluid Systems (STFS) at Technical University Darmstadt conducted an assessment of different modeling approaches to include differential diffusion effects in flamelet models. They simulated case B1 with LES and the FPV model and achieve generally good agreement in terms of mixture fraction conditioned flame structure on the fuel lean side, but mispredict major species on the fuel rich side. Although differential diffusion has been included in the FPV tables they argue that the competition between molecular and turbulent transport, which is not captured as such in the tables, is responsible for the differences.

Table 1.3 gives an overview about the previous simulations of flames from the oxy–fuel flame series.

The stochastic fields LES results by Hansinger, Pfitzner, and Sabelnikov [93] are part of the present work and will be discussed with more detail in Section 6.3.

Group	Case	Cells	TCI	Chemistry	Ref.
Cambridge Univ.	A1, A3	2.3 mio.	CMC	16 species	[71]
EKT	A1, A3 B3	2.8 mio.	ESF	FPV table	[166, 167]
STFS	B1	2.4 mio.	presumed PDF	FPV table	[79]
UniBW	B1, B2	4.1 mio.	ESF	19 species	[93]

Table 1.3: Simulations of the oxy–fuel jet flame.

1.4   Thesis outline

The first part of this work deals with the fundamentals of turbulent flows in Chapter 2. It reviews the essential governing equations that allow to describe turbulent flows mathematically and it introduces the LES concept. Chapter 3 is dedicated to the phenomena of turbulent combustion. Different flame modes, including the idea of partially premixed combustion, are explained and the difficulties arising from the interaction between turbulence and chemical reactions and its implication for numerical models are highlighted. In the following Chapter 4 the Flamelet/Progress Variable and the Eulerian Stochastic Fields method are presented in detail. Chapter 5 summarizes the numerical methods used in this work. The three different numerical test cases of partially premixed flames are presented, analyzed, and discussed in Chapter 6. Finally, a conclusion is drawn and an outlook is given in Chapter 7.

Chapter 2

Turbulent flows

The motion of turbulent flows can be described and predicted mathematically using a set of conservation equations for mass and momentum. This set of governing equations is commonly referred to as the *Navier-Stokes* equations. The first Section 2.1 of this chapter is intended to present these equations in a general fashion. In Section 2.2 the thermo–chemical relations are established. Section 2.3 briefly explains the stochastic nature of turbulence and the scale separation concept inherent to the idea of *Large Eddy Simulation*. The filtered conservation equations are derived and three sub–grid scale (SGS) turbulence closure models are presented. It should be noted that these ideas in the numerical description of turbulent flows can be found among a wide variety of disciplines, e.g., atmospheric sciences, life sciences and medicine, chemical engineering, hydrodynamics, astrophysics, to name only a few of them. However, they also form the basis to grasp the difficulties in simulating turbulent combustion systems, which are discussed in Chapter 3. For a more detailed review on turbulent flows and their mathematical description the reader is referred to the books by Pope [225] and Batchelor [13].

2.1 Governing transport equations

Any fluid consists of individual molecules and the fluid's motion is the result of the inter-action of these molecules. Given the extremely large amount of molecules within a control volume[1] it is virtually impossible to describe mathematically the mechanics of fluids based on a molecular scale. Therefore, the *continuum hypothesis* is applied, which states that a fluid can be considered continuous if the mean free path of the individual molecules is much smaller than the geometric length scale in the flow field (i.e. the Knudsen number Kn $\ll$ 1, see [13]). From this Eulerian point of view the basic governing laws for the conservation of mass, momentum, and energy can be used to derive the equations which describe the transport of momentum, species and energy in fluids. The differential form of this set of equations dates back to the 19th century when it was formulated independently by Claude Louis Marie Henri Navier, Siméon Denis Poisson, Barré de Saint-Venant and George Gabriel Stokes for Newtonian fluids. However, only the names of Navier and Stokes have prevailed to entitle these equations and they are now commonly known as the *Navier-Stokes* equations.

   In the following, the conservation equations for mass, momentum, enthalpy, and species mass fractions are presented in their differential form for compressible, Newtonian fluids,

---

[1] At ambient conditions 1 l of air consists of approximately 2.6×10^{22} molecules [44].

adopting the Einstein summation convention (i.e. $u_i u_i = \sum_i^3 u_i u_i = u_1 u_1 + u_2 u_2 + u_3 u_3$). A detailed derivation of the *Navier-Stokes* equations can be found, e.g., in the book by Schlichting [244].

Conservation of mass

Mass can neither be created nor destroyed, but has to be conserved within a given control volume. Hence, the temporal change of mass within this volume can only be accomplished through a convective mass flux over the volume surfaces. In compressible flows the temporal variation of the density ρ is then equal to the convective transport of ρ through the volume boundaries with the local velocity component u_j. In differential form it reads:

$$\frac{\partial \rho}{\partial t} + \frac{\partial (\rho u_j)}{\partial x_j} = 0 \; , \tag{2.1}$$

where u_j and x_j denote the jth-component of the velocity vector and the position in cartesian coordinates, t denotes the time component.

Conservation of momentum

According to Newton's laws of motion the impulse ρu_i changes only as a result of external forces. Neglecting volume forces, such as gravitational forces, the relevant external forces acting on a fluid volume are surface forces, as a result of the pressure gradient $\partial p / \partial x_i$, and viscous forces, expressed in the form of the viscous stress tensor τ_{ij}. These terms have to be in balance with the temporal change and the convection of the impulse:

$$\frac{\partial (\rho u_i)}{\partial t} + \frac{\partial (\rho u_i u_j)}{\partial x_j} = -\frac{\partial p}{\partial x_i} + \frac{\partial \tau_{ij}}{\partial x_j} \; . \tag{2.2}$$

In this work only Newtonian fluids are considered. This means *Stoke's hypothesis* does apply and the viscous stress tensor τ_{ij} is given by

$$\tau_{ij} = \mu \left(S_{ij} - \frac{2}{3} \frac{\partial u_k}{\partial x_k} \delta_{ij} \right) \; , \tag{2.3}$$

where μ is the molecular viscosity and δ_{ij} is the Kronecker delta. The symmetric strain rate tensor S_{ij} reads:

$$S_{ij} = \frac{1}{2} \left(\frac{\partial u_j}{\partial x_i} + \frac{\partial u_i}{\partial x_j} \right) \; . \tag{2.4}$$

Transport of species

In reactive flows, many species are involved and it is of interest to describe the spatial and temporal changes in the concentration of each species k. The composition of a mixture with a number of N species can be expressed via the mass fraction Y_k for each species:

$$Y_k = \frac{m_k}{m_{\text{tot}}} \; , \tag{2.5}$$

where m_tot denotes the total mass of the fluid mixture and m_k is the mass of species k within the control volume. The transport equation for species mass fractions then becomes:

$$\frac{\partial(\rho Y_k)}{\partial t} + \frac{\partial(\rho u_j Y_k)}{\partial x_j} = \frac{\partial J_{j,k}}{\partial x_j} + \dot{\omega}_k \; . \tag{2.6}$$

$J_{j,k}$ is the jth-component component of the diffusive species flux vector and contains species mass fluxes as a result of spatial concentration, pressure, and temperature gradients (*Soret effect*). For a multi component mixture an exact formulation reads [125]:

$$J_{j,k} = \frac{\rho Y_k}{X_k \mathcal{M}} \sum_{l=1}^{N} M_l \mathcal{D}_{kl} \left(\frac{\partial X_l}{\partial x_j} + (X_l - Y_l) \frac{1}{p} \frac{\partial p}{\partial x_j} \right) - \frac{D_k^\text{T}}{T} \frac{\partial T}{\partial x_j} \; , \tag{2.7}$$

where M_l is the molecular weight, $X_{\{k,l\}}$ the species mole fraction, of species k and l, respectively, $\mathcal{M}$ is the mixture averaged molecular weight, T is the temperature, D_k^T is the thermal diffusion coefficient of species k, and $\mathcal{D}_{kl}$ is the multicomponent diffusion coefficient of species k into species l. A computationally less costly approximation for $J_{j,k}$ can be expressed in terms of *Fick's law* [143], based on the mass fraction gradients and the correction velocity u_j^c:

$$J_{j,k} = -\rho \left(D_k \frac{\partial Y_k}{\partial Y_j} - Y_k u_j^c \right) \; . \tag{2.8}$$

Equation (2.8) neglects mass fluxes due to pressure and temperature gradients. The multi-component diffusion coefficient $\mathcal{D}_{kl}$, which is computed from rigorous kinetic gas theory and is based on the Chapman-Enskog solution [18], simplifies to a mixture averaged diffusion coefficient D_k for each species k. This is known as the *Hirschfelder-Curtiss* approximation [99]:

$$D_k = \frac{1 - Y_k}{\sum_{l \neq k} X_l / \mathcal{D}_{kl}} \; . \tag{2.9}$$

Since the diffusion coefficients D_k differ between species, as a consequence of different molecular structure and atomic weight, the sum over the first term on the RHS[2] of Eq. (2.8) is not necessarily zero. However, to ensure mass conservation the sum over the diffusive fluxes of all species needs to be zero ($\sum_{k}^{N} J_{j,k} = 0$). This is achieved by adding a species weighted correction diffusion velocity u_j^c in Eq. (2.8). Following [143, 217] the jth component of the velocity vector is given by:

$$u_j^c = \sum_{k=1}^{N} D_k \frac{\partial Y_k}{\partial x_j} \; . \tag{2.10}$$

Apart from the *Hirschfelder-Curtiss* approximation the diffusion coefficient D_k can also be expressed in terms of the dimensionless Lewis number of the kth species (Le$_k$), which is defined as the ratio of thermal diffusivity of the mixture and molecular diffusivity of the kth species:

$$\text{Le}_k = \frac{\lambda}{\rho c_\text{p} D_k} \; , \tag{2.11}$$

where c_p is the specific heat capacity of the mixture at constant pressure and λ is the thermal conductivity of the mixture. This approach is simple and allows to account for the

---

[2]$\sum_{k}^{N} D_k \frac{\partial Y_k}{\partial Y_j}$

differential diffusion effects between species. However, it requires knowledge of Le_k for each species. Even simpler is the *unity Lewis number* assumption approach, which is based on the idea that all Lewis numbers Le_k are constant and equal to 1 (each species has the same diffusion coefficient). It is straight forward to implement such an approach in code and is computationally less demanding than the evaluation of $\mathcal{D}_{kl}$ to obtain D_k. In this case the diffusion coefficient is a constant $D_k = D = const.$, so the differential diffusion velocity is zero and Eq. (2.8) simplifies to

$$J_{j,k} = -\rho D_k \frac{\partial Y_k}{\partial x_j} \; . \tag{2.12}$$

Most existing commercial CFD codes are based on this assumption. Unless stated differently the *unity Lewis number* assumption approach is used throughout this work. However, if *differential diffusion* effects are neglected this can lead to large discrepancies with respect to the local flame structure and thermo–chemical properties. Usually this is the case when the mixture has a high H_2 content, which diffuses much faster than heavier hydrocarbons.

The last term on the RHS in the species transport equation (2.6) denotes the reaction source term $\dot{\omega}_k$ of species k due to chemical reaction. In Chapter 3 it is explained in detail how it is evaluated.

Conservation of energy

Analogous to the conservation of mass, energy can neither be created nor destroyed, but change its appearance. The conservation equation for energy can be written in various ways, e.g., as an equation for total energy, total or sensible enthalpy, or for the temperature. In the context of turbulent reacting flows the energy is commonly expressed in the form of enthalpy. However, all formulations can be transferred into each other. A descriptive overview can be found in [217]. Since the numerical implementation of the energy conservation equation in the employed OpenFOAM code is based on the sensible enthalpy h_s it is presented that way:

$$\frac{\partial(\rho h_\mathrm{s})}{\partial t} + \frac{\partial(\rho u_j h_\mathrm{s})}{\partial x_j} = \frac{\mathrm{D}p}{\mathrm{D}t} + \tau_{ij}\frac{\partial u_i}{\partial x_j} + \dot{Q} - \frac{\partial J_{s,j}}{\partial x_j} + \dot{\omega}_\mathrm{T} \; . \tag{2.13}$$

$\frac{Dp}{Dt} = \frac{\partial p}{\partial t} + u_j\frac{\partial p}{\partial x_j}$ is the material derivative of the pressure and accounts for enthalpy changes due to pressure fluctuations, $\tau_{ij}\frac{\partial u_i}{\partial x_j}$ is the viscous heating source term, $\dot{Q}$ is a heat source term, $J_{\mathrm{s},j}$ is the diffusive heat flux, and $\dot{\omega}_\mathrm{T}$ is the heat release due to chemical reaction. Equation (2.13) can be simplified as the considered flows in this work are only weakly compressible and pressure fluctuations can be ignored $\left(\frac{Dp}{Dt} = 0\right)$. Viscous heating can be neglected $(\tau_{ij}\frac{\partial u_i}{\partial x_j} = 0)$ as the investigated flow problems are in the low Mach number regime (Ma< 0.3), and no radiative heat sources are considered $\dot{Q} = 0$. The sensible enthalpy transport equation then simplifies to:

$$\frac{\partial(\rho h_\mathrm{s})}{\partial t} + \frac{\partial(\rho u_j h_\mathrm{s})}{\partial x_j} = -\frac{\partial J_{s,j}}{\partial x_j} + \dot{\omega}_\mathrm{T} \; . \tag{2.14}$$

The diffusive enthalpy flux $J_{s,j}$ consists of heat conduction due to temperature gradients and a flux of enthalpy due to the diffusion of individual species:

$$J_{\text{s},j} = \underbrace{-\lambda \frac{\partial T}{\partial x_j}}_{heat\ conduction} + \underbrace{\sum_{k=1}^{N} (J_{k,j} h_{\text{s},k})}_{species\ inter\ diffusion} \quad , \tag{2.15}$$

with $h_{\text{s},k}$ as the sensible enthalpy of species k ($\sum_k h_{\text{s},k} = h_{\text{s}}$). The heat release source term is computed as:

$$\dot{\omega}_{\text{T}} = -\sum_{k}^{N} \dot{\omega}_k h_k^0 \tag{2.16}$$

where $\dot{\omega}_k$ are species source terms and h_k^0 is the standard enthalpy of formation for species k. Heat fluxes due to concentration gradients (*Dufour effect*) are neglected. These are considerably small in reacting flow systems [99].

2.2 Thermo–chemical relations

In the following section important thermo–chemical relations are introduced which are needed to describe the thermodynamic state of reacting flows and close the system of conservation equations presented in Section 2.1.

Mixtures

In a multi–component mixture it is useful to work with dimensionless species fractions. One is the species *mass fraction* Y_k, which has already been introduced in Eq. 2.5. Likewise, the species *mole fraction* X_k can be determined as:

$$X_k = \frac{n_k}{n_{tot}} \ , \tag{2.17}$$

with n_k as the specific mole number and $n_{tot} = \sum_{k=1}^{N} n_k$. If not stated differently, in this work the mass fraction Y_k will be used exclusively to quantify the distribution of species in the multi–component mixture. Rather trivial, but worth to mention is the fact that all mass and mole fractions have to add up to one:

$$\sum_{k=1}^{N} Y_k = 1 \ , \qquad \sum_{k=1}^{N} X_k = 1 \ .$$

Ideal gas

Further, it is common to consider mixtures at ambient pressure conditions as *ideal gases*. This allows a linear relation between pressure p and density ρ to describe the thermodynamic state:

$$p = \frac{\rho \mathcal{R} T}{\mathcal{M}} \ , \tag{2.18}$$

with the universal gas constant $\mathcal{R} = 8.3144$ J mol^{-1} K^{-1}, and the mean molar mass $\mathcal{M}$, which is computed from the individual molar masses M_k of the species:

$$\mathcal{M} = \frac{1}{\sum_{k=1}^{N} Y_k / M_k} \tag{2.19}$$

Caloric relations

The energetic state of a mixture is expressed in this work in terms of the enthalpy h, which is the sum of the sensible enthalpy h_s and the chemical enthalpy of formation h_c. For ideal gases h is computed as:

$$h = \underbrace{\int_{T_0}^{T} c_\mathrm{p}(T')\mathrm{d}T'}_{h_\mathrm{s}} + \underbrace{\sum_{k}^{N} Y_k h_k^0}_{h_\mathrm{c}} \; . \tag{2.20}$$

Here, the reference temperature is set to $T_0 = 298.15$ K, h_k^0 is the formation enthalpy of species k, and c_p is the mixture averaged mean heat capacity at constant pressure and has a non–linear relation to the temperature. To compute the species specific heat capacities c_p,k, comprehensive reference data from experiments or molecular simulations can be used. This quantity can be expressed in polynomial form as a function of temperature in form of the 4 term NASA–polynomials [30]:

$$c_\mathrm{p,k} = \frac{\mathcal{R}}{\mathcal{M}} \left(a_{1,k} + a_{2,k}T + a_{3,k}T^2 + a_{4,k}T^3 + a_{5,k}T^4 \right) \; . \tag{2.21}$$

Through integration of Eq. (2.21) the enthalpy for each species h_k can be recovered:

$$h_k = \frac{\mathcal{R}}{\mathcal{M}} \left(a_{0,k} + a_{1,k}T + \frac{a_{2,k}}{2}T^2 + \frac{a_{3,k}}{3}T^3 + \frac{a_{4,k}}{4}T^4 + \frac{a_{5,k}}{5}T^5 \right) \; . \tag{2.22}$$

The enthalpy and heat capacity of the mixture can then be expressed as ideal mixture:

$$h = \sum_{k}^{N} Y_k h_k \; , \qquad\qquad c_\mathrm{p} = \sum_{k}^{N} Y_k c_\mathrm{p},k \; . \tag{2.23}$$

With these relations for the enthalpy (2.20) and the specific heat capacity (2.21), the temperature of the mixture can be iteratively determined, given as input the species composition, the enthalpy, and the species dependent polynomial coefficients $a_{n,k}$. The thermochemical properties can be calculated in general with a confidence of 1% in the temperature range between 150 and 3000 K [30], which is sufficiently accurate for the investigated configurations in this work.

Transport properties

The molecular viscosity is temperature dependent and determined according to the correlation of Sutherland [263]:

$$\mu = \frac{A_\mathrm{s}\, T^{3/2}}{T + T_\mathrm{s}} \; , \tag{2.24}$$

with the model constants $A_\mathrm{s} = 1.67 \cdot 10^{-6}$ Pas and $T_\mathrm{s} = 170.6$ K. The thermal conductivity of the mixture is computed based on the relation proposed by Eucken [18]:

$$\lambda = \mu c_\mathrm{v} \left(1.32 + \frac{1.77\, \mathcal{R}}{c_\mathrm{v}\, \mathcal{M}} \right) \; , \tag{2.25}$$

where $c_\mathrm{v} = c_\mathrm{p} - \mathcal{R}/\mathcal{M}$ denotes the specific heat capacity at constant volume.

2.3 Large Eddy simulation

In Large Eddy Simulations (LES) only the large scales of motion, i.e., the large eddies, are computed exactly, whereas the effect of the smallest scales needs to be modeled with a sub–grid turbulence model. The following section presents the general concept of LES as it is used in this work.

2.3.1 Turbulence and energy cascade

For a better understanding of the idea behind the LES approach it is helpful to take a closer look at the description of turbulence and the energy cascade.

In the regime of laminar flow, stream lines are in parallel and all disturbances from the initial or boundary conditions are dampened through the fluid's dynamic viscosity μ. In other words, inertial forces are dampened by viscosity, which inhibits momentum exchange perpendicular to the main flow direction. Given a flow configuration with the geometric length scale $\mathcal{L}$ and the fluid viscosity μ, it is the bulk flow velocity $\mathcal{U}$ that determines if the flow transitions from a laminar to a turbulent flow regime. This phenomenon has been studied by Reynolds [236] in 1883 and led to the formulation of the non–dimensional Reynolds number Re [237], which is the ratio between inertial forces and the kinematic viscosity $\nu = \mu/\rho$:

$$\mathrm{Re} = \frac{\mathcal{U}\mathcal{L}\rho}{\mu} = \frac{\mathcal{U}\mathcal{L}}{\nu} \tag{2.26}$$

The Reynolds number allows to quantify and compare the degree of turbulence among different configurations[3]. So, if the Reynolds number is large enough, small perturbations in the initial or boundary conditions will be amplified and lead to the chaotic, non–reproducible state of motion known as turbulence. The flow becomes rotational and three-dimensional with randomly arranged vortex structures of different size and frequency. As a consequence, turbulent motions greatly enhance the transport of mass, momentum and energy. This so called *turbulent diffusion* can exceed the molecular diffusion by several orders of magnitude [184]. Therefore, technical devices, which require a fast mixing process, operate at high Reynolds numbers.

Despite its quasi–chaotic character, turbulent flows are a superposition of eddies of length scales l. These are usually expressed as a frequency in terms of the wave number k:

$$k = \frac{2\pi}{l} \ . \tag{2.27}$$

Each eddy with wave number k has an energy $\mathcal{E}(k)$; the integral over the whole range of k yields the *turbulence kinetic energy* (TKE):

$$\mathrm{TKE} = \int \mathcal{E}(k)\mathrm{d}k \ . \tag{2.28}$$

Based on the ideas introduced by Richardson [239], Kolmogorov [137] formulated the concept of the *energy cascade*. The turbulent energy spectrum $\mathcal{E}(k)$ is depicted in Figure 2.1 and was modeled according to [225] for the hypothetical conditions of Re = 100,000 and $\mathcal{L} = 1$ m. Based on the underlying physical effects, it can be divided into three regimes:

---

[3]For example, pipe flows are considered turbulent if Re > 2300, independently of the fluid and pipe diameter.
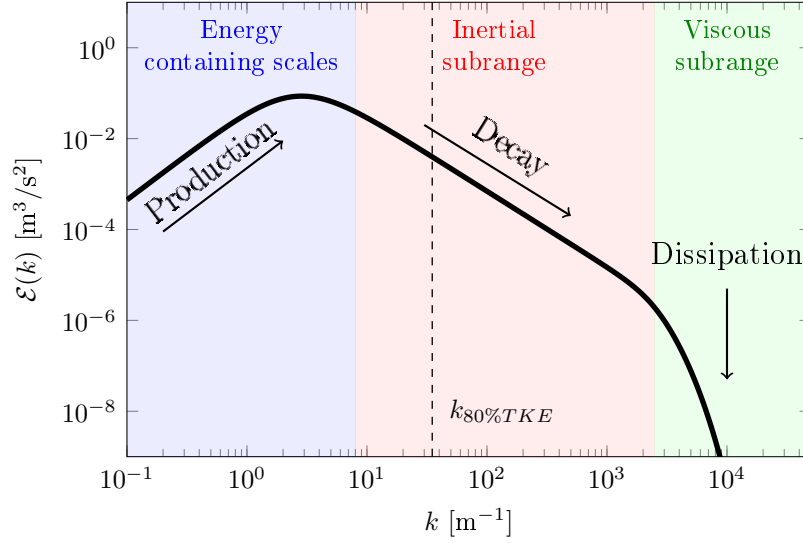
Figure 2.1: Turbulent energy spectrum $\mathcal{E}(k)$ (——) over the wave number k and cut off wave number $k_{80\%TKE}$ where 80% of TKE is reached (- - -).

Energy containing scales: On the large scales (blue region in Fig. 2.1) the production of turbulence dominates. The initial and boundary conditions, i.e. the inflow conditions and the geometry of the flow configuration, cause a shearing of the flow field which results in fluctuations in the mean flow field. The eddies are highly an-isotropic and geometry dependent. At these scales TKE is generated and advected with the mean flow field, dissipation does not play a role yet. The wave number with the highest energy corresponds to the integral length scale of the flow l_I (here $k \approx 1-2$ m^{-1}), which is comparable to the size of $\mathcal{L}$.

Inertial subrange: In this regime (red region in Fig. 2.1) it is assumed that dissipation and turbulent fluctuations are in balance, this is why it is also called the *universal equilibrium range* [13]. The larger, energy containing eddies successively break up and transfer their energy to the smaller ones; with increasing wave number the energy decays. It is also important to mention that eddies of this size ($l < \frac{1}{6}l_\mathrm{I}$, here $k \approx 8$ m^{-1}) are statistically isotropic, i.e. their orientation is not affected anymore by the boundary or initial conditions [137]. In the inertial subrange the energy depends only on the wave number k and the dissipation rate ϵ, which is assumed to be constant:

$$\mathcal{E}(k) = C_\mathrm{k}\epsilon^{2/3}k^{-5/3} \; , \tag{2.29}$$

with the Kolmogorov constant $C_\mathrm{k} = 1.5$.

Viscous subrange: At the highest wave numbers (green region in Fig. 2.1) turbulence kinetic energy is dissipated to heat due to molecular viscosity of the fluid and the energy spectrum converges to zero with a faster decay rate than in the inertial subrange. Based on dimension analysis [137] the Kolmogorov length scale l_η, i.e. the size of the smallest eddies in the specturm (here $k \approx 10^4$), can be described mathematically as:

$$l_\eta = \left(\frac{\nu^3}{\epsilon}\right)^{1/4} \; . \tag{2.30}$$

It depends only on the kinematic viscosity ν and the dissipation rate ϵ of the fluid.
Similar to the global Reynolds number Re it is also possible to formulate a turbulence
Reynolds number $\mathrm{Re_t}$ for the integral length scales and a Kolmogorov Reynolds number
Re_η:

$$\mathrm{Re_t} = \frac{u_i' l_\mathrm{I}}{\nu} \ , \tag{2.31}$$

$$\mathrm{Re}_\eta = \frac{\epsilon^{1/3} l_\eta^{4/3}}{\nu} = 1 \ . \tag{2.32}$$

u_i' denotes the velocity fluctuation in i-direction around the time averaged mean $\overline{u}_i$. According to the Reynolds decomposition the transient velocity component u_i is composed
as:

$$u_i = \overline{u}_i + u_i' \ . \tag{2.33}$$

Finally, a relation between $\mathrm{Re_t}$, l_η, and l_I can be constituted for the case of isotropic
turbulence [65]:

$$\frac{l_\mathrm{I}}{l_\eta} = \mathrm{Re_t^{3/4}} \ . \tag{2.34}$$

For a detailed review on the theory and mathematical descriptions of turbulence the reader
is referred to the books by Batchelor [13], Fröhlich [65], Piomelli [211], and Pope [225].

2.3.2   LES concept

As explained in the previous section turbulence is a multi scale problem. The large scale
structures carry most of the energy, are highly an-isotropic, affected by the flow geometry,
whereas the smallest scales are dissipativ and isotropic. It is clear that a model-free and
physically correct simulation in the sense of a DNS has to cover all these scales of turbulence.
So to say, the numerical domain needs to be at least (usually much larger) of the size of the
geometrical length scale $\mathcal{L}$, while the grid needs to be fine enough to resolve the Kolmogorov
scale l_η. Given the relation in Eq. (2.34) with increasing turbulence Reynolds numbers (usu-
ally $\mathrm{Re_t}$ increases as a result of higher flow velocites $\mathcal{U}$) of the flow configuration the number
of grid points in a three dimensional DNS scales as $\mathrm{Re_t^{9/4}}$. Given the polynomial increase
in computational costs with increasing Reynolds number DNS are limited to low Reynolds
number applications and are therefore not practical for engineering-like configurations.
In LES only the large scales of motion, which depend on the boundary conditions, must be
resolved. The small scales with their isotropic nature, which only transmit energy to smaller
scales (energy cascade), are modeled. These models introduce residual stresses, whose main
purpose is to reproduce the energy transfer accurately and mimic the dissipative effect on
the smallest scales. When the cut off filter width is in the inertial subrange of the spec-
trum, the resolution required by an LES is nearly independent of the Reynolds number [39].
Compared to DNS the computational costs of LES are far less Reynolds number dependent.

A question remains: How to choose the cut off filter width? Pope [225] argues in terms
of resolved and modeled kinetic energies, which together sum up to the TKE of the whole
energy spectrum. He proposes that the resolved part TKE_{res} should contribute to at least
80% of TKE, while the modeled part on the SGS scale TKE_{SGS} should not be more than
20%. A measure for the quality of the filter width in LES is the so called Pope criteria

$$M = \frac{\mathrm{TKE}_{SGS}}{\mathrm{TKE}_{SGS} + \mathrm{TKE}_{res}} \ , \tag{2.35}$$

where $M = 0$ would correspond to a DNS, $M = 1$ to a RANS, and $M \leq 0.2$ is a good value for LES.

It should be mentioned that the cut off filter width in LES is no tuning parameter, but it is implicitly given through the resolution of the mesh where the LES filter width is computed based on the cube root of the cell volume: $\Delta = \sqrt[3]{V_{cell}}$. The cut off wave length, so that $M \leq 0.2$, is then given as $k_{80\%TKE} = 2\pi/\Delta$. For the exemplary energy spectrum presented in Figure 2.1 it is illustrated with the vertical dashed line.

2.3.3   Filtering and filtered transport equations

Filtering

The separation of resolved and unresolved scales is mathematically achieved through the application of a low-pass filter. An arbitrary scalar $\phi = \phi(\mathbf{x})$ is then filtered through the spatial convolution with the filter operator $\mathcal{G}$ on the domain Ω as [151]:

$$\overline{\phi}(\mathbf{x}) = \int_{\Omega} \phi(\mathbf{x}')\mathcal{G}(\mathbf{x} - \mathbf{x}')\mathrm{d}\mathbf{x}' \ , \tag{2.36}$$

$\overline{\phi}$ denotes the filtered and ϕ the unfiltered quantity at the spatial location $\mathbf{x}$. Since all LES in this work have been conducted on cartesian grids with hexahedral cells the employed filter is a top-hat filter [247]. In one dimensional notation the filter operator reads for each spatial coordinate $i = 1,2,3$:

$$\mathcal{G}(x_i - x_i') = \frac{1}{\Delta} \ \mathcal{H} \left(\frac{1}{2}\Delta - |x_i - x_i'| \right) \ , \tag{2.37}$$

where $\mathcal{H}$ denotes the heaviside step function. In LES, filtering is often not done explicitly but is implicitly achieved through the choice of the numerical grid where the cell size is the filter width Δ. Hence, the computed quantities are already the filtered values and resemble the spatial mean on the given control volume, i.e. the computational cell.

In compressible flows, the high variations of density can be treated through the use of a Favre-filter, defined as:

$$\widetilde{\phi} = \frac{\overline{\rho\phi}}{\overline{\rho}} \ . \tag{2.38}$$

$\widetilde{\phi}$ is the Favre-filtered scalar. With this definition the scalar and vector components of the flow field can be decomposed into a Favre-filtered and a sub–grid scale component:

$$\phi = \widetilde{\phi} + \phi'' \ . \tag{2.39}$$

The filtered component describes the resolved scales of the flow field, i.e. it covers all time and length scales, which are larger than the filter width Δ, while the SGS component has to be modeled with adequate turbulence models. More details about the mathematical properties of the filter operator can be found in the books by Fröhlich [65] and Sagaut [242].

Filtered transport equations

Applying both filter operations, the continuity, momentum, scalar, and enthalpy equations read:

Continuity

$$\frac{\partial \overline{\rho}}{\partial t} + \frac{\partial \overline{\rho}\widetilde{u}_i}{\partial x_i} = 0 \ , \tag{2.40}$$

Momentum

$$\frac{\partial \left(\overline{\rho}\widetilde{u}_i\right)}{\partial t} + \frac{\partial \left(\overline{\rho}\widetilde{u}_i\widetilde{u}_j\right)}{\partial x_j} = -\frac{\partial \overline{p}}{\partial x_i} + \frac{\partial}{\partial x_j}\left[\overline{\tau}_{ij} - \tau_{ij}^{sgs}\right] \ , \tag{2.41}$$

with

$$\overline{\tau}_{ij} = \overline{\mu}\left(\frac{\partial \widetilde{u}_i}{\partial x_j} + \frac{\partial \widetilde{u}_j}{\partial x_i} - \frac{2}{3}\frac{\partial \widetilde{u}_k}{\partial x_k}\delta_{ij}\right) \ , \tag{2.42}$$

Species

$$\frac{\partial \left(\overline{\rho}\widetilde{Y}_k\right)}{\partial t} + \frac{\partial \left(\overline{\rho}\widetilde{u}_j\widetilde{Y}_k\right)}{\partial x_j} = -\frac{\partial}{\partial x_j}\left[\widetilde{J}_{k,j} - J_{k,j}^{sgs}\right] + \overline{\dot{\omega}}_k \ , \tag{2.43}$$

Sensible enthalpy

$$\frac{\partial \left(\overline{\rho}\widetilde{h}_{\mathrm{s}}\right)}{\partial t} + \frac{\partial \left(\overline{\rho}\widetilde{u}_j\widetilde{h}_{\mathrm{s}}\right)}{\partial x_j} = -\frac{\partial}{\partial x_j}\left[\widetilde{J}_{\mathrm{s},j} - J_{\mathrm{s},j}^{sgs}\right] - \sum_k^N \overline{\dot{\omega}}_k h_k^0 \ , \tag{2.44}$$

with

$$\widetilde{J}_{j,k} = -\overline{\rho}D_k\frac{\partial \widetilde{Y}_k}{\partial x_j} \ , \tag{2.45}$$

$$\widetilde{J}_{\mathrm{s},j} = -\lambda\frac{\partial \widetilde{T}}{\partial x_j} + \sum_{k=1}^N \left(\widetilde{J}_{k,j}\widetilde{h}_{\mathrm{s},k}\right) \ . \tag{2.46}$$

Compared to the unfiltered equations the filter operator (2.37) introduces additional terms in the transport equations (2.41) - (2.44), which resemble the small scale, or sub–grid effects of turbulence onto the large, resolved scales. In particular these are the SGS strain rate tensor:

$$\tau_{ij}^{sgs} = \overline{\rho}(\widetilde{u_iu_j} - \widetilde{u}_i\widetilde{u}_j) \ , \tag{2.47}$$

the sub–grid scale flux of species:

$$J_{k,j}^{sgs} = \overline{\rho}(\widetilde{u_jY_k} - \widetilde{u}_j\widetilde{Y}_k) \ , \tag{2.48}$$

and the sub–grid scale flux of sensible enthalpy:

$$J_{\mathrm{s},j}^{sgs} = \overline{\rho}(\widetilde{u_jh_{\mathrm{s}}} - \widetilde{u}_j\widetilde{h}_{\mathrm{s}}) \ . \tag{2.49}$$

As all these terms contain unknown quantities which cannot be computed on the resolved scale ($\widetilde{u_iu_j}$, $\widetilde{u_jY_k}$ and $\widetilde{u_jh_{\mathrm{s}}}$) they need to be modeled with adequate sub–grid scale models. Three of them will be presented in Section 2.3.4.

A further unknown quantity in the filtered species transport equation (2.43) that requires modeling is the filtered species source term $\overline{\dot{\omega}}_k$. Its correct modeling is one of the key challenges in turbulent combustion simulations, due to the highly non–linear interaction of sub–grid scale velocity fluctuations and the time scales of the chemical reaction. Two modeling approaches for $\overline{\dot{\omega}}_k$ will be presented in detail in Chapter 3.1.

2.3.4   Sub–grid scale modeling

The contribution of the unresolved scales in the filtered conservation equations has to be considered via a closure model, the *turbulence model*. It needs to reflect the influence of small-scale turbulence on the filtered variables. Turbulent structures in this wave number range can be regarded as nearly isotropic and therefore relatively simple modeling approaches can be applied. The models are essentially designed for the correct representation of the dissipation of turbulence kinetic energy in the range of high wave numbers (red region in Fig. 2.1). Fröhlich [65] provides an overview on the most widely used turbulence models. In this work three sub–grid turbulence models are presented, which belong to the class of vortex viscosity models and are based on the Boussinesq approximation, according to which the turbulent shear stress tensor is a function of the turbulent vortex viscosity μ_t:

$$\tau_{ij}^{sgs} = -2\mu_t \left(\widetilde{S}_{ij} - \frac{1}{3}\widetilde{S}_{kk}\delta_{ij} \right) \ . \tag{2.50}$$

Introducing the turbulent Prandtl Pr_t and Schmidt Sc_t numbers the sub–grid scale flux of species and sensible enthalpy can be modeled as:

$$J_{k,j}^{sgs} = -\frac{\mu_t}{Sc_\mathrm{t}}\frac{\partial \widetilde{Y}_k}{\partial x_j} \ , \tag{2.51}$$

$$J_{\mathrm{s},j}^{sgs} = -\frac{\mu_t}{Pr_\mathrm{t}}\frac{\partial \widetilde{h}_\mathrm{s}}{\partial x_j} \ . \tag{2.52}$$

The turbulent Prandtl and Schmidt numbers are assumed to be constant and equal ($Pr_\mathrm{t} = Sc_\mathrm{t} = 0.7$). However, this is a modeling assumption and these numbers are in reality not a constant but can be much larger or smaller than 0.7 [156].

If Pr_t and Sc_t are considered constant, then only μ_t needs to be modeled. In the following the Smagorinsky, the Vreman, and the WALE turbulence models are presented since they have been used throughout the present work.

Smagorinsky model

This model was proposed already 1963 by Smagorinsky [255] in the context of numerical weather forecasting and has found its way to Large Eddy Simulations. It is up to now one of the most widely used turbulence models. This algebraic model assumes a balance between production and dissipation of turbulence kinetic energy on the sub–grid scale. Based on Prandtl's mixing length hypothesis [226] the turbulent viscosity is proportional to the smallest resolved length scales (i.e. the filter width Δ) and the resolved strain rate tensor $\widetilde{S}_{ij}$:

$$\mu_t = \overline{\rho}(C_\mathrm{s}\Delta)^2\sqrt{2\widetilde{S}_{ij}\widetilde{S}_{ij}} \ . \tag{2.53}$$

C_s denotes the Smagorinsky constant. In the literature there can be found values between 0.065 for highly turbulent cases and 0.24 for decaying isotropic turbulence [65]; it is also possible to determine C_s dynamically [76]. In this work a value of $C_\mathrm{s} = 0.17$ is used. It is important to mention that the Smagorinsky model performs well for free shear flows under the assumption of isotropic turbulence.

Vreman model

In laminar and transitional flow regions the Smagorinsky model generates a very high turbulent viscosity, which is nonphysical. Therefore, Vreman [273] formulated another algebraic model to determine the turbulent viscosity:

$$\mu_t = \overline{\rho} C_{\mathrm{V}} \sqrt{\frac{B_\beta}{\alpha_{ij}\alpha_{ij}}} \ , \tag{2.54}$$

with the model constant $C_{\mathrm{V}} = 0.07$, which has been obtained from studies of isotropic turbulence. The Vreman model was found to perform better in channel flows and transitional mixing layers. Like the Smagorinsky model it solely depends on the resolved velocity gradient and the filter width Δ:

$$B_\beta = \beta_{11}\beta_{22} + \beta_{11}\beta_{33} + \beta_{22}\beta_{33} - \beta_{12}^2 - \beta_{13}^2 - \beta_{23}^2 \ ,$$

with $\beta_{ij} = \Delta^2 \alpha_{ki}\alpha_{kj}$ and $\alpha_{ij} = \frac{\partial \widetilde{u}_i}{\partial x_j}$.

WALE model

The model that has been used primarily in this work is the WALE (Wall-Adapting Local Eddy–viscosity) model. It has been proposed by Nicoud and Ducros [191] especially for wall bounded flows as it is able to mimic the local an-isotropic behavior of turbulence and the imbalance of turbulence production and dissipation in the vicinity of walls, e.g. in pipe flows. However, it also performs very well in the case of free shear flows [14]. The turbulent viscosity is computed as:

$$\mu_t = \overline{\rho}(C_{\mathrm{w}}\Delta)^2 \frac{\left(s_{ij}^d s_{ij}^d\right)^{2/3}}{\left(\widetilde{S}_{ij}\widetilde{S}_{ij}\right)^{5/2} + \left(s_{ij}^d s_{ij}^d\right)^{5/4}} \ , \tag{2.55}$$

with the WALE constant $C_{\mathrm{w}} = 0.325$ and:

$$s_{ij}^d = \frac{1}{2}\left(\left(\frac{\partial \widetilde{u}_j}{\partial x_i}\right)^2 + \left(\frac{\partial \widetilde{u}_i}{\partial x_j}\right)^2\right) - \frac{1}{3}\delta_{ij}\left(\frac{\partial \widetilde{u}_k}{\partial x_k}\right)^2 \ . \tag{2.56}$$

2.3.5 Statistical moments

For a comparison of transient flow simulations with experimental data it is necessary to extract time averaged statistical quantities from the flow simulations. In particular these are the first and the second moments of a scalar or vector component ϕ. The first moment is computed as:

$$\langle \phi \rangle = \frac{1}{\mathcal{T}} \int_{t=0}^{\mathcal{T}} \widetilde{\phi}(t) \mathrm{d}t \ . \tag{2.57}$$

The second moment is determined as:

$$\langle \phi''^2 \rangle = \frac{1}{\mathcal{T}} \int_{t=0}^{\mathcal{T}} \left(\langle \phi \rangle - \widetilde{\phi}(t)\right)^2 \mathrm{d}t \ . \tag{2.58}$$

The time interval $\mathcal{T}$ for the statistical averaging should be chosen sufficiently large, so that the moments have converged. They should not change anymore, even if a larger interval $\mathcal{T} \to \infty$ is chosen. Moreover, care has to be taken that during the averaging process the numerical solution is not biased by artifacts of the initial conditions.

Chapter 3

Turbulent combustion

In this chapter the theoretical background on combustion processes will be introduced. Throughout this chapter, if not stated differently, the expression *combustion processes* refers to the oxidation of methane (CH_4) and oxygen (O_2), the latter one usually as a compound of *air*. However, the principles of combustion apply in the same way to any other gaseous mixture of fuel and oxidizer.

Methane is the shortest and most simply structured hydrocarbon, it is readily available in the form of natural gas or can be generated synthetically. The chemical kinetics of the methane/air combustion process have been studied well over the last decades [116]. In the field of combustion under turbulent conditions, methane is both studied extensively in laboratory scale flames [7–9, 61, 171, 246], to gain fundamental insights on physical processes and the interplay between chemical reactions and turbulence, as well in industry-like combustion chambers [175, 259] with the intention to design real world applications. It is therefore the motivation in turbulent combustion modeling to devise mathematical models which are able to predict accurately the thermo–chemical processes, both in laboratory flames, and large-scale combustors, which can be employed in computational fluid dynamics (CFD) simulations at reasonable computational cost. As will be shown in this chapter, the main difficulty in LES of turbulent reactive flows arises from the unclosed filtered species source terms $\overline{\dot{\omega}}_k$ as they appear in the Favre-filtered species transport equations (2.43). More precisely, the difficulties can be separated into two categories, which have to be considered individually:

- **Chemical reaction kinetics.** Although the global conversion from reactants to products in the methane/oxygen combustion process can be written down in a simple balance equation[1] the detailed conversion from methane/air reactants to products involves more then 53 species and over 300 individual reactions. Some reactions proceed faster than others, i.e. their chemical time scales may differ several orders of magnitude and sub-reactions are intertwined with each other. Since chemical reactions take place according to deterministic laws they can be predicted via ordinary differential equations which are solved with numerical tools. However, based on the number of involved species this can be computationally very demanding and is a limiting factor in many turbulent combustion simulations.

- **Turbulence–chemistry interaction** (TCI). Turbulence causes strong mixing at the smallest scales and may interfere with the chemical reactions. For example, small

---

[1]This is anticipated from Sec. 3.2: $CH_4 + 2\,O_2 \longrightarrow CO_2 + 2\,H_2O$.

eddies can perturb the reaction zone, this can lead to local extinction of the flame. On the other hand, the heat release of the reaction causes strong gradients in the temperature field, which in turn causes strong gradients in the density and viscosity field and scatters back onto the flow field. As mentioned, chemical reactions occur at different time scales, these can differ from the time scale of turbulence.

This chapter starts with a general description of the different flame modes, which are governed by the local mixing between fuel and oxidizer. The flame mode has an impact on the flame structure and defines the modeling approach. The basics about reaction kinetics and the reaction mechanisms which have been used in this work are then introduced. The difficulty with the interaction between turbulence and chemistry, briefly mentioned in the previous paragraph, will be discussed in more detail in the last two sections.

3.1   Flame modes

The following section describes different flame modes that are often found within combustion chambers. The classification is based on the local mixing conditions between fuel and oxidizer and determines the local flame structure, pollutant formation, and temperature distribution. More importantly, the differentiation into *non–premixed*, *premixed*, and *partially premixed* combustion was historically manifested in the combustion community, as modelers devised combustion models exclusively for the simplified assumptions of either purely premixed or non–premixed combustion. Partially premixed and stratified combustion has recently gained attention as practical combustion devices can feature local inhomogeneities in the mixture composition, which exhibit characteristics of both premixed and non–premixed flames and poses new challenges for combustion modelers. The presented test cases in Chapter 6 are of the form of non–premixed and partially premixed combustion.

3.1.1   Non–premixed combustion

In non–premixed flames, also termed diffusion flames, fuel and oxidizer are initially separated. They gradually mix until they burn in the reaction zone at around stoichiometric conditions. The transport of fuel and oxidizer into the reaction zone is the result of a diffusive process. Typical technically relevant examples of non–premixed combustion are combustion chambers in aircraft engines, rockets, diesel engines, or industrial furnaces. Non–premixed combustors are considered simpler to design and provide high operational safety as the reactants are initially separated [217].

As the combustion progress is governed through the mixing of fuel and oxidizer it is useful to quantify this state via a normalized mixture fraction Z, which is a conserved scalar that represents the local fuel share (burnt/unburnt) in a mixture. Two definitions of mixture fractions are presented here. The classical formulation of the mixture fraction is based on fuel (Y_F) and oxygen (Y_{O_2}) mass fractions [205, 217]:

$$Z = \frac{sY_\mathrm{F} - Y_{\mathrm{O}_2} + Y_{\mathrm{O}_2,2}}{sY_{\mathrm{F},1} + Y_{\mathrm{O}_2,2}} \ , \tag{3.1}$$

where s denotes the stoichiometric oxygen-to-fuel ratio (for $\mathrm{CH}_4/\mathrm{O}_2$ $s = 4$), $Y_{\mathrm{F},1}$ is the fuel mass fraction in the fuel stream, and $Y_{\mathrm{O}_2,2}$ denotes the oxygen mass fraction in the oxidizer

stream (for air $Y_{O_2,2} = 0.232$). A different formulation was introduced by Bilger, Stårner, and Kee [17] and is based on the composition of the elements C, H, and O:

$$Z_{Bilger} = \frac{2(Y_C - Y_{C,2})/M_C + (Y_H - Y_{H,2})/2M_H - (Y_O - Y_{O,2})/M_O}{2(Y_{C,1} - Y_{C,2})/M_C + (Y_{H,1} - Y_{H,2})/2M_H - (Y_{O,1} - Y_{O,2})/M_O} \ , \tag{3.2}$$

where Y_s indicates the elemental mass fraction and M_s the atomic weight of element s. Subscripts 1 and 2 denote the mass fractions in the fuel and oxidizer stream, respectively. Bilger's formulation is often used to determine the mixture fraction from experimental measurement data. Both formulations for the mixture fraction in Eq. (3.1) and Eq. (3.2) yield identical results only under the *unity Lewis number* assumption when the diffusivities of the individual species are the same. The stoichiometric mixture fraction Z_{st} can be determined as:

$$Z_{st} = \left(1 + s\frac{Y_{F,1}}{Y_{O_2,2}}\right)^{-1} \ . \tag{3.3}$$

(a) Schematic of a diffusion flame.   (b) Flame structure of a diffusion flame.
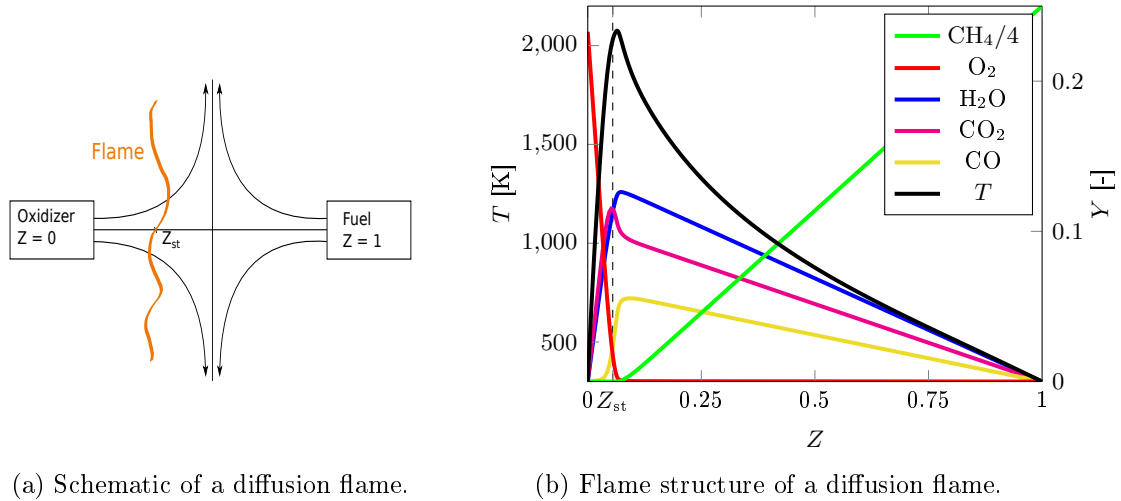
Figure 3.1: Schematic of a non–premixed counterflow flame (a) where pure fuel ($Z = 1$) and pure oxidizer ($Z = 0$) diffuse into each other. The flame is localized in the reaction zone around Z_{st}. The flame structure of major species is illustrated in (b) for a pure CH_4/air diffusion flame. At $Z_{st} = 0.055$ the temperature peaks, reactants are consumed, and products are formed. CH_4 is scaled with a factor of 0.25 for better comparison with other species.

For the combustion of pure methane ($Y_{F,1} = 1$) in air, the stoichiometric mixture fraction is $Z_{st} = 0.055$. Figure 3.1 illustrates the concept of a diffusion flame with separated fuel and oxidizer supply (a) and shows the temperature and major species distribution in mixture fraction space (b). The structure and the thickness of the reaction zone in a steady diffusion flame is not constant but governed by the mixing process and the flow conditions, rather then the chemical kinetics. An important parameter in non–premixed combustion is the instantaneous scalar dissipation rate χ defined by:

$$\chi = 2D|\nabla Z|^2 \ . \tag{3.4}$$

It has the dimension of $[\mathrm{s}^{-1}]$ and can be interpreted as diffusion velocity in mixture fraction space with D being the constant diffusivity of all species under the *unity Lewis number* assumption .

3.1.2 Premixed combustion

Contrary to the diffusion flame in premixed combustion fuel and oxidizer are homogeneously mixed at the molecular level before the mixture is ignited and the chemical reactions take place. Examples for premixed combustion are spark ignition engines, lean premixed gas turbine combustors, and household burners. The fresh gas mixtures can be characterized with the, in premixed combustion commonly used, normalized equivalence ratio ϕ defined as:

$$\phi = s \, \frac{Y_{\mathrm{F,u}}}{Y_{\mathrm{O_2,u}}} = \frac{Z}{1-Z} \frac{(1-Z_{\mathrm{st}})}{Z_{\mathrm{st}}} \ . \tag{3.5}$$

The mixture fraction is denoted as previously with Z, the fuel and oxygen mass fractions in the unburnt mixture are denoted $Y_{\mathrm{F,u}}$ and $Y_{\mathrm{O_2,u}}$, respectively. $\phi = 1$ represents a mixture at stoichiometric conditions, values of ϕ less than one characterize a lean, and values greater then one a rich mixture.

Once the homogeneous mixture is ignited with a heat source it is possible for the flame front to propagate through the fresh gas mixture, given the mixture is within the flammability limits, which are approximately between $0.5 \leq \phi \leq 1.5$. The fresh gas and the burnt products are separated only by a thin reaction zone, the thermal flame thickness δ_{th}, which is typically of the order of 0.1-1 mm for hydrocarbon laminar flames at ambient pressure. Because of the corresponding thermal fluxes, fresh gases are preheated and then start to burn, eventually resulting in a local imbalance between diffusion of heat and chemical consumption what leads to the propagation of the flame front. The propagation speed s_L of a laminar flame depends on various parameters such as the fuel and oxidizer composition, fresh gases temperature, strain, and pressure and is between $0.1 \leq s_{\mathrm{L}} \leq 0.4$ m/s for methane/air flames at ambient conditions. Laminar flame speeds are typically determined with 1D numerical codes with detailed chemistry [83] or from experiments [86].

Figure 3.2 shows a premixed flame and its structure. (a) shows a schematic configuration where unburnt reactants (with temperature T_{u} and inflow velocity u_{u}) with an equivalence ratio of $\phi = 1$ are provided from the left. After the reaction the burnt combustion products leave the domain to the right. The flame front propagates with the laminar flame speed s_{L} in negative x-direction. If the inflow velocity of the fresh gas is chosen to be $u_{\mathrm{u}} = s_{\mathrm{L}}$ then the flame front remains stationary in the reference coordinate system. The flame structure is depicted in (b). The fresh gas approaches the thin reaction zone (the orange shaded region) and is preheated in the preheat zone (blue shaded) as a result of the heat release due to the chemical reactions. In the reaction zone the reaction takes place and the fresh gas is consumed, major products (CO_2, H_2O, CO) are formed, and the temperature rises very steeply. This causes a rapid decrease in density and an increase in the velocity of burnt gas u_{b}. After the reaction zone the temperature still increases until the burnt gas temperature T_{b} is reached at chemical equilibrium conditions. As the temperature profile monotonously increases and T_{b} and T_{u} are usually known it is common practice in premixed combustion to describe the reactions progress via a normalized reaction progress variable c based on temperature [217]:

$$c = \frac{T - T_{\mathrm{u}}}{T_{\mathrm{b}} - T_{\mathrm{u}}} \ . \tag{3.6}$$

(a) Schematic of a premixed flame.

(b) Flame structure of a premixed flame.
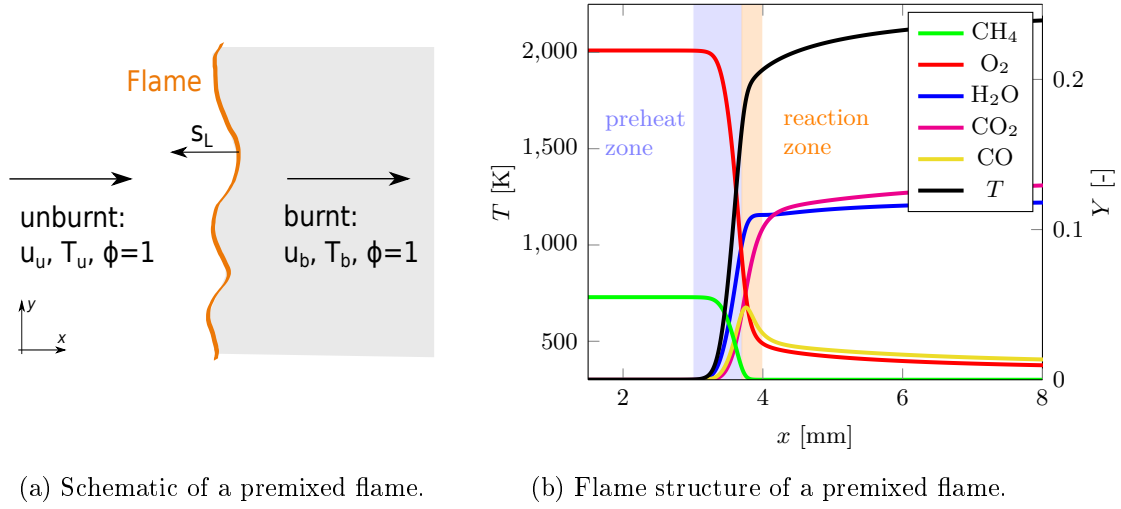
Figure 3.2: Schematic of a 2D premixed flame (a) where fuel and oxidizer are supplied in positive x-direction (from left to right). The flame structure is illustrated in (b) for a stationary premixed CH_4/air flame at $\phi = 1$. The preheat and reaction zones are highlighted with the blue and orange shaded regions.

The previously mentioned thermal flame thickness δ_{th} can be understood as the thickness of the reaction zone and is a characteristic length scale of the flame. It is determined according to [217]:

$$\delta_{th} = \frac{T_b - T_u}{\max\left(\left|\frac{dT}{dx}\right|\right)} \ , \tag{3.7}$$

where T_b and T_u are the temperatures of the fresh gas and the burnt gas, respectively, and $\frac{dT}{dx}$ is the temperature gradient inside the flame front in x-direction. Based on δ_{th} the chemical time scale or flame transit time τ_c is defined by

$$\tau_c = \frac{\delta_{th}}{s_L} \ . \tag{3.8}$$

In premixed combustion the chemical kinetics, which implicitly define the laminar flame speed s_L, control the burning rate. Hence, the burnt gas temperature T_b and the pollutant formation is only governed by the fresh gas temperature T_u, the operating pressure p, and the fresh gas composition in terms of the equivalence ratio ϕ. This is an aspect which favours the application of premixed flames in technical combustion systems as the combustion process takes place within a well-defined regime with high efficiency and good predictability of the exhaust gas emissions. The drawback, compared to diffusion flames, are increased safety issues, as the flame can propagate upstream into the fresh gas reservoir and cause a flashback.

3.1.3 Partially premixed combustion

The previously presented classification of flames into premixed and non–premixed combustion modes describe two idealized conditions which are useful to study the fundamental combustion physics in flames and derive adequate combustion models that are suitable for one case or another. However, the combustion process in industry relevant combustors is more complex and oftentimes cannot be classified as a pure diffusion or fully premixed

flame. All these states which are found in between of the two are commonly named as *partially premixed* combustion. The term refers here to compositions where the fluid parcel is inhomogeneous in the sense that it covers a wide range of mixture fractions, including flammable and non–flammable fluid.

Partial premixing can occur in pilot stabilized non–premixed flames, e.g., in the Sandia flame series [10, 124], where partial premixing of fuel and oxidizer with combustion products is the result of localized extinction, which becomes prevalent as these flames gradually approach blow–off. The mixtures feeding the reaction zone layer are then not always pure fuel and pure oxidizer, mixing continues to occur in this fluid parcel so that diffusion-like reaction zones as well as premixed propagating layers may co-exist in close proximity. A special case of partial premixing are *stratified flames* where the mixture fraction is generally within the flammability limits. This is for example the case in a premixed flame with an inhomogeneous mixture of reactants. Local gradients in the equivalence ratio can be present, causing the flame front to propagate with different laminar flame speeds. This leads to an altered flame structure compared to premixed flames. An example for a stratified flame is the Darmstadt stratified flame series [20]. Flames where the prevailing combustion mode transitions between premixed and non–premixed combustion are denoted *mixed–mode* or *multi–regime* flames. Examples are the Darmstadt multi-regime burner [32] and the Sydney piloted flame with inhomogeneous inlet [9, 174], the latter one is studied in detail within the present work.

It is important to emphasize that partial premixing is not necessarily at a disadvantage. Partial premixing of fuel and oxidizer can have indeed beneficial aspects for the heat release rates, the flame stabilization process, pollutant emissions, and it can improve the fuel efficiency, which is why it is used widely in stationary gas turbines [77]. However, the challenge remains on the side of combustion modeling, as the models ideally need to be universal in being capable to cope with conditions across the full range of combustion modes, from pre-mixed to non–premixed. It is therefore one aspect of this work to quantitatively compare different combustion models which are able to cope with partially premixed combustion. The respective models will be introduced in Chapter 4.

More information on partially premixed flames and stratified combustion can be found in the recent review articles by Masri [170] and Lipatnikov [157].

3.2   Chemical reactions

Combustion, in its most common sense, can be understood as redox reaction between a fuel and an oxidant. If the gaseous reactant mixture is ignited new molecules, the combustion products, are formed under exothermic heat release. For the considered methane/air combustion the global reaction from reactants to products reads:

$$CH_4 + 2\,O_2 \longrightarrow CO_2 + 2\,H_2O \ . \tag{3.9}$$

However, the global reaction is the result of several hundred elementary reactions and the species are only formed under the condition of global chemical equilibrium. This implies that all intermediate species, which are produced by elementary reactions, are also consumed by subsequent reactions, so that the final reaction products are CO_2 and H_2O only. If one of the elementary reactions is perturbed or inhibited, than the global equilibrium is not reached and intermediate radicals and species, such as CO, OH, H_2O_2, HCO, etc., can be

among the final combustion products. For an exact description of turbulent reactive flows, instead of considering only the global chemical equilibrium, it is necessary to quantify the formation and temporal evolution of intermediate species via elementary reactions. The foundation to describe the *reaction manifold* are the chemical kinetics.

3.2.1 Chemical kinetics

All chemical reactions take place at a definite rate and depend on the conditions of the system, such as the concentrations c_k of the reactants[2], the temperature T, and pressure p. The rate of a reaction may then be expressed as the rate of decrease of the concentration of a reactant or the rate of increase of a reaction product.

For a chemical system with N_r elementary reactions the kinetic mechanism can be written in the form:

$$\sum_{k=1}^{N} \nu'_{k,l} \mathcal{M}_k \rightleftharpoons \sum_{k=1}^{N} \nu''_{k,l} \mathcal{M}_k; \quad l = 1 \ldots N_r \ . \tag{3.10}$$
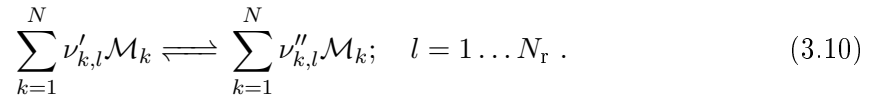
The chemical symbol of species k is denoted $\mathcal{M}_k$, $\nu'_{k,l}$ and $\nu''_{k,l}$ are the stoichiometric coefficients for the forward and backward direction in the l-th reaction. The reactions can be computed both in forward and backward direction with the respective reaction rate coefficients $k_{l,f}$ (forward) and $k_{l,b}$ (backward). These are strongly temperature dependent and can be expressed with the Arrhenius law [3]:

$$k_{l,f} = A_{l,f} T^{b_l} \exp\left(-E_{A_{l,f}}/(\mathcal{R}T)\right) \ . \tag{3.11}$$

Apart from the temperature T and the universal gas constant $\mathcal{R}$ the equation contains the pre-exponential factor $A_{l,f}$, the temperature exponent b_l and the activation energy $E_{A_{l,f}}$, which are all constant for the l-th reaction in the kinetic mechanism.

Once the reaction rate coefficients are known the production rate of species k in reaction l is given by:

$$r_l = k_{l,f} \prod_{k=1}^{N} c_k^{\nu'_{k,l}} - k_{l,b} \prod_{k=1}^{N} c_k^{\nu''_{k,l}} \ . \tag{3.12}$$

The temporal change of the concentration c_k is then determined as:

$$\frac{\mathrm{d}c_k}{\mathrm{d}t} = \sum_{l}^{N_r} \left(\nu''_{k,l} - \nu'_{k,l}\right) r_l \ . \tag{3.13}$$

Finally, the reaction source term from the species transport equation (2.6) is computed as:

$$\dot{\omega}_k = M_k \frac{\mathrm{d}c_k}{\mathrm{d}t} \ . \tag{3.14}$$

The set of equations in (3.13) is a system of *Ordinary Differential Equations* (ODE). The reaction mechanism determines the number of involved species and elementary reactions which results in N equations, each of them with N_l summands. Obviously, the more

---

[2]The concentration of a species can be computed based on the mass fractions Y_k and molar masses M_k of the involved species: $c_k = \rho \frac{Y_k}{M_k}$

species and reactions involved, the more expensive is the numerical evaluation of the reaction source terms. The computational costs are also affected by the stiffness of the system. When the chemical time scales of the reactions vary several orders of magnitude it increases as well. In this work the ODE integration is done on the central processing unit (CPU) with the highly optimized library Sundials CVODE [149]. In recent years there have also been attempts to externalize the ODE integration onto the graphics processing unit (GPU) [52, 84, 251, 253] with speed up factors in the range of $5 - 10$ compared to the conventional ODE integration on the CPU.

For more information about chemical reaction kinetics the books by Gardiner [69], Glassman and Yetter [81], Kee, Coltrin, and Glarborg [125], and Warnatz, Maas, and Dibble [279] are recommended.

3.2.2   Methane/air reaction mechanisms

There exists a variety of methane/air reaction mechanisms which can be used for the numerical evaluation of the reaction rates. Governed by the computational costs and the complexity of the underlying combustion problem either a detailed, a reduced, or a global mechanism can be employed.

The GRI-3.0 [256] from the Gas Research Institute is the most widely known detailed reaction mechanism for the combustion of methane in air. It contains 53 species and 325 elementary reactions (in its current version 3.0). Compared to experiments it predicts very well the ignition delay times, species, and radical formations under a wide range of operating conditions. However, given the number of involved species, it is computationally impracticable to use the GRI-3.0 in large scale, industry-relevant reactive flow simulations [161]. It serves for the detailed simulation of academic configurations, one dimensional parametric studies, and the validation and optimization of reduced mechanisms [1].

Based on detailed mechanisms skeletal mechanisms and analytically reduced chemistries (ARC) can be derived. The idea is to remove as many species and elementary reactions as possible while maintaining the general prediction quality in terms of ignition times, adiabatic flame temperature, or laminar flame speed. The idea is based on the mathematical analysis of the time scales and species in a reaction mechanism. Typically, between 10 to 30 species and up to 50 reactions are retained in the final kinetic scheme, with most of the stiffness removed. Due to their still quite high computational expenses, analytically reduced mechanisms are restricted to small hydrocarbons so far, but are a valuable tool for detailed simulations in the LES context. Applying the directed relation graph (DRG) method [160] Lu and Law [159] derived the *Lu30* mechanism with only 30 species and 184 reactions from the GRI-3.0 [256]. However, the complete nitrogen chemistry is removed in this mechanism. Using the computational single perturbation (CSP) method [158] eleven quasi steady state (QSS) [243] species could be determined which replaces transport equations by analytical expressions in the *Lu30*. This reduction allows to shrink it to a 19-species mechanism (*Lu19*) [159]. The *Lu19* mechanism is the one which is used mainly throughout this work, unless stated differently. Based on the GRI-1.2 (an older version of the GRI-3.0) Sankaran et al. [243] derive a similar mechanism based on analytical reduction with only 13 species (*Lu13*). More information about the state of the art design of specific ARC and their application in LES can be found in the PhD thesis by Felden [51].

Globally fitted mechanisms are the most simple ones and usually incorporate only 5 to

10 species with no more than one to six global reactions. These mechanisms are optimized against a set of flame characteristics over a specified parameter range and yield good results, e.g., on adiabatic flame temperature, laminar flame speed at a certain equivalence ratio, or burnt gas state. They are computationally very efficient as they avoid the use of radical species, whose time-scales and concentrations are much lower. However, as a result of reducing the number of elementary reactions, they can only be employed within a very narrow range of operating conditions where their predictions are reliable. Examples are the mechanisms by Westbrook and Dryer [282], and Franzelli et al. [62] (*BFER*), both with six species, and three, respectively two reaction steps. The BFER mechanism is only used in this work for a simulation of a premixed bunsen flame, presented in the Appendix C. Global mechanisms are usually used for premixed and (lean) partially premixed combustion. The original mechanism by Jones and Lindstedt [118] contains six species and four reactions steps. It has been extended by Frassoldati et al. [63] (*JL-R*) to ten species and six reaction steps to account for the dissociation effects of water and oxygen. It is still considered a global mechanism but has also been used for the simulation of non–premixed flames [117] or the simulation of rocket combustion chambers [181].

The previously mentioned mechanisms are only some examples out of a wide variety of reaction mechanisms which can be used for the oxidation of methane in air. The choice of mechanism always depends on the specific simulation problem, if it is a premixed or non–premixed flame, if the combustion environment is highly turbulent or rather laminar, and which are the quantities of interest that need to be modeled. Eventually, it is always a compromise between accuracy and computational efficiency.

3.2.3 Comparison of reaction mechanisms

In this section the following mechanisms: BFER, JL-R, Lu13, Lu19, and Lu30, are compared against the GRI-3.0. The quantitative analysis is based on three generic configurations: the freely propagating flame to obtain the laminar flame speed s_{L}, the perfectly stirred reactor to determine the ignition delay, and the counterflow diffusion flame to get the temperature and species distribution in a laminar flamelet. Finally, a conclusion is drawn considering the computation times.

Laminar flame speed

Simulations of 1D freely propagating premixed methane/air flames at ambient conditions have been conducted at different equivalence ratios ϕ to obtain the laminar flame speed s_{L}. The CANTERA [82] library was used in python as simulation tool (see also the CANTERA tutorials by CERFACS [50]). Figure 3.3 shows s_{L} for the different mechanisms over a wide range of equivalence ratios $0.5 < \phi < 1.5$; the reference mechanism GRI-3.0 is highlighted with a red solid line. Laminar flame speeds are an important parameter in the simulation of premixed and partially premixed combustion. They are a result of the fresh gas consumption rate and quantify the propagation velocity of the reaction zone in a stationary coordinate system.

Excellent agreement with the GRI-3.0 can be observed for the Lu19 and Lu30. The Lu13 is still in fairly good agreement, though there are small deviances around stoichiometry and on the fuel rich side. The BFER mechanism predicts the flame speeds very well on the fuel lean side up to a stoichiometric mixture ($\phi \leq 1$). On the fuel rich side its performance is
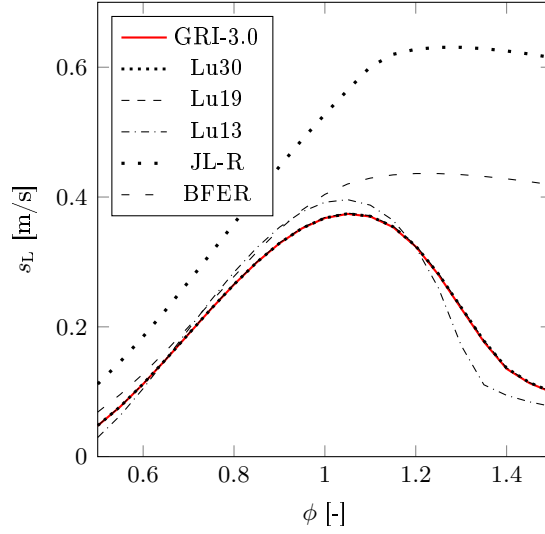
Figure 3.3: Comparison of laminar flame speeds s_L for different mechanisms and equivalence ratios ϕ at ambient conditions and $T_u = 300$ K.

quite poor as the flame speeds are highly overpredicted. However, this is not a drawback of the mechanism, as it has been designed specifically for lean premixed combustion [62] and should only be used for such configurations. A very poor prediction of the flame speed is given by the JL-R mechanism, especially on the fuel rich side where s_L is overpredicted by a factor of 2-3.

Ignition delay

The perfectly stirred, homogeneous reactor is a 0D configuration, i.e. there is no spatial, but only a temporal evolution of the quantities it contains. It allows to compute the evolution of a mixture over time under specific conditions towards its equilibrium state. This evolution can be viewed as a sort of *autoignition* of the mixture, given a sufficiently high initial temperature is set to initiate the formation of radicals from the stable species, which start the chain of elementary reactions. Of interest here is the ignition delay, which can be defined as the time until the steepest temperature gradient or the peak in the heat release is observed.

The autoignition tests have been performed at stoichiometric conditions ($Z_{st} = 0.055$, $\phi = 1$, $p = 1$ bar) with OpenFOAM using the `canteraChemistry` module. The overall simulation time was $t_{tot} = 4$ ms, with a fixed time step of $dt = 1e^{-7}$ s, the initial conditions are given in Table 3.1. The temporal evolution of temperature T, heat release rate $\dot{Q}$, and

T_{init} [K]	1600
Y_{CH_4}	0.055
Y_{O_2}	0.22
Y_{N_2}	0.725

Table 3.1: Initial conditions of the autoignition test.

CO and H_2 mass fractions are shown in Figure 3.4. Based on the GRI-3.0 reference solution
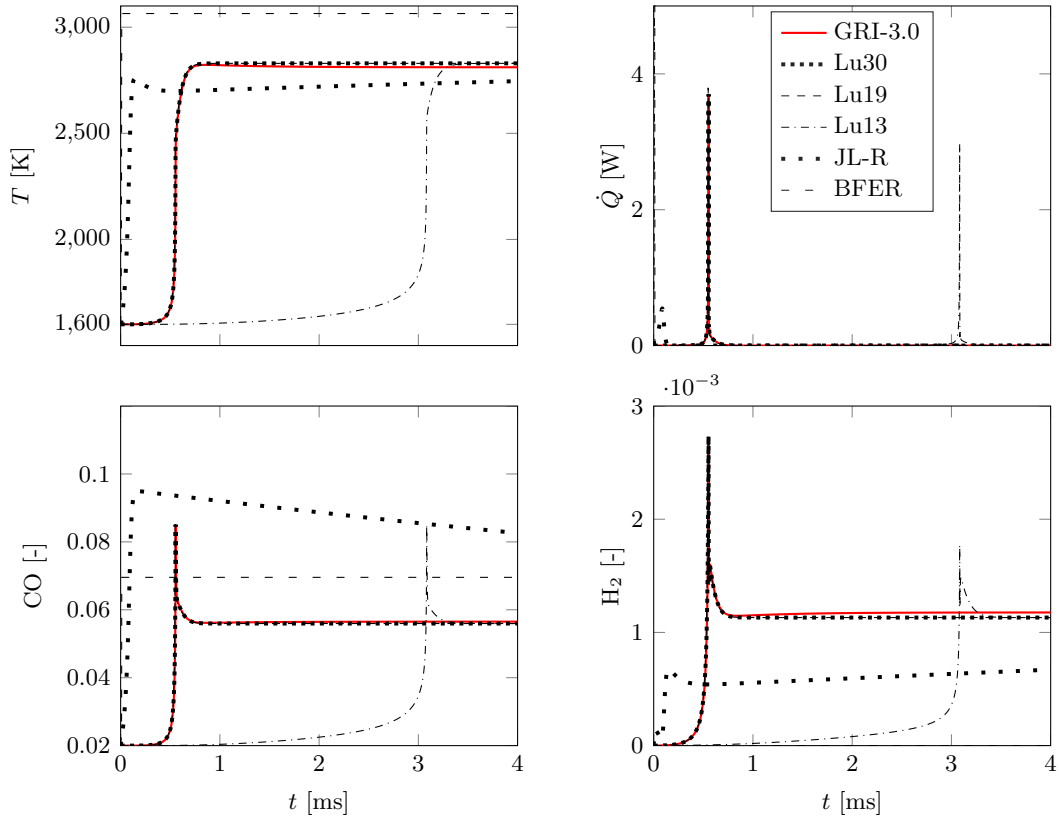
Figure 3.4: Comparison of ignition delay of temperature T, heat release $\dot{Q}$, CO, and H_2 mass fractions.

(red solid) the ignition delay time is approximately $t_{ig} = 0.7$ ms. Lu30 and Lu19 achieve excellent agreement with the GRI-3.0 in terms of ignition delay time, heat release peak, and CO and H_2 profiles. The Lu13 mechanism performs notably worse. The ignition is initiated too late, after approximately 3 ms. The heat release and the H_2 mass fractions at the ignition point are also underpredicted. To complete the picture, the results of the two global mechanisms are shown, too. Global mechanisms have no or only very few radicals, this is a crucial prerequisite for the ignition process, the results are therefore very poor and both mechanisms show almost no ignition delay.

Counterflow diffusion flame

The steady counterflow diffusion flame is another generic 1D combustion problem. As it was already mentioned in Section 3.1.1 it is an idealized set up describing non–premixed combustion where fuel and oxidizer are initially separated. Driven by molecular diffusion the components gradually mix into each other and ideal combustion conditions are reached at stoichiometry Z_{st}. There, the flame stabilizes as the chemical reactions take place and products are formed.
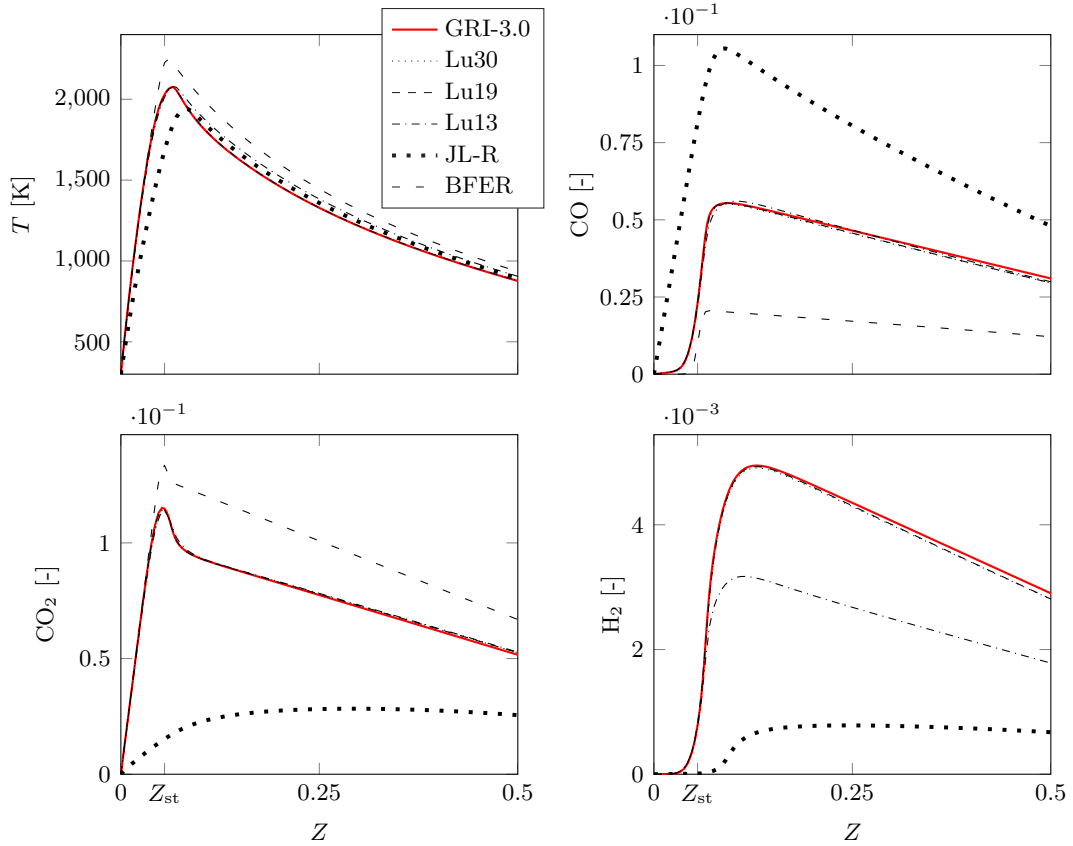
Figure 3.5: Temperature and species profiles (CO, CO_2, H_2) over mixture fraction $0 \leq Z \leq 0.5$ for the counter flow diffusion flame with different mechanisms at ambient pressure.

The counterflow diffusion flames are computed in OpenFOAM in mixture fraction space via the flamelet equations (the equations and the flamelet concept will be introduced in Section 4.2) and with the different reaction mechanisms. The scalar dissipation rate at

stoichiometry is set to $\chi_{st} = 1$. The boundary conditions are pure CH_4 ($Z = 1$) and pure air ($Z = 0$), the inlet temperatures of the fuel and oxidizer streams are $T_{CH_4} = T_{air} = 300$ K.

Figure 3.5 illustrates the temperature and mass fraction profiles for the combustion products CO, CO_2, and H_2 over the mixture fraction range $0 \leq Z \leq 0.5$. Excellent agreement with the GRI-3.0 reference solution is again found for the Lu30 and Lu19, both for temperature, and species profiles. The Lu13 is in fairly good agreement, only with slight overestimations of temperature on the fuel rich side. However, the H_2 mass fraction is underpredicted almost by a factor of 2. The two global mechanisms BFER and JL-R obtain satisfactory agreement with the reference temperature profile, though they either under, or overestimate the adiabatic flame temperature around stoichiometry. However, the species profiles cannot be reproduced with these two mechanisms and large deviations can be observed over the whole range of Z.

Conclusion

All three examples revealed excellent agreement of Lu19 and Lu30 mechanisms when compared against the GRI-3.0 reference data. However, not every mechanism is suited for every combustion problem, and vice versa not every combustion problem requires necessarily a skeletal or detailed mechanism. If, for instance, a lean freely propagating premixed flame is to be simulated, the two step BFER mechanism should be sufficient, as laminar flame speeds are in very good agreement with the GRI-3.0 (see Fig. 3.3). On the contrary, if a non–premixed flame configuration, including extinction and re-ignition events, is to be simulated, a more complex mechanism is needed. Global mechanisms are here not capable of reproducing the ignition process, also, the Lu13 should not be the mechanism of choice in such cases. Another criteria in the selection of suitable mechanisms is also given by the computation times, i.e. the computational costs associated with the respective chemical scheme. Based on the counterflow diffusion flame simulations in OpenFOAM the computation times are compared from an average of 100 time steps with a fixed step width of $dt = 1e^{-7}$ s. The normalized speed up factors are compared against the GRI-3.0 in Table 3.2. Note that this comparison includes the computational speed up for the evaluation of the chemical reaction scheme with less species plus the increased speed up associated with the solution of fewer species transport equations. Given the excellent performance of

GRI-3.0	Lu30	Lu19	Lu13	JL-R	BFER
1	2.7	3.6	9.8	26.6	47.9

Table 3.2: Comparison of normalized speed up factors against the GRI-3.0.

the Lu19 and the notable speed up against the GRI-3.0 it will be the chemical scheme of choice throughout the present work. Recently, the Lu19 has also been applied in a DNS of a partially premixed flame by Zirwes et al. [293]. They provide a detailed validation of the Lu19 against the GRI-3.0 based on species profiles in a 1D freely propagating flame and achieve also excellent agreement.

3.3 Turbulence–chemistry interaction

In Section 3.1 the different flame modes were presented and the flame structures were explained with the help of simplified and laminar flame configurations. In technically relevant

combustion devices the combustion process is usually highly turbulent and the previously described laminar flame modes are substituted by a regime where turbulence and combustion affect each other. When a flame front is exposed to turbulent flows, the turbulent fluctuations are modified by combustion because of the strong flow accelerations through the flame front induced by heat release and the large changes in kinematic viscosity. This mechanism may increase the turbulent velocity fluctuations, so called *flame-generated turbulence*. On the contrary it can also dampen these fluctuations. The flame structure can also be altered by turbulence, which may favor the chemical reactions. However, it can also completely inhibit the reactions, leading eventually to extinction and blow-off.

So to say, the superposition of combustion physics with the chaotic velocity fluctuations in turbulent flows is complex and covers time and length scales which differ several orders of magnitude. Usually, there is no way to solve a turbulent combustion problem in an analytical manner and numerical simulations are needed.

This section briefly outlines the difficulties of turbulence–chemistry interaction in combustion modeling and presents different combustion regimes, which depend on the turbulence intensity. For more information on this topic the reader is referred to the books by Peters [205] and Poinsot and Veynante [217].

3.3.1 Regimes of turbulent premixed combustion

In premixed turbulent combustion, eddies stretch and fold the flame front leading to an increase in flame surface area A_T compared to a laminar flame surface are A_L, followed by an increased volumetric heat production. A turbulent premixed flame front is depicted schematically in Figure 3.6. The turbulent flow distorts the flame front so that at each moment in time the instantaneous flame surfaces have different shapes. Compared to the laminar case, the flame fronts are unsteady and irregularly wrinkled. Turbulent eddies (blue swirls) deform the flame front as they pass through the flame. In general, the turbulent flame thickness and flame speeds s_T in a volumetric control volume are higher than in the laminar case as a result of an increased flame surface A_T compared to the planar laminar flame surface A_L. The local laminar flame speeds $s_L(\mathbf{x})$ at each point on the flame front can also change as the front experiences different stretch rates which has an impact on the chemical reaction rates. Except in DNS, the turbulent flame front is rarely fully resolved in numerical simulations. Usually the cell averaged turbulent flame speed s_T or the flame wrinkling as relation of wrinkled flame surface to planar surface A_T/A_L have to be modeled.

As the structure of the flame front highly depends on the turbulence intensity and the size of the vortexes it is useful to classify the degree of flame wrinkling into different regimes of combustion. Figure 3.7 shows the modified regime diagram according to Borghi [22] in the modified version by Peters [204]. Herein, different length scales of are used. The turbulence intensity is represented by the magnitude of the velocity fluctuations u'. Non-dimensional numbers are used to separate the different regimes. The Damköhler number Da relates the time scales of turbulence τ_I (integral time scale) and chemical reactions $\tau_c = \delta/s_L$. The Karloviz number Ka relates the flame thickness δ to the Kolmogorov length scale l_η. They are defined as:

$$\mathrm{Da} = \frac{\tau_I}{\tau_c} = \frac{l_I s_L}{\delta u'} \;, \tag{3.15}$$
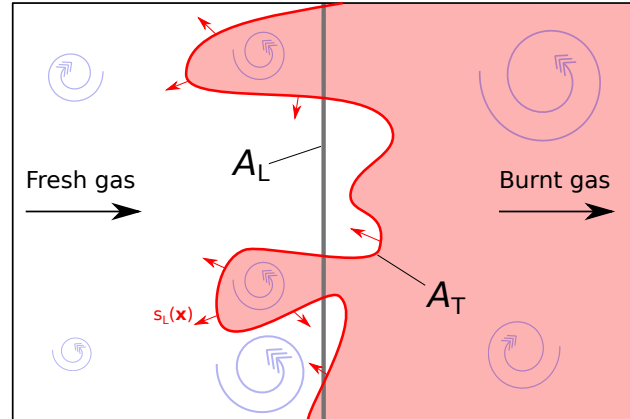
Figure 3.6: Turbulent premixed flame front. The flame surface area is wrinkled and increased by turbulent eddies.

and

$$\mathrm{Ka} = \left(\frac{\delta}{l_\eta}\right)^2 \; . \tag{3.16}$$

The line $\mathrm{Re_t} = 1$ separates turbulent flames from laminar flames, i.e. even if there are moderate velocity fluctuations all flames where the turbulent Reynolds number (2.31) $\mathrm{Re_t} \leq 1$ can be considered *laminar*. The region separated by $\mathrm{Ka} = 1$ denotes the condition that the flame thickness is equal to the Kolmogorov length scale, i.e. the smallest eddies are still of the size of the flame front and the vortices cannot perturb the inner structure of the flame. The lower-right corner ($\mathrm{Ka} \leq 1$) is subdivided into *wrinkled* and *corrugated flames*. In both cases the inner flame structure remains unaffected by turbulence and flame stretch has no effect. In the corrugated regime, however, turbulence is sufficiently high to separate and isolate pockets of fresh gas from the flame brush. Increasing the degree of turbulence the flames enter the *thin reaction zone* ($1 < \mathrm{Ka} < 100$). Here, the Kolmogorov scale is smaller than the flame thickness δ but still larger than the reaction zone δ_{th}. The eddies can enter the preheat zone and thicken it, the actual reaction layer remains unaffected. However, the flame structure can be altered and flame stretch plays a role. The region above $\mathrm{Ka} > 100$ is considered highly turbulent. As the eddies in this regime are smaller than the reaction zone they can enter it and disturb the chemical reaction as time scales are faster than the reaction ($\mathrm{Da} \leq 1$). This may lead to local extinction and the flame can no longer be considered as given separation layer between fresh gas and burnt products, i.e. the flame front exhibits *broken reaction zones*.

3.3.2   Regimes of turbulent non–premixed combustion

Unlike in turbulent premixed flames, the regime description is more difficult in turbulent non–premixed combustion. First, reactants have to mix before the reaction takes place and the reactions are governed by the mixing process. Fast mixing, compared to chemistry, may lead to premixed combustion. The second difficulty arises from the fact that diffusion flames do not exhibit well-defined characteristic scales. A diffusion flame does not feature a propagation speed and the local flame thickness depends much more on the flow conditions than in premixed flames.
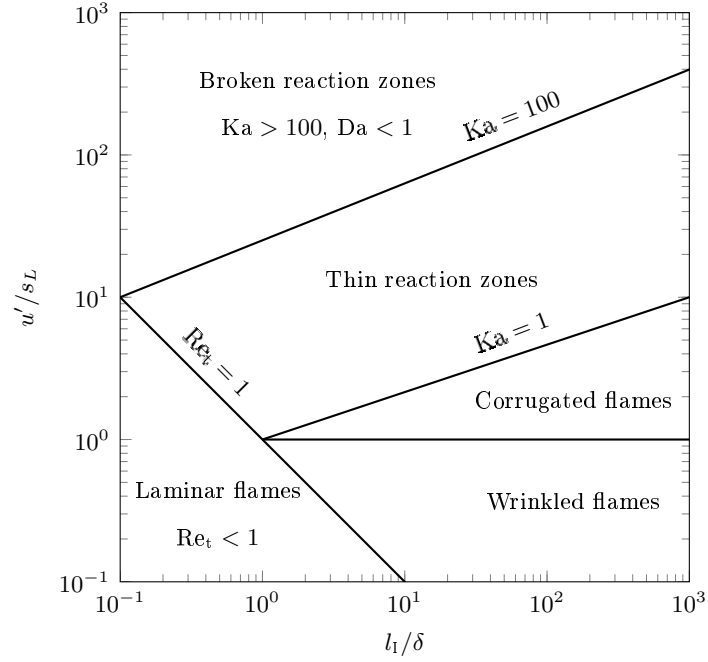
Figure 3.7: Premixed combustion regime diagram according to [204] with logarithmic axis scaling.

Figure 3.8 provides a simple classification of combustion regimes based on the turbulent Reynolds and Damköhler numbers. The Damköhler number (3.15) has already been introduced and relates the integral time scale of turbulence τ_I to the chemical time scales τ_c. If the degree of turbulence is low ($\mathrm{Re_t} \leq 1$) the flame remains laminar and is not of interest here. In the turbulent case ($\mathrm{Re_t} < 1$) a distinction between the *flamelet*, *unsteady*, and *extinction* regime is made. To differentiate the regimes, the local flame Damköhler number Da^{fl} is needed:

$$\mathrm{Da}^{fl} = \frac{\tau_f}{\tau_c} \approx \frac{1}{\chi_{st}\tau_c} \; . \tag{3.17}$$

As mentioned before, it is difficult to obtain a local flame time scale, this is why it is appoximated with the mixture fraction scalar dissipation rate at stoichiometery χ_{st} as $\tau_f \approx 1/\chi_{st}$. χ_{st} can be understood as an inverse time scale of the diffusion process. It is not constant throughout the flame, but changes with the local flow conditions in space and time. Da^{fl} can be related to Da as:

$$\mathrm{Da} \approx 2\sqrt{\mathrm{Re_t}}\mathrm{Da}^{fl} \; . \tag{3.18}$$

In the flamelet regime the Damköhler number is high, meaning the chemical reactions are fast compared to the turbulence time scale. The flame front adopts sufficiently fast to the turbulent motions and the inner structure of the flame is expected to remain the same as in the laminar case. This assumption builds the foundation for the widely used *laminar flamelet* combustion model. When the flame Damköhler number is below the laminar flamelet assumption (LFA) ($\mathrm{Da}^{fl} < \mathrm{Da}_{LFA}$) the flame becomes unsteady and exhibits localized extinction and re-ignition phenomena. However, the flame is still able to burn. Below the delimitation of extinction ($\mathrm{Da}^{fl} < \mathrm{Da}_{ext}$) chemical reactions are too slow and the
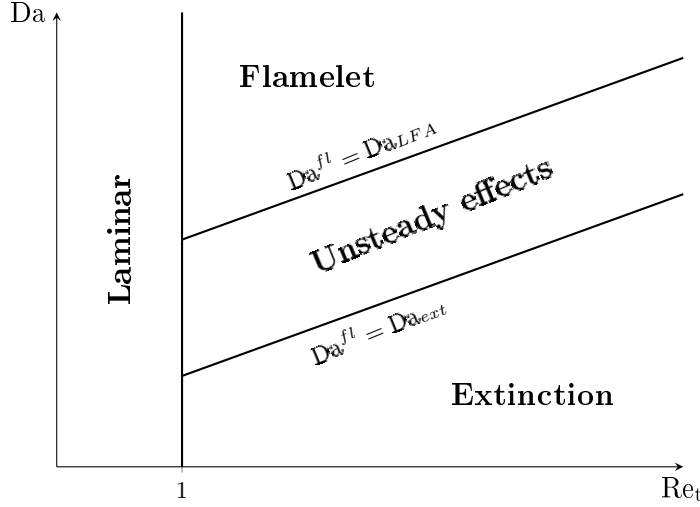
Figure 3.8: Non–premixed combustion regime diagram according to [217] based on the turbulent Reynolds and Damköhler number.

flame experiences quenching and blow-off. Stable burning conditions are not possible any more as the local mixture composition changes faster than the time needed by the chemical reactions to convert reactants to products.

An exact a-priori or analytical determination of Da_{LFA} and Da_{ext} is difficult and usually they are estimated from high fidelity simulations, e.g. as done in a DNS study by Cuenot and Poinsot [43].

3.3.3 The role of the sub–grid PDF in filtered combustion simulation

Before the actual combustion models are introduced a short and general example is considered to illustrate the role of the sub–grid PDF in combustion LES.

First, consider the adiabatic flame temperature T to be a non-linear function of the mixture fraction Z in the form of $f : Z \rightarrow T$, as it was presented in Figure 3.5 in the context of a non–premixed counterflow diffusion flame. Second, the LES cell is considered to be a super cell, consisting of $3 \times 3 \times 3 = 27$ DNS cells, as depicted in Figure 3.9 (a). Each DNS cell contains an individual scalar value for the mixture fraction $Z_{i,j,k}$, where $i,j,k \in \{1; 2; 3\}$. The histogram of an arbitrary LES sub–grid distribution of Z is shown in Figure 3.9 (b). The filtered mean $\widetilde{Z}$ can be easily obtained from the individual $Z_{i,j,k}$ as $\widetilde{Z} = 1/27 \sum_{i,j,k}^{3} Z_{i,j,k} = 0.1025$. Note that the presented SGS distribution of Z is not from an actual DNS, the random values have been sampled from a normal distribution with mean 0.1 and a standard deviation of 0.05, i.e. $\widetilde{Z} \approx \mathrm{E}[Z] = 0.1$ and $\widetilde{Z''^2} \approx \mathrm{var}[Z] = 0.0025$. The term DNS is used in this context only as a reference, since DNS resolves all length scales there is no sub–grid contribution.

In the next step, the non-linear mapping function is applied to obtain the temperatures $T_{i,j,k} = f(Z_{i,j,k})$. The histogram of the temperature distribution is shown in Figure 3.10 (a). It is evident that this distribution is not a normal one anymore, it is also heavily skewed as a result of the non-linear mapping f. The filtered temperature can again be computed as an ensemble average, i.e. $\widetilde{T} = 1/27 \sum_{i,j,k}^{3} T_{i,j,k} = 1726$ K. However, from the LES transport
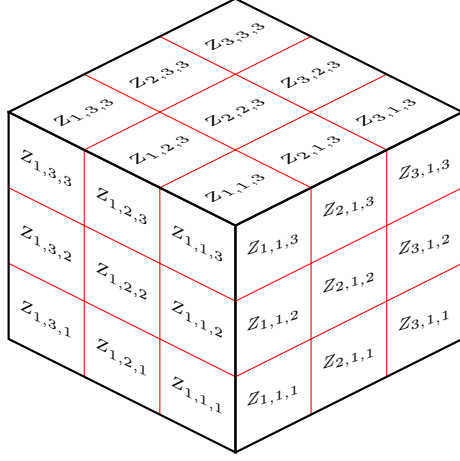
(a) LES cell consisting of $3 \times 3 \times 3$ DNS cells with individual mixture fractions $Z_{i,j,k}$.
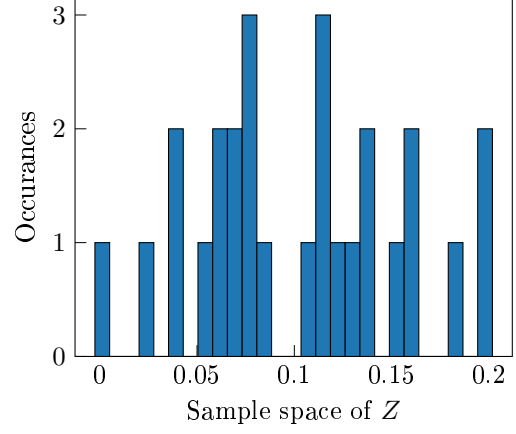
(b) LES sub–grid distribution of Z.

Figure 3.9: LES cell composed of DNS cells and histogram of the sub–grid distribution of Z.
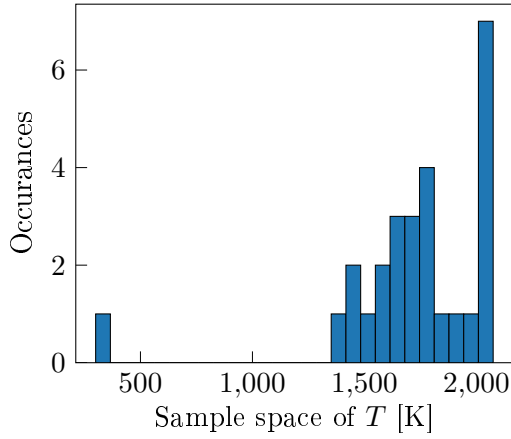
(a) LES sub–grid distribution of the temperature.
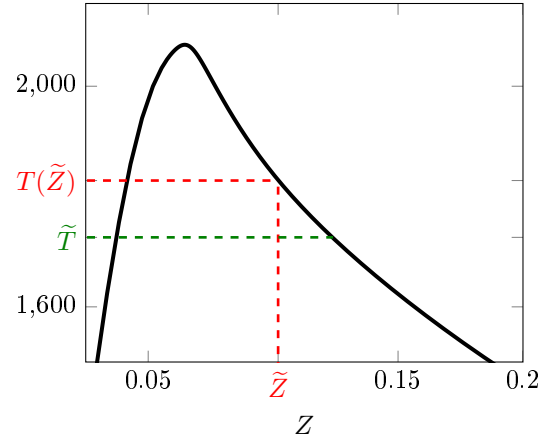
(b) Comparison of $\widetilde{T}$ vs. $T(\widetilde{Z})$.

Figure 3.10: Histogram of the sub–grid distribution of T and comparison of filtered temperature $\widetilde{T}$ with the temperature of the filtered mixture fraction $T(\widetilde{Z})$ as a function of Z.

equations only the controlling variable $\widetilde{Z}$ is known, and not the individual $Z_{i,j,k}$. If $\widetilde{Z}$ is used to predict the mean temperature in the LES cell as $T(\widetilde{Z}) = f(\widetilde{Z}) = 1827$ K it is actually higher than $\widetilde{T}$. This is illustrated in Figure 3.10 (b). Due to the non-linear relation between the two thermo-chemical states Z and T, and the high sub-grid variance of Z, $\widetilde{T}$ cannot be obtained any more through direct mapping of $\widetilde{Z}$ since $\widetilde{T} \neq T(\widetilde{Z})$. The sub–grid PDF $\widetilde{\mathcal{P}}_{sgs}(Z)$ of Z is therefore needed:

$$\widetilde{T} = \int T(Z)\widetilde{\mathcal{P}}_{sgs}(Z) \, \mathrm{d}Z \ .$$

From Figure 3.9 (b) it becomes clear that a certain level of sub–grid variance $\widetilde{Z''^2}$ is needed to form a non-trivial PDF $\widetilde{\mathcal{P}}_{sgs}(Z)$. In other words, if $\widetilde{Z''^2} \to 0$ then the PDF shrinks to a δ-function $\widetilde{\mathcal{P}}_{sgs}(Z) \approx \delta(Z - \widetilde{Z})$. In this case the filtered temperature can be approximated with the temperature from the filtered mixture fraction $\widetilde{T} \approx T(\widetilde{Z})$. So far, this aspect is given very little attention in the literature and previous studies on combustion LES. Therefore, the magnitude of the sub–grid variance $\widetilde{Z''^2}$ will also be investigated in this work and it will be analyzed to what extent it is legitimate to presume a δ-function for the sub–grid PDF $\widetilde{\mathcal{P}}_{sgs}(Z)$.

Chapter 4

Stochastic Fields and FPV combustion model

In the previous chapters, the fundamentals of Large Eddy Simulation were outlined, and the complex nature of turbulent combustion phenomena was discussed. A general overview on current trends in combustion modeling has already been given in Section 1.3.2. In this chapter the two combustion models, which are used throughout this work are presented. These are the Eulerian Stochastic Fields (ESF) method, which belongs to the family of transported PDF methods and the flamelet/progress variable (FPV) model, which uses tabulated chemistry and a presumed PDF approach.

4.1   Eulerian Stochastic Fields method

4.1.1   Filtered density function

Before the PDF transport equation and the ESF method can be introduced, a definition of the filtered sub–grid PDF that describes the instantaneous distribution of the reactive scalars within the LES filter volume, is given here. The one-point marginal (or *fine–grained*) probability density function $\mathcal{P}_\alpha$ of any scalar quantity ϕ_α, i.e. species or enthalpy, at any time t and any point $\mathbf{x}$ in space can be described as:

$$\mathcal{P}_\alpha(\psi_\alpha; \mathbf{x},t) = \delta(\psi_\alpha - \phi_\alpha(\mathbf{x},t)) \ , \tag{4.1}$$

where ψ_α is the 'phase space' for the scalar quantity ϕ_α, i.e. it describes the accessible sample space. δ is a Dirac delta function with the following properties with $\underline{\psi} = [\psi_1,...,\psi_N]$ and $\underline{\phi} = [\phi_1,...,\phi_N]$, where N is the number of involved scalars:

$$\int_{-\infty}^{+\infty} \delta(\underline{\psi}) \mathrm{d}\underline{\psi} = 1 \ , \tag{4.2}$$

$$\int_{-\infty}^{+\infty} f(\underline{\psi}) \delta(\underline{\psi} - \underline{\phi}) \mathrm{d}\underline{\psi} = f(\underline{\phi}) \ . \tag{4.3}$$

In reactive flows, with the large number of species involved in the combustion process, the joint PDF $\mathcal{F}(\underline{\psi}; \mathbf{x},t)$ for the entire set of scalars $\underline{\psi}$ is of interest. It is obtained as the product

of the fine–grained probabilities $\mathcal{P}_\alpha$ for each scalar quantity ϕ_α [221]:

$$\mathcal{F}(\underline{\psi}; \mathbf{x}, t) = \prod_{\alpha=1}^{N} \delta(\psi_\alpha - \phi_\alpha(\mathbf{x}, t)) \,, \tag{4.4}$$

The filtered and density weighted joint SGS PDF $\widetilde{\mathcal{P}}_{sgs}$ is then obtained through convolution of Eq. (4.4) with the LES filter kernel $\mathcal{G}$, as described in Eq. (2.36):

$$\widetilde{\mathcal{P}}_{sgs}(\underline{\psi}; \mathbf{x}, t) = \frac{1}{\bar{\rho}} \int_\Omega \rho(\mathbf{x} - \mathbf{x}') \prod_{\alpha=1}^{N} \delta(\psi_\alpha - \phi_\alpha(\mathbf{x}, t)) \, \mathcal{G}(\mathbf{x} - \mathbf{x}') \mathrm{d}\mathbf{x}' \,. \tag{4.5}$$

The SGS PDF $\widetilde{\mathcal{P}}_{sgs}$ is of N dimensions and describes the probability that the scalar value ϕ_α is observed within the interval ψ_α and $\psi_\alpha + \mathrm{d}\psi_\alpha$ for a particular flow realization. In the LES context the SGS PDF is an instantaneous quantity which only describes probable states within the filter volume in a statistical sense. It worth to mention that $\widetilde{\mathcal{P}}_{sgs}$ does not contain any information on two point correlations or the temporal evolution of the scalar composition.

As with any other probability density function, all statistical moments can be obtained from $\widetilde{\mathcal{P}}_{sgs}$. The filtered scalar mean $\widetilde{\phi}_\alpha$ is the first moment and can be determined as:

$$\widetilde{\phi}_\alpha = \int_{-\infty}^{+\infty} \psi_\alpha \widetilde{\mathcal{P}}_{sgs}(\underline{\psi}; \mathbf{x}, t) \mathrm{d}\psi_\alpha \,, \tag{4.6}$$

the second moment, the sub–grid variance ϕ_α'', is obtained as:

$$\phi_\alpha'' = \sqrt{\int_{-\infty}^{+\infty} \psi_\alpha^2 \widetilde{\mathcal{P}}_{sgs}(\underline{\psi}; \mathbf{x}, t) \mathrm{d}\psi_\alpha - \left(\widetilde{\phi}_\alpha\right)^2} \,. \tag{4.7}$$

4.1.2   PDF transport equation

The spatial and temporal evolution of the one-point, one-time joint sub–grid PDF can be described with a transport equation. The benefit of such an approach is that species reaction source terms appear in closed form. The general concept for PDF transport equations has first been introduced by Dopazo and O'Brien [48] and was further elaborated for the RANS context by Pope [221, 222]. Following the procedures described by Colucci et al. [42], Gao and O'Brien [67], and Jaberi et al. [110] the conservation equation for the joint SGS PDF $\widetilde{\mathcal{P}}_{sgs}(\underline{\psi})$ in the LES context reads:

$$\underbrace{\bar{\rho}\frac{\partial \widetilde{\mathcal{P}}_{sgs}(\underline{\psi})}{\partial t}}_{\mathrm{I}} + \underbrace{\bar{\rho}\widetilde{u}_j\frac{\partial \widetilde{\mathcal{P}}_{sgs}(\underline{\psi})}{\partial x_j}}_{\mathrm{II}} + \underbrace{\sum_{\alpha=1}^{N} \frac{\partial}{\partial \psi_\alpha}\left(\bar{\rho}\dot{\omega}_\alpha \widetilde{\mathcal{P}}_{sgs}(\underline{\psi})\right)}_{\mathrm{III}} =$$

$$-\underbrace{\frac{\partial}{\partial x_j}\left[\left((\widetilde{\rho u_j} - \bar{\rho}\widetilde{u}_j)|\underline{\phi} = \underline{\psi}\right)\widetilde{\mathcal{P}}_{sgs}(\underline{\psi})\right]}_{\mathrm{IV}}$$

$$-\underbrace{\sum_{\alpha=1}^{N}\frac{\partial}{\partial \psi_\alpha}\left[\left(\overline{\frac{\mu}{\sigma}\frac{\partial \phi_\alpha}{\partial x_j}}\bigg|\underline{\phi} = \underline{\psi}\right)\widetilde{\mathcal{P}}_{sgs}(\underline{\psi})\right]}_{\mathrm{V}} \,. \tag{4.8}$$

The PDF transport equation (4.8) is formulated for the assumption of equal diffusivities (Le = 1) and consists of five (I-V) terms that will be explained hereafter. Term I describes the temporal evolution of $\widetilde{\mathcal{P}}_{sgs}$, and Term II accounts for the convective transport on the resolved scales. Chemical reactions are contained in Term III, note that reaction source term $\dot{\omega}_\alpha$ appears in closed form, so no additional sub–grid TCI combustion model is needed, only the thermo–chemical scheme has to be provided (usually via a reduced chemical mechanism). Term IV represents scalar conditioned convective transport on the sub–grid scale. It requires closure as it results from SGS velocity fluctuations that are not resolved on the LES grid. Usually this is achieved with a gradient flux model [111, 252]:

$$
\left((\widetilde{\rho u_j} - \widetilde{\rho}\widetilde{u}_j) | \underline{\phi} = \underline{\psi} \right) \widetilde{\mathcal{P}}_{sgs}(\underline{\psi}) = -\frac{\mu_t}{\sigma_t} \frac{\partial \widetilde{\mathcal{P}}_{sgs}(\underline{\psi})}{\partial x_j} \; . \tag{4.9}
$$

Term V represents the molecular diffusion of the PDF. σ denotes the Schmidt or Prandtl number, depending if species or enthalpy is treated. This term also requires modeling since it contains scalar gradients that cannot be represented by the one-point PDF. First, it is decomposed to:

$$
\begin{aligned}
-\sum_{\alpha=1}^{N} \frac{\partial}{\partial \psi_\alpha} &\left[\left(\overline{\frac{\mu}{\sigma} \frac{\partial \phi_\alpha}{\partial x_j}} \Big| \underline{\phi} = \underline{\psi} \right) \widetilde{\mathcal{P}}_{sgs}(\underline{\psi}) \right] = -\frac{\partial}{\partial x_j} \left[\frac{\mu}{\sigma} \frac{\partial \widetilde{\mathcal{P}}_{sgs}(\underline{\psi})}{\partial x_j} \right] \\
-\underbrace{\sum_{\alpha=1}^{N} \sum_{\beta=1}^{N} \frac{\partial^2}{\partial \psi_\alpha \partial \psi_\beta} \left[\left(\overline{\frac{\mu}{\sigma} \frac{\partial \phi_\alpha}{\partial x_j} \frac{\partial \phi_\beta}{\partial x_j}} \Big| \underline{\phi} = \underline{\psi} \right) \widetilde{\mathcal{P}}_{sgs}(\underline{\psi}) \right]}_{\mathcal{M}_{sgs}(\underline{\psi}; \mathbf{x}, t)} \; .
\end{aligned} \tag{4.10}
$$

The first term on the right hand side of this equation (4.10) accounts for the effects of molecular diffusion in spatial transport of the PDF and is closed. The second term contains the filtered conditional scalar dissipation rates and accounts for the effect of molecular mixing on the sub–grid scale and requires modeling. Usually it is referred to as the *micro mixing* term $\mathcal{M}_{sgs}(\underline{\psi}; \mathbf{x}, t)$. An ideal mixing model has to satisfy certain criteria [178, 225, 262] to be in accordance with the laws of physics. The most important ones are, the model must not change the mean of the scalars on the sub–grid scale, the scalar variance must decrease, the joint PDF of inert scalars should relax to a joint Gaussian in the case of isotropic turbulence, and mixing should occur locally in the composition space.

   In the present work the interaction by exchange with the mean (IEM) [272], also named linear mean-square estimation (LMST) [48] model will be used. There are several other models available, such as the modified Curl's model (MC) [112], the Euclidean minimum spanning tree (EMST) model [262], the shadow positioning mixing model (SPMM) [223], and the parameterized scalar profile (PSP) model [178]. The IEM model has several modeling deficits, most importantly the joint PDF of inert scalars does not relax to a Gaussian. However, Jaberi et al. [110] and Raman and Pitsch [233] could demonstrate that in LES the IEM model provides sufficiently accurate results. It has to be mentioned that the impact of the employed mixing model is more evident in the RANS context. In LES, the large scale energetic motions and scalar fluctuations are resolved and the SGS mixing provided through the IEM model may be adequate for many practical situations [228] and there is so far no evidence that more complex modeling approaches would perform significantly better in LES. Moreover, it follows a straight forward implementation. For a detailed comparison of different mixing models the reader is referred to [36, 37, 179, 235].

With the IEM approach the mixing term $\mathcal{M}_{sgs}(\underline{\psi}; \mathbf{x},t)$ is modeled as:

$$\mathcal{M}_{sgs}(\underline{\psi}; \mathbf{x},t) = \frac{\overline{\rho}}{2\tau_{sgs}} \sum_{N}^{\alpha=1} \frac{\partial}{\partial \psi_\alpha} \left[\left(\psi_\alpha - \widetilde{\phi}_\alpha(\mathbf{x},t) \right) \widetilde{\mathcal{P}}_{sgs}(\underline{\psi}) \right] \ , \tag{4.11}$$

with the SGS mixing time scale τ_{sgs} approximated as [117]:

$$\frac{1}{\tau_{sgs}} = C_\mathrm{D} \frac{\mu + \mu_t}{\overline{\rho}\Delta^2}. \tag{4.12}$$

Here, Δ is the LES filter width and C_D is the micro–mixing constant. It is usually assumed to be 2.0 [5, 64, 122]. However, variations of C_D from 0.68 to 2.3 have also been reported [228]. Its influence will be investigated in the present work.

With the previously described modeling approaches the PDF transport equation (4.8) can be re-written as:

$$\begin{aligned}
\overline{\rho}\frac{\partial \widetilde{\mathcal{P}}_{sgs}(\underline{\psi})}{\partial t} + \overline{\rho}\widetilde{u}_j \frac{\partial \widetilde{\mathcal{P}}_{sgs}(\underline{\psi})}{\partial x_j} + \sum_{\alpha=1}^{N} \frac{\partial}{\partial \psi_\alpha} \left(\overline{\rho}\dot{\omega}_\alpha \widetilde{\mathcal{P}}_{sgs}(\underline{\psi}) \right) \ = \ & \\
-\frac{\partial}{\partial x_j} \left[\left(\frac{\mu}{\sigma} + \frac{\mu_t}{\sigma_t} \right) \frac{\partial \widetilde{\mathcal{P}}_{sgs}(\underline{\psi})}{\partial x_j} \right] - \frac{\overline{\rho}}{2\tau_{sgs}} \sum_{\alpha=1}^{N} \frac{\partial}{\partial \psi_\alpha} \left[\left(\psi_\alpha - \widetilde{\phi}_\alpha(\mathbf{x},t) \right) \widetilde{\mathcal{P}}_{sgs}(\underline{\psi}) \right] \ . &
\end{aligned} \tag{4.13}$$

4.1.3 Monte Carlo methods

In its current form the modeled PDF transport equation (4.13) cannot be solved with standard difference methods due to its high dimensionality. The computational cost increases exponentially with the number of involved scalars. When for example the 19 species Lu19 mechanism [159] is used it is currently not feasible (and probably will not be in the near future) to solve the PDF transport equation with conventional analytical methods. Instead, Monte Carlo methods can be used to constitute a *stochastic partial differential equation* (SPDE) which is equivalent to Eq. (4.13). This is based on the principle of statistically equivalent systems. It means that although two systems may instantly have different states, they can produce the same statistical moments.

The foundation of this approach is that the PDF transport equation can be seen as a generalized diffusion process. A mathematical formulation of this process is given by the *Fokker-Planck* equation [68]. In one dimension it has the following form for a probability density function $p(S(t),t)$ of the stochastic variable $S(t)$:

$$\frac{\partial}{\partial t} p(S(t),t) = -\frac{\partial}{\partial S_\alpha(t)} \left[\mathcal{A}(S(t),t)p(S(t),t) \right] + \frac{\partial^2}{\partial S^2} \left[\mathcal{D}(S(t),t)p(S(t),t) \right] \ . \tag{4.14}$$

In this equation (4.14) S would correspond to the sample space ψ_α of species α in the PDF transport equation (4.13). $\mathcal{A}$ is a drift term and $\mathcal{D}$ is the diffusion coefficient. The solution of equation (4.14) is equivalent to the solution of the *stochastic differential equation* (SDE) which obtains the same probability density function. In *Itô* formalism it reads:

$$\mathrm{d}\mathbf{S}^n(t) = \mathcal{A}^n(\mathbf{S}^n(t),t)\mathrm{d}t + \sqrt{2\mathcal{D}^n(\mathbf{S}^n(t),t)}\mathrm{d}W^n \ . \tag{4.15}$$

$\mathbf{S}^n$ represents the n-th stochastic sample with the independent stochastic variable S, i.e. $\mathbf{S}^n = [S^1,...,S^n]$. $\mathrm{d}W^n$ is the increment of the *Wiener Process* of the n-th stochastic realization. It is also known as *Brownian Motion*, a normal distributed random walk. The

increments are statistically independent, since the Wiener Process itself is a Markov Process. It is modeled as:

$$dW^n = \mathcal{N}(0,1)\sqrt{dt} \ , \tag{4.16}$$

where $\mathcal{N}(0,1)$ represents a random sample drawn from a normal distribution with 0 mean and a variance of 1. This leads to important properties of the Wiener increment. With $d\mathbf{W} = [dW^1, ...,dW^n]$ these are:

$$\langle d\mathbf{W} \rangle = 0 \ , \tag{4.17}$$

$$\langle d\mathbf{W}^2 \rangle = dt \ . \tag{4.18}$$

The temporal evolution of the stochastic variable $\mathbf{S}^n(t)$ can then be described as:

$$\mathbf{S}^n(t) = \mathbf{S}^n(t_0) + \int_{t_0}^t \mathcal{A}^n(\mathbf{S}_t(t),t')dt' + \int_{t_0}^t \sqrt{2\mathcal{D}^n(\mathbf{S}^n(t),t')}dW^n \ . \tag{4.19}$$

For the numerical solution of Equation (4.19) the increment of the stochastic part needs to be evaluated every time step, i.e. between times t_i and t_{i+1} as:

$$\int_{t_{i-1}}^{t_i} \sqrt{2\mathcal{D}^n(\mathbf{S}^n(t),t)}dW^n = \sqrt{2\mathcal{D}^n(\mathbf{S}^n(t),t)}[W(t_i) - W(t_{i-1})] \ . \tag{4.20}$$

Alternatively the SDE (4.15) can also be written using the *Stratonovich* formalism:

$$d\mathbf{S}^n(t) = \mathcal{A}^n(\mathbf{S}^n(t),t)dt + \sqrt{2\mathcal{D}^n(\mathbf{S}^n(t),t)} \circ dW^n \ , \tag{4.21}$$

where $\circ$ implies Stratonovich calculus. The stochastic part of this integral is defined as:

$$\int_{t_{i-1}}^{t_i} \sqrt{2\mathcal{D}^n(\mathbf{S}^n(t),t)} \circ dW^n = [\mathcal{D}^n(\mathbf{S}^n(t_i),t_i) + \mathcal{D}^n(\mathbf{S}^n(t_{i-1}),t_{i-1})]^{1/2} [W(t_i) - W(t_{i-1})] \ , \tag{4.22}$$

in this case the Wiener term is evaluated at the midpoint of every time step. Eqs. (4.20) and (4.22) correspond to different Fokker-Planck equations and produce different PDFs for the same initial conditions. However, the PDFs are statistically equivalent and Itô and Stratonovich SDEs can be transformed into one another.

4.1.4   Original Stochastic Fields formulation

The PDF equation (4.13) is usually solved with stochastic Monte Carlo methods as described in the previous section. As an alternative to standard Lagrangian Monte Carlo Particle methods [75, 186, 219, 220, 231], Valiño [268] proposed the Eulerian Stochastic Fields method. In the following, it is abbreviated with ESF–O, as it refers to the original formulation of the Stochastic Fields method. Valiño [268] constructs the joint PDF $\widetilde{\mathcal{P}}_{sgs}$ from N_s continuous scalar fields. Each of these fields contains a composition of the N scalars $\zeta_\alpha^n(\mathbf{x},t)$ for $1 \leq n \leq N_s$ and $1 \leq \alpha \leq N$. Equation (4.13) can be converted into a Fokker-Planck equation that describes the evolution of the Eulerian composition PDF. Using the Itô formalism the stochastic equivalent SPDE describing the evolution of the N_s stochastic fields that represent $\widetilde{\mathcal{P}}_{sgs}$ reads:

$$d\overline{\rho}\zeta_\alpha^n \ + \ \frac{\partial \overline{\rho}\widetilde{u}_j \zeta_\alpha^n}{\partial x_j}dt \ - \ \frac{\partial}{\partial x_j}\left[\left(\frac{\mu}{\sigma} + \frac{\mu_t}{\sigma_t}\right)\frac{\partial \zeta_\alpha^n}{\partial x_i}\right]dt =$$
$$\overline{\rho}\left(\frac{2}{\overline{\rho}}\left(\frac{\mu}{\sigma} + \frac{\mu_t}{\sigma_t}\right)\right)^{1/2}\frac{\partial \zeta_\alpha^n}{\partial x_j}dW_j^n \ - \ \frac{\overline{\rho}}{2\tau_{sgs}}\left(\zeta_\alpha^n - \widetilde{\phi}_\alpha\right)dt \ - \ \overline{\rho}\dot{\omega}_\alpha^n(\zeta^n)dt \ . \tag{4.23}$$

The first term on the RHS represents the *stochastic velocity* which models the effect of turbulent sub–grid diffusion and contains the increment of the Wiener term. It can be thought of as a random advection term that de-correlates the individual fields on the scale of the filter width. The magnitude of the random advection is determined through the turbulence intensity (via μ_t) and the local scalar gradient of the individual field $\frac{\partial \zeta_\alpha^n}{\partial x_i}$. Note that the stochastic velocity term has no influence on the first moments (the filtered values):

$$\sum_{n=1}^{N_s} \left(\frac{2}{\overline{\rho}} \left(\frac{\mu}{\sigma} + \frac{\mu_t}{\sigma_t} \right) \right)^{1/2} \frac{\partial \zeta_\alpha^n}{\partial x_j} \mathrm{d}W_j^n = 0 \ . \tag{4.24}$$

$\mathrm{d}W_j^n$ is the increment of the Wiener process for the n-th field and spatial direction j.

The micro mixing term is modeled with the IEM model, as already introduced in Eq. (4.13), with the micro mixing time scale τ_{sgs}, modeled as in Equation (4.12). This term acts as a counter part to the stochastic velocity and takes care that the fields do not decorrelate indefinitely. It is also the only term that links the individual stochastic field realization to the cell filtered scalar value via $\widetilde{\phi}_\alpha$. The third term on the RHS contains the chemical reaction rates and appears in closed form.

It should be noted that each single realization of a stochastic field ζ_α^n is not necessarily a physical realisation of the particular field [122, 227, 268, 269] in contrast to the Favre filtered mean value evaluated as $\widetilde{\phi}_\alpha = \frac{1}{N_s} \sum_{n=1}^{N_s} \zeta_\alpha^n$. Moreover, the fields are perceived smooth over the filter width, i.e. the individual field has no scalar SGS fluctuation and is fully resolved, which allows to treat the reaction source term $\dot{\omega}_\alpha^n$ in closed fashion. They are twice differentiable and continuous in space. They are also continuous in time but not differentiable due to the Wiener term [268].

The group around Vladimir Sabelnikov [195, 240, 241, 257, 258] formulated the ESF–O equation by means of a Stratonovich formalism. Although, throughout this work strictly the Itô formalism will be used, the SPDE is given here in Stratonovich notation for completeness:

$$\begin{aligned}
\mathrm{d}\overline{\rho}\zeta_\alpha^n \ &+ \ \frac{\partial \overline{\rho}\widetilde{u}_j \zeta_\alpha^n}{\partial x_j} \mathrm{d}t \ - \ \frac{\partial}{\partial x_j} \left[\left(\frac{\mu}{\sigma} + \frac{\mu_t}{\sigma_t} \right) - \frac{1}{2} \left(\frac{\mu}{\sigma} + \frac{\mu_t}{\sigma_t} \right) \right] \frac{\partial \zeta_\alpha^n}{\partial x_i} \mathrm{d}t = \\
&\overline{\rho} \left(\frac{2}{\overline{\rho}} \left(\frac{\mu}{\sigma} + \frac{\mu_t}{\sigma_t} \right) \right)^{1/2} \frac{\partial \zeta_\alpha^n}{\partial x_j} \circ \mathrm{d}W_j^n \ - \ \frac{\overline{\rho}}{2\tau_{sgs}} \left(\zeta_\alpha^n - \widetilde{\phi}_\alpha \right) \mathrm{d}t - \ \overline{\rho}\dot{\omega}_\alpha^n \left(\zeta^n \right) \mathrm{d}t \ .
\end{aligned} \tag{4.25}$$

A difference to Eq. (4.23) is that in the Stratonovich formulation the filtering of the stochastic velocity term is non-zero and corresponds to a diffusion term:

$$\sum_{n=1}^{N_s} \left(\frac{2}{\overline{\rho}} \left(\frac{\mu}{\sigma} + \frac{\mu_t}{\sigma_t} \right) \right)^{1/2} \frac{\partial \zeta_\alpha^n}{\partial x_j} \circ \mathrm{d}W_j^n = - \left(\frac{\mu}{\sigma} + \frac{\mu_t}{\sigma_t} \right) \frac{\partial^2 \zeta_\alpha^n}{\partial x_j^2} \ . \tag{4.26}$$

Both equations (4.23) and (4.25) have different numerical implications, but can be transformed into one another and lead to the same PDF, given a sufficient high number N_s of fields is used. The main benefit of the Itô formalism is its simpler numerical implementation and that it collapses into a simple scalar transport equation even if only a single field is used. For a non-reactive scalar this would still result in a correct first moment (the filtered value). In contrast, the result of the Stratonovich equation (4.25) would have no physical meaning in this case. Generally, the Stratonovich implementation requires a high number of stochastic fields to obtain the correct first moment [72].

For a direct comparison between the two implementations the PhD thesis by Garmory [72] is recommended.

4.1.5 Modified Stochastic Fields formulation

Valiño, Mustata, and Letaief [269] presented a revised version of the original stochastic fields formulation (in this work the new version will be referred to as ESF formulation). In contrast with the original formulation [268] (ESF–O), the spurious Wiener term associated with the molecular diffusion is removed from the stochastic velocity term (first term on the RHS). Therewith, the stochastic fields evolution is also consistent in the laminar limit and the stochastic term does not produce any spurious (unphysical) fluctuations. The modified ESF equation reads:

$$
\begin{aligned}
\mathrm{d}\overline{\rho}\zeta_\alpha^n \; + \; & \frac{\partial \overline{\rho}\widetilde{u}_j \zeta_\alpha^n}{\partial x_j}\mathrm{d}t \; - \; \frac{\partial}{\partial x_j}\left[\left(\frac{\mu}{\sigma}+\frac{\mu_t}{\sigma_t}\right)\frac{\partial \zeta_\alpha^n}{\partial x_i}\right]\mathrm{d}t = \\
& \overline{\rho}\left(\frac{2}{\overline{\rho}}\left(\frac{\mu_t}{\sigma_t}\right)\right)^{1/2}\frac{\partial \zeta_\alpha^n}{\partial x_j}\mathrm{d}W_j^n \; - \; \frac{\overline{\rho}}{2\tau_{sgs}}\left(\zeta_\alpha^n - \widetilde{\phi}_\alpha\right)\mathrm{d}t - \; \overline{\rho}\dot{\omega}_\alpha^n\left(\zeta^n\right)\mathrm{d}t \; .
\end{aligned}
\tag{4.27}
$$

The molecular diffusion is also excluded from the micro mixing time scale τ_{sgs}:

$$
\frac{1}{\tau_{sgs}} = C_\mathrm{D}\frac{\mu_t}{\overline{\rho}\Delta^2}.
\tag{4.28}
$$

Recently, Wang, Zhang, and Pant [278] reported on the mathematical inconsistency of the ESF method and provided correction terms for the RANS context for the case of a single scalar field. They [278] argue that the second and any higher moments of scalars obtained from the ESF method are not consistent with the actual PDF equation (4.13). According to them, the original ESF formulation [268] (ESF–O) introduces spurious production of scalar variance, whereas the modified formulation [269] (ESF) introduces a spurious dissipation effect to the scalar variance. In the present work, no correction terms have yet been considered due to various reasons. First, Wang et al. [278] clearly stated that the first moments obtained with the ESF method are correct, which is eventually the quantity one interested in. Second, they [278] based their analysis on RANS where the second moments are more important and of higher magnitude as the computational cells are larger. Third, they [278] state that the inconsistency does especially matter at small Reynolds numbers where turbulent diffusivity D_t is considerably small, e.g. [278] used test cases at Re = 20. Since in the present work highly turbulent test cases are considered the error is expected to be rather small. Moreover, the correction terms have been derived for the single scalar case only. A straight forward extension to the multi-species/scalar case is not obvious. In this work, both the ESF and ESF–O will be directly compared.

4.1.6 ESF including Differential Diffusion

In the present work, the ESF method has been extended to account for differential diffusion. The modified PDF transport equation for the density weighted sub–grid PDF $\widetilde{\mathcal{P}}_{sgs}$, which assumes the gradient flux hypothesis and uses the interaction by exchange with the mean

(IEM) [47] mixing model, reads:

$$
\overline{\rho}\frac{\partial \widetilde{\mathcal{P}}_{sgs}(\underline{\psi})}{\partial t} + \overline{\rho}\widetilde{u}_j \frac{\partial \widetilde{\mathcal{P}}_{sgs}(\underline{\psi})}{\partial x_j} = -\sum_{k=1}^{N+1}\frac{\partial}{\partial \psi_k}\left(\overline{\rho}\dot{\omega}_k(\underline{\psi})\widetilde{\mathcal{P}}_{sgs}(\underline{\psi})\right)
$$

$$
-\overline{\rho}\sum_{k=1}^{N+1}\frac{\partial}{\partial \psi_k}\left[\left\langle\frac{1}{\rho}\frac{\partial \delta J_{k,j}}{\partial x_j}\bigg|\widetilde{\underline{H}} = \underline{\psi}\right\rangle_{sgs}\right]\widetilde{\mathcal{P}}_{sgs}(\underline{\psi}) \qquad (4.29)
$$

$$
+\frac{\partial}{\partial x_j}\left[\left(\frac{\mu_t}{\sigma_t}\right)\frac{\partial \widetilde{\mathcal{P}}_{sgs}(\underline{\psi})}{\partial x_j}\right] - \overline{\rho}\frac{C_D}{\tau_{sgs}}\sum_{k=1}^{N+1}\frac{\partial}{\partial \psi_k}\left[(\psi_k - \widetilde{\phi}_k)\widetilde{\mathcal{P}}_{sgs}(\underline{\psi})\right] \ ,
$$

with

$$
\left\langle\frac{1}{\rho}\frac{\partial \delta J_{k,j}}{\partial x_j}\bigg|\widetilde{\underline{H}} = \underline{\psi}\right\rangle_{sgs} = \left\langle\frac{1}{\rho}\frac{\partial J_{k,j}}{\partial x_j}\bigg|\widetilde{\underline{H}} = \underline{\psi}\right\rangle_{sgs} - \overline{\rho}\frac{C_D}{\tau_{sgs}}\left(\psi_k - \widetilde{\phi}_k\right). \qquad (4.30)
$$

$\underline{\psi}$ in Eq. (4.29) denotes a $N+1$ dimensional vector–function in a sample space corresponding to the $N+1$ dimensional vector–function $\widetilde{\underline{H}} = (\widetilde{\underline{Y}}, \widetilde{h}_s)$ and $J_{N+1,j} = J_{s,j}$, where N accounts for the number of species and the subscript s refers to the sensible enthalpy. C_D and τ_{sgs} denote the mixing constant and the SGS time–scale, respectively; $\sigma_t = 0.7$ is the turbulent Schmidt or Prandtl number, and $\widetilde{\phi}_k$ denotes the Favre filtered mean value of scalar k, $1 \leq k \leq N + 1$. The reaction source terms $\dot{\omega}_k$ appear in Eq. (4.29) in closed form, but Eq. (4.29) is not yet closed, because of the second term on the right hand side. Namely this term describes the effects of the differential diffusion of the mass fractions in the flame. One approach to close this term is known from McDermott and Pope [172] for particle methods. In this work, the approach from Valiño, Mustata, and Letaief [269] is extended to close this term taking into account the differential diffusion effects, and widen the ESF Monte Carlo method proposed by [240, 268] to solve the tPDF equation (4.29). $\widetilde{\mathcal{P}}_{sgs}$ is constructed from N_s stochastic $N + 1$ dimensional vector $\zeta_k^n(\mathbf{x},t)$ fields, $1 \leq n \leq N_s$. These fields obey to stochastic partial differential equations (SPDEs) that are stochastically equivalent to the tPDF Eq. (4.29). Using the Itô formalism, the SPDEs read:

$$
\mathrm{d}\overline{\rho}\zeta_k^n \ + \ \frac{\partial \overline{\rho}\widetilde{u}_i \zeta_k^n}{\partial x_j}\mathrm{d}t = -\ \overline{\rho}\dot{\omega}_k^n\left(\zeta^n\right)\mathrm{d}t
$$

$$
-\frac{\partial \delta J_{k,j}^n(\zeta_k^n)}{\partial x_j}\mathrm{d}t + \frac{\partial}{\partial x_j}\left(\frac{\mu_t}{\sigma_t}\frac{\partial \zeta_k^n}{\partial x_j}\right)\mathrm{d}t + \overline{\rho}\left(\frac{2}{\overline{\rho}}\frac{\mu_t}{\sigma_t}\right)^{1/2}\frac{\partial \zeta_k^n}{\partial x_j}\mathrm{d}W_i^n \qquad (4.31)
$$

$$
-\overline{\rho}\frac{C_d}{2\tau_{sgs}}\left(\zeta_k^n - \widetilde{\phi}_k\right)\mathrm{d}t \ ,
$$

where

$$\delta J_{k,j}^n(\zeta_k^n) = -\rho^n \left(D_k^n \, \frac{\partial \zeta_k^n}{\partial x_j} - \zeta_k^n \, u_j^{c,n}(\zeta_k^n) \right) \,,$$

$$\delta J_{N+1,j}^n(\zeta_{N+1}^n) = -\lambda^n \, \frac{\partial T^n}{\partial x_j} + \sum_{k=1}^{N} \delta J_{k,j}^n(\zeta_k^n) h_{s,k}^n \,,$$

$$u_j^{c,n}(\zeta_k^n) = \sum_{k=1}^{N} D_k^n \, \frac{\partial \zeta_k^n}{\partial x_j} \,, \tag{4.32}$$

$$D_k^n = D_k(\zeta_k^n) \,,$$

$$\rho^n = \rho(\zeta_k^n) \,,$$

$$\lambda^n = \lambda(\zeta_k^n) \,,$$

$$h_{s,k}^n = h_{s,k}(T^n) \,;$$

the stochastic fields T^n correspond to temperature T. The Wiener term $\mathrm{d}W_i^n = \gamma_i^n \sqrt{\mathrm{d}t}$ is evaluated with γ_i^n, again as dichotomic random value of $\{-1; +1\}$. The micro mixing time scale τ_{sgs} is modeled as in Eq. 4.12 with $C_D = 2$. This formulation, accounting for differential diffusion, is referred to as ESF-DD method.

4.1.7 SGS statistics

From the individual stochastic fields instantaneous sub–grid statistics can be obtained at the spatial location $\mathbf{x}$ and time t. Apart from the filtered mean values (first moments) $\mathrm{E}[\phi(\mathbf{x},t)]$, these are the sub–grid variance $\mathrm{var}[\phi(\mathbf{x},t)]$ (second moments), as well as the covariance $\mathrm{cov}[\phi_1(\mathbf{x},t),\phi_2(\mathbf{x},t)]$, and the correlation coefficient $\mathrm{corr}[\phi_1(\mathbf{x},t),\phi_2(\mathbf{x},t)]$ between two scalars ϕ_1 and ϕ_2. For a given number of stochastic fields N_s these are:

$$\mathrm{E}[\phi(\mathbf{x},t)] = \widetilde{\phi} = \frac{1}{N_s} \sum_{i=1}^{N_s} \phi_i \,, \tag{4.33}$$

$$\mathrm{var}[\phi(\mathbf{x},t)] = \widetilde{\phi''^2} = \frac{1}{N_s} \sum_{i=1}^{N_s} (\phi_i - \mathrm{E}[\phi])^2 \,, \tag{4.34}$$

$$\mathrm{cov}[\phi_1(\mathbf{x},t),\phi_2(\mathbf{x},t)] = \widetilde{\phi_1''\phi_2''} = \frac{1}{N_s} \sum_{i=1}^{N_s} (\phi_{1,i} - \mathrm{E}[\phi_1]) (\phi_{2,i} - \mathrm{E}[\phi_2]) \,, \tag{4.35}$$

$$\mathrm{corr}[\phi_1(\mathbf{x},t),\phi_2(\mathbf{x},t)] = R_{\phi_1\phi_2} = \frac{\widetilde{\phi_1''\phi_2''}}{\sqrt{\widetilde{\phi_1''^2}\widetilde{\phi_2''^2}}} \,. \tag{4.36}$$

4.2 Flamelet/progress variable model

4.2.1 Progress variable definition

The FPV model uses two scalars to parameterize the thermo–chemical state space: one is the mixture fraction Z describing the state of mixing between fuel (pure fuel: $Z = 1$) and oxidizer (pure oxidizer: $Z = 0$), the other one is the progress variable PV which is a linear combination of reaction and intermediate products describing best the reaction's progress. Several definitions of the progress variable are admissible [107]. For example, Pierce and Moin [209] used:

$$PV = Y_{\mathrm{CO_2}} + Y_{\mathrm{H_2O}} \ , \tag{4.37}$$

Ihme and Pitsch [104] used:

$$PV = Y_{\mathrm{CO_2}} + Y_{\mathrm{CO}} \ , \tag{4.38}$$

while Ramaekers [230] proposed:

$$PV = \frac{Y_{\mathrm{CO_2}}}{M_{\mathrm{CO_2}}} + \frac{Y_{\mathrm{CO}}}{M_{\mathrm{CO}}} + \frac{Y_{\mathrm{H_2O}}}{M_{\mathrm{H_2O}}} \ . \tag{4.39}$$

Generally, the optimal choice and definition of the progress variable is still an active field of research [11] and no universal statements can be made. The requirements for the progress variable are that it is solely composed from species mass fractions which are reaction products and not contained in the fuel or oxidizer streams. For example, Mahmoud et al. [166] used a progress variable only composed from the normalized H_2O mass fraction ($PV = Y_{\mathrm{H_2O}}/M_{\mathrm{H_2O}}$), since the simulated oxy–fuel case contained CO_2 in the co-flow and H_2 in the fuel stream. In the present work the definition by Ramaekers [230] is used.

In the same way as the progress variable the source term of the progress variable ω_{PV} is constructed from a linear combination of the individual source terms. For instance, if the progress variable is defined as in (4.39) the source term is:

$$\dot{\omega}_{PV} = \frac{\dot{\omega}_{\mathrm{CO_2}}}{M_{\mathrm{CO_2}}} + \frac{\dot{\omega}_{\mathrm{CO}}}{M_{\mathrm{CO}}} + \frac{\dot{\omega}_{\mathrm{H_2O}}}{M_{\mathrm{H_2O}}} \ . \tag{4.40}$$

4.2.2 Table generation

The idea of the FPV model is that all thermo–chemical quantities $\phi = \{Y_1, Y_2, ..., \alpha, \mu, c_{\mathrm{p}}, \rho, \dot{\omega}_{PV}, T\}$ are stored in structured tables and can be accessed during the reactive flow simulation as a function of Z and PV as $\phi = \mathcal{F}(Z, PV)$, with $\mathcal{F}$ being the FPV library. To populate the library, laminar one dimensional flamelets are used which can either be generated from non–premixed counterflow diffusion flamelets, as it was initially proposed by [209], or from flamelets of freely propagating flames. The latter approach is similar to the Flamelet Generated Manifold (FGM) combustion model [193, 194] which is used for premixed combustion.

The following subsection briefly outlines how the tables are populated with either ways.

Counterflow diffusion flame

As mentioned in Section 3.3.2 the scalar dissipation rate can be understood as an inverse time scale [s^{-1}] and is defined as:

$$\chi = 2D_Z \left| \nabla Z \right|^2 \ , \tag{4.41}$$

with D_Z being the diffusivity of the mixture fraction. Laminar counterflow diffusion flamelets are then computed as a function of mixture fraction Z for different scalar dissipation rates χ. The generic set up has already been illustrated in Figure 3.1a where oxidizer and fuel are initially separated and diffuse into one another. Under the *unity Lewis number* assumption ($Le_k = Le = 1$) the problem can be described in mixture fraction space as one dimensional configuration [202] with the following conservation equations for species Y_k and enthalpy h, known as the flamelet equations:

$$\rho \frac{\partial Y_k}{\partial t} = \rho \frac{\chi}{2} \frac{\partial^2 Y_k}{\partial^2 Z^2} + \dot{\omega}_k \ , \tag{4.42}$$

and

$$\rho \frac{\partial h}{\partial t} = \rho \frac{\chi}{2} \frac{\partial^2 h}{\partial^2 Z^2} \ . \tag{4.43}$$

For the solution of the flamelet equations, commercial and open-source codes can be employed. In this work the freely available tool `FlameMaster` [214] has been used with the GRI-3.0 chemical mechanism.

Steady flamelets are then computed at different scalar dissipation rates χ, starting with values closes to zero, up to dissipation rates where the flame extinguishes. To obtain a fully orthogonal table a normalized progress variable PV_n is introduced, where each PV is normalized with the maximum possible PV at a given mixture fraction Z as:

$$PV_n = \frac{PV}{PV_{max|Z}} \ . \tag{4.44}$$

For the normalization usually the PV values of the flamelet with highest flame temperature are taken. Figure 4.1 shows the temperature over mixture fraction Z along constant

Figure 4.1: Iso-lines of normalized progress variable in temperature–mixture fraction space for the non–premixed flamelets.

PV_n iso-lines for flamelets with pure methane and air. Normalization has been achieved with the flamelet that yields the highest adiabatic flame temperature, here highlighted in red. The tables are then constructed through linear interpolation from the flamelet data points onto a uniformly spaced grid with 501 grid points in Z and normalized PV dimension. Figure 4.2 shows such a manifold for the temperature (a) and the progress variable

source term $\dot{\omega}_{PV}$ (b) as a function of Z and normalized PV from non–premixed flamelets with CH_4 as fuel and air as oxidizer.

(a) Temperature manifold

(b) Source term manifold

Figure 4.2: Temperature T and source term $\dot{\omega}_{PV}$ manifold in Z and normalized PV space from non–premixed flamelets.

Freely propagating flame

One dimensional laminar freely propagating flames can only be computed within the flammability limits $(0.01 < Z < 0.15)$ for constant mixture fraction values. The one dimensional balance equations for the free flames (see e.g. [125, 205, 217]) are solved here with the CANTERA library [82] and the GRI-3.0 mechanism. Figure 4.3 illustrates the iso-lines of nor-
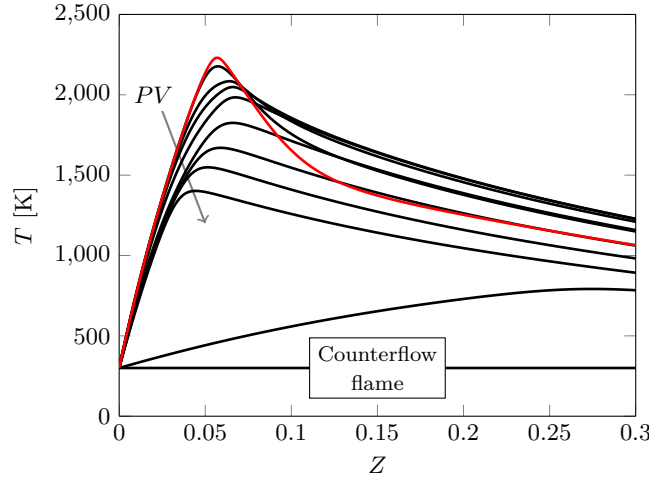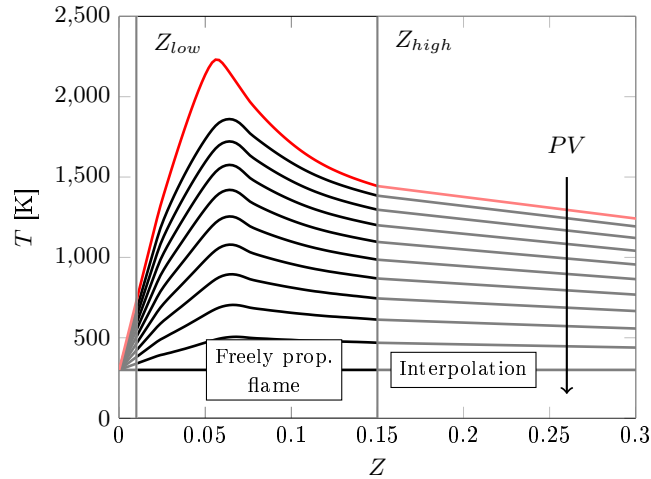

Figure 4.3: Iso-lines of normalized progress variable in temperature–mixture fraction space for the premixed flamelets. Interpolation in regimnes outside of the flamability limit.

malized progress variables over mixture fraction and temperature. The flamelets have been

generated within the lower and upper flammability limits of $Z_{low} = 0.01$ and $Z_{high} = 0.15$. To populate the manifold over the whole range of $Z \in [0,1]$ the thermo-chemical states are linearly interpolated between Z_{low} and $Z = 0$, and between Z_{high} and $Z = 1$. The red line highlights again the normalization progress variable where the highest adiabtic flame temperatures are reached.

Figure 4.4 shows the temperature (a) and progress variable source term (b) manifolds in Z and normalized PV space. Like in the non–premixed case, the manifolds have been obtained through linear interpolation from the laminar flamelet data onto an equidistant cartesian grid. The visual differences between Fig. 4.4 and Fig. 4.2 in the temperature field and the magnitude of $\dot{\omega}_{PV}$, which is one order of magnitude higher in the non–premixed case, are a result of the different flame structures in both generic configurations.

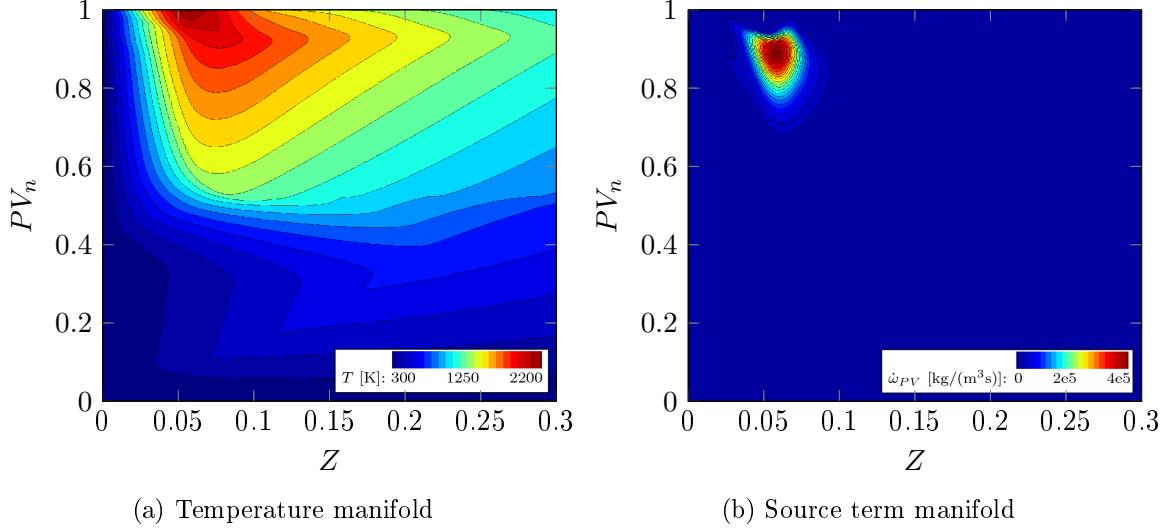

(a) Temperature manifold   (b) Source term manifold
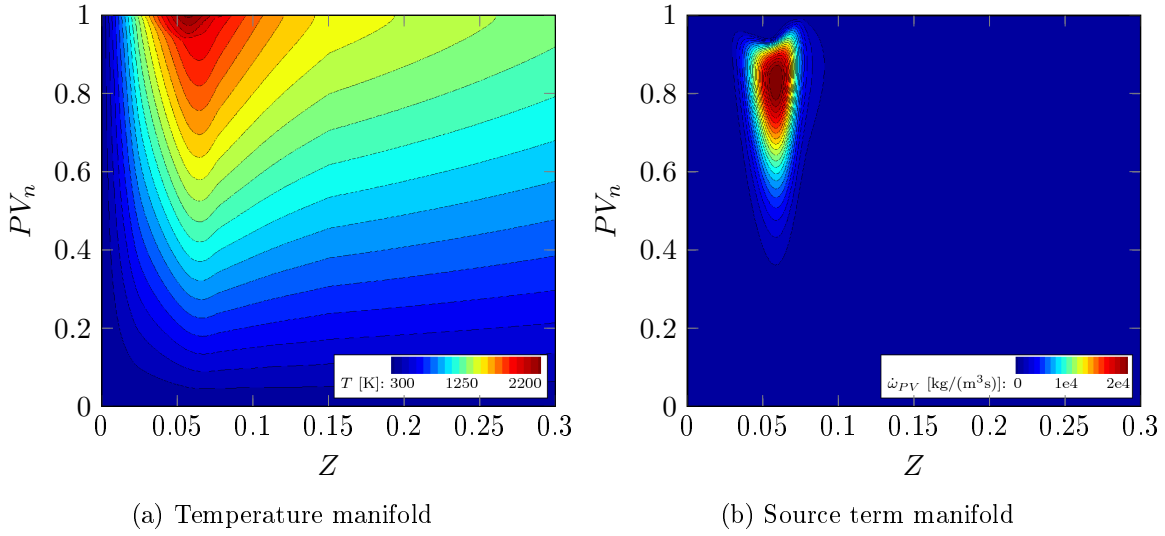
Figure 4.4: Temperature T and source term $\dot{\omega}_{PV}$ manifold in Z and normalized PV space from premixed flamelets.

Presumed PDF

To account for TCI on the sub–grid scale in the LES context the thermo–chemical data base ϕ has to be convoluted with a joint sub–grid PDF $\widetilde{\mathcal{P}}_{sgs}(Z,PV)$ which describes the SGS fluctuations of Z and PV in a statistical manner:

$$\widetilde{\phi} = \int_0^1 \int_0^1 \phi(Z,PV)\widetilde{\mathcal{P}}_{sgs}(Z,PV)\mathrm{d}Z'\mathrm{d}PV' \ . \tag{4.45}$$

Using Bayes' theorem the joint PDF can be written in terms of a conditional PDF, $\widetilde{\mathcal{P}}_{sgs}(PV|Z)$, and a marginal PDF, $\widetilde{\mathcal{P}}_{sgs}(Z)$, as:

$$\widetilde{\mathcal{P}}_{sgs}(Z,PV) = \widetilde{\mathcal{P}}_{sgs}(Z)\widetilde{\mathcal{P}}_{sgs}(PV|Z) \ . \tag{4.46}$$

The mixture fraction SGS fluctuations are modeled with a two parametric presumed β-PDF which has been shown to be a good approximation for a passive (non–reactive) scalar [114]:

$$\widetilde{\mathcal{P}}_{sgs}(Z) = Z^{(\alpha-1)}(1 - Z)^{(\beta-1)}\frac{\Gamma(\alpha + \beta)}{\Gamma(\alpha)\Gamma(\beta)} \ , \tag{4.47}$$

with Γ as the gamma function [68], α, and β are the β-PDF parameters, which define its shape depending on the mean mixture fraction $\widetilde{Z}$, and the SGS variance of the mixture fraction $\widetilde{Z''^2}$ as:

$$\alpha = \widetilde{Z} \left(\frac{\widetilde{Z}(1 - \widetilde{Z})}{\widetilde{Z''^2}} - 1 \right) , \qquad (4.48)$$

$$\beta = (1 - \widetilde{Z}) \left(\frac{\widetilde{Z}(1 - \widetilde{Z})}{\widetilde{Z''^2}} - 1 \right) . \qquad (4.49)$$

Pierce and Moin [209] propose to approximate the conditional PDF, $\widetilde{\mathcal{P}}_{sgs}(PV|Z)$, with a marginal PDF, $\widetilde{\mathcal{P}}_{sgs}(PV)$, under the assumption of statistical independence between Z and PV. They presumed the PDF to be a dirac distribution:

$$\widetilde{\mathcal{P}}_{sgs}(PV) = \delta(PV - \widetilde{PV}) , \qquad (4.50)$$

arguing that the scale of validity of the flamelet solution is larger than the scale of the LES filter, therefore SGS fluctuations in PV-space can be neglected.
With the substitution of the mixture fraction variance $\widetilde{Z''^2}$ by the unmixedness:

$$\widetilde{\zeta} = \frac{\widetilde{Z''^2}}{\widetilde{Z}(1 - \widetilde{Z})} , \qquad (4.51)$$

which scales between 0 and 1, the LES filtered FPV data base $\widetilde{\phi}$ is then obtained as:

$$\widetilde{\phi} = \mathcal{F}(\widetilde{Z}, \widetilde{PV}, \widetilde{\zeta}) . \qquad (4.52)$$

Note that the previously presented simplifications and assumptions are reduction strategies to reduce the model complexity. The statistical independence of Z and PV should be carefully evaluated and does hold only for large filter widths around stoichiometric conditions [102]. The analysis of DNS [38, 293] and experimental [11] data showed that Z and PV, depending on the definition of the latter one, may be correlated in partially premixed flames. Regarding the dirac distribution as the presumed PDF for PV, Ihme and Pitsch [103, 104] tested different marginal distributions as an alternative and achieved slightly better predictions of extinction and re-ignition in the Sandia flames D and E than with the dirac distribution.

4.2.3   LES implementation

To use the FPV library $\widetilde{\phi}$ finally in LES, the flow solver has to solve two more transport equations in addition to Eqs. (2.40) and (2.41), one for the mixture fraction Z, and one for the progress variable PV including the progress variable source term (4.40). Since this combustion model directly provides the filtered temperature $\widetilde{T}$ and species $\widetilde{Y}_k$ from the FPV database $\widetilde{\phi}$ no enthalpy (2.44) and species (2.43) transport equations need to be solved in the adiabatic case.

Mixture fraction:

$$\frac{\partial \overline{\rho}\widetilde{Z}}{\partial t} + \frac{\partial \overline{\rho}\widetilde{u}_j\widetilde{Z}}{\partial x_j} = \frac{\partial}{\partial x_j}\left(\overline{\rho}D_Z\frac{\partial \widetilde{Z}}{\partial x_j} - \overline{\rho}(\widetilde{u_jZ} - \widetilde{u}_j\widetilde{Z})\right) , \qquad (4.53)$$

Progress variable:

$$\frac{\partial \overline{\rho}\widetilde{PV}}{\partial t} + \frac{\partial \overline{\rho}\widetilde{u}_j\widetilde{PV}}{\partial x_j} = \frac{\partial}{\partial x_j}\left(\overline{\rho}D_{PV}\frac{\partial \widetilde{PV}}{\partial x_j} - \overline{\rho}(\widetilde{u_jPV} - \widetilde{u}_j\widetilde{PV})\right) + \overline{\rho}\widetilde{\dot{\omega}}_{PV} . \qquad (4.54)$$

D_{PV} and D_Z are the progress variable and mixture fraction diffusivity. With the *unity Lewis number* assumption these are obtained as $D_{PV} = D_Z = \lambda/(\rho c_{\mathrm{p}})$. Residual terms in Eqs. (4.53-4.54) are closed with the gradient flux hypothesis using the turbulent viscosity μ_t from the SGS turbulence model and the turbulent Schmidt number Sc_t:

$$\widetilde{u_jZ} - \widetilde{u}_j\widetilde{Z} = -\frac{\mu_t}{Sc_t}\frac{\partial \widetilde{Z}}{\partial x_j} , \qquad (4.55)$$

$$\widetilde{u_jPV} - \widetilde{u}_j\widetilde{PV} = -\frac{\mu_t}{Sc_t}\frac{\partial \widetilde{PV}}{\partial x_j} . \qquad (4.56)$$

The mixture fraction variance $\widetilde{Z''^2}$ can be obtained either algebraically, e.g., with the equilibrium approach as proposed by [209], or with a transport equation. Knudsen et al. [135] evaluated algebraic models with DNS data and found transport equation models to perform better. Therefore, the mixture fraction variance is solved in this work with a transport equation [126]:

$$\frac{\partial \overline{\rho}\widetilde{Z''^2}}{\partial t} + \frac{\partial \overline{\rho}\widetilde{u}_j\widetilde{Z''^2}}{\partial x_j} = \frac{\partial}{\partial x_j}\overline{\rho}\left(D_Z + \frac{\mu_t}{Sc_t}\right)\frac{\partial \widetilde{Z''^2}}{\partial x_j} - 2\overline{\rho}\widetilde{\chi} + 2\overline{\rho}\left(D_Z + \frac{\mu_t}{Sc_t}\right)\left(\frac{\partial \widetilde{Z}}{\partial x_j}\right)^2 . \qquad (4.57)$$

An algebraic model [126] is then used to describe the scalar dissipation rate χ, which is composed from a resolved and a SGS contribution as:

$$2\overline{\rho}\widetilde{\chi} = 2D_Z\left(\frac{\partial \widetilde{Z}}{\partial x_j}\right)^2 + C_\chi\frac{\mu_t}{Sc_t}\frac{\widetilde{Z''^2}}{\Delta^2} , \qquad (4.58)$$

with the constant $C_\chi = 2.0$ and the filter width Δ.

Chapter 5

Numerical aspects

For the simulations in the work presented here, the open source flow solver OpenFOAM[1] in version 4.1 has been used. OpenFOAM uses the finite volume method for discretizing the flow equations and supports unstructured numerical meshes. An overview of many of the available discretization methods and numerical solution approaches and a Error estimation of the methods are shown in the work of Jasak [113]. Newer summaries that reflect the current state of development can be found in the official documentation [85]. Since the flow solver is freely accessible, it is possible to modify the `C++` based source code and implement own models. Over the past years the institute's internal OpenFOAM package has been extended and thermodynamics and combustion models have been added, as documented in previous dissertations by Frank [60], Keppeler [127], Müller [181], Pohl [216], and Zips [290]. The combustion models presented in Chapter 4 were adopted from or implemented based on these previous works.

5.1 Pressure based solver

For all simulations in this work an implicit Euler method of second order was used for temporal discretization. The convective terms in the momentum equation (2.41) are discretized with a second order central differences scheme. The convective terms of the species (2.43) and enthalpy (2.44) equations are also discretized with a second order central differences scheme in addition with a van Leer limiter [150] to avoid non-physical oscillation of the flux term.

The flow velocities of the investigated flames are all within the low Mach regime (Ma < 0.3). Under these conditions a pressure based algorithm has the advantage over density based methods that the linear equation system is less stiff. Therefore, no preconditioning procedure is required for the use of larger time steps. The flow solver uses an adaptation of the PISO-algorithm (Pressure Implicit with Splitting of Operators) for compressible flows [109], in which instead of a transport equation for the density, an equation for the development of the pressure is solved.

Low Mach approach

For flows in the low Mach regime and with low compressibility effects a Low Mach approach for the solution of the PISO-algorithm can be chosen. The approximation is given hereafter,

---

[1]www.openfoam.com

following [152].

The low Mach number equations are found by expanding the flow variables ρ, T, u_j, and p, as a power series in $\epsilon = \gamma \mathrm{Ma}^2$, with γ as the ratio of specific heats $c_\mathrm{p}/c_\mathrm{v}$.

$$\rho = \rho^0 + \rho^1 + \mathcal{O}(\epsilon^2) \ , \tag{5.1}$$

$$u_j = u_j^0 + \epsilon u_j^1 + \mathcal{O}(\epsilon^2) \ , \tag{5.2}$$

$$T = T^0 + \epsilon T^1 + \mathcal{O}(\epsilon^2) \ , \tag{5.3}$$

$$p = \frac{pT}{\gamma \mathrm{Ma}^2} = \frac{1}{\epsilon} p^0 + p^1 + \mathcal{O}(\epsilon) \ . \tag{5.4}$$

The pressure has been decomposed into two contributions; the thermodynamic pressure p^0, and the hydrodynamic pressure p^1, hereafter referred to as p_d. The consequence of this is two-fold, first knowing that $\epsilon = \gamma \, \mathrm{Ma}^2 \ll 1$, the pressure appearing in the material derivative term of the energy equation is predominantly the thermodynamic pressure p^0. Secondly, the spatially uniform nature of p^0 means that the pressure appearing in the gradient term of the momentum equations is uniquely p_d. The momentum (2.2) and the enthalpy equation (2.13) may then be re-written in terms of p^0 and p_d:

$$\frac{\partial(\rho u_i)}{\partial t} + \frac{\partial(\rho u_i u_j)}{\partial x_j} = -\frac{\partial p_\mathrm{d}}{\partial x_i} + \frac{\partial \tau_{ij}}{\partial x_j} \ , \tag{5.5}$$

and

$$\frac{\partial(\rho h_\mathrm{s})}{\partial t} + \frac{\partial(\rho u_j h_\mathrm{s})}{\partial x_j} = \frac{\mathrm{D}p^0}{\mathrm{D}t} + \tau_{ij}\frac{\partial u_i}{\partial x_j} + \dot{Q} - \frac{\partial J_{s,j}}{\partial x_j} + \dot{\omega}_\mathrm{T} \ , \tag{5.6}$$

with the following equation of state to close the system :

$$\rho = \frac{p^0 \mathcal{M}}{\mathcal{R}T} \ . \tag{5.7}$$

The only contribution to the pressure material derivative $\frac{\mathrm{D}p^0}{\mathrm{D}t}$ in the enthalpy equation is the partial time derivative as the term p^0 is constant in space. The simulated cases are atmospheric flames, i.e. the compuatational domain is open to the atmosphere, the thermodynamic pressure is also constant over time. Therefore, the material derivative can be set to zero in this work: $\frac{\mathrm{D}p^0}{\mathrm{D}t} = 0$.

Numerical implementation

The non-linear term in the momentum equation (5.5) is $\frac{\partial(\rho u_i u_j)}{\partial x_j}$, or in differential form $\rho(\mathbf{u} \cdot \nabla)\mathbf{u}$, with $\mathbf{u}$ being the velocity vector. In linearized form it reads [113]:

$$(\mathbf{u} \cdot \nabla)\mathbf{u} = a_\mathrm{P}\mathbf{u}_\mathrm{P} + \sum_N a_\mathrm{N}\mathbf{u}_\mathrm{N} \ , \tag{5.8}$$

where a_P and a_N are the coefficient matrices for point P and the neighboring points N that satisfy the continuity equation (2.1), $\mathbf{u}_\mathrm{P}$ is the velocity at a given point P. In order to derive the pressure equation, a semi-discretised form of the momentum equation is used [113]:

$$a_\mathrm{P}\mathbf{u}_\mathrm{P} = \mathbf{H}(\mathbf{u}) - \nabla p_\mathrm{d} \ . \tag{5.9}$$

with

$$\mathbf{H}(\mathbf{u}) = -\sum_N a_{\mathrm{N}}\mathbf{u}_N + \frac{\mathbf{u}^{source}}{\Delta t} \ . \tag{5.10}$$

Solving for $\mathbf{u}$, multiplying with ρ, and taking the divergence of the continuity equation (2.1) gives:

$$\nabla \cdot \left(\frac{\rho}{a_{\mathrm{P}}} \nabla p_{\mathrm{d}} \right) = \nabla \cdot \left(\frac{\rho}{a_{\mathrm{P}}} \mathbf{H}(\mathbf{u}) \right) - \frac{\partial \rho}{\partial t} \ . \tag{5.11}$$

The density ρ in the time derivative can be recast as $\rho = \psi p^0$, with $\psi = \mathcal{M}/(\mathcal{R}T)$. The pressure equation then reads:

$$\frac{\partial \psi p^0}{\partial t} - \nabla \cdot \left(\frac{\rho}{a_{\mathrm{P}}} \nabla p_{\mathrm{d}} \right) + \nabla \cdot \left(\frac{\rho}{a_{\mathrm{P}}} \mathbf{H}(\mathbf{u}) \right) = 0 \ . \tag{5.12}$$

5.2 Numerical aspects of the Stochastic Fields method

5.2.1 Random number generator

In LES simulations with the ESF method usually only a small number of stochastic fields is used [64, 94, 122, 123], due to limited computational resources. As shown in Equation (4.16), the Wiener increments $\mathrm{d}W^n$ of the n-th stochastic field are computed with a random number drawn from a normal distribution $\mathcal{N}(0,1)$ with 0 mean and a variance of 1. However, using Gaussian random numbers for a low number of stochastic fields can introduce errors. Most importantly, the property of the Wiener increment $\langle \mathrm{d}\mathbf{W} \rangle = 1/N_s \sum_{n=1}^{N_s} \mathrm{d}W^n = 0$ is not ensured. For this reason, the normal distribution is approximated with a dichotomic vector $\mathcal{N}(0,1) \approx \{-1,1\}$, which is a weak first order approximation [68]. The Wiener increment is then given as $\mathrm{d}W^n = \gamma^n \sqrt{\mathrm{d}t}$, with γ^n being randomly sampled from the dichotomic vector. It guarantees also for a low number of fields $\langle \mathrm{d}\mathbf{W} \rangle = 0$ and $\langle \mathrm{d}\mathbf{W}^2 \rangle = \mathrm{d}t$.

To demonstrate this behavior, Figure 5.1 illustrates individual realizations of $\mathbf{S}^n$ according to Equation (4.15) in grey for $N_s = 10$, in (a) with γ^n being sampled from $\mathcal{N}(0,1)$, and in (b) with γ^n being sampled from $\{-1,1\}$. The black line shows the time conditioned mean values $\langle \mathbf{S}_n | t \rangle$, mathematically it should always be 0. Note that only in (b) the mean value is constantly 0.

5.2.2 Numerical implementation

The equations for the transport of the individual stochastic fields ζ_α^n (Eq. 4.27) are *convective-diffusion-reaction* equations. Due to its stiffness the chemical source term $\dot{\omega}_\alpha$ is not included in the *convection-diffusion* part, but is treated separately. Operator splitting is therefore performed as described in [54].

To obtain $\zeta_\alpha^n(t_m)$ at time step t_m the stochastic differential equation (4.27) can be formulated as:

$$\zeta_\alpha^n(t_m) = \zeta_\alpha^n(t_{m-1}) + \mathcal{K}(\zeta_\alpha^n(t_{m-1})) + \mathcal{S}(\zeta_\alpha^n(t_{m-1})) + \mathcal{M}_{sgs}(\zeta_\alpha^n(t_{m-1}), \widetilde{\phi_\alpha}(t_{m-1})) + \dot{\omega}(\zeta_\alpha^n(t_{m-1}))\mathrm{d}t \ , \tag{5.13}$$

with

$$\mathcal{K}(\zeta_\alpha^n(t_{m-1})) = \frac{\partial \overline{\rho}\widetilde{u}_j \zeta_\alpha^n(t_{m-1})}{\partial x_j}\mathrm{d}t \ - \ \frac{\partial}{\partial x_j}\left[\left(\frac{\mu}{\sigma} + \frac{\mu_t}{\sigma_t} \right) \frac{\partial \zeta_\alpha^n(t_{m-1})}{\partial x_i} \right]\mathrm{d}t \ , \tag{5.14}$$
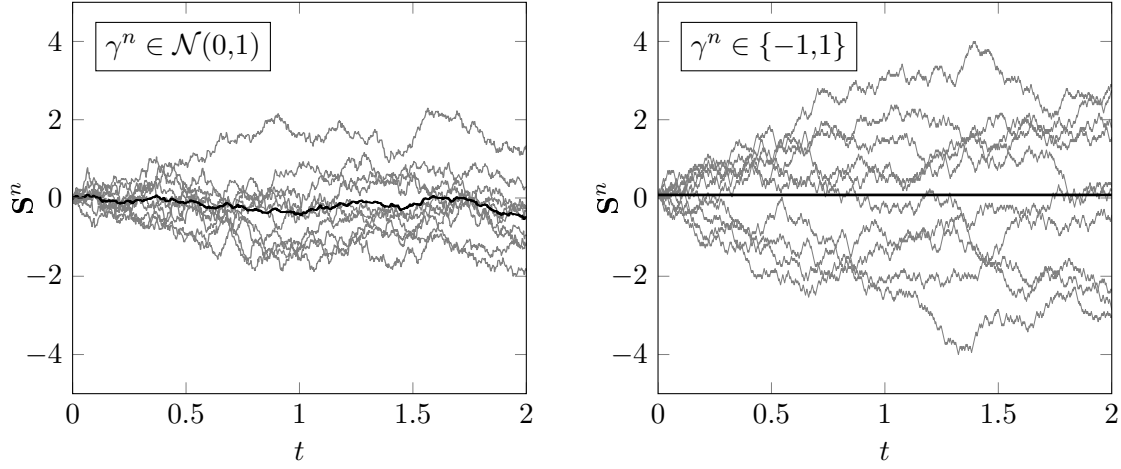
Figure 5.1: Individual realizations of $\mathbf{S}_n$ (grey) according to Eq. (4.15) with $\mathcal{A}_n = 0$ and $\mathcal{D}_n = const. = 1/2$ up to $t_{end} = 2$ for a constant time increment $dt = 0.002$. The initial condition was $\mathbf{S}_n(t = 0) = 0$. (a) shows realizations with $\gamma^n \in \mathcal{N}(0,1)$, (b) with $\gamma^n \in \{-1,1\}$ as dichotomic random value. The black line shows the time conditioned means $\langle \mathbf{S}_n | t \rangle$.

$$\mathcal{S}(\zeta_\alpha^n(t_{m-1})) = \overline{\rho} \left(\frac{2}{\overline{\rho}} \left(\frac{\mu_t}{\sigma_t} \right) \right)^{1/2} \frac{\partial \zeta_\alpha^n(t_{m-1})}{\partial x_j} \mathrm{d}W_j^n \ , \tag{5.15}$$

$$\mathcal{M}_{sgs}(\zeta_\alpha^n(t_{m-1}), \widetilde{\phi_\alpha}(t_{m-1})) = -\frac{\overline{\rho}}{2\tau_{sgs}} \left(\zeta_\alpha^n(t_{m-1}) - \widetilde{\phi}_\alpha(t_{m-1}) \right) \mathrm{d}t \ . \tag{5.16}$$

The solution steps are then:

1. **Convection-diffusion**
   The convection-diffusion term $\mathcal{K}(\zeta_\alpha^n(t_{m-1}))$ is solved with an implicit second order Euler scheme (as in any other scalar transport equation). The stochastic term $\mathcal{S}(\zeta_\alpha^n(t_{m-1}))$ has to be evaluated with a first order Euler-Maryuama explicit scheme. As it contains the increment of the Wiener term $\mathrm{d}W_j^n$ only a first order scheme is possible [68].

2. **Micro Mixing**
   The discretization of the micro-mixing term is rather simple and it is evaluated explicitly.

3. **Chemical source terms**
   The final step includes the integration of the stiff chemical source terms. Therefore, the first order Newton based Sundials CVODE solver is used [292].

Chapter 6

Simulation results

This chapter presents the simulation results of the three test cases that were briefly introduced in Section 1.3.3. They are all simulated with the ESF and FPV combustion model. The results are quantitatively compared against experimental data. The chapter starts with the Sydney/Sandia piloted flame with inhomogeneous inlet. The second case focuses on the Sandia Flame F. Finally, a hydrogen enriched oxy–fuel flame is presented.

6.1 Piloted flame with inhomogeneous inlet

The first simulated set up is case FJ200-5GP-Lr75-57 from the piloted flame series with inhomogeneous inlet, investigated by Barlow et al. [9] and Meares and Masri [174]. The setup is therefore interesting as the flame exhibits both a premixed flame mode close to the inlet, which transitions to a diffusion dominated mode further downstream. Due to these mixed mode characteristics and moderate local extinction effects this flame is not easy to simulate with standard combustion models. The LES results are compared against experimental data from 2015[1] and the quasi-DNS (qDNS) results[2] from [293]. Some of the results presented hereafter have already been published in Hansinger et al. [94].

6.1.1 Experimental setup

The main pipe of the burner consists of an outer tube with diameter $D = 7.5$ mm providing air (oxidizer) and a retractable inner tube with an inner diameter of $d = 4$ mm providing the fuel (methane). The wall thickness of both tubes is 0.25 mm. The burner is surrounded by a concentric pilot which is 18 mm in diameter. The axial position of the inner tube defines the degree of homogeneity between fuel and oxidizer at the main pipe outlet. If the fuel tube is completely recessed ($L_r = 300$ mm), oxidizer and fuel are assumed to be perfectly mixed. If the inner tube ends at the pilot plane ($L_r = 0$ mm), fuel and oxidizer are completely separated. The test case that is investigated in the following, case FJ200-5GP-Lr75-57, has a recess length of $L_r = 75$ mm. Hence, the mixture leaves the main pipe in an inhomogeneously mixed state before it gets ignited by the surrounding hot pilot stream. The pilot stream consisted of burnt products of C_2H_2, H_2, CO_2, N_2, O_2, which were mixed in proportions to match stoichiometric conditions of burnt CH_4 and air ($T_{st} = 2226$ K at $Z_{st} = 0.055$). This aspect is referred to in the case name with the abbreviation 5GP, for five

---

[1]available at: `http://web.aeromech.usyd.edu.au/thermofluids/database.php`
[2]available at: `http://vbt.ebi.kit.edu/index.pl/specialtopic/DNS-Links`

gas pilot. The bulk flow jet velocity of the fuel/air mixture is at $U_J = 57$ m/s, corresponding to a Reynolds number of Re $= 26800$, the pilot and surrounding air co-flow streams have mean velocities of $U_P = 26.6$ m/s, and $U_{Co} = 15$ m/s, respectively. The burner is placed in a wind tunnel with a cross section of 0.15×0.15 m. The inflow temperatures of fuel and air are $T_F = T_{Co} = 300$ K.

Figure 6.1 shows a schematic of the burner with dimensions in [mm]. Table 6.1 provides an overview of the relevant dimensions and flow velocities.
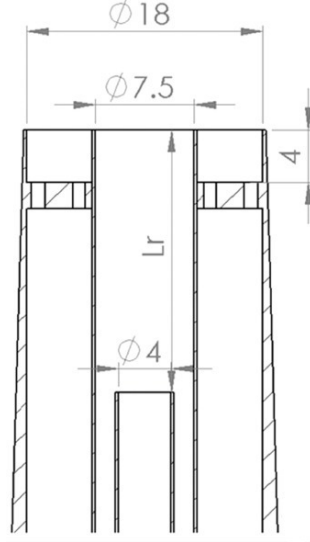
D	7.5 mm
d	4 mm
L_r	75 mm
U_J	57 m/s
U_P	26.6 m/s
U_{Co}	15 m/s
$T_{F,Co}$	15 m/s
T_{st}	2226 K

Figure 6.1: Schematic of the Sydney burner with dimensions in mm. Reprinted from [9] with permission of Elsevier.

Table 6.1: Relevant geometric dimension and flow velocities of the Sydney case FJ200-5GP-Lr75-57.

6.1.2 Numerical setup

6.1.2.1 Computational domain and inlet boundary conditions

The non–reactive mixing process between fuel and air in the main pipe was not part of the combustion LES. Instead, three consecutive simulations have been performed in cooperation with the Engler-Bunte-Institute at Karlsruhe Institute of Technology (KIT) to generate accurate transient inlet conditions for the subsequent reactive flow simulations, as described in [293]. The three precursor simulations are:

- LES of the fuel in the inner pipe (P).

- LES of the air flow in the annulus between inner pipe and main pipe (P).

- A non–reactive quasi-DNS of the flow and the mixing in the recessed main pipe (A).

This is illustrated schematically in Figure 6.2. The domain of the precursor LES (P) on the left consists of two pipes: (1) an inner pipe with diameter $d = 4$ mm and a length of $L/d = 6.25$. It provides the methane with a bulk velocity $\overline{U} = 67$ m/s. (2) An annular pipe with an inner diameter of 4.5 mm, an outer diameter of $D = 7.5$ mm and a length of $L/D = 3.3$ that provides air with a velocity of $\overline{U} = 59.5$ m/s. The time step was set to

1×10^{-7} s and the mesh for the inner pipe consists of 2 million cells while the annular pipe consists of 1 million cells, both made of purely hexahedral cells. The WALE [191] sub–grid model was used for turbulence closure.
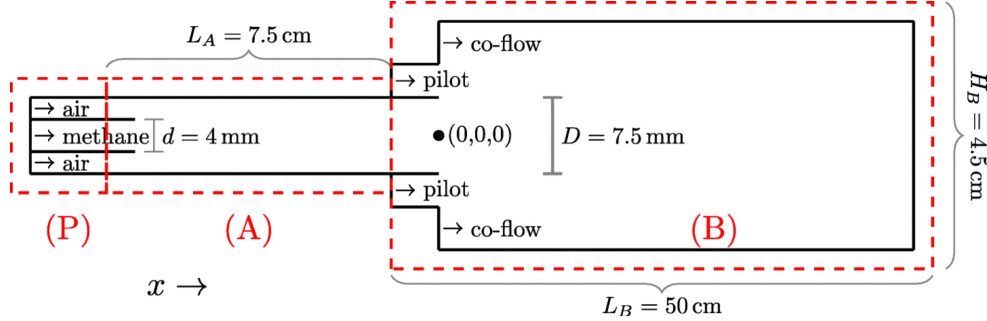

Figure 6.2: Schematic drawing of the computational domains (not to scale): (P) Precursor LES for generating the flow in the pipes. (A) Non-reactive quasi-DNS for the mixing of methane and air. (B) Reactive LES of the flame. Reprinted from [293] with permission of Springer Nature.

The second domain (A) is for the non–reactive mixing of the methane and air flows has a total length of 10 D, it ends 1 D upstream from the burner pipe exit. The inner pipe is retracted by 7.5 cm with respect to exit of the burner into the combustion chamber in (B) in order to generate inhomogeneous mixing conditions. At the outlets of domain (P), velocity profiles were sampled at a rate of 1×10^{-7} s which are used as inlet boundary conditions for the simulation in domain (A). The computational grid for domain (A) was block structured and consisted of 150 million purely hexahedral cells. The mesh was refined radially with a smallest resolution of 5 μm at the walls. Velocity data and CH_4, O_2, and N_2 mass fractions were sampled at the outlet of domain (A) every 1×10^{-7} s and served as transient inlet boundary conditions for the main pipe in domain (B). Domain (B) was then used for the reactive flow LES of the flame. It has a total axial length of 68 D and a diameter of 6 D. Its inlet plane is connected to the outlet plane of domain (A) at $x = -D$. Figure 6.3 shows instantaneous snap shots of the mixture fraction Z (a) and the x-component of the velocity U_x (b) that was sampled at the outlet of domain (A). The inhomogeneous distribution of Z over the cross section of the main pipe is clearly visible.

6.1.2.2 Computational meshes

Three different block structured meshes have been used for the combustion LES in domain (B). These are the *fine* (F) mesh with 4.6 million cells, the *medium* (M) mesh with 2.8 million cells, and the *coarse* (C) mesh with 1 million cells. All three of them are topologically similar. Local mesh refinement is applied in the core region of the fuel jet and where shear layers between jet and pilot stream are expected to resolve velocity gradients. Grid stretching has been applied in radial direction and in flow direction beyond $x/D = 20$. Figure 6.4 shows the cell size Δ for the three meshes, computed as $\Delta = \sqrt[3]{V_c}$, where V_c denotes the cell volume. As a reference, the Kolmogorov length l_η, as it was computed in [293], is given, too. As shown, the cell sizes are between 0.2 and 0.7 mm, depending on the mesh and the axial position, in the core region and where the flame is expected ($r/D < 3/2$). At the walls, which confine the domain, a slip boundary condition (BC) was applied for the velocity, and
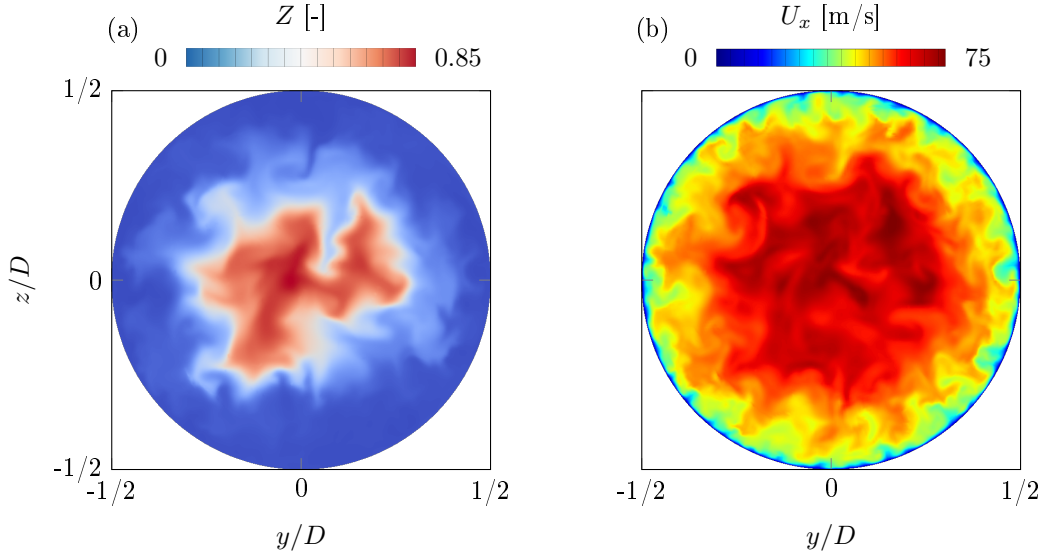
Figure 6.3: Instantaneous snap shots of the mixture fraction Z (a) and the x-component of the velocity U_x (b) distribution in the main pipe; sampled at the outlet of the quasi-DNS in domain (A).

for temperature, species, and pressure a zero gradient BC was used. At the domain outlet a zero gradient BC was used for the velocity, species, and temperature. For the pressure, a total pressure BC was applied.

An additional *very fine* (VF) mesh with 60 millon cells has been used for non–reactive flow simulations only and to validate the quality of the other meshes. Table 6.2 provides an overview of the different meshes.
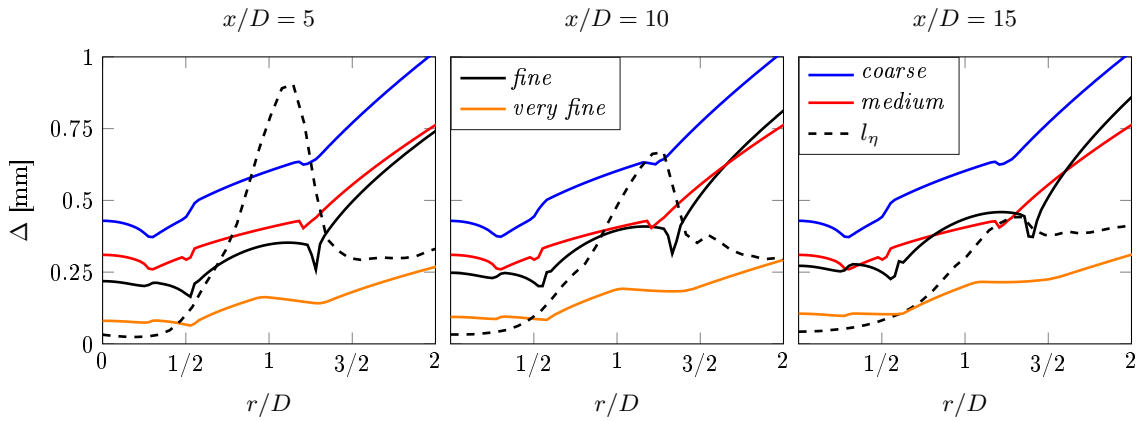
Figure 6.4: Filter widths Δ of different meshes over radial position r at different axial planes. For comparison the Kolmogorov length l_η as computed in [293], is presented, too.

6.1.3   Results of the non–reactive simulations

The investigated test case has been one of the target flames of the 14th international workshop on turbulent non–premixed flames (TNF) [265]. One of the workshop's findings was

Mesh name	*coarse* (C)	*medium* (M)	*fine* (F)	*very fine* (VF)
No. of cells	1×10^6	2.8×10^6	4.6×10^6	60×10^6
Non–reactive	✓	✓	✓	✓
Reactive	✓	✓	✓	-

Table 6.2: Overview of meshes for the Sydney flame.

that this configuration challenges not only the combustion models, but also the turbulence modeling in terms of an accurate reproduction of the flow velocities and the turbulent diffusion of mixture fraction. To further investigate this aspect, simulations of two non–reactive configurations have been carried out. The first configuration uses a cold pilot stream at $T_{\mathrm{P}cold} = 300$ K. To keep the pilot's Reynolds number identical to the hot pilot case the inflow velocity is set to $U_{\mathrm{P}_{cold}} = 3.26$ m/s. The second non–reactive case uses the identical setup as the reactive case, i.e. a hot pilot and the same inflow, but the chemical reactions have been deliberately switched off. Although this may not seem physically correct, it allows to study the turbulent diffusion of mixture fraction under the influence of the hot pilot stream.

Both of these non–reactive cases have been simulated on the four, previously described meshes (C, M, F, VF) in order to first have a highly resolved reference solution (VF) for further model validation, and second to demonstrate mesh convergence of the *fine*, *medium*, and *coarse* mesh, which are used in the subsequent combustion simulations.

Figure 6.5 shows the time and circumferentially averaged mean and RMS values of axial velocity U_x, and mixture fraction Z of the non–reactive cold pilot case at different axial positions, obtained by averaging the flow simulation over 10 ms (approx. 15 flow through times, based on the experimentally investigated range of $0 \leq x/D \leq 30$). The velocities from the *very fine* and *fine* mesh are in good agreement with the experiments and both of them are almost indistinguishable. On the contrary, the velocities from the *coarse* simulation show a tendency to underpredict the experimental mean in the center region of the jet by approximately 10%. The mixture fraction results in the second row show a high discrepancy between *medium*, *coarse* and *fine* simulations, especially close to the jet exit at $x/D = 5$. While the *medium* results slightly overpredict those of the *fine* case, the *coarse* one underpredicts these by about 20% close to the jet exit.

Figure 6.6 shows the same results on all three meshes for the non–reactive case with the hot pilot, including the temperature which can be considered as passive scalar. While there are significant differences in the velocity and mixture fraction fields between the *fine* and *coarse* simulation in the cold case, there are only minor differences between all four simulations in the hot pilot case. The simulated velocities are identical and the mixture fraction mean values show only differences in the core region of the jet up to $x/D = 10$, with the *fine* solution being closer to the *very fine* result. The same observation is made for the temperature, where the results are very similar and only show small differences in the peaks of the mean values. Generally, there is good agreement between all four simulations.

Additional figures from the non–reactive case can be found in Appendix B.1.1.

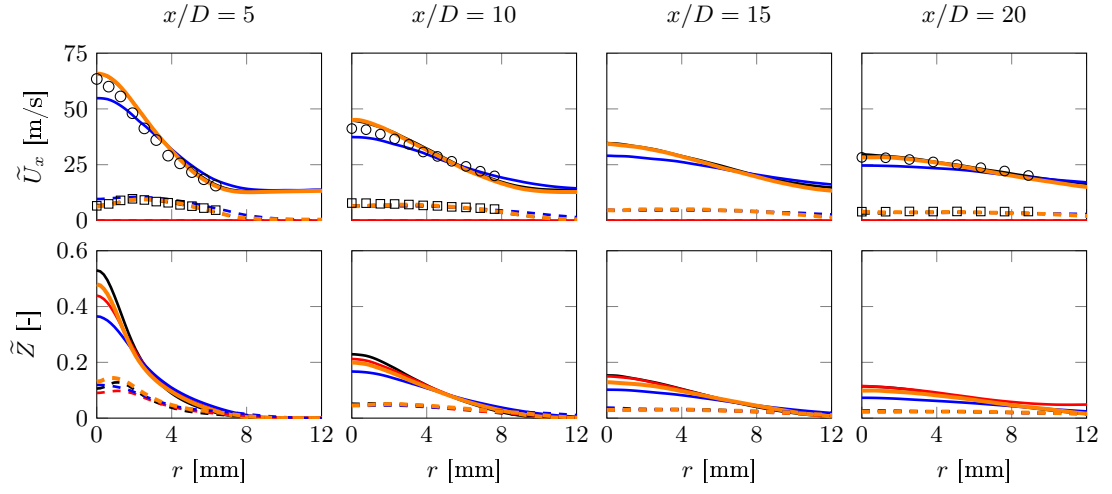Figure 6.5: Radial distribution of time averaged mean and RMS values for the non–reactive cold pilot case.

Mean: ∘ Exp, — *very fine*, — *fine*, — *medium*, — *coarse*; RMS: □ Exp, - - - *very fine*, - - - *fine*, - - - *medium*, - - - *coarse*.
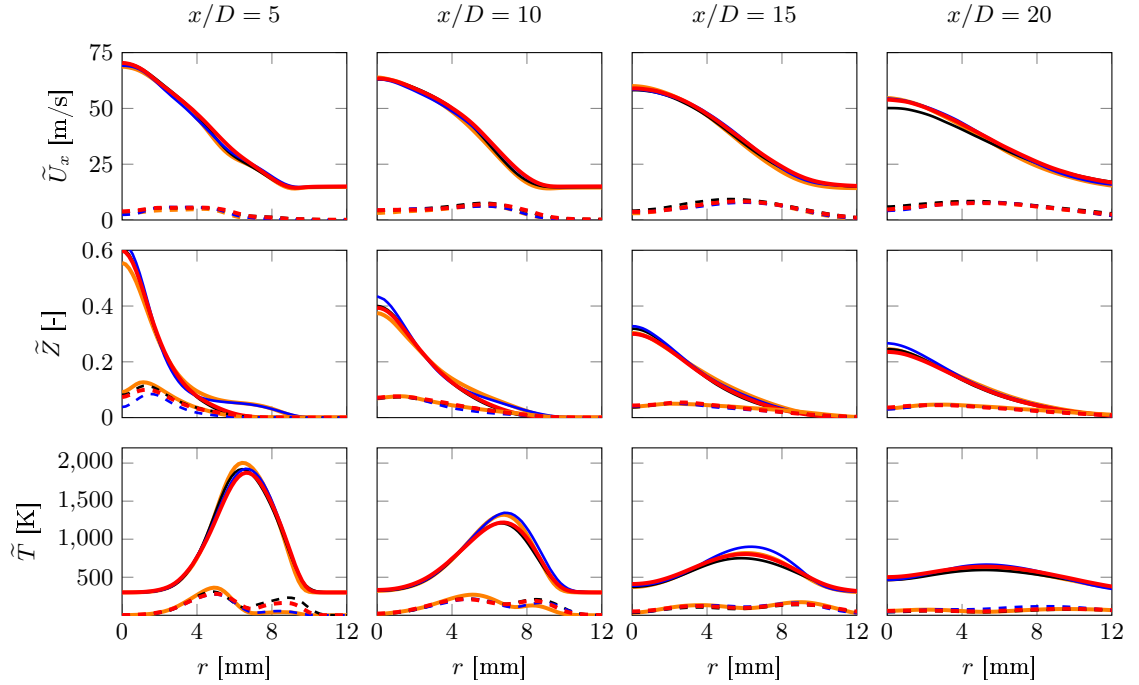

Figure 6.6: Radial distribution of time averaged mean and RMS values for the non–reactive hot pilot case. The color coding is the same as in Fig. 6.5.

6.1.4   Results of the reactive simulations

6.1.4.1   Baseline reactive flow simulations

In the following, results of the *medium line* reactive flow simulations on all three meshes (C,M,F) are presented. It is termed *medium line*, as it was intended to reproduce the experimental data and the results of the qDNS by [293] with high accuracy. Furthermore, these simulations serve as a reference for parameter variations and the comparison of combustion models.

Table 6.3 gives an overview on the different setups. All cases use the ESF combustion model (the modified version of Eq. 4.23) in combination with the Lu19 chemical mechanism and a number of $N_s = 8$ stochastic fields, as recommended by [64, 122, 123]. The WALE model [191] is used for turbulence closure. Figure 6.7 shows instantaneous snap-

Name	Mesh	TCI model	Chemistry	N_s	SGS model
CASE-F-ESF-lu19-8	F	ESF	Lu19	8	WALE
CASE-M-ESF-lu19-8	M	ESF	Lu19	8	WALE
CASE-C-ESF-lu19-8	C	ESF	Lu19	8	WALE

Table 6.3: Overview of the numerical setups for the *medium line* simulations.

shots of temperature (a) and mixture fraction (b) from CASE-F-ESF-lu19-8. The Pope criteria M (2.35) is illustrated in Figure 6.8. It shows that for all three meshes the SGS turbulence contribution is around or below 20% in the core region of the jet, therefore the meshes are well suited for LES. Time averaged mean and RMS values have been obtained
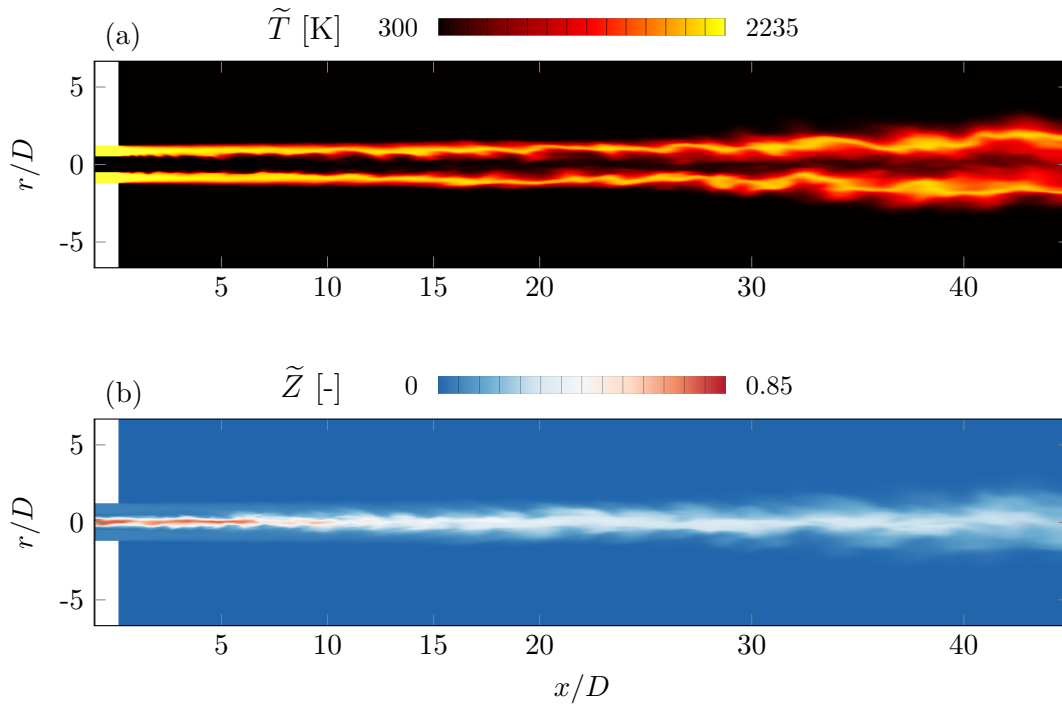

Figure 6.7: Snapshots of instantaneous temperature T (a) and mixture fraction Z (b) fields for the reactive case on the *medium* mesh.
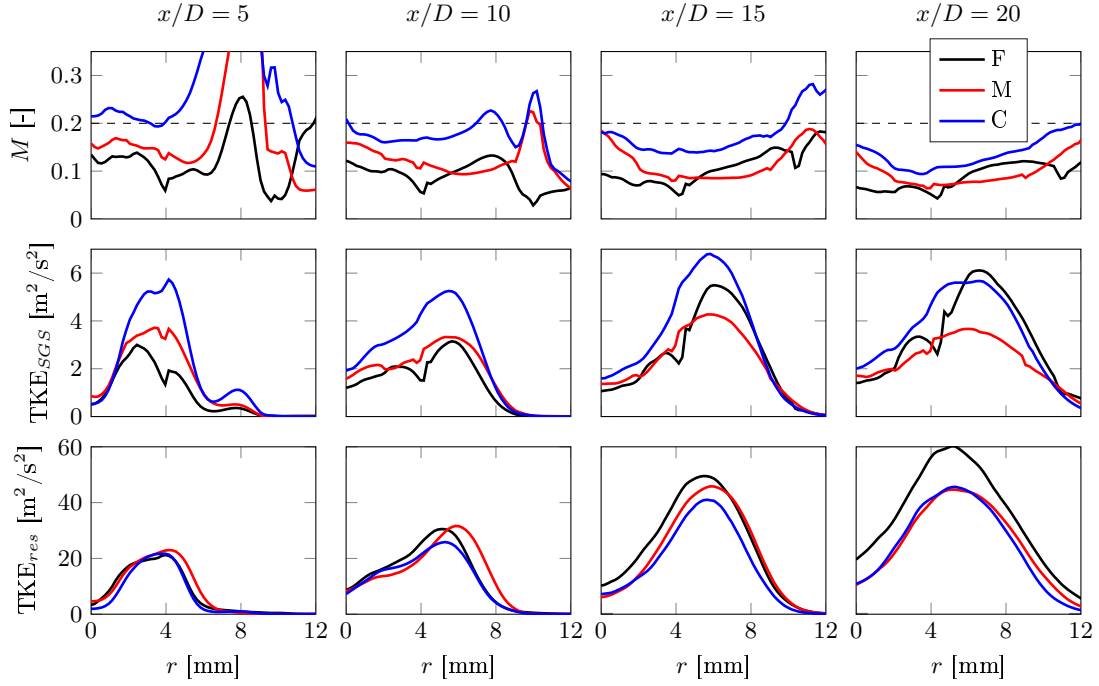
Figure 6.8: Ratio M (2.35) between modeled and total TKE, and the modeled and resolved TKE.

by averaging over 10 ms which corresponds to approximately 15 flow through times within the experimentally investigated range between $0 \leq x/D \leq 30$. Figure 6.9 compares the results of the reactive flow simulations on the *coarse* (blue), *medium* (red) and *fine* (black) mesh with experimental data and the qDNS [293] (green) at different axial positions. Presented are the temperature, mixture fraction and several major and minor species, as well as the heat release $\dot{Q}$. Solid lines depict the mean, dashed lines represent RMS values.

The temperature results (1st row) on the three meshes are almost identical. Near the pipe exit plane ($x/D \leq 10$) they are also in very good agreement with experimental data and the qDNS results. Further downstream temperatures on the outer flame region ($r \geq 6$ mm) are overpredicted, when compared to the experiments. However, the mean values are still in good agreement with the high-fidelity qDNS data. The qDNS RMS values are slightly higher at the outer flame region, indicating higher turbulent fluctuations of the temperature field in the shear layer between flame and co-flow.

The simulated mixture fractions (2nd row) agree very well close to the jet inlet ($x/D = 5$), although all three simulations overpredict the experimental mixture fraction in the core region of the jet. Further downstream, the qDNS predicts well the experiments, also in the center of the jet, while the LES results continue to show the tendency of predicting too high mixture fractions in the jet center but do not show significant differences among the two of them. It is speculated that the chosen turbulence modeling approach in LES underestimates the production of turbulent diffusivity, which underpredicts scalar fluxes on the sub–grid scale. However, the accurate prediction of Z is one of the difficulties of the investigated test case, as it has been reported and discussed at the TNF-14 workshop[3] among several other groups.

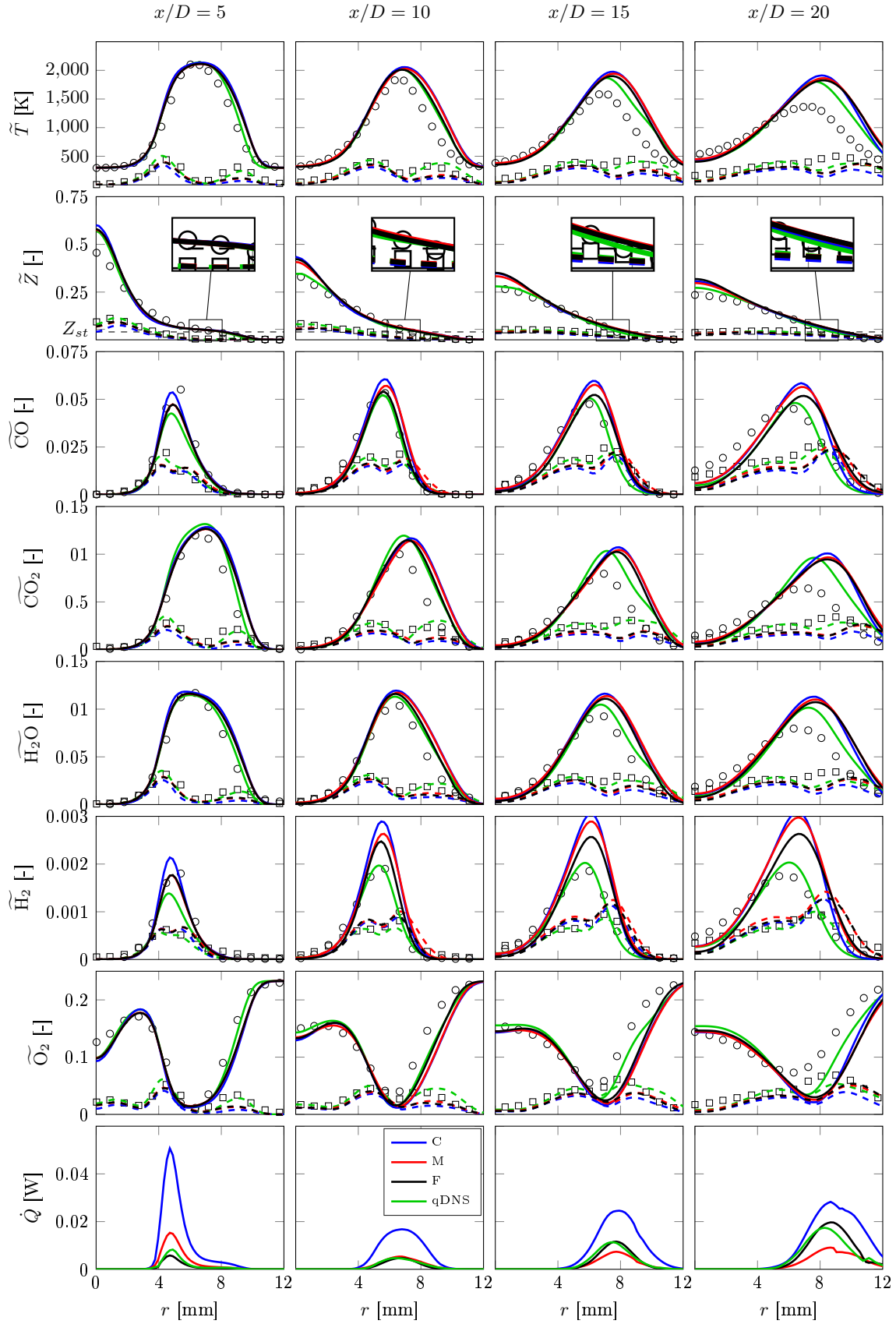[3]www.tnfworkshop.org/workshop-proceedings/tnf14-workshop/

Figure 6.9: Radial mean and RMS values of different flow quantities for the reactive cases as in Tab. 6.3, the qDNS data with mean as solid lines and the RMS as dashed lines. Experiments: ∘ mean, □ RMS.

The next rows show the results for selected major and minor species. For the major species (O_2, H_2O, CO_2) they follow a similar tendency. The results generally agree very well and are also in good agreement with experimental and qDNS results in the first section of the domain, while they differ further downstream on the outer flame region. However, no significant mesh dependency is evident. For the minor species (CO, H_2) the situation is different. Apparently, the resolution of the mesh does have an influence on the accuracy of the results and H_2 is overpredicted. The best agreement with experimental data is seen for the qDNS, followed by the results on the *fine*, *medium*, and *coarse* mesh.

The last row depicts and compares the mean heat release $\dot{Q}$ from the simulations and is presented in [W] (no experimental data is shown as this quantity has not been measured). While qDNS, *fine*, and *medium* results agree very well and their peaks gradually increase in downstream direction, the heat release from the *coarse* mesh has its peak at $x/D = 5$. Moreover, it is approximately more than eight times higher. It then decreases at $x/D = 10$ and increases again until it is finally in the same order of magnitude as qDNS and *medium* results at $x/D = 20$. It is assumed that the *medium* mesh is already fine enough to resolve reactions zones, which explains why it coincides so well with the qDNS, while the *coarse* mesh is – despite using the ESF combustion model – too coarse to adequately predict the heat release in the front region where the flame is in a predominantly premixed combustion mode. This assumption is supported by a recent study from Picciani et al. [208] who showed that the ESF method significantly overpredicts the fuel consumption rate in premixed combustion when the grid spacing is not in the order of magnitude of the laminar flame thickness. Fuel consumption rate and heat release rate are both a result of the species reaction rates and tend to be overpredicted on the *coarse* mesh. This could explain the $\dot{Q}$ peak at $x/D = 5$, which decreases and is in better agreement further downstream, where the flame transitions to a non–premixed combustion mode. Figure 6.10 compares the instantaneous temperature in mixture fraction space from the experiments (1st row), and the results obtained from the *fine* (F) (2nd row), *medium* (M) (3rd row), and *coarse* (C) (4th row) mesh at the different axial locations. The 5th row presents the mean value of temperature conditional on mixture fraction $\langle \widetilde{T} | \widetilde{Z} \rangle$, here are also the qDNS results included. In order to guarantee comparability among the plots the samples are taken at the same radial locations as in the experiments and always the same number of scatter points is displayed. Figure 6.11 shows scatter data for the CO mass fraction.

The experimental temperature data show the transition from the partially premixed/auto–ignition state close to the inlet ($x/D = 5$) to a non–premixed diffusion flame further downstream. On all meshes this transition is reproduced very well. Visually, the simulation results are also in good qualitative agreement with the experiments, demonstrating the suitability of the employed combustion modeling approach to cope with different combustion regimes. Minor differences can be seen at $x/D = 20$ where the experiments show some extinction and re–ignition events between $0 \leq Z \leq 0.1$. These are not represented in the simulations. However, this is not attributed to the combustion model itself, it is rather speculated that these events are a result of the turbulent breakup of the flame in the rear part, which is not reproduced well in the LES. The scatter data in Figure 6.11 indicate a similar behavior for the CO mass fraction. Although this species is usually difficult to model the scatter plots of all cases are in very good agreement with the experiments and qDNS. The experimental peak values of CO mass fraction around stoichiometry are slightly underpredicted. Conditional mean values have been obtained from the scatter data by averaging the scatter data over the mixture fraction in bins of $\Delta Z = 0.001$. The quantitative
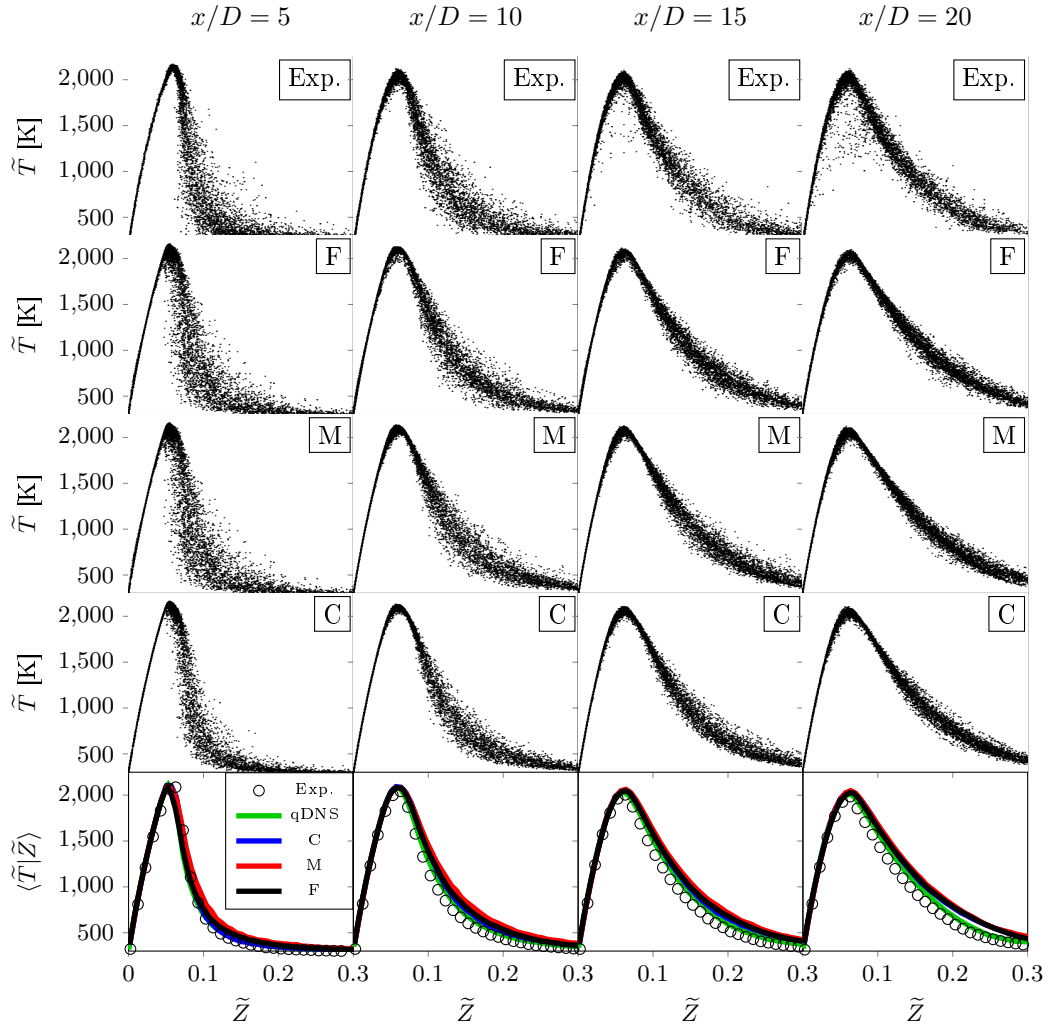
Figure 6.10: Scatter plots of temperature $\widetilde{T}$ and mixture fraction conditional temperature $\langle \widetilde{T}|\widetilde{Z}\rangle$ at different axial locations.
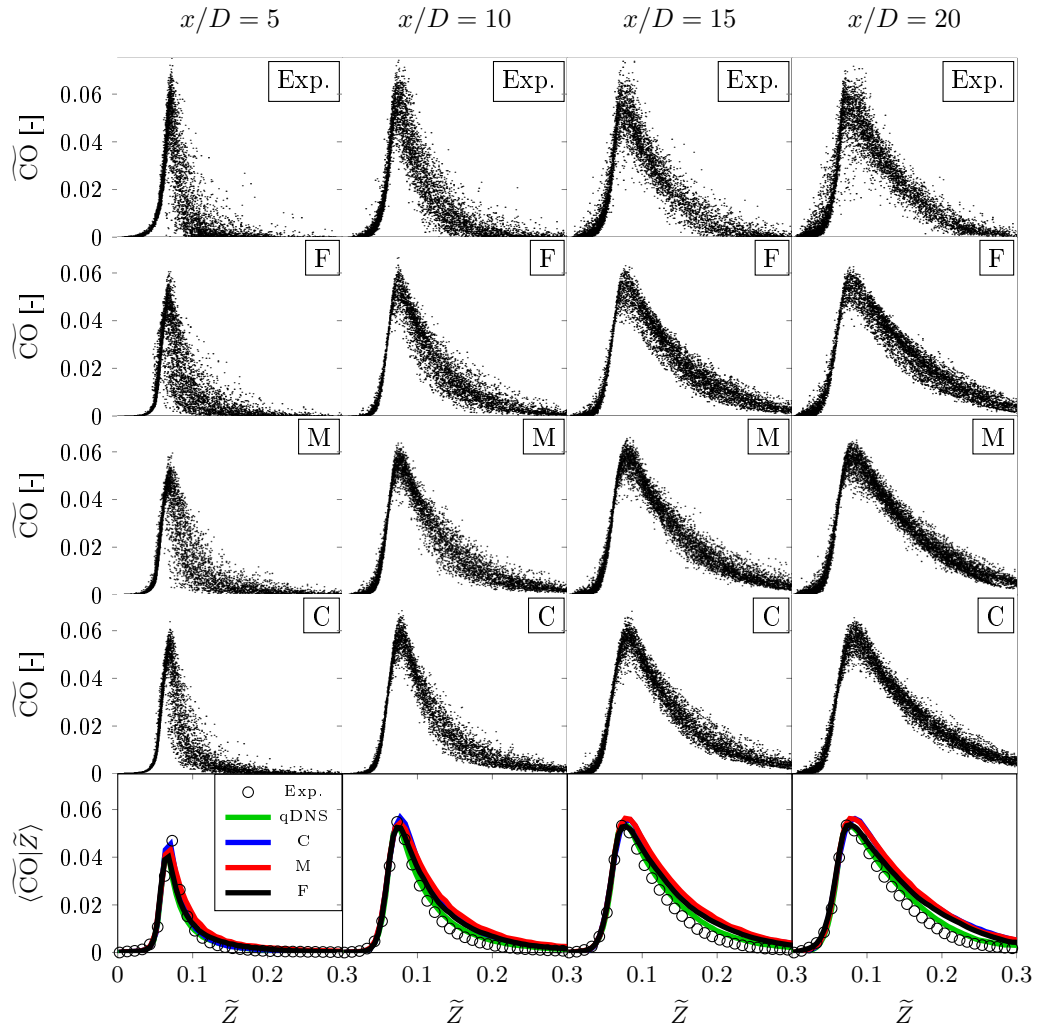
Figure 6.11: Scatter plots of CO mass fraction and mixture fraction conditional CO mass fraction $\langle \widetilde{CO}|\widetilde{Z} \rangle$ at different axial locations.

comparison of the conditional temperatures in the 5th row of Figure 6.10 shows very good agreement between the LES, the experiments, and the qDNS. Further downstream, the LES results start to differ from the experiments on the fuel rich side, but are still close to the qDNS data. All three LES coincide very well, no significant difference can be seen between them. The conditional values of CO (Fig. 6.11, 5th row) show very good agreement for all LES cases on the fuel lean side at all downstream locations. Around stoichiometry and up to $\widetilde{Z} = 0.1$ the *fine* mesh shows better agreement with the qDNS. Towards the fuel rich side the LES results tend to overpredict CO mass fractions.
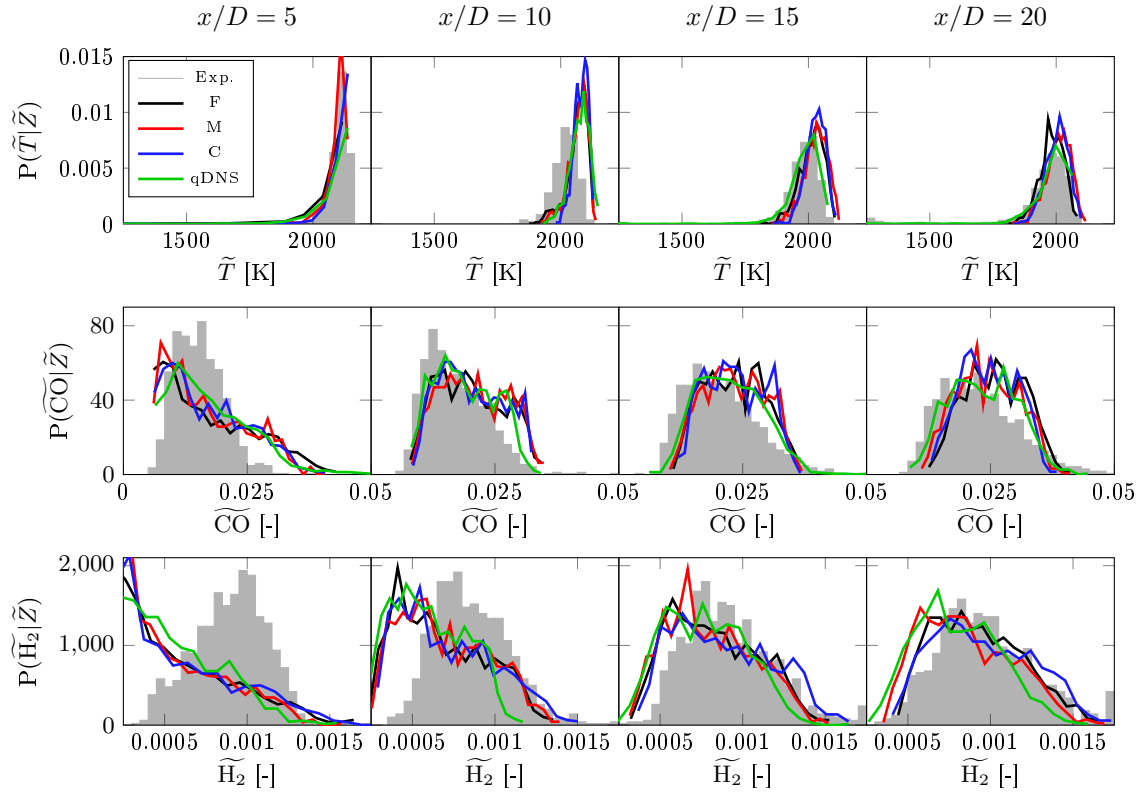
Figure 6.12: PDFs of temperature, CO, and H_2O mass fractions within the mixture fraction interval $0.005 \leq Z \leq 0.006$.

While scatter plots provide a useful visual insight into the flame structure and the degree of local extinction at each measurement position, conditional statistics of temperature and reactive scalars might be more useful for a quantitative comparison between simulation and experiments and to assess the quality of the employed combustion model. Figure 6.12 shows the PDFs of temperature, as well as CO, and H_2 mass fractions conditional on mixture fraction within the interval $0.005 \leq \widetilde{Z} \leq 0.006$ around stoichiometry, i.e. where the highest temperatures are expected. All PDFs have been normalized, so that they integrate to one. Experimental data is presented in the form of (grey) histograms, while LES and qDNS data are shown in the form of line plots. As expected from the previous analysis, the temperature PDFs of LES and qDNS generally agree well. At $x/D = 10$ the experiments show the highest probability for temperature at around 2000 K, while all three simulations have a shifted peak at 2100 K, i.e. predict higher temperatures with a higher probability. Further downstream, the probability of predicting temperatures at 2000 K is slightly overpredicted

by all LES. Regarding the probabilities of CO and H_2 mass fractions, all simulations are in good agreements with the measurements, except for H_2 at the plane $x/D = 5$. Here, the experiments indicate a normal distribution centered around 0.001, whereas the simulations all consistently exhibit an exponentially-shaped distribution with maxima at $H_2 = 0$. This may be due to the use of different pilot flame compositions. While the simulations assume a fully burnt CH_4/air mixture at an equivalence ratio of $\phi = 1$ it is a five component gas mixture in the experiment. Apart of CH_4 one of the components is H_2, which eventually contributes to the large deviations in the PDFs of H_2.

Trends in the probability of local extinction can be compared further by calculating the burning index BI_T based on temperature. BI_T is computed from the individual temperatures T_i of all samples N within the mixture fraction interval $0.05 < \widetilde{Z} < 0.06$ around stoichiometry:

$$BI_T = \frac{1}{N} \sum_{i=1}^{N} \frac{T_i - 300}{2100 - 300} \ . \tag{6.1}$$

Here 300 K is the inlet temperature for both fuel and coflow inlet, the burnt temperature has been chosen as 2100 K, which was the maximum temperature that has been measured in the experiments [9]. Figure 6.13 compares the burning indices of the experimental data with the results from *medium*, *coarse*, and qDNS [293] simulation. All BI_T reproduce well the trend of local extinction from the measurements.

At $x/D = 5$ the burning index of the *coarse* and *medium* result matches the experimental index with $BI_T = 1$, while the *fine* simulation indicates only slightly the effects of local extinction. Further downstream, all LES and qDNS results show a very similar BI_T and follow the trend of local extinction observed in the experiments, though, they all predict a slightly higher burning state. Compared with the index values obtained from the qDNS, the LES results are in very good agreement.
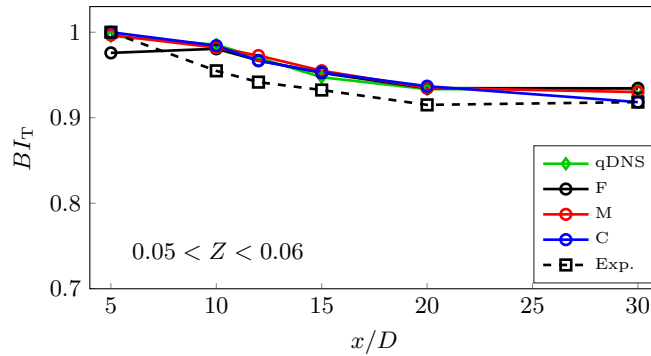
Figure 6.13: Burning index BI_T at different axial positions.

6.1.4.2   Comparison of chemical mechanisms and FPV manifolds

The previous results showed that the chosen combustion modeling approach provides already very good agreement with the experimental and qDNS data, with different degrees of accuracy, depending on the mesh resolution. However, the modeling approach is founded on two pillars: the TCI closure, which is the ESF method, and the representation of the thermo–chemistry, which was established with the Lu19 mechanism. As it was demonstrated

in Section 3.2.2, the analytically reduced Lu19 mechanism shows very good agreement with a detailed mechanism, such as the GRI-3.0.

In the following it will be analyzed how a variation of the chemical mechanism, a variation of the transport model with differential diffusion, and an exchange of the ESF method with the FPV combustion model affect the overall quality of the simulation results. The mechanisms that are employed for the ESF method are the Lu13 and the JL-R. Both showed less good agreement with the GRI-3.0 than the Lu19 in the generic examples of Section 3.2.2. However, both are associated with lower computational costs. Two cases with the FPV combustion model are considered, one with a manifold generated from laminar premixed flamelets, the other one with a manifold based on laminar counter flow diffusion flamelets. The respective cases are listed in Table 6.4, all were simulated on the *medium* mesh. Figure 6.14 compares the radial mean and RMS results for the six different cases, as

Name	Mesh	TCI model	Chemistry	N_s	SGS model
CASE-M-ESF-lu19-8	M	ESF	Lu19	8	WALE
CASE-M-ESF-DD-lu19-8	M	ESF-DD	Lu19	8	WALE
CASE-M-ESF-lu13-8	M	ESF	Lu13	8	WALE
CASE-M-ESF-JLR-8	M	ESF	JL-R	8	WALE
CASE-M-FPV-PREMIX	M	β-PDF	premixed FPV	-	WALE
CASE-M-FPV-NONPRE	M	β-PDF	non–premixed FPV	-	WALE

Table 6.4: Simulations with a variation of the chemical mechanism.

a reference the qDNS and experimental results are plotted again. Differential Diffusion does play a negligible role in this configuration. However, the prediction of the H_2 mass fractions slightly improves in CASE-M-ESF-DD-lu19-8. For other quantities of interest, the ESF-DD model is not better than the ESF model (both with Lu19). The results of the Lu13 and Lu19 are very similar and show only minor differences. However, CASE-M-ESF-lu13-8 achieves a better prediction of the H_2 mass fractions (4th row) than CASE-M-ESF-DD-lu19-8 with the Lu19 mechanism and differential diffusion. This is rather surprising, since the Lu13 is less complex than the Lu19 mechanism and is speculated that this is rather a favorable coincidence in the present configuration, as the Lu13 generally underpredicts H_2 mass fractions, as shown for a counter flow diffusion flame in Fig. 3.5. The results with the JL-R mechanism are not satisfying. Although some species, such as H_2O or the temperature are predicted fairly well, the overall prediction quality is rather poor. The two FPV cases show a similar behavior. The predicted temperatures are in good agreement with the reference CASE-M-ESF-lu19-8, the same accounts for H_2O and CO_2 mass fractions, although CASE-M-FPV-NONPRE shows more deviations on the fuel rich side. The minor species (CO and H_2) mass fractions are strongly overpredicted by both FPV manifolds. This is presumably because non-equilibrium effects do play a role in this flame. These are not captured as such in the FPV manifolds which were generated from steady, laminar flamelets. Different definitions of PV, or the inclusion of a second progress variable could also improve the prediction accuracy for some quantities of interest. However, a detailed analysis is beyond the scope of the present work.

The mixture fraction conditional plots of $\widetilde{T}$ and $\widetilde{CO}$ in Figure 6.15 support these findings. While the results of the Lu13 are equal to the Lu19, the results of the JL-R underpredict the conditional temperatures and CO mass fractions. The conditioned temperature of CASE-
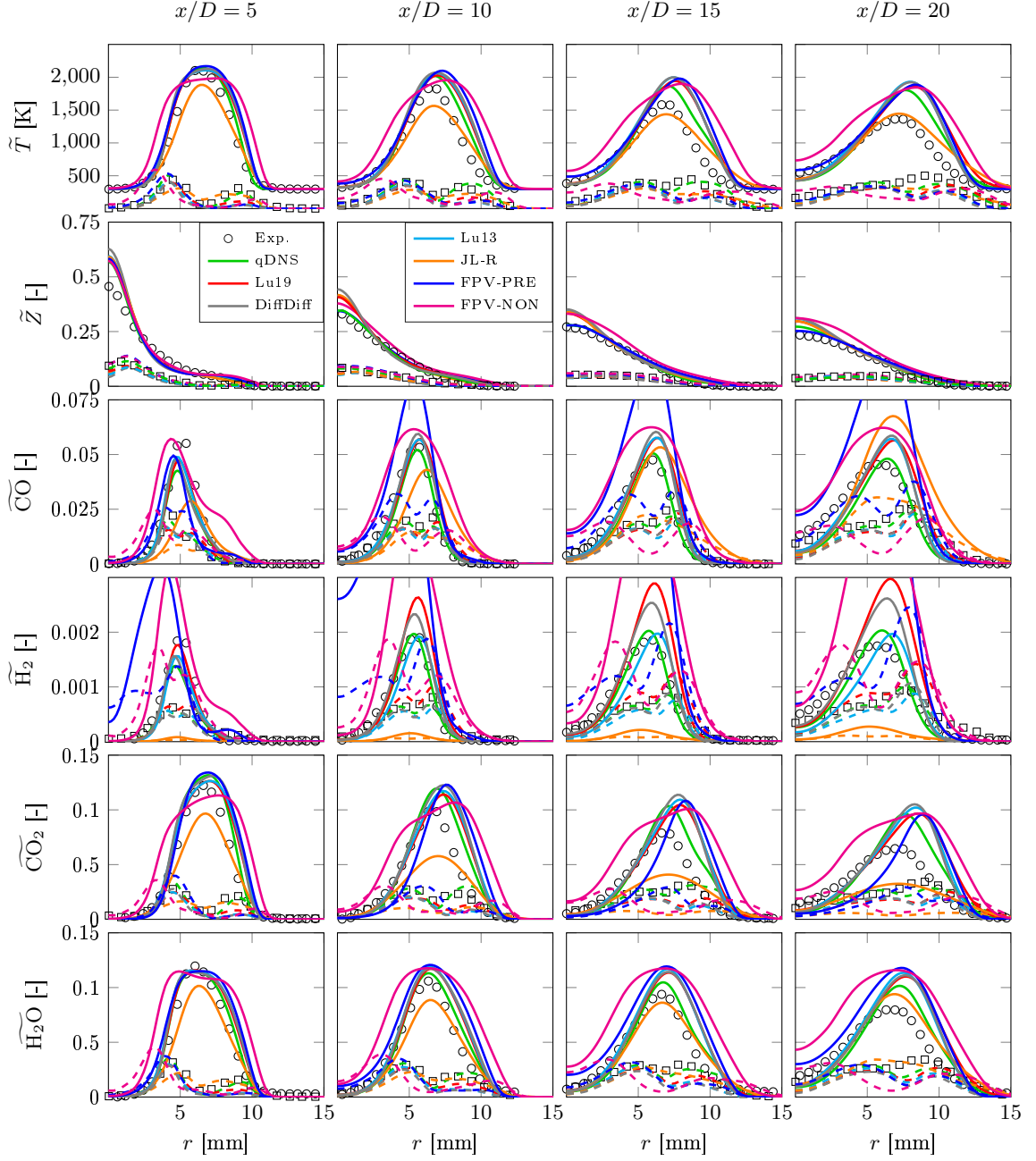
Figure 6.14: Comparison of mean and RMS values obtained with different chemical mechanisms: —— CASE-M-ESF-lu19-8, —— CASE-M-ESF-lu13-8, —— CASE-M-ESF-JLR-8, —— CASE-M-ESF-DD-lu19-8, —— CASE-M-FPV-PREMIX, —— CASE-M-FPV-NONPRE, solid is mean, dashed is RMS. Experiments: ○ mean, □ RMS.

M-FPV-PREMIX is in very good agreement with CASE-M-ESF-lu19-8, on the contrary CASE-M-FPV-NONPRE overpredicts the temperature quite a lot on the fuel rich side ($\widetilde{Z} > 0.1$). The mixture fraction conditioned CO mass fractions are also much too high for both FPV cases, except for CASE-M-FPV-PREMIX at $x/D = 5$. At this location the flame is still close to the premixed combustion mode which is likely the reason that the premixed FPV manifold resembles well the actual flame mode.
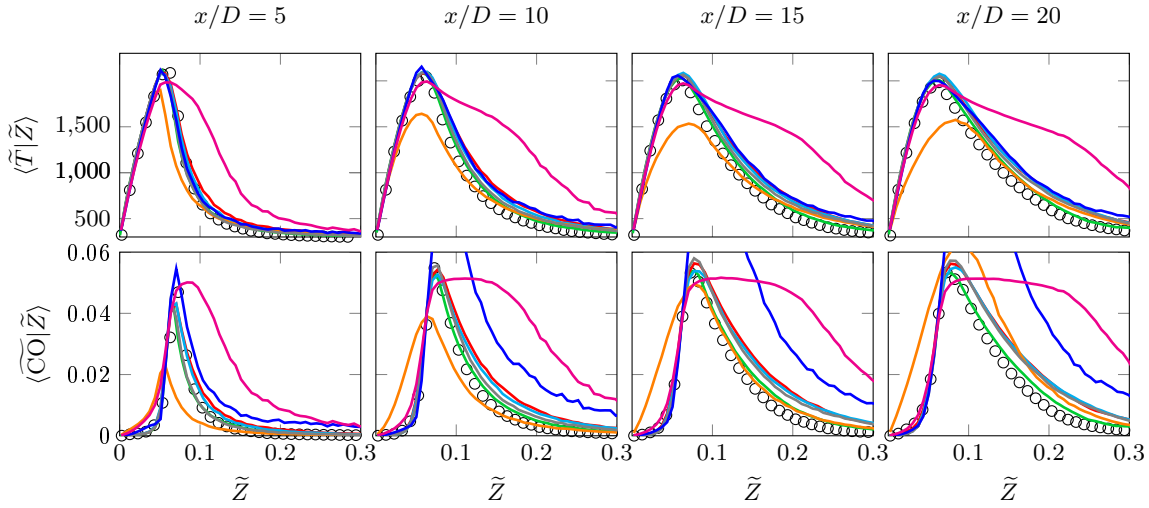

Figure 6.15: Comparison of mixture fraction conditioned temperatures and CO mass fractions obtained with different chemical mechanisms: —— CASE-M-ESF-lu19-8, —— CASE-M-ESF-lu13-8, —— CASE-M-ESF-JLR-8, —— CASE-M-ESF-DD-lu19-8, —— CASE-M-FPV-PREMIX, —— CASE-M-FPV-NONPRE.

6.1.4.3   Comparison between ESF and ESF-O method

Figure 6.16 presents a direct comparison of the ESF (red, CASE-M-ESF-lu19-8) (4.27) and ESF-O (blue, CASE-M-ESF-O-lu19-8) (4.23) methods against the experimental and qDNS data for $\widetilde{T}$, $\widetilde{Z}$, CO, and CO_2. As it can be observed there are some differences in the mean (solid) and RMS (dashed) values of both formulations of the ESF method, except for the mixture fraction. Most notably are the differences in scalar peak values (around $r \approx 7$ mm) and in the shear layer between pilot and coflow ($10 \leq r \leq 15$ mm). The ESF-O method tends to predict lower peak values of the radial mean fields compared to the ESF method, but higher temperatures and CO_2 mass fractions in the outer shear layer between pilot and coflow. Since there are no chemical reactions in the outer shear layer it seems that the ESF-O method is also affecting the mixing process.

The reason for the comparison is not to indicate which of the two models is more suitable, but to demonstrate that both formulations lead to similar results. For example, the CO mass fractions from the ESF-O method are in better agreement with qDNS data than the ESF method. Vice versa, the ESF method compares better with the qDNS for temperature and CO_2 mass fraction.

Figure 6.17 compares the mixture fraction conditional temperature and CO mass fractions. Generally, the differences between the ESF and ESF-O formulation are small, e.g. compared to the qDNS data. The conditional peak values of $\widetilde{T}$, and $\widetilde{CO}$ are slightly smaller for

the ESF-O method, on the other hand the predictions on the fuel rich side ($\widetilde{Z} > 0.15$) are slightly higher.

6.1.4.4 Effect of number of stochastic fields N_s

In this section it is investigated if, and how the number of stochastic fields N_s affects the accuracy of the filtered simulation results. Based on previous studies with the ESF method [120–122] a number of $N_s = 8$ stochastic fields has been established to be sufficient to describe the SGS scalar fluctuations. Therefore, additional simulations with different numbers of $N_s = 8$, 16 and 64 stochastic fields and laminar finite rate chemistry (neglecting TCI) were conducted to compare the impact of N_s. All these simulations have been carried out on the *coarse* mesh only, because the influence of the number of fields is expected to increase on coarser meshes. The respective cases are listed in Table 6.5.

Name	Mesh	TCI model	Chemistry	N_s	SGS model
CASE-C-LAM-lu19	C	-	Lu19	-	WALE
CASE-C-ESF-lu19-8	C	ESF	Lu19	8	WALE
CASE-C-ESF-lu19-16	C	ESF	Lu19	16	WALE
CASE-C-ESF-lu19-64	C	ESF	Lu19	64	WALE

Table 6.5: Simulations with different numbers N_s of stochastic fields.

Figure 6.18 compares the radial mean and RMS results (only presented: $\widetilde{T}$, $\widetilde{Z}$, $\widetilde{CO}$, $\widetilde{CO_2}$) of the four simulations with different number of stochastic fields; qDNS and experimental data are not shown in this plot as the focus is on a direct comparison between the simulation results. However, as it can be seen there are only small differences in the radial mean and RMS results. Figure 6.19 depicts the mean values of temperature and CO mass fraction conditional on mixture fraction. Again, independent of N_s all simulations exhibit very similar results. Minor differences can be seen for the laminar chemistry case in the CO mass fraction at $x/D = 5$ and 10 where the conditional values are slightly lower. However, based on the underlying results it cannot be confirmed that a high number of N_s fields improves the overall accuracy significantly. As a matter of fact, using laminar finite rate chemistry, which means deliberately neglecting the sub–grid fluctuation of the reactive scalars and approximating $\overline{\dot{\omega}}_k \approx \dot{\omega}_k$, is already accurate enough in the present configuration.

6.1.4.5 Analysis of SGS data

In this subsection the sub–grid activity and statistics of the individual stochastic fields is analyzed and compared.

First, the assumption of statistical independence between the mixture fraction Z and a normalized reaction progress variable PV_n, which is often made, is further investigated from CASE-C-ESF-Lu19-64. The common assumption states that the joint sub–filter probability distribution $\widetilde{\mathcal{P}}_{sgs}(Z,PV_n)$ can be approximated by a convolution of the marginal probability distributions $\widetilde{\mathcal{P}}_{sgs}(Z,PV_n) \approx \widetilde{\mathcal{P}}_{sgs}(Z)\widetilde{\mathcal{P}}_{sgs}(PV_n)$, assuming statistical independence between both variables [209]. Statistical independence demands that both variables are not correlated, so they need to have a correlation coefficient of zero ($R_{ZPV_n} = 0$). The opposite, that uncorrelated variables are automatically independent is also not true. In order to check if this assumption is valid for the given test case, the correlation coefficient R_{ZPV_n} (Eq. 4.36)
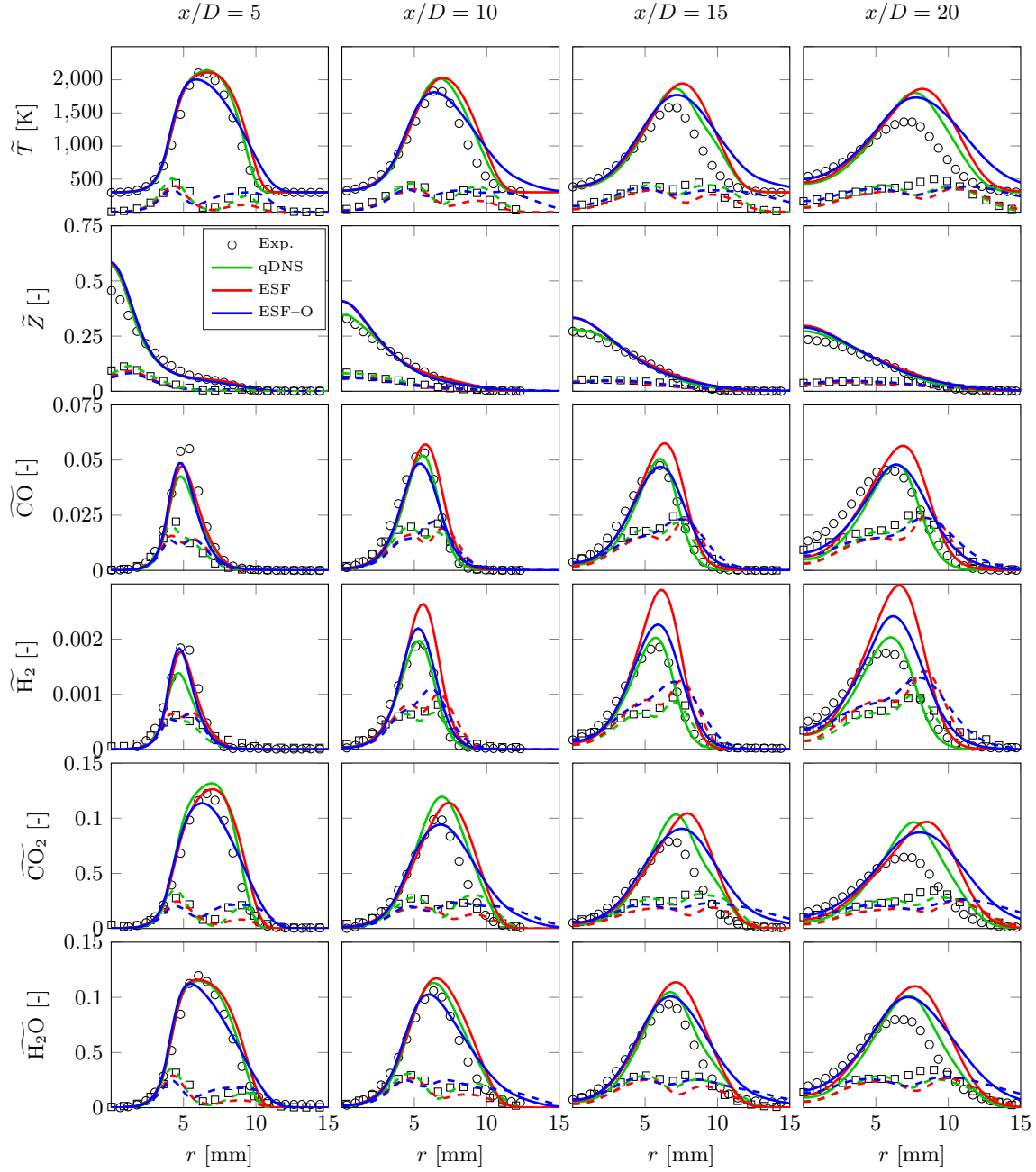
Figure 6.16: Direct comparison of mean and RMS values simulated on the *medium* mesh with the ESF and the original ESF-O (4.23) formulation, each with $N_s = 8$ stochastic fields.

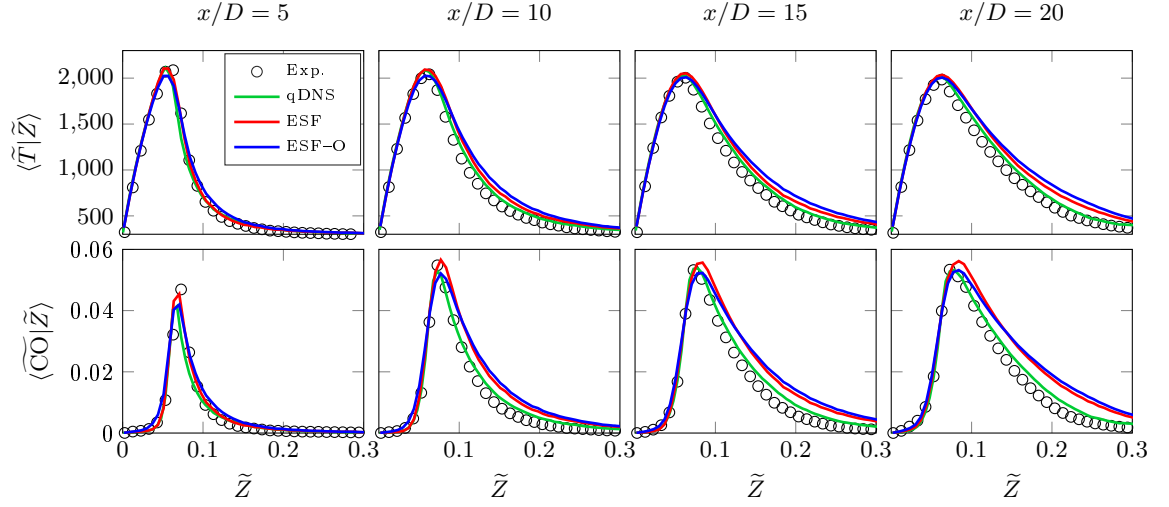Figure 6.17: Direct comparison of mixture fraction conditional mean values of temperature and CO mass fraction simulated on the *medium* mesh with the ESF and the original ESF-O (4.23) formulation, each with $N_s = 8$ stochastic fields.
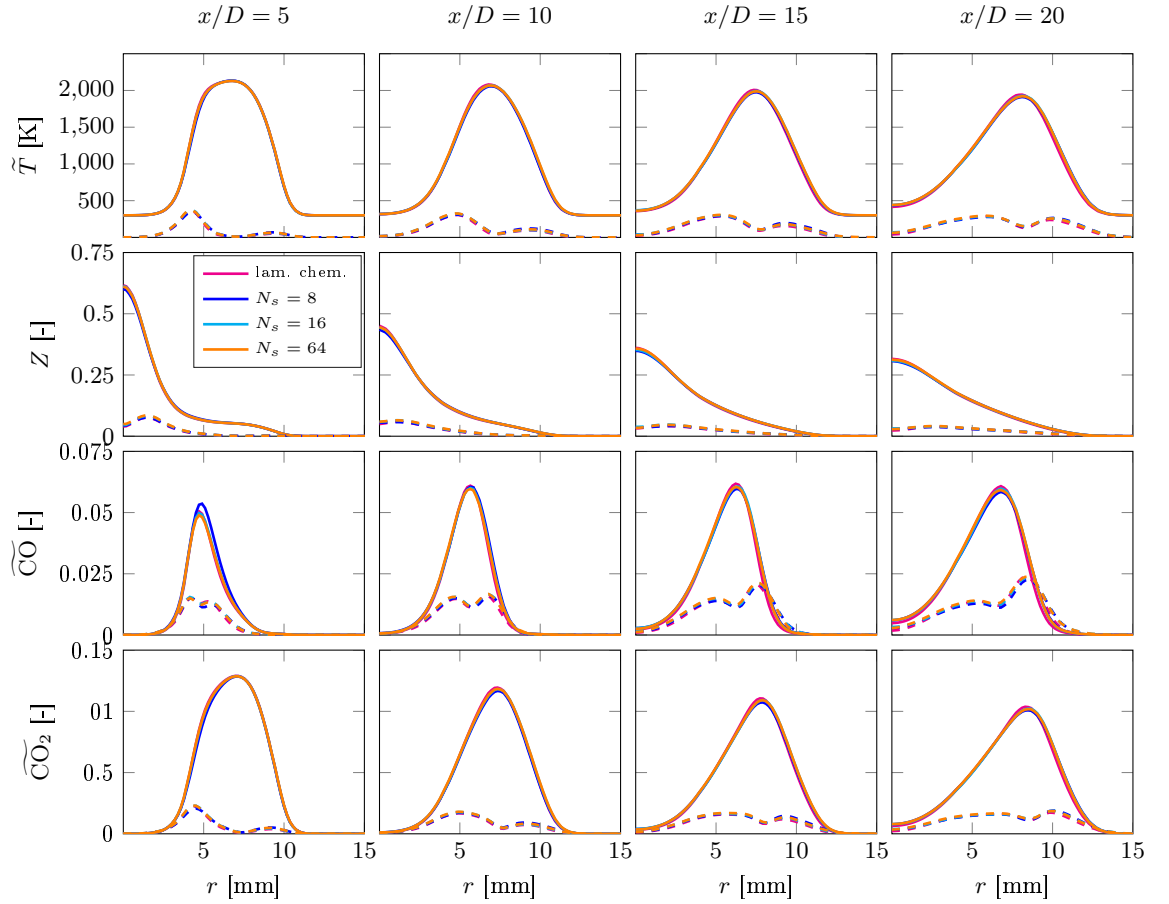

Figure 6.18: Comparison of radial distribution of mean and RMS values using different numbers of N_s stochastic fields.
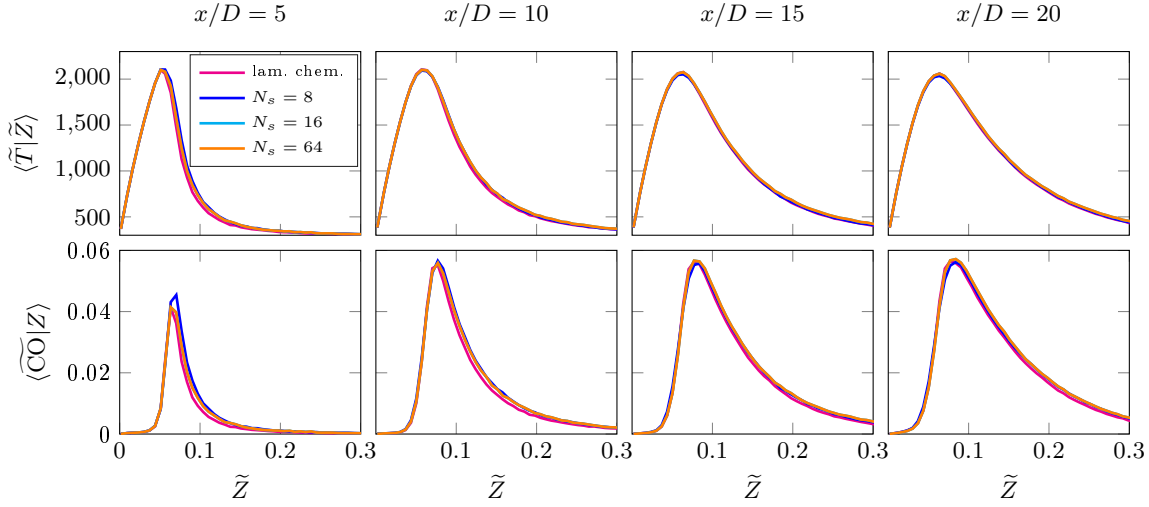
Figure 6.19: Comparison of mixture fraction conditional mean values of temperature and CO mass fraction using different numbers of N_s stochastic fields.
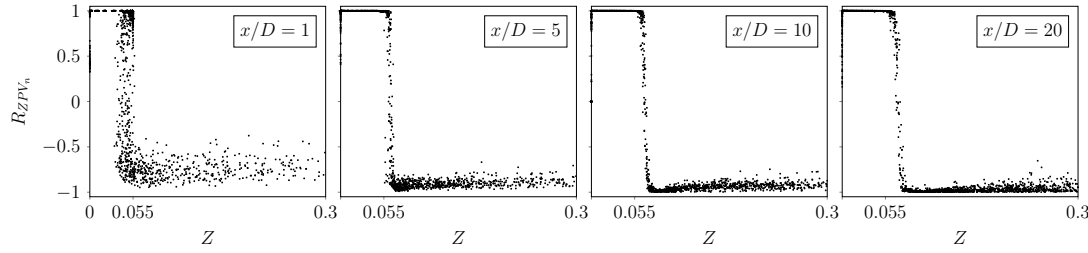
Figure 6.20: Scatter data of correlation coefficient R_{ZPV_n} over mixutre fraction Z

has been computed from the individual stochastic fields based on the covariance $\widetilde{Z''PV_n''}$ (Eq. 4.35) of mixture fraction and progress variable and the individual variances of $\widetilde{Z''^2}$ and $\widetilde{PV_n''^2}$ (Eq. 4.34). The expectations $\mathrm{E}[Z]$ and $\mathrm{E}[PV_n]$ are approximated with the respective filtered mean values $\widetilde{Z}$ and $\widetilde{PV_n}$ (Eq. 4.33). Figure 6.20 shows the scatter data of R_{ZPV_n} over the mixture fraction at different axial positions. It can be seen that, independent of the axial position, the samples are positively correlated ($R_{ZPV_n} \approx 1$) on the fuel rich and negatively correlated on the fuel lean side ($R_{ZPV_n} \approx -1$), with a transition point around stoichiometry. It appears that close to the exit, where the flame is in a partially premixed state, the correlation between Z and PV_n is slightly suppressed; further downstream, where the flame evolves towards a non–premixed flame, the correlation (both negative and positive) is more evident. As mentioned before, for Z and PV_n to be uncorrelated it is necessary that $|R_{ZPV_n}| \ll 1$ and this assumption clearly does not hold.

Figure 6.21 shows the temporal evolution of the temperature at a fixed point ($x/D = 5$, $r = D$) in the shear layer and reaction zone between fuel jet and hot pilot for the first millisecond of simulation time (approx. 2200 time steps) from CASE-C-ESF-lu19-8. The thick black solid line shows the filtered temperature $\widetilde{T}$, the temperatures of the individual fields are shown in grey, the red shaded region illustrates the RMS ($\sqrt{\widetilde{T''^2}}$) around the mean. Two aspects are worth mentioning here. First, the individual fields need some time

to evolve until they decorrelate properly and constitute a PDF with a standard deviation around the mean. In this particular simulation this is the case after approximately 0.15 ms (200-300 time steps). Second, although at the given location the filter width is with $\Delta x \approx 0.6$ mm still very fine the individual fields may decorrelate strongly. This can be seen after 0.45 ms where individual fields predict temperatures between almost 2000 K at the maximum and as low as 1200 K.
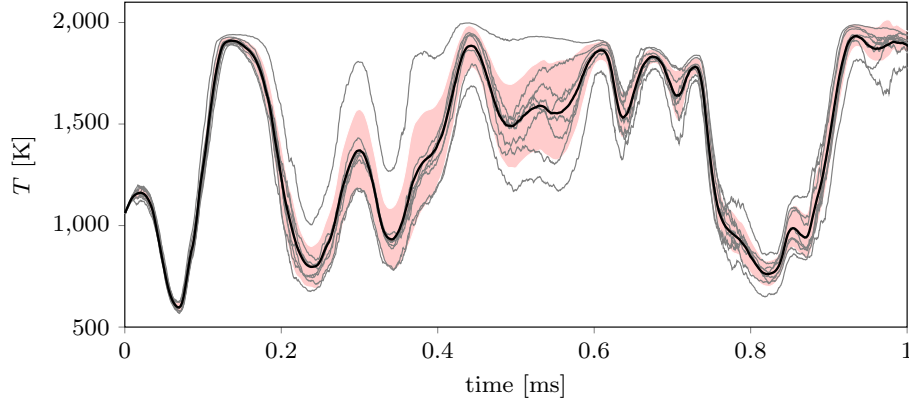
Figure 6.21: Time series of the filtered temperature $\widetilde{T}$ (black) and individual stochastic fields realizations T^n (grey). The RMS around the mean is shaded in red.

Figure 6.22 provides a quantitative comparison of the time averaged sub–grid fluctuation of mixture fraction and temperature between the cases with different meshes, number N_s of stochastic fields and stochastic fields formulations (ESF and ESF-O). The gray shaded region indicates the location of the reaction zone. The first row shows the resolved RMS $\sqrt{\langle \widetilde{Z}''^2 \rangle}$ (solid) and sub–grid RMS $\sqrt{\langle \widetilde{Z''^2} \rangle}$ (dashed) of the mixture fraction. On the *fine* mesh (black) the resolved fluctuation of Z is about three times higher than the SGS contribution. On the contrary, on the *coarse* mesh (blue) $\sqrt{\langle \widetilde{Z}''^2 \rangle}$ and $\sqrt{\langle \widetilde{Z''^2} \rangle}$ are almost of the same magnitude. For the simulation on the *medium* mesh with the ESF (red) and the ESF-O (cyan) the RMS values are somewhere in between. Using more N_s stochastic fields as in CASE-C-ESF-lu19-64 (orange) apparently reduced the SGS RMS (dashed), when compared to its counter part with $N_s = 8$ (blue).

The second row shows the contribution of the SGS RMS in percentage to the overall mixture fraction fluctuation in terms of M_Z:

$$M_Z = \frac{\sqrt{\langle \widetilde{Z''^2} \rangle}}{\left(\sqrt{\langle \widetilde{Z}''^2 \rangle} + \sqrt{\langle \widetilde{Z''^2} \rangle} \right)} \ . \tag{6.2}$$

Note, this is similar to the Pope criteria in Eq. 2.35 where a value of $M_Z = 0$ would be obtained for a DNS and $M_Z = 100$ for a RANS. As it can be seen, the sub–grid variance generated by the stochastic fields is significant. For the *fine* mesh M_Z is constantly between 20 and 30%, whereas for the *coarse* mesh it is even between 40 and 50%. M_Z for the other cases is located in between. No significant difference can be observed between the ESF and ESF-O method in the reaction zone. The observation from the first row are confirmed,

increasing N_s reduces M_Z (compare orange and blue lines). An interesting observation is also that M_Z is relatively constant over the radius and the axial position, with the exception of $x/D = 5$.

The third row depicts the sub–grid $\sqrt{\langle \widetilde{T''^2} \rangle}$ (dashed) and resolved $\sqrt{\langle \widetilde{T}''^2 \rangle}$ (solid) RMS of the temperature. Most of the resolved temperature fluctuations can be seen on the *fine* mesh (which is expected) and has its peak at $x/D = 5$ in the reaction zone with about 400 K. Generally, the SGS fluctuations are rather small for all cases. Beginning with $x/D = 10$, CASE-M-ESF-O-lu19-8 (cyan) shows the highest resolved and sub–grid temperature fluctuation. Apparently, the higher SGS temperature fluctuation scatters back onto the resolved temperature.

A more quantitative comparison is given in the fourth row, which shows the contribution of the SGS RMS of the temperature to the overall temperature fluctuations in terms of M_T:

$$M_T = \frac{\sqrt{\langle \widetilde{T''^2} \rangle}}{\left(\sqrt{\langle \widetilde{T}''^2 \rangle} + \sqrt{\langle \widetilde{T''^2} \rangle} \right)} \; . \tag{6.3}$$

Although CASE-C-ESF-lu19-8 (blue) exhibits a notable peak at $x/D = 5$, M_T is relatively constant within the reaction zone for all cases at all axial position and ranges between 10% and 30%.

Finally, in the last row the SGS (dashed) and resolved (solid) temperature fluctuations are normalized with the filtered mean temperature $\widetilde{T}$. As it can be seen, the actual contribution of the sub–grid temperature fluctuation (dashed) is, especially in the reaction zone very low, independently of the mesh resolution, the number of stochastic fields, or the specific stochastic fields formulation (ESF and ESF-O).

This analysis shows that there may be significant sub–grid activity, depending on the mesh resolution, the number of stochastic fields, and the specific stochastic fields formulation, in terms of mixture fraction variance. The underlying sub–grid mixture fraction PDF does also account for a sub–grid temperature variance and fluctuation, however, compared to the resolved temperatures in the reaction zone, the sub–grid temperature fluctuations are rather small. This might be a reason why there has not been observed any notable effect on the time averaged or mixture fraction conditional temperatures when the number N_s of stochastic fields was varied, as it was outlined in Section 6.1.4.4.

6.1.4.6   Quantitative comparison

For a more quantitative comparison between different simulations the Wasserstein metric is used, as proposed by [115]. Based on scatter data, the metric computes the dissimilarity between the simulation data and a reference data set, which in this case is the qDNS data [293].

Figure 6.23 shows the stacked W_2 metric based on the data of the temperature T, and CO_2, CO, H_2 mass fractions. The normalized W_2 value represents the averaged difference between samples from the two distributions (the simulation and the qDNS). The stacked approach allows for a more holistic error analysis, as the contribution from each variable to the overall dissimilarity becomes visible. As such, a value of $W_2 = 0.5$ can be interpreted as a difference between simulation and qDNS data at the level of 0.5 times the standard deviation. A detailed interpretation of the metric is outlined in Appendix A.
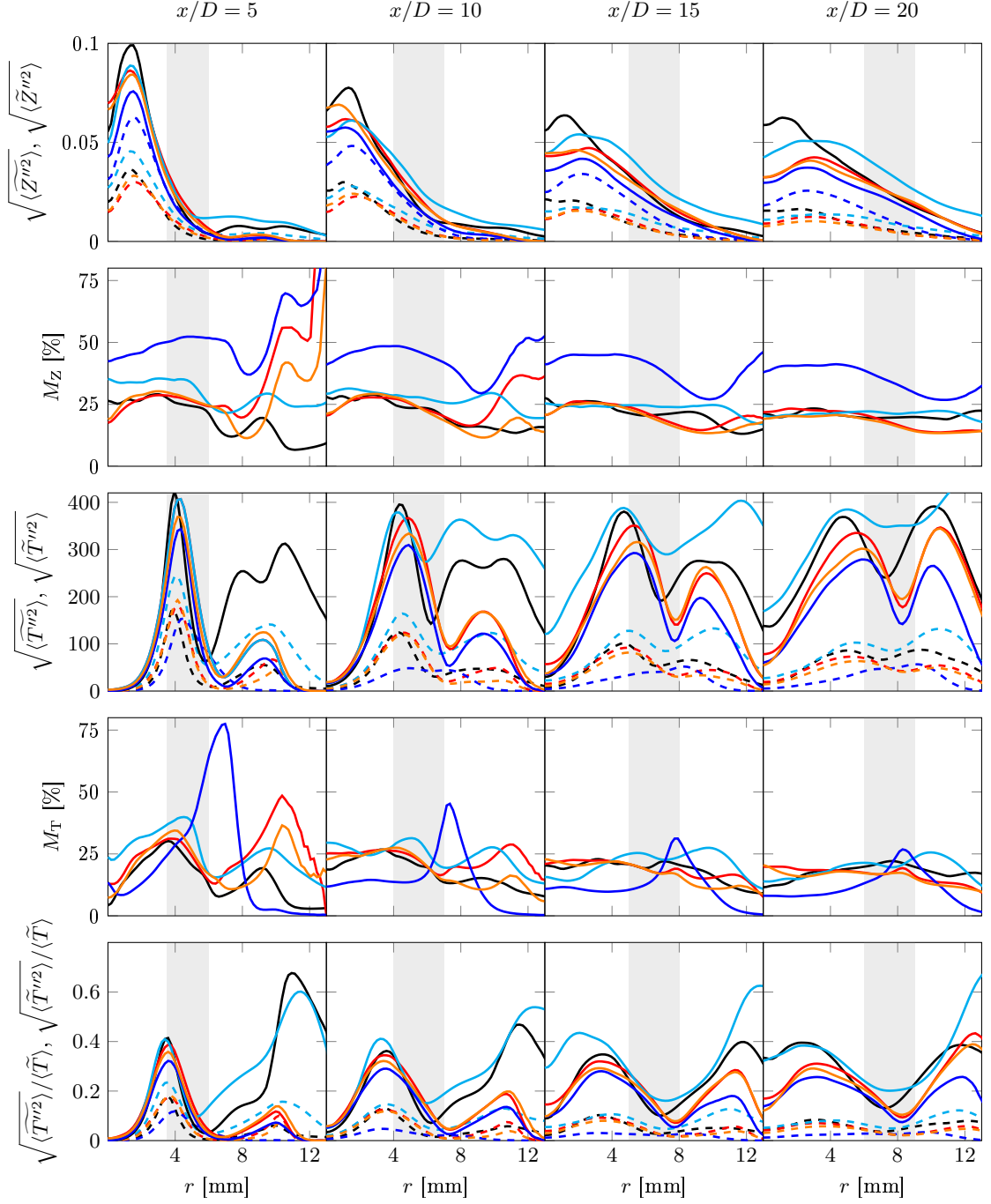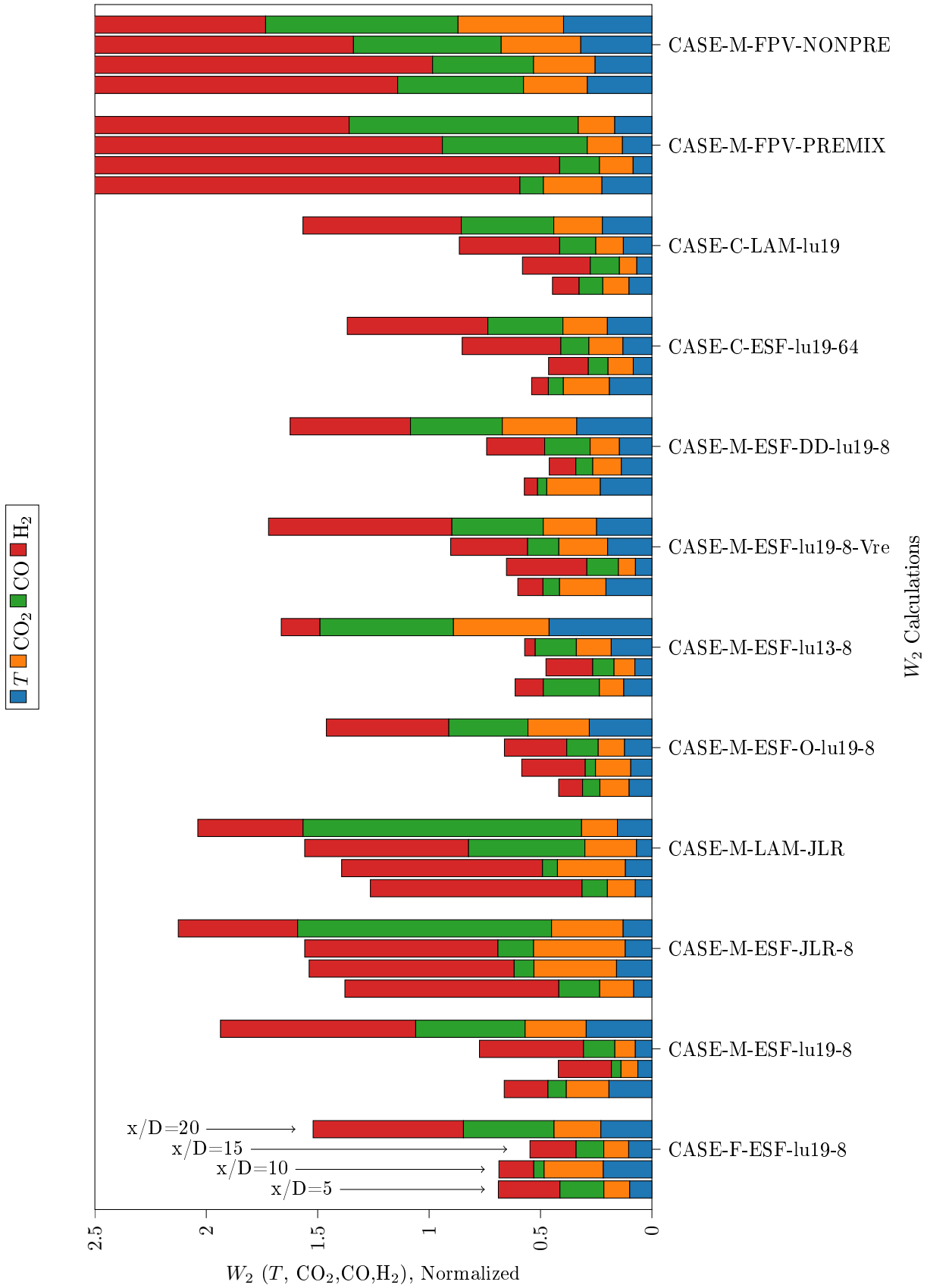
Figure 6.22: Analysis of sub–grid (dashed) and resolved (solid) fluctuation of mixture fraction and temperature. Color legend: —— CASE-F-ESF-lu19-8, —— CASE-M-ESF-lu19-8, —— CASE-C-ESF-lu19-8, —— CASE-M-ESF-O-lu19-8, —— CASE-C-ESF-lu19-64.

Figure 6.23: Contribution and comparison of single quantities to stacked W_2-metric at different axial positions for selected simulations.

For each case depicted in Figure 6.23 there can be found four bars, one for the W_2 value at each axial position $x/D = 5$, $x/D = 10$, $x/D = 15$, and $x/D = 20$. Each bar is composed from four stacks, each of them represents the contribution of T (blue), CO_2 (orange), CO (green), and H_2 (red) to the dissimilarity between simulation and qDNS data.

The main findings that can be extracted from the compact representation in Figure 6.23 are discussed hereby. All cases have in common that the simulation results are generally in better agreement in the front part of the flame ($x/D \leq 15$). The contribution of the temperature (blue) and CO_2 mass fraction (orange) to the overall dissimilarity is relatively low and all simulation approaches predict the temperatures fairly well, including the simulation with the FPV combustion model and the premixed manifold. However, it is difficult to tell which of the cases performs best in terms of T and CO_2 mass fraction. The metrics are rather similar, although different meshes and reaction mechanisms have been used. Comparing the metrics for the CO and H_2 mass fractions, larger differences can be found. In most cases their contribution makes up the highest share to the overall dissimilarity. It is also evident that more complex reaction mechanisms (Lu13 and Lu19) predict these species better than the JL-R mechanism. The prediction with the FPV combustion model for these species is rather poor.

6.1.4.7   Computational times

Finally, the normalized simulation times on the *medium* mesh are compared in Figure 6.24. The normalization is based on the FPV simulation. Note that this is only meant as a rough comparison, as the individual simulations have been carried out on different HPC systems (SuperMUC at the LRZ and our local inhouse cluster) with different numbers of processors and different processor architectures. These facts all distort a direct one-to-one comparison. The CPU time is computed as the average over 100 consecutive time steps and is normalized by the number of processors. Nevertheless, it becomes evident that the ESF simulation with
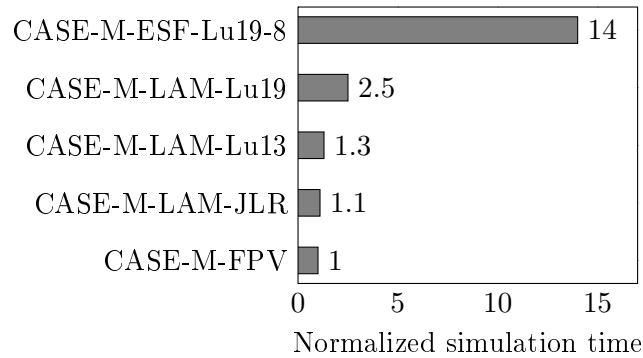
Figure 6.24: Comparison of normalized computational times.

$N_s = 8$ fields consumes significantly more computational time. The reason that the FPV simulation is not much faster than the finite rate simulation with the JL-R mechanism relies in the fact that, although no reaction rates had to be computed, the FPV case needed more PISO loops to converge and had additional computational overhead from the FPV table interpolation.

6.1.5 Summary

The Sydney mixed–mode flame configuration FJ200-5GP-Lr75-57 has been successfully simulated on different meshes with LES. The temperature and CO scatter plots, as well as statistical analysis of the probability of local extinction and the burning index BI_T are in very good agreement with qDNS and experimental data.

The employed combustion models were the Eulerian Stochastic Fields (both the original [268] and the modified [269] version) method with different chemical mechanisms and the FPV model with a premixed and a non–premixed combustion manifold. All models, except for the FPV approach with the non–premixed manifold, show acceptable to good agreement for the temperature. Regarding minor and major species (CO_2, CO, H_2) there is a tendency that the results improve on finer meshes and with more complex reaction mechanisms. Both FPV approaches fail to predict these quantities adequately. Also, the effect of differential diffusion was found to be of little importance in this flame configuration.

The impact of the number of stochastic fields N_s was also investigated and found to be negligible. The time averaged and mixture fraction conditional simulation results do not change or improve, regardless of whether $N_s = 1$ or $N_s = 64$ is used. These findings are also confirmed by the analysis with the Wasserstein metric.

6.2   Sandia Flame F

The Sandia flame series comprises three different non–premixed, piloted, turbulent methane/air flames (D, E, and F) that are operated at different jet Reynolds numbers. The flames have been studied intensively throughout the past 20 years [7, 10, 124, 246] and serve as a benchmark for the validation of turbulent combustion models, since a wide variety of scalar and velocity measurements are available.

With a Reynolds number of Re = 44,800 Flame F is already close to blow-off with strong turbulence-chemistry interaction and exhibits a high amount of localized extinction and re-ignition events. Consequently, it features a significant degree of partial premixing between unburnt fuel and oxidizer what makes it the most challenging flame from the series to simulate. Therefore, Flame F is an ideal candidate for an extensive analysis of combustion models for partially premixed combustion.

In this work the simulations are compared against the measurement data[4] from Barlow and Karpetis [10] and Schneider et al. [246].

6.2.1   Experimental setup

The main jet consists of a mixture of 25 vol.-% of methane and 75 vol.-% of air at a temperature of 294 K. This corresponds to a mixture fraction of $Z = 1$, according to Bilger's definition (3.2).

The flame is stabilized using a pilot jet, which consists of a lean burnt methane/air mixture at an equivalence ratio of $\phi = 0.77$ and a temperature of $T_\mathrm{P} = 1860$ K at a mixture fraction of $Z = 0.271$. The coflow consists of air ($Z = 0$) at a temperature $T_\mathrm{Co} = 291$ K. The stoichiometric mixture fraction is equal to $Z_\mathrm{st} = 0.351$ with a stoichiometric temperature of $T_\mathrm{st} = 2226$ K. The bulk velocities of the fuel jet and the pilot are $U_\mathrm{F} = 99.2$ and $U_\mathrm{P} = 22.8$ m/s. The diameter of the fuel pipe is $D = 7.2$ mm, the annular inner diameter of the pilot is $D_\mathrm{P} = 18.2$ mm.

Figure 6.25 gives a schematic idea of the setup. Table 6.6 lists the relevant geometric dimensions of the burner and the inlet flow velocities and temperatures.
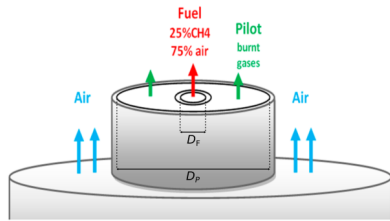
D	7.2 mm
D_P	18.2 mm
U_F	99.2 m/s
U_P	22.8 m/s
U_Co	0.9 m/s
T_P	1860 K
T_F	294 K
T_Co	291 K
T_st	2226 K

Figure 6.25: Schematic of the Sandia Flame configuration. Adopted and modified from [166] under the Creative Commons Attribution License.

Table 6.6: Relevant geometric dimensions and inlet conditions of Sandia Flame F.

---

[4]Available at `https://tnfworkshop.org/data-archives/pilotedjet/ch4-air/`.

6.2.2 Numerical setup

The computational domain extends $100D$ in axial direction and to $10D$ in radial direction. Turbulent inlet boundary conditions are used at the fuel inlet, which have been generated from a separate precursor pipe flow LES with 20 million cells. A constant velocity block profile is applied for pilot and coflow.

The reference mesh used in this work is 3D axial-symmetric and consists of about 3.5 million cells (*fine* F). An additional *very coarse* (VC) mesh with 0.4 million cells is used for comparison and to study the impact of the combustion model. The meshes are topologically similar and comprise local mesh refinement in the region of the shear layers. Figure 6.26 shows the filter width Δ over the radial position at different axial positions. Figure 6.27
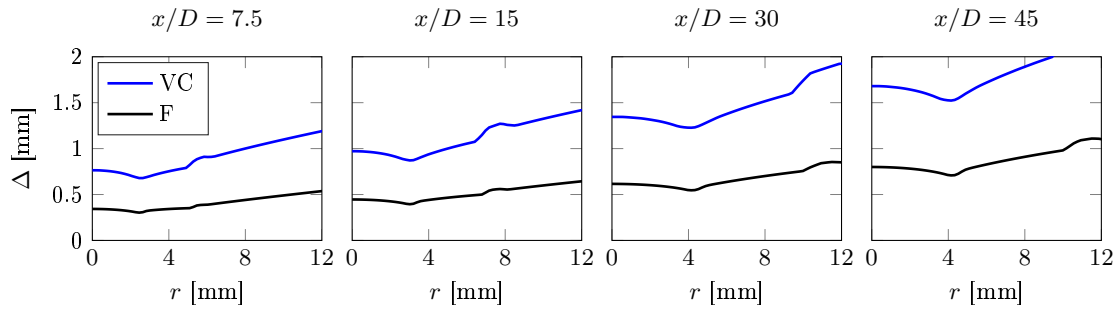
Figure 6.26: Filter widths Δ of the different Sandia Flame F meshes plotted over the radial position r at axial planes $x/D = 7.5, 15, 30, 45$.

depicts the LES resolution criteria M (2.35), the modeled TKE_{SGS}, and resolved TKE_{res} turbulence kinetic energy for both meshes. As it can be seen, the *very coarse* mesh does not fulfill the criteria of $M < 0.2$ at $x/D < 15$ in order to be considered an adequately resolved LES mesh. This is a deliberate choice and in the further analyzes it will be investigated how the ESF method performs on such coarse meshes (which are actually considered too coarse for LES).

6.2.3 Simulation results

6.2.3.1 Reaction mechanisms and FPV manifolds

At first, the ESF combustion model with the Lu19 and Lu13 and the FPV model with a premixed and a non–premixed manifold are compared on the *fine* and *very coarse* mesh. Table 6.7 provides an overview on the setups and case names. Figure 6.28 compares the

Name	Mesh	TCI model	Chemistry	N_s	SGS model
F-F-ESF-lu19-8	F	ESF	Lu19	8	WALE
F-VC-ESF-lu19-8	VC	ESF	Lu19	8	WALE
F-F-ESF-lu13-8	F	ESF	Lu13	8	WALE
F-F-FPV-PREMIX	F	β-PDF	premixed FPV	-	WALE
F-F-FPV-NONPRE	F	β-PDF	non–premixed FPV	-	WALE

Table 6.7: Flame F cases with a variation of the combustion model.
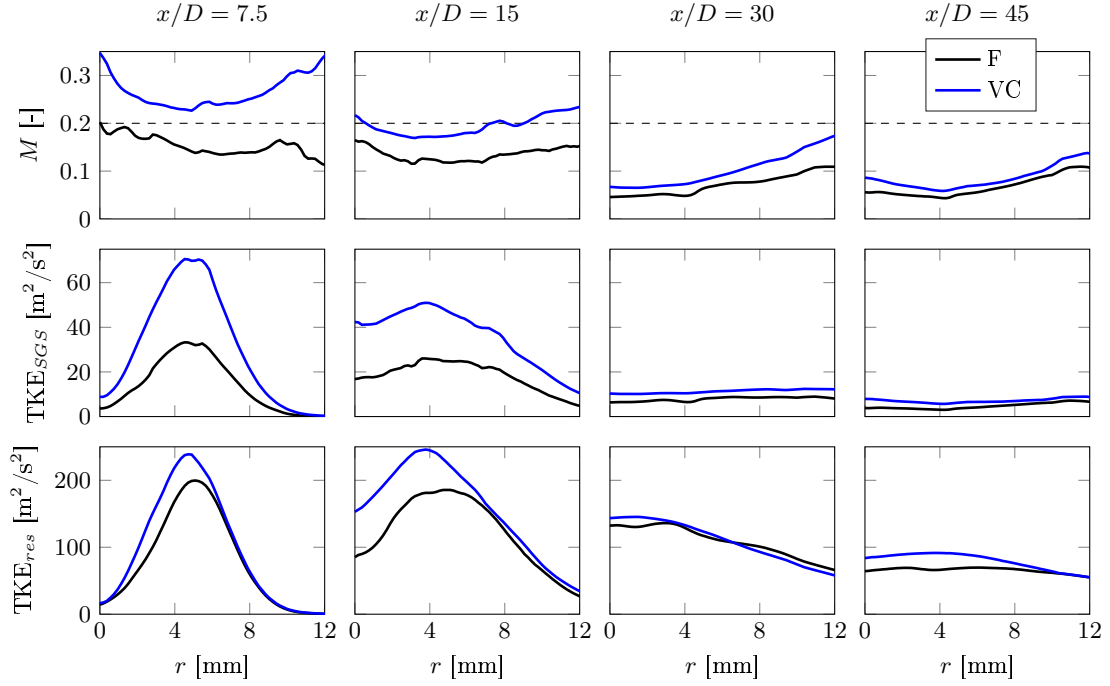
Figure 6.27: Ratio M, modeled TKE_{SGS}, and resolved TKE_{res} for Flame F.

instantaneous temperature fields from the ESF simulations on the two different meshes. Note the higher degree of resolved flame wrinkling of the flame on the F mesh.

The temperature and $\dot{\omega}_{PV}$ source term manifolds for the premixed and non–premixed FPV database are depicted in the Appendix in Figure B.6 and Figure B.5, respectively. The progress variable PV is based on the normalized CO_2, CO, and H_2O mass fractions, as defined in Eq. (4.39), $\dot{\omega}_{PV}$ is defined as in Eq. (4.40). The non–premixed manifold was constructed from counterflow diffusion flamelets, which have been created with `FlameMaster` using the GRI-3.0 mechanism. The premixed manifold was generated from 150 laminar freely propagating flamelets between $0.1 \leq Z \leq 0.6$ with CANTERA using the GRI-3.0 mechanism. Beyond the flammability limits the manifold was interpolated linearly to the boundaries of the manifold at $Z = 0$ and $Z = 1$, where the experimental boundary conditions (Sec. 6.2.1) were imposed. The mixture fraction at the pilot was set to $Z_\text{P} = 0.27$ [12].

Figure 6.29 compares the time averaged and circumferentially averaged experimental data with the results from the simulations as listed in Table 6.7. Shown are the temperature, the mixture fraction, CO_2, H_2O, CO, and H_2 mass fractions. Temporal averaging has been performed over a simulation time of 15 ms (five flow through times at $x/D = 30$). All results predict the temperature well. Interestingly, the F-F-FPV-PREMIX setup with the premixed FPV manifold is closest to the experiments, whereas the ESF simulations overpredict the temperature peaks in the front part ($x/D \leq 15$). Further downstream all results are similar and in agreement with the experiments. Another interesting observation is that all three ESF simulations are very similar, independently of the reaction mechanism (Lu13 or Lu19) and the mesh resolution. The mixture fraction $\widetilde{Z}$ is matched well in the front section of the flame ($x/D \leq 15$), while it is overpredicted in the rear part. Regarding the species mass fractions there are more differences. While there are only small differences between the simulation results for the CO_2 and H_2O mass fractions, CO and H_2 are gen-
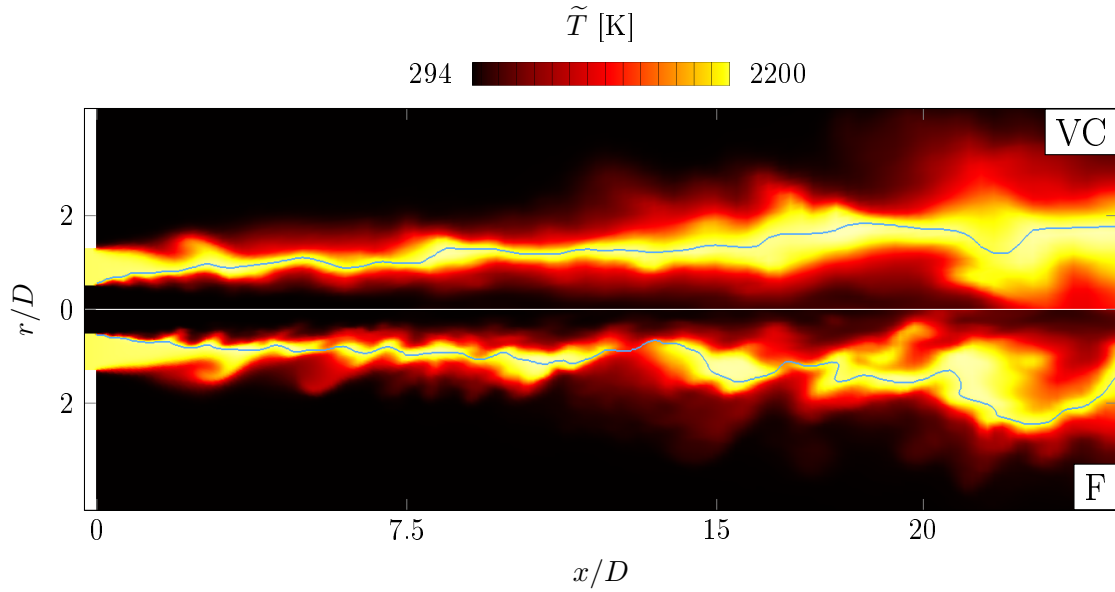
Figure 6.28: Comparison of instantaneous resolved temperature fields. Top: Simulation on the *very coarse* (VC) mesh. Bottom: Simulation on the *fine* (F) mesh. The blue iso-line illustrates the stoichiometric mixture fraction Z_{st}.

erally overpredicted by the simulations. The best agreement can be seen for the two ESF simulations on the *fine* mesh, whereas both FPV approaches overpredict the peak values of CO and H_2 by a factor of two. For H_2 there is also a more significant difference between the results on the very coares and fine mesh.

Figure 6.30 and 6.31 depicts the scatter plots for $\widetilde{T}$ and CO mass fraction. The first row shows the experimental data, the following rows show the respective simulation results, the last row shows the mixture fraction conditional plots. The experimental temperature data show a lot of localized extinction events up to $x/D = 30$. These events are not very pronounced in the simulation data, except for the F-F-FPV-PREMIX setup, which exhibits localized extinction with temperatures below the steady laminar flamelet solution. Therefore, F-F-FPV-PREMIX shows also the best agreement with the experimental data in terms of the conditional values $\langle \widetilde{T}|\widetilde{Z}\rangle$. For the CO mass fraction the best agreement can be found for the ESF cases with finite rate chemistry. However, there is very little difference between the Lu13 and Lu19 results and between the different meshes (F and VC).

Additional scatter plots for the H_2 and OH mass fractions can be found in Figure B.8 and B.9 in the Appendix.

An ESF simulation with the JL-R mechanism has also been carried out. However, this mechanism does not seem suitable for the high scalar dissipation rates in Flame F as the flame gets blown off (see Figure B.7 in the Appendix). For comparison, setup F-F-ESF-lu19-8 was also simulated with the Vreman turbulence model, but no significant differences were found when compared to the WALE turbulence model. The choice of the turbulence model is therefore assumed to be of marginal importance.

The FPV simulations show generally good agreement with ESF simulations where finite rate chemistry is used. However, a more direct comparison is favorable. To this end, an instantaneous time step of case F-F-ESF-lu19-8 has been taken where $\widetilde{Z}$, $\widetilde{Z''^2}$, $\widetilde{PV}$, and $\widetilde{\dot{\omega}}_{PV}$
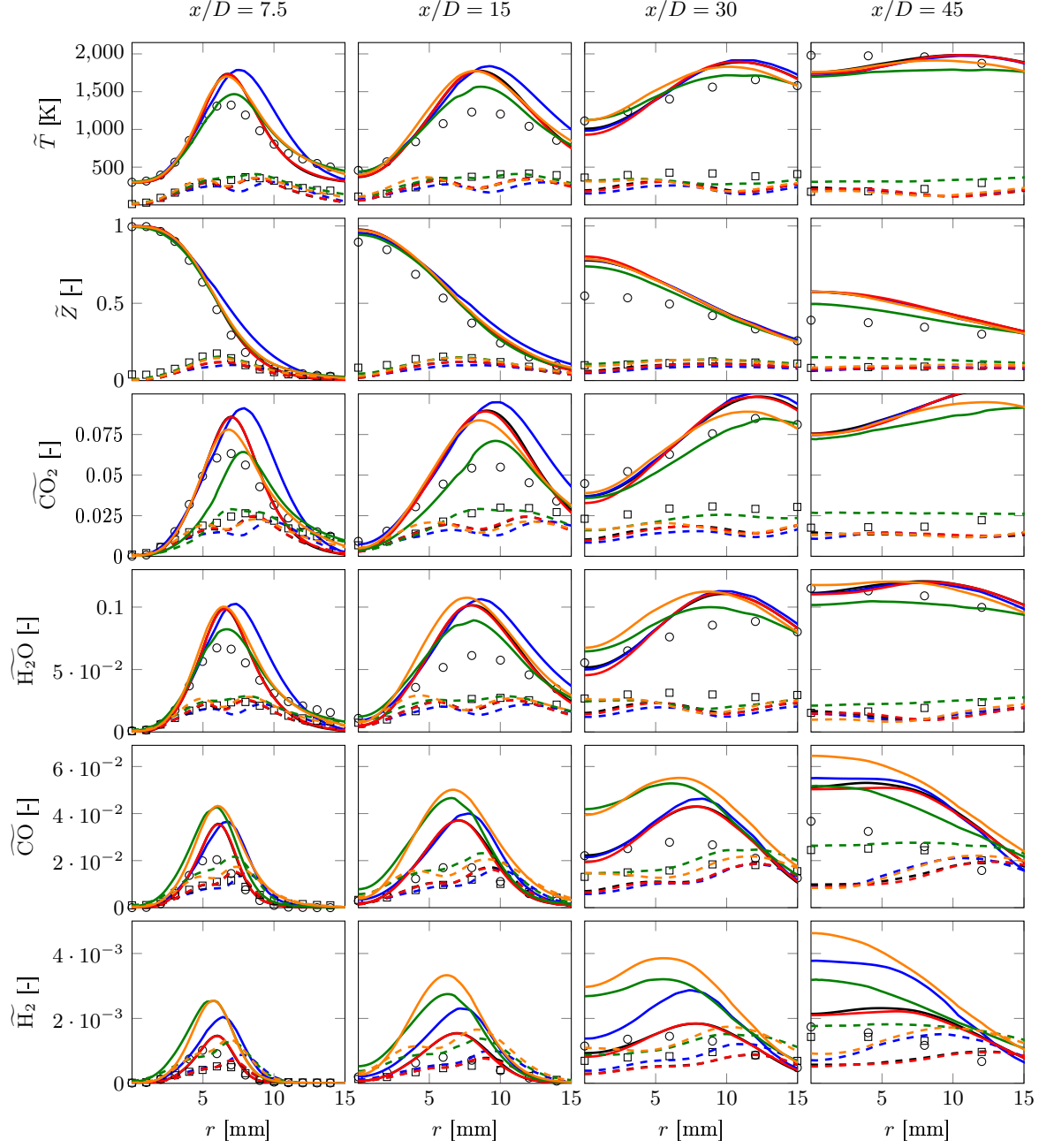
Figure 6.29: Comparison of radial distribution of $\widetilde{T}$, $\widetilde{Z}$, and selected species in Flame F. The color legend is: ——F-F-ESF-lu19-8, ——F-VC-ESF-lu19-8, ——F-F-ESF-lu13-8, ——F-F-FPV-PREMIX, ——F-F-FPV-NONPRE. Solid refers to mean, dashed to RMS quantities. Experiments: ○ mean, □ RMS.
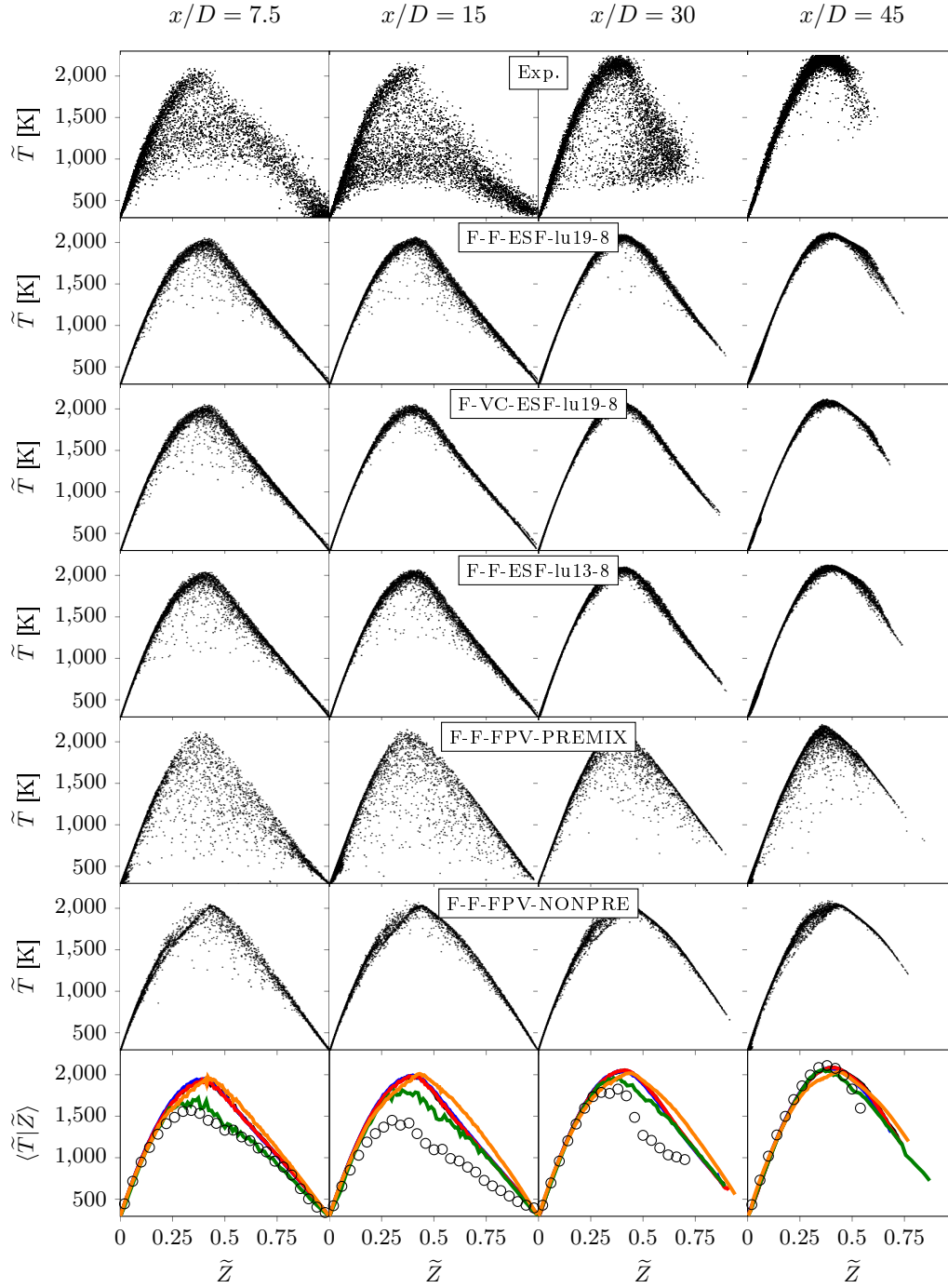
Figure 6.30: Scatter plots of temperature $\widetilde{T}$ and mixture fraction conditional temperature $\langle\widetilde{T}|\widetilde{Z}\rangle$ at different axial locations. The color coding is the same as in Fig. 6.29.
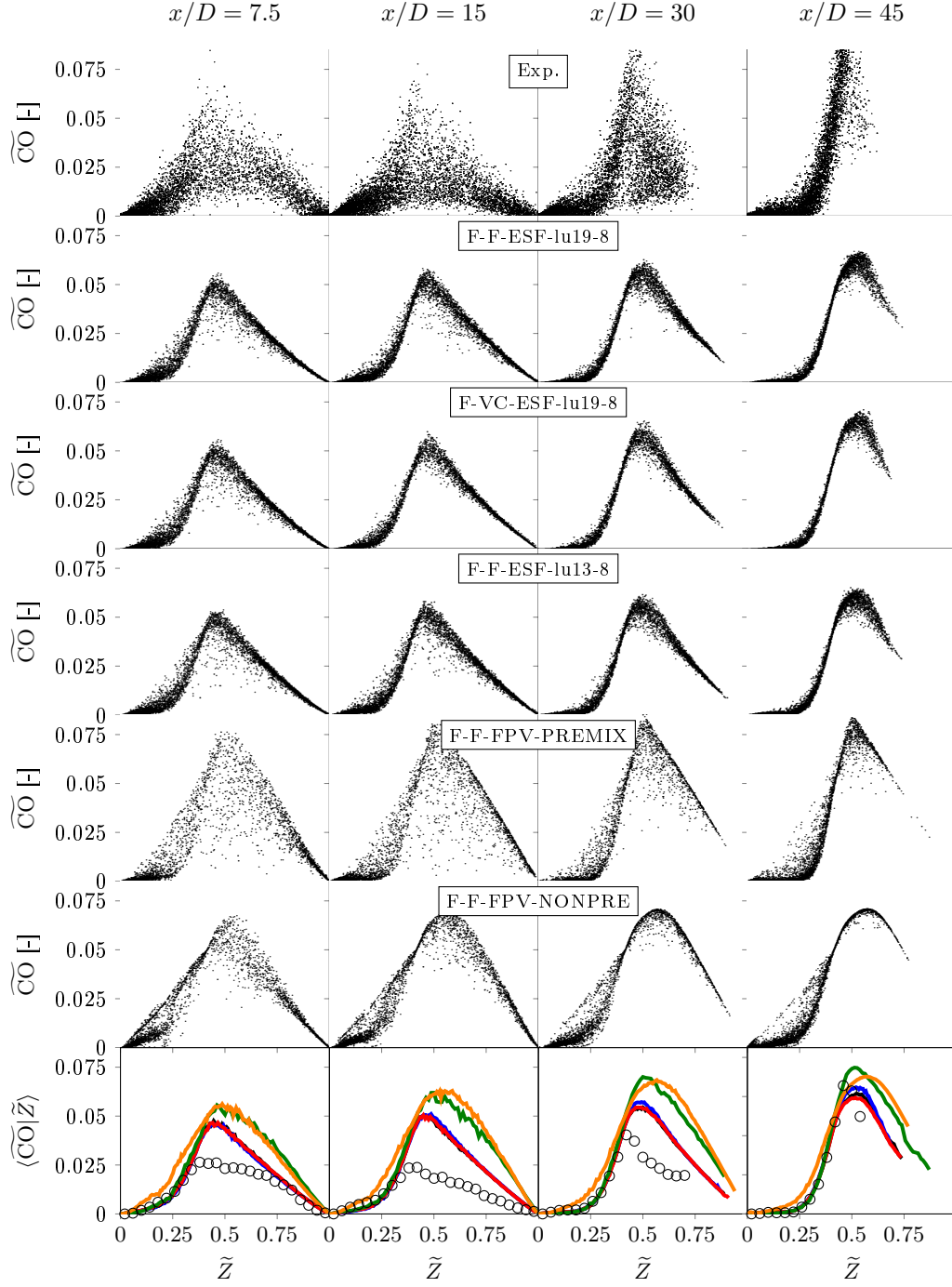
Figure 6.31: Scatter plots of CO mass fraction and mixture fraction conditional CO mass fraction $\langle \widetilde{CO}|\widetilde{Z}\rangle$ at different axial locations. The color coding is the same as in Fig. 6.29.

have been extracted. $\widetilde{PV}$ was computed based on the species mass fractions of CO_2, CO, H_2O and $\widetilde{\omega}_{PV}$ is based on the respective species reaction rates. Using $\widetilde{Z}$, $\widetilde{Z''^2}$, and $\widetilde{PV}$ as table input parameters both the premixed and non-premixed FPV manifold were accessed to query $\widetilde{T}$, $\widetilde{\omega}_{PV}$, $\widetilde{CO}$, and $\widetilde{H_2}$. In Figure 6.32, these quantities are compared against the instantaneous results from the finite rate simulation (F-F-ESF-lu19-8). The results from both manifolds are generally in good agreement with the data from the finite rate simulation. The prediction from the non–premixed FPV manifold appears to be slightly closer to the Lu19 results. However, comparing $\widetilde{\omega}_{PV}$ it can be seen that the progress variable source terms from the finite rate case are much higher than the ones that are stored in the FPV manifolds.
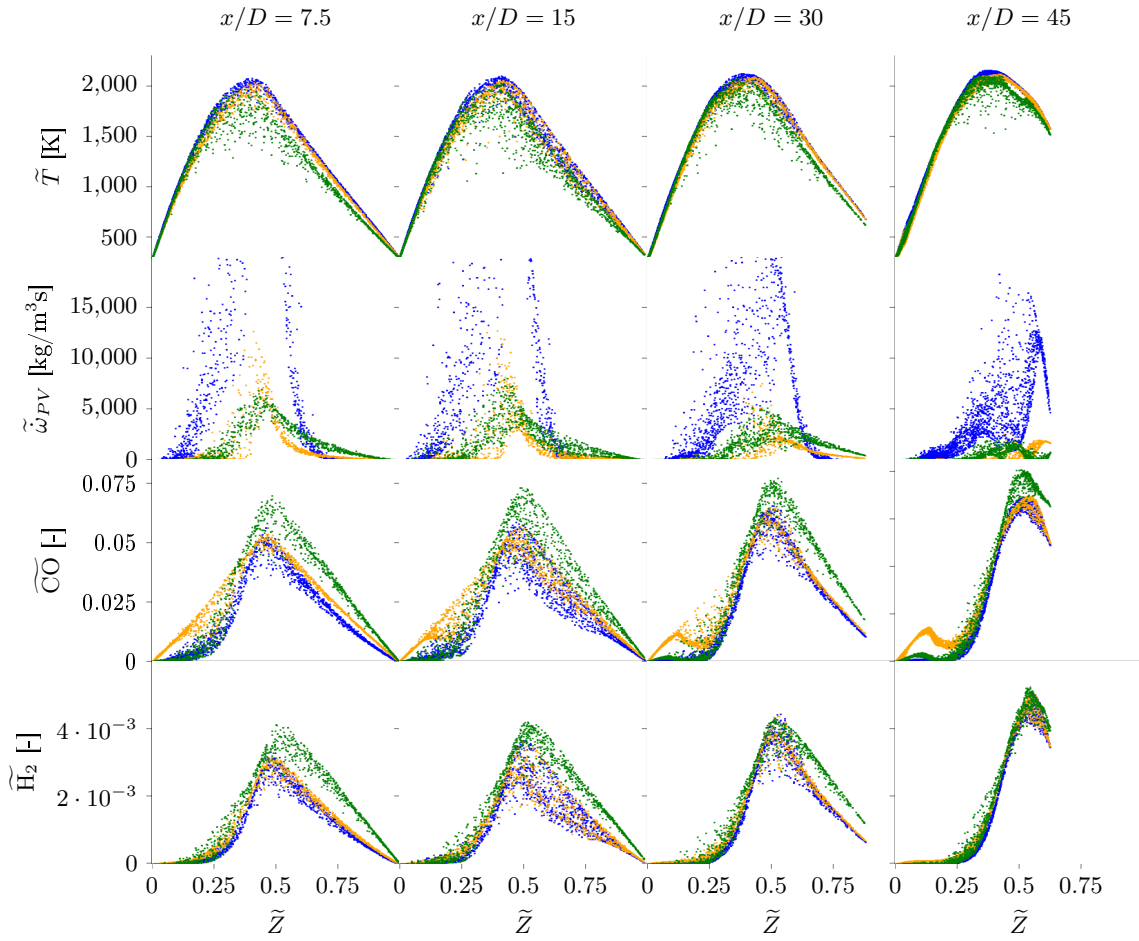
Figure 6.32: Direct comparison of $\widetilde{T}$, $\widetilde{\omega}_{PV}$, $\widetilde{CO}$, and $\widetilde{H_2}$ computet with: ● Lu19 chemistry, ● Premixed manifold, ● Non–Premixed manifold.

6.2.3.2   Influence of ESF formulation and N_s fields

In this subsection it is analyzed if, and how the different ESF formulations (4.23 and 4.27) and the number N_s of stochastic fields impacts the simulation results. A simulation where the micro mixing constant C_D in the IEM model is set to 0.2 (see (4.28), the default value

is $C_D = 2.0$) is also considered, as well as a laminar finite rate simulation, which neglects TCI. The different setups are summarized in Table 6.8. All simulations were carried out on the *very coarse* mesh, where the effect of the ESF method is expected to be more evident. Figure 6.33 compares the time averaged mean and RMS values for temperature and CO

Name	Mesh	TCI model	Chemistry	N_s	C_D
F-VC-ESF-lu19-8	VC	ESF	Lu19	8	2.0
F-VC-LAM-lu19	VC	-	Lu19	-	2.0
F-VC-ESF-lu19-32	VC	ESF	Lu19	32	2.0
F-VC-ESF-O-lu19-8	VC	ESF-O	Lu19	8	2.0
F-VC-ESF-lu19-8-Cd0.2	VC	ESF	Lu19	8	0.2

Table 6.8: Variation of the chemical mechanism.

mass fraction, Figure 6.34 shows the mixture fraction conditional values for the temperature and CO mass fraction. The results are very similar for the different setups, both for the temporal or conditional mean values. Only very marginal differences can be observed for $\widetilde{CO}$ at $x/D > 30$. Apparently, neither the choice of the ESF formulation (4.23 and 4.27), nor the number N_s of stochastic fields, nor the mixing constant C_D have a noticeable effect on the simulation results, i.e. using $N_s = 32$ is not better then neglecting TCI.
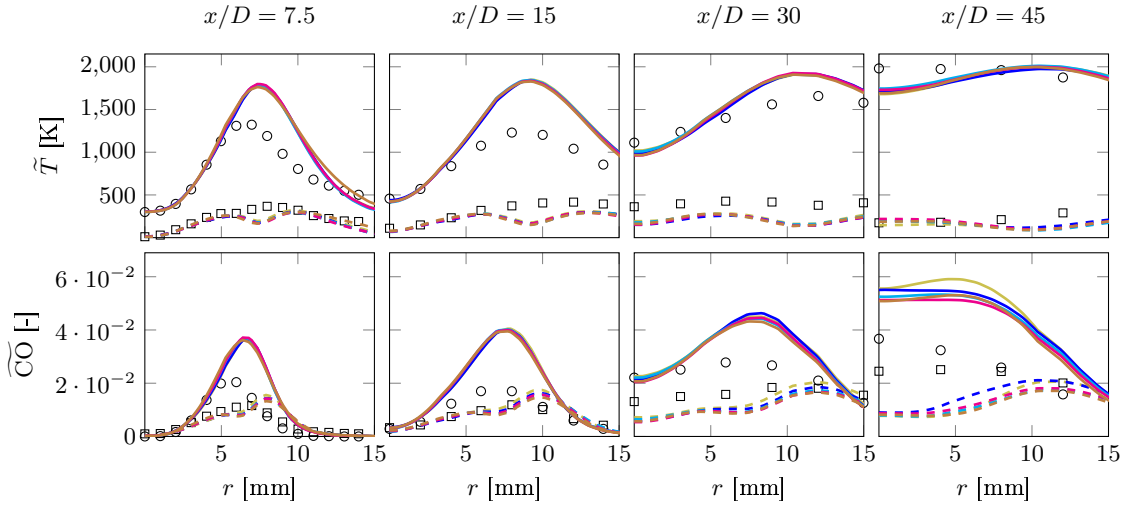
Figure 6.33: Radial mean (solid) and RMS (dashed) values of $\widetilde{T}$ and CO mass fraction. Legend: —— F-VC-ESF-lu19-8, —— F-VC-LAM-lu19, —— F-VC-ESF-lu19-32, —— F-VC-ESF-lu19-8-Cd0.2, —— F-VC-ESF-O-lu19-8. Experiments: ∘ mean, □ RMS.

6.2.3.3   Analysis of SGS data

Figure 6.35 gives a quantitative comparison of the time averaged sub–grid fluctuation of mixture fraction and temperature between cases with different meshes, number of stochastic fields N_s and stochastic fields formulations (4.23 and 4.27). The gray shaded region indicates qualitatively the location of the reaction zone. The first row shows the resolved RMS $\sqrt{\langle \widetilde{Z''^2} \rangle}$
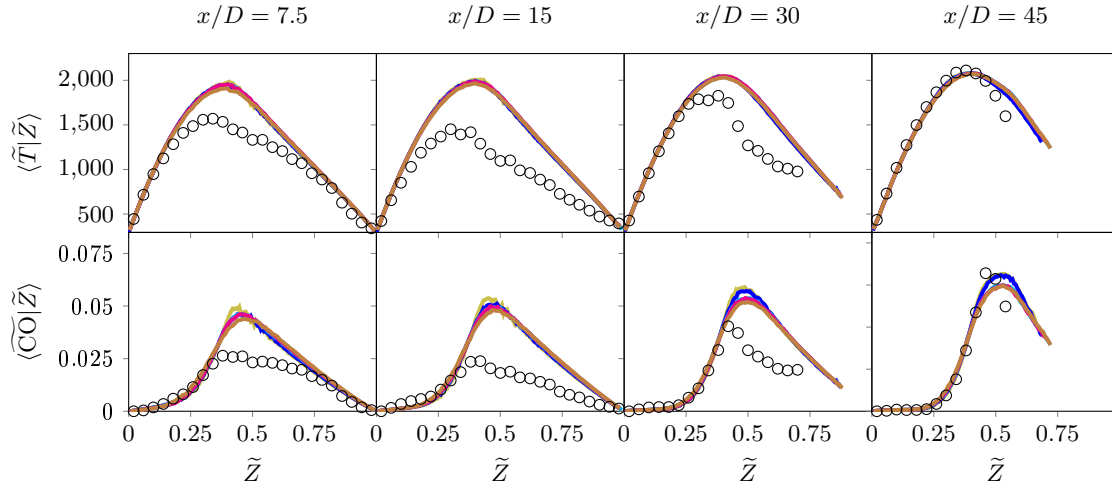
Figure 6.34: Mixture fraction conditional plots for $\widetilde{T}$ and CO mass fraction. Legend: ——F-VC-ESF-lu19-8, ——F-VC-LAM-lu19, ——F-VC-ESF-lu19-32, ——F-VC-ESF-lu19-8-Cd0.2, ——F-VC-ESF-O-lu19-8. Experiments: ○ mean, □ RMS.

(solid) and sub–grid RMS $\sqrt{\langle \widetilde{Z''^2} \rangle}$ (dashed) of the mixture fraction. On the *fine* mesh (black) the resolved fluctuation of Z is the highest, whereas $\sqrt{\langle \widetilde{Z''^2} \rangle}$ is the smallest. The highest SGS fluctuation is achieved by the ESF-O formulation (brown), this is also seen in terms of M_Z (6.2). A similar observation can be made for the temperature fluctuations (3rd and 4th row), the SGS contribution is the smallest on the *fine* mesh and is the highest with the ESF-O method. However, as M_T (6.3) indicates, there is no difference regarding the SGS fluctuations, no matter if $N_s = 8$ (blue) or $N_s = 32$ (magenta) stochastic fields are used. In the last row the SGS (dashed) and resolved (solid) temperature fluctuations are normalized with the filtered mean temperature $\widetilde{T}$. As it can be seen, the actual contribution of the sub–grid temperature fluctuation (dashed) in the reaction zone is very low, independently of the mesh resolution, the number of stochastic fields, or the specific stochastic fields formulation (ESF and ESF-O).

A reduction of the micro-mixing constant C_D, as it can be seen from Figure 6.35, has no effect on the sub–grid statistics, although this constant is reduced by a factor of 10 compared to the proposed value of 2.0 [122, 179, 228]. It is therefore interesting to have a closer look at the stochastic velocity and the micro-mixing term from ESF transport equation (4.27). Figure 6.36 shows scatter data of the stochastic velocity (black) and the micro-mixing (red) term from case F-VC-ESF-lu19-32. The samples are taken from the stochastic PDEs that transport the CH_4 mass fraction and were normalized with the density (shown in $[s^{-1}]$). Only by comparing the magnitudes of the two terms it becomes clear that the impact of the IEM term (red) is marginal on the SPDE when compared to the stochastic velocity (black). Consequently, the choice of C_D (which impacts the IEM term) is rather negligible. The analysis also underpins the assumption that the choice of the micro-mixing model is in general rather negligible in LES.

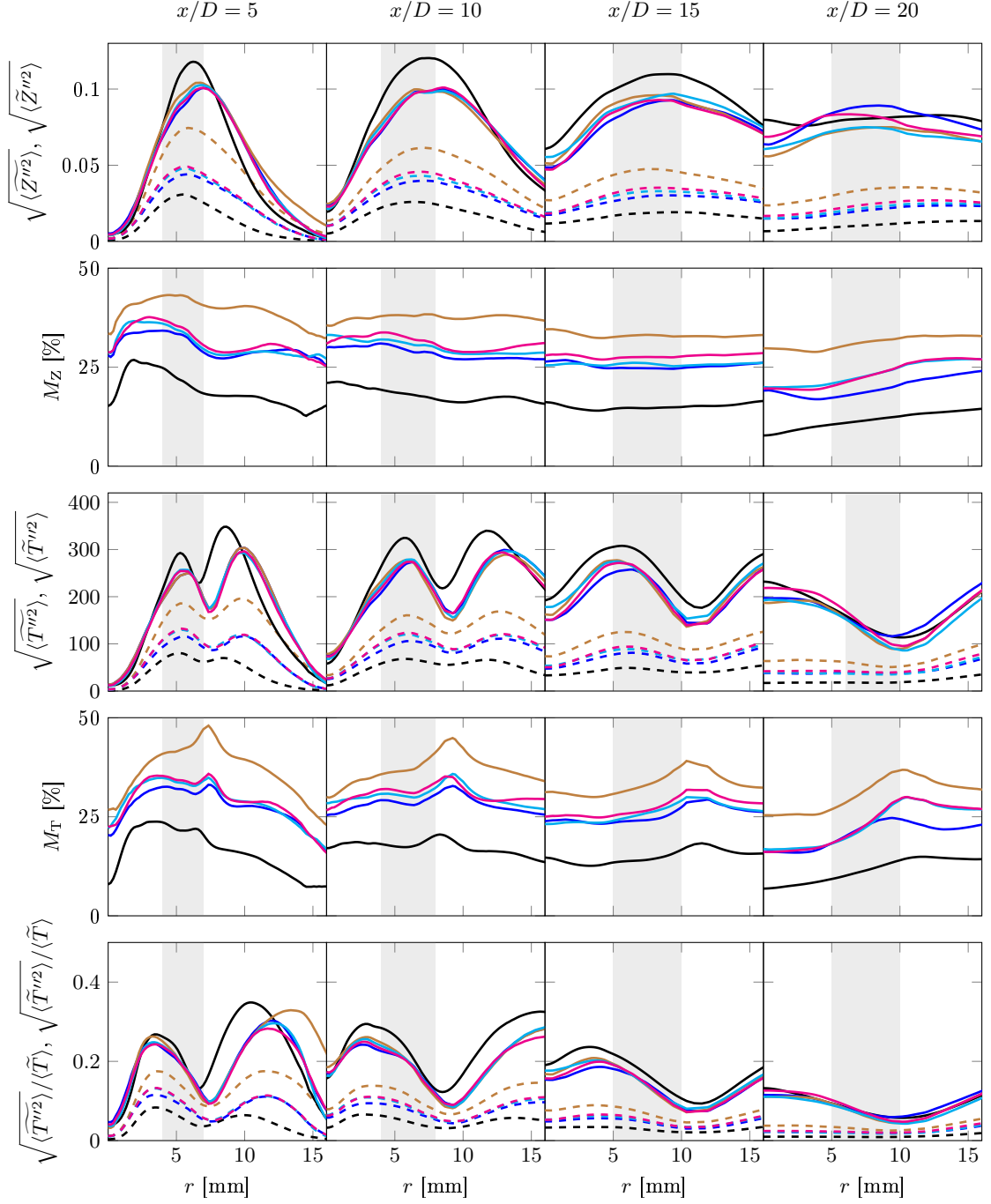Figure 6.35: Analysis of sub–grid (dashed) and resolved (solid) fluctuation of mixture fraction and temperature. Color legend: ——F-F-ESF-lu19-8, ——F-VC-ESF-lu19-8, ——F-VC-ESF-lu19-32, ——F-VC-ESF-lu19-8-Cd0.2, ——F-VC-ESF-O-lu19-8.
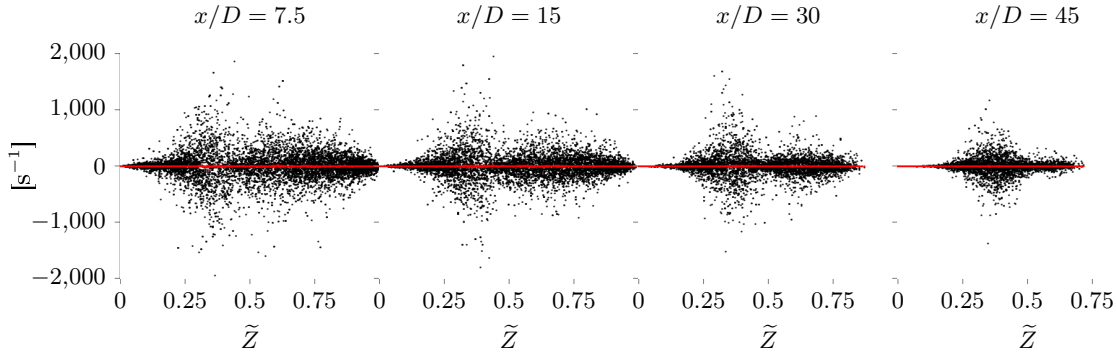
Figure 6.36: Comparison of the stochastic velocity (black) and the micro-mixing (red) term from the stochastic PDEs that transport the CH_4 mass fraction.

6.2.3.4   Quantitative comparison

Figure 6.37 shows the stacked W_2 metric based on the data of $\widetilde{T}$, and CO_2, CO, H_2 mass fractions. The detailed interpretation of the metric is outlined in Appendix A. For each case in Figure 6.37 is represented with four bars, one for the W_2 value at each axial position $x/D = 7.5$, $x/D = 15$, $x/D = 30$, and $x/D = 45$. Each bar is composed from four stacks, each of them represents the contribution of $\widetilde{T}$ (blue), CO_2 (orange), CO (green), and H_2 (red) to the dissimilarity between simulation and experimental measurement data.

The main findings are: Temperature and CO_2 mass fractions are reproduced equally well by all cases, independently of the reaction mechanism or the mesh resolution. The FPV simulations show a slightly worse W_2 metric. This is interesting, since case F-F-FPV-PREMIX showed good agreement in terms of radial mean and RMS values for temperature (Fig. 6.29). Apparently, the distribution of the temperature scatter data in this case shows a high dissimilarity when compared to the experimental scatter data and only the first two moments are in good agreement. As seen from the previous analysis, the number of stochastic fields N_s does not significantly affect the simulation results. However, comparing the cases F-F-ESF-lu19-8 ($N_s = 8$) and F-F-LAM-lu19 (no TCI), there is a slight indication that neglecting the sub–grid TCI deteriorates the prediction quality in the rear part of the flame ($x/D \geq 30$).

6.2.4   Summary

The Sandia Flame F configuration has been simulated using the ESF method and the FPV combustion model. Two different meshes were used, a *fine* mesh with 3.5 million cells and a *very coarse* mesh with only 0.4 million cells. Based on the Pope criteria M (2.35) the latter one is actually too coarse (Fig. 6.27) to be used as LES mesh. However, the analysis showed that the results for temperature and major species are similar on both meshes, differences were found for minor species (H_2, CO). The results with the FPV combustion model are slightly worse than the ones obtained with the ESF method with respect to minor species, but show good agreement for $\widetilde{T}$ and CO_2 mass fractions for the premixed manifold. There is also no significant difference between the Lu13 and Lu19 mechanism, whereas the JL-R mechanism was not to found suitable for this configuration. Regarding the ESF method, no significant evidence was found that a higher number of stochastic fields would increase

Figure 6.37: Contribution and comparison of single quantities to stacked W_2-metric at different axial positions for selected simulations.
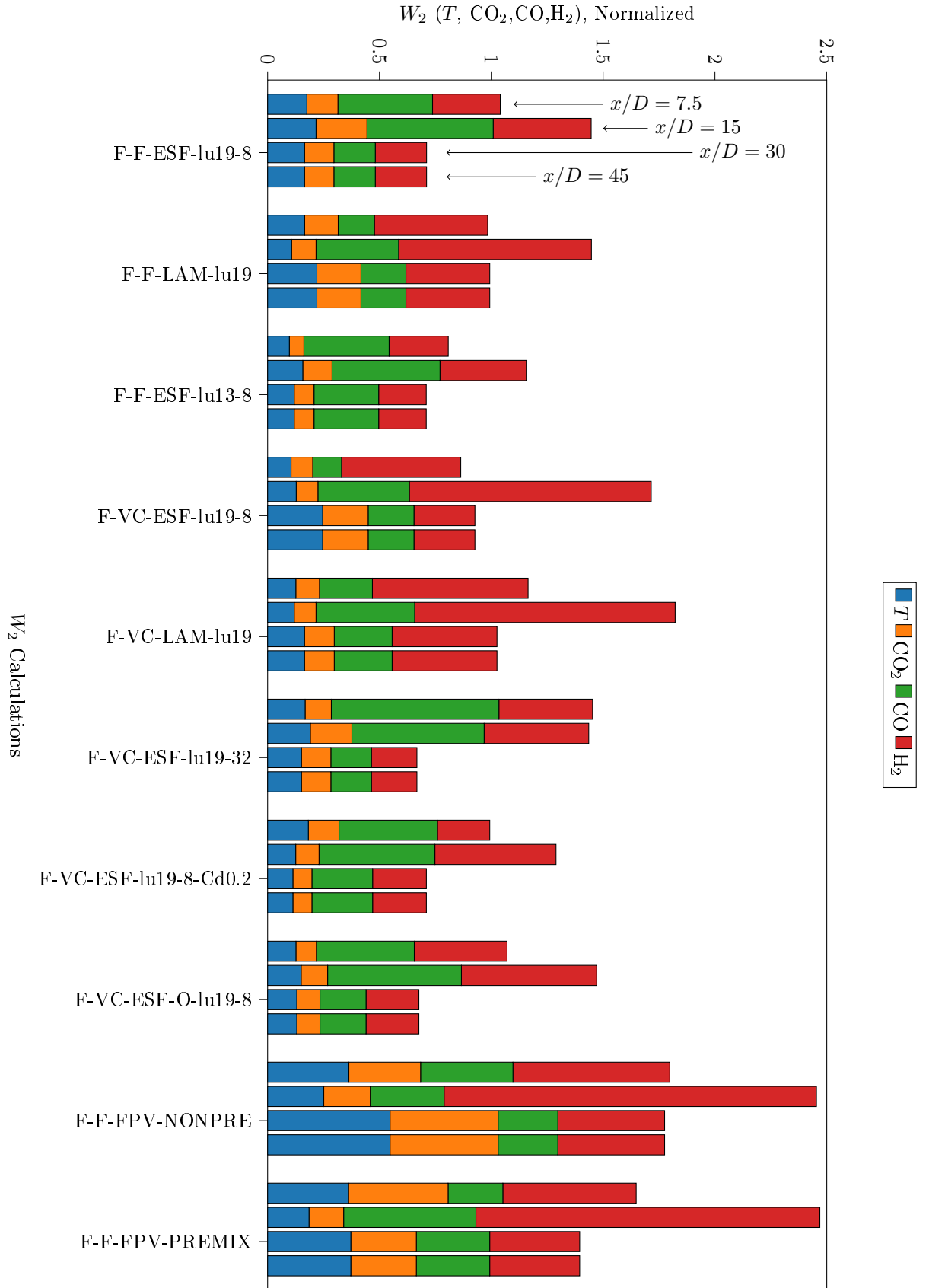
the prediction quality. Even on the *very coarse* mesh the simulations with laminar finite rate chemistry are as accurate as the ESF simulation with $N_s = 32$, although a high level of sub–grid fluctuation in mixture fraction space could be proven.

6.3   Oxy–fuel jet flame

As a mitigation strategy against climate change carbon capture and storage (CCS) technologies might provide a way of effectively reducing CO_2 emissions. Among different CCS techniques oxy–fuel combustion has proven to be a technologically and economically feasible process [153]. In the combustion process an oxidizer mixture based on O_2 diluted with CO_2 is used. The resulting combustion products are H_2O and CO_2 solely, the latter one can be captured and stored. Diluting the oxidizer stream with CO_2 was found necessary to decrease and obtain flame temperatures similar to those in air combustion [45]. However, given the different heat transfer properties of CO_2, oxy–fuel flames are much more prone to extinction than it is seen in air-fuel flames with the same O_2 content in the oxidizer [45]. Enriching the fuel stream with H_2 may therefore be necessary for stabilization, but does change the flame structure as differential diffusion effects play a role.

Differential diffusion characterizes the physical process of observing species specific transport rates in multi–component, inhomogeneous, mixtures. This effect is particularly observed in laminar premixed flames with significant amounts of H_2, whereas it can be neglected in most turbulent non–premixed methane/air configurations. However, in a recent experimental study, Sevault et al. [250] investigated a series of turbulent non-premixed CO_2 diluted oxy–fuel jet flames. They reported that differential diffusion effects are present in the near nozzle region playing a dominant role in the flame stabilization process. Depending on the degree of H_2 enrichment in the fuel stream and the jet Reynolds number (Re ranging between 12,000 and 18,000) the flames also show significant levels of localized extinction in the near-field. Hence, from the perspective of combustion modeling this configuration is challenging as the complex interplay between differential diffusion and turbulence–chemistry interaction (TCI) has to be accounted for.

Therefore, in this study the ESF method to account for differential diffusion in combination with the Lu19 mechanism [159] are used. From the flame series [250] case B1 and B2 were simulated to study the impact of differential diffusion at different jet Reynolds numbers on the flame structure and localized extinction.

6.3.1   Experimental setup

The experimentally investigated flame series by Sevault et al. [250] are non–piloted, non–premixed oxy–fuel jet flames. The fuel pipe has an inner diameter of $D = 5$ mm and a wall thickness of 0.5 mm. It is surrounded by an outer tube (diameter 96.5 mm) carrying the oxidizer stream. The whole setup is placed in a wind tunnel with a cross–section of 250 mm by 250 mm which is operated with air. The oxidizer is composed of 32 vol-% O_2 and 68 vol-% CO_2. The flames considered in this study are B1 and B2, both with 55 vol-% H_2 and 45 vol-% CH_4 in the fuel stream. This results in a stoichiometric mixture fraction of $Z_{st} = 0.0535$, based on Bilger's definition (3.2), and an adiabatic flame temperature of $T_{st} = 2250$ K at stoichiometry. The bulk fuel jet velocities U_F at the inlet are 78.6 m/s for flame B1 (Re = 12,000) and 98.2 m/s for flame B2 (Re = 15,000); the coflow speeds U_{Co} are 0.622 m/s and 0.778 m/s, respectively. The flow velocity of the air in the wind tunnel is 0.5 m/s to accompany the coflow. This allowed Sevault et al. [250] to measure from $1D$ to $20D$ above the nozzle without ambient air mixing into the probe volume. Therefore, no combustion chamber was needed, which was important for the investigation of localized extinction in these flames. Table 6.9 provides an overview of the operating parameters. Figure 6.38 gives an impression of the experimental setup.

Flame	H$_2$ vol-% in fuel	Y_{H_2} in fuel	O$_2$ vol-% in coflow	Y_{O_2} in coflow	U_F [m/s]	U_{Co} [m/s]	D [mm]
B1	55	0.1331	32	0.255	78.6	0.622	5
B2	55	0.1331	32	0.255	98.2	0.778	5

Table 6.9: CO$_2$-diluted oxy–fuel jet flame properties.
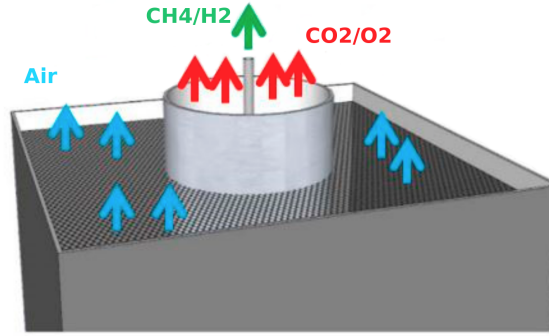
Figure 6.38: Schematic of the experimental setup of the oxy–fuel flame. Reprinted and modified from [166] under the Creative Commons Attribution License.

6.3.2 Numerical setup

For the simulations, two block structured hexahedral meshes were used. The *base* mesh (B) consists of 4.1 million cells and is used for most of the analysis. In addition, a coarsened *medium* (M) mesh consisting of 3 million cells was used to study the grid dependency. All meshes have the same domain which extends $11D$ in radial direction at the inlet and $15D$ at the outlet plane. The latter one is located $80D$ in stream wise x-direction. The region $-1 \leq x/D \leq 0$ of the jet flow in the fuel pipe is also part of the simulation domain. A mesh refinement was applied in the regions of shear layers and where the flame is expected. Figure 6.39 shows the cell sizes Δ for the different meshes. Turbulent inlet velocity boundary conditions have been generated via a highly resolved precursor pipe flow LES on 20 million cells. Time integration is done with a second order implicit scheme. Discretization of the convective momentum terms is done by a second order central differences scheme (CDS). The convective terms in scalar transport equations are discretized by a second order CDS with a van Leer limiter. The time step is limited to fulfill the criterion $CFL_{max} < 0.25$. The WALE turbulence models were used to model the turbulent viscosity.

6.3.3 Simulation results

6.3.3.1 Preliminary observations

Sevault et al. [250] reported that all flames stayed attached to the nozzle and extinction started not below $x/D < 3$. From the LES results this observation can be confirmed for flames B1 and B2. Flame B1, the one which showed the best stabilization and lowest degree of extinction in the experiments, was also simulated with the unity Lewis assumption and equal diffusivities ($D_k = D_{th} = $ const.), as it is implemented in most industrial CFD codes. Figure 6.40 shows snapshots of the instantaneous temperature with the iso-line of

Figure 6.39: Filter widths Δ of the different oxy fuel meshes plotted over the radial position r at axial planes $x/D = 1, 3, 5, 10$.

stoichiometric mixture fraction in blue for the ESF simulation with differential diffusion (upper half) and the ESF simulation with the Le = 1 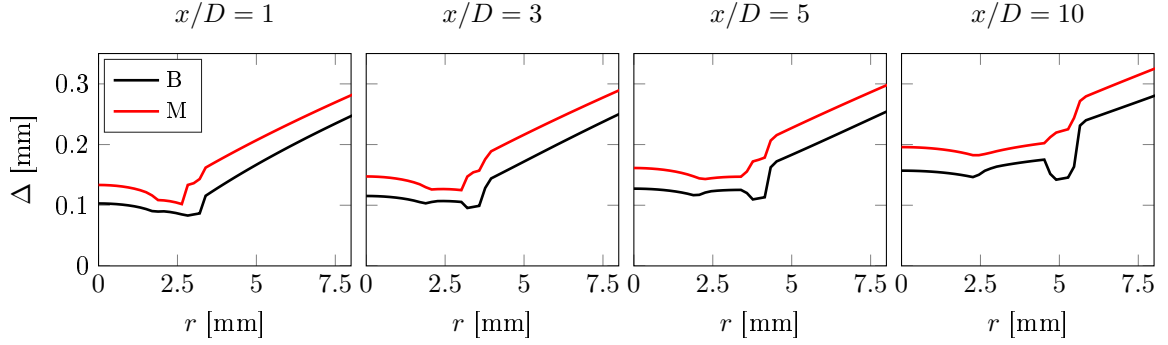assumption (lower half), both on the B mesh. The flame with differential diffusion is anchored at the fuel pipe and appears to be fully burning. On the contrary, the flame with unity Lewis assumption is heavily lifted and does not burn below $x/D = 10$. Note that both simulations had the same initial conditions, which was a fully burning anchored flame. It is therefore assumed that detailed multi-component transport is essential for the stabilization of the flame, independent of the computational mesh refinement.

6.3.3.2 Baseline simulations

The baseline simulations for case B1 and B2 were carried out on the *base* mesh with the ESF-DD combustion model and $N_s = 8$ fields. Table 6.10 lists the setup of the respective cases.

Name	Flame	Mesh	TCI model	Chemistry	N_s	SGS model
B1-B-ESF-DD-lu19-8	B1	B	ESF-DD	Lu19	8	WALE
B2-B-ESF-DD-lu19-8	B2	B	ESF-DD	Lu19	8	WALE

Table 6.10: Baseline simulation setups of the flames B1 and B2.

Figure 6.41 shows the Pope criteria M, as well as TKE_{SGS} and TKE_{res} for the base mesh. M is mainly far below the threshold of 0.2. Figures 6.42 and 6.43 show the mixture fraction conditional averages for temperature and major species mass fractions over $\widetilde{Z} \in [0,0.5]$ for case B1 and B2. The averaged values have been obtained from scatter data taken at the respective axial planes ($x/D = 1, 3, 5$). Samples have been taken every 500 time steps (approximately every 0.13 ms) to ensure statistical independence. The dashed vertical line indicates the location of Z_{st}. Very good agreement can be seen for the temperature in B1, only showing slightly higher values on the fuel rich side. The location and magnitude of the conditional peak temperatures are reproduced very well. For B2, these agree well close to the nozzle but the conditional peak at $x/D = 5$ is underpredicted by around 400 K. In both cases the peak is located around Z_{st} at further downstream locations ($x/D \geq 5$), while it is shifted away from Z_{st} towards the fuel rich side close to the nozzle at $x/D = 1$. This phenomenon is discussed in [250] and attributed to differential diffusion as the light weight
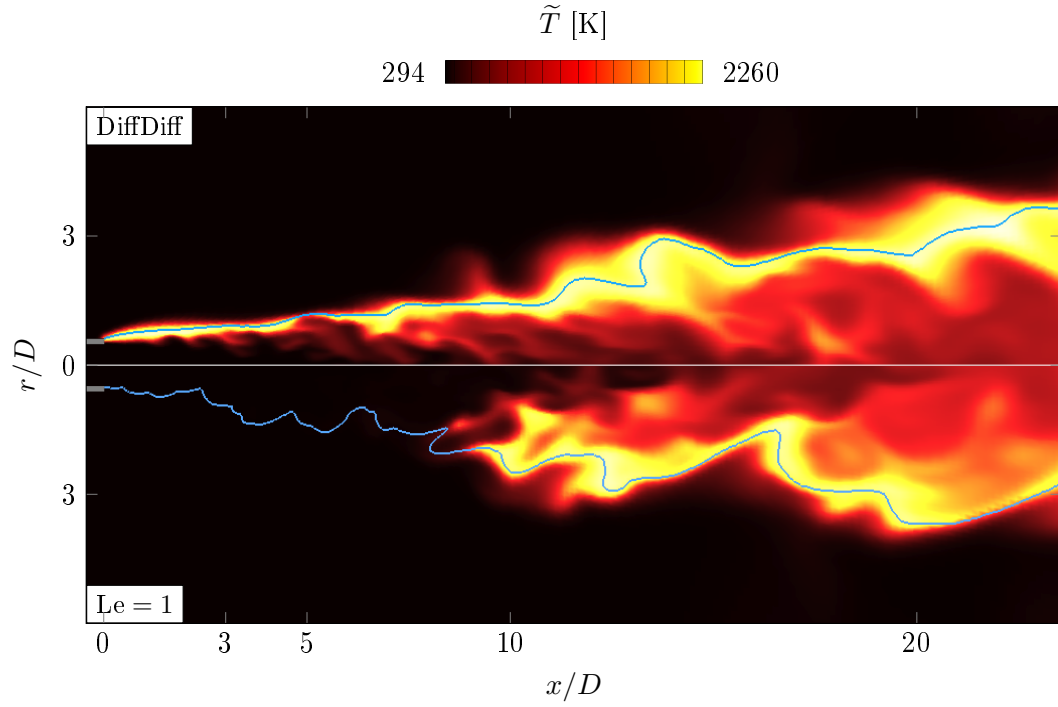
Figure 6.40: Comparison of instantaneous resolved temperature field in flame B1: ESF with differential diffusion (top) and unity Lewis number assumption (bottom). The blue iso-line illustrates the stoichiometric mixture fraction Z_{st}.
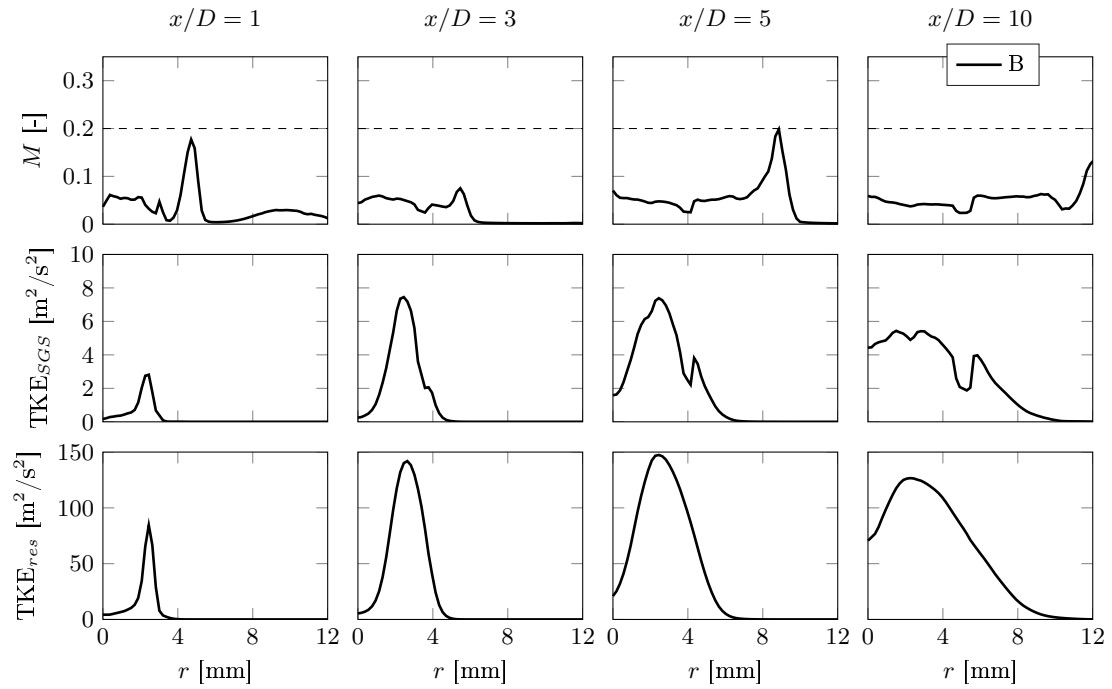

Figure 6.41: Ratio M, modeled TKE_{SGS}, and resolved TKE_{res} for case B1 and the *base* mesh.

species H diffuses faster through the relatively thin reaction zone. According to [148] the shift is a consequence of reduced heat release in the presence of product dissociation on the fuel lean side. So, the heat release peaks on the rich side, inducing the shift of the maximum flame temperature towards the rich side. It is also argued by [250] that the shift may be more pronounced due to the high CO_2 content on the lean side, characterized by higher heat capacity. Sevault et al. [250] argue that the shift is even more pronounced through the high CO_2 content on the lean side, which has a higher heat capacity than N_2 when air is used as oxidizer. Further downstream the flame thickens and molecular transport is superimposed with turbulent mixing, causing the peak in temperature to migrate back towards Z_{st}.

All presented species show very good agreement with the experiments on the fuel lean side and around Z_{st} in both cases. However, on the rich side there are differences. O_2 and CO_2 mass fractions are slightly overpredicted beginning at $x/D = 3$, this is even more evident for case B2. Since these two species are in the oxidizer coflow it is speculated that they get mixed into the fuel jet due to turbulent transport. CO levels and peaks on the fuel rich side are underpredicted, again the situation is more dramatic for case B2. Sevault et al. [250] explained the relatively high CO levels (compared to air combustion) with the high CO_2 content in the coflow. Contrary to N_2, CO_2 is not an inert species but competes with O_2 for atomic hydrogen. This leads to additional formation of CO through the reaction: $CO_2 + H \leftrightarrow CO + OH$. This particular reaction is covered by the employed mechanism. However, since it is an analytically reduced mechanism, optimized for methane/air combustion, it is possible that the reaction is understated for the present oxy–fuel case. Furthermore, Heil et al. [98], who conducted experiments on CO_2 diluted oxy–fuel flames, reported that the CO levels are highly sensitive to the O_2/CO_2 ratio. A variation of only 3 vol-% in O_2 can change the CO level by almost 50%. The low H_2O levels in case B2 indicate an incomplete combustion regime, this corresponds to the low temperatures at $x/D = 5$.

To further quantify the level of localized extinction Sevault et al. [250] used the fully burning probability (FBP). It is defined as the probability of finding a burning state in a narrow band of width 2Λ centered around the mixture fraction with the highest temperature (not necessarily Z_{st}) in the scatter samples of each axial plane. A burning state is defined where the sampled temperature is $T > 1700$ K; Λ is taken as 0.02 [250]. From all scatter samples the FBP has been computed and is compared with the experimental values in Figure 6.44. The LES for case B1 only shows very little extinction and agrees well with the experiments, only at $x/D = 3$ extinction is less pronounced in the simulation. In case B2 the LES matches well the degree of extinction at $x/D = 3$ but shows a lower FBP at $x/D = 5$. This could explain the high O_2 mass fractions on the fuel rich side (Fig. 6.43, $x/D = 5$). More O_2 gets mixed into the fuel stream as its consumption is lower in the reaction zone. However, the trend of increased extinction at a higher jet Reynolds number is well captured.

Figure 6.45 shows time averaged mean and RMS profiles of temperature $\widetilde{T}$, the mixture fraction $\widetilde{Z}$, and major species mass fractions (H_2, CH_4, O_2, CO_2, CO, H_2O) over the radial position at different axial positions for flame B1 and B2. Circumferential averaging has been performed over 15 ms of simulation time (corresponds to approx. 15 flow through times at $x/D = 20$). Close to the nozzle ($x/D = 3$) it can be seen that the mixture fraction diffuses slightly faster in the simulation but match the experiments well. With increasing downstream location the mean and RMS values of the mixture fraction tend to be in very good agreement with the experiments. The results for species mass fractions H_2, CH_4, and

Figure 6.42: Mean conditional temperature (i.e. $\langle \widetilde{T} | \widetilde{Z} \rangle$) and species mass fractions for case B1. The color legend is: H_2 ——, CO ——, CO_2 ——, CH_4 ——, O_2 ——, H_2O —— with LES as solid line (——) and experiments as circles ($\circ$).
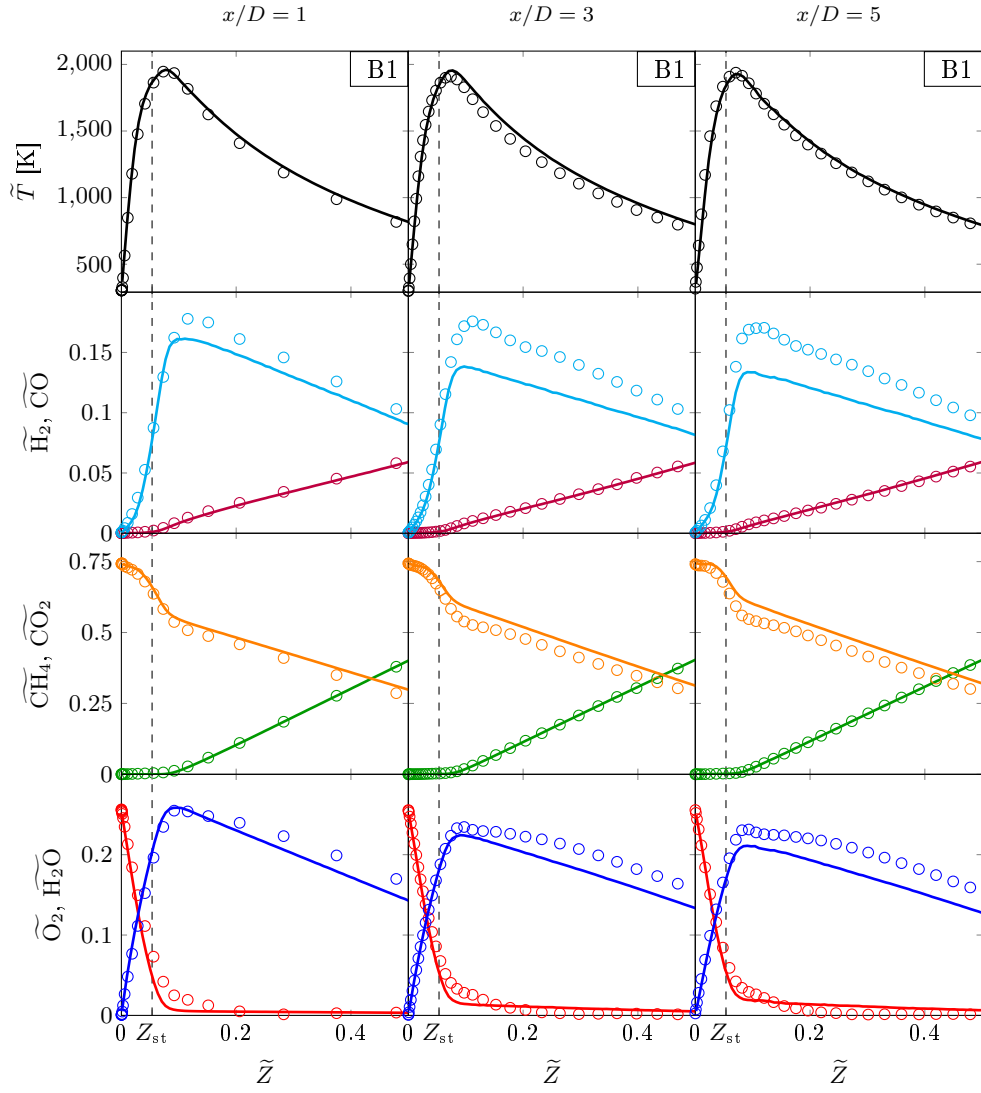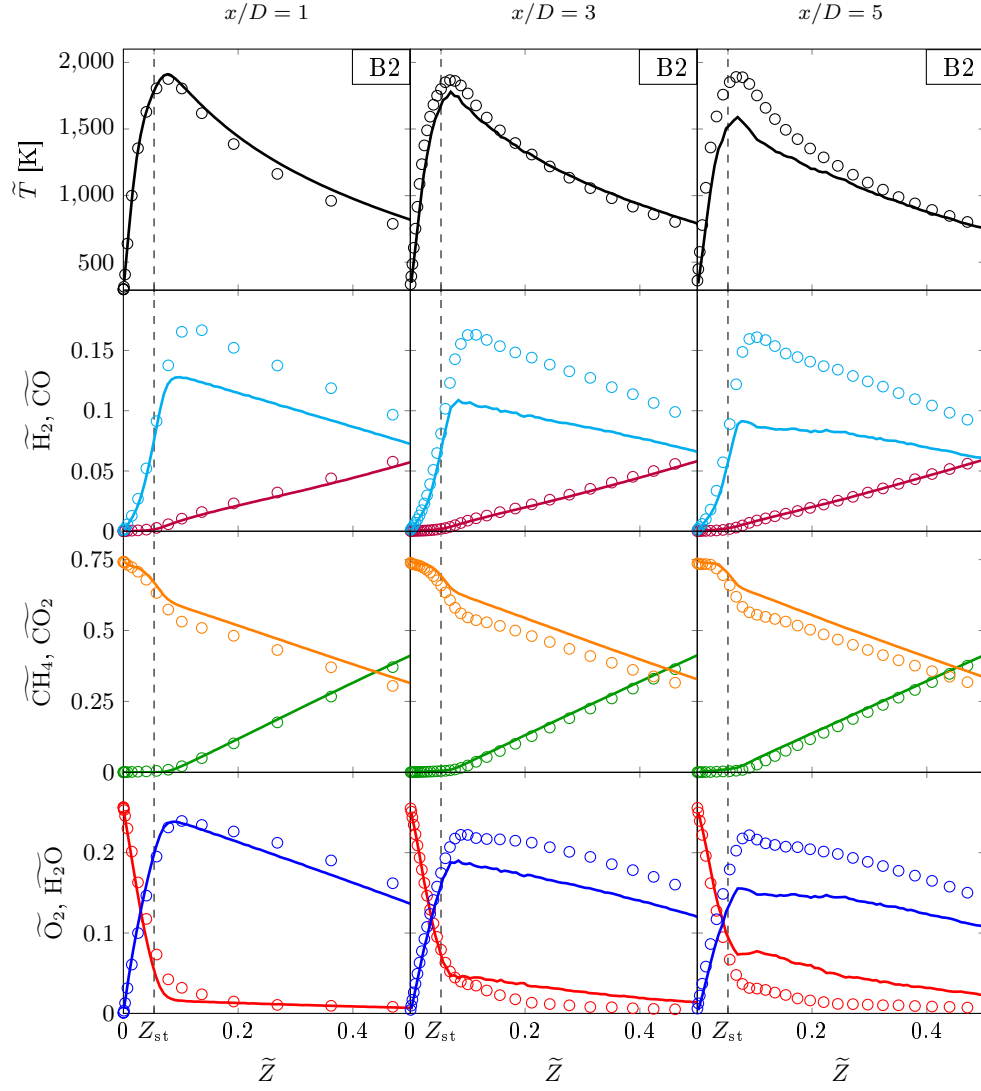
Figure 6.43: Mean conditional temperature (i.e. $\langle \widetilde{T} | \widetilde{Z} \rangle$) and species mass fractions for case B2. The color legend is: H_2 ——, CO ——, CO_2 ——, CH_4 ——, O_2 ——, H_2O —— with LES as solid line (——) and experiments as circles (○).
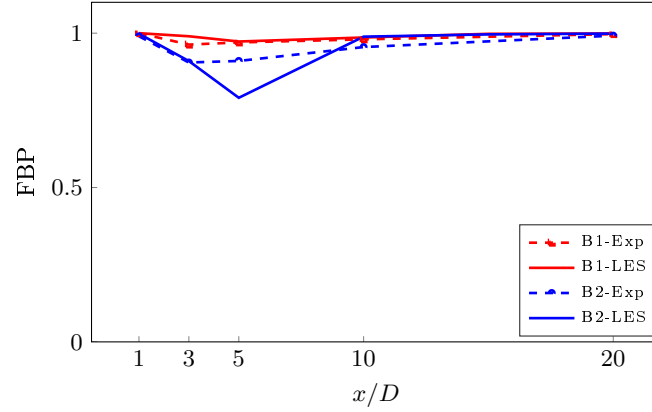
Figure 6.44: Fully burning probability (FBP) for LES and experimental data of flame B1 and B2.

CO_2 generally agree very well with the experimental data, although H_2 and CH_4 seem to diffuse faster in radial direction up to $x/D = 5$ (as already seen with the mixture fraction). The peak values of the mean temperature are slightly overpredicted and the location of the peaks is shifted approximately 1 mm away from the center of the jet at all axial positions, compared to the experiments. Similar behavior can be observed for H_2O, O_2, and CO, the peaks of the latter one are also underpredicted by the LES in both cases and more notably in case B2. The scalar mixing process in the center of the jet and the shear layer between jet and reaction zone are predicted well by the LES. However, the thermal reaction zone gets too thick, which can be seen especially in the T and O_2 profiles. Moreover, the RMS values of some scalars (O_2, CO, H_2O) do not match the experimental data in the region of the shear layer between reaction zone and coflow (around $r = 8$ mm for $x/D = 10$). This could indicate that the LES underpredicts turbulent fluctuations in this particular region, hence, allowing the flame to extend further in radial direction.

The effect of radiation on the temperature has also been investigated with the optically thin radiation model (OTRM) according to [8]. However, the impact of radiation on the temperature was found to be less than 2% in the region where the data is analyzed ($x/D <$ 20), it is therefore rather negligible for the simulated flame temperatures.

6.3.3.3 Influence of differential diffusion

Apart from the shift of the peak temperature in mixture fraction space, the influence of differential diffusion can be quantified with the differential diffusion parameter Z_{HC}. It is defined as the difference between the elemental mixture fractions of hydrogen atoms Z_H and carbon atoms Z_C [6]:

$$Z_{HC} = Z_H - Z_C = \frac{Y_H - Y_{H,\text{oxidator}}}{Y_{H,\text{fuel}} - Y_{H,\text{oxidator}}} - \frac{Y_C - Y_{C,\text{oxidator}}}{Y_{C,\text{fuel}} - Y_{C,\text{oxidator}}} \ . \tag{6.4}$$

Figure 6.46 presents $\widetilde{Z}_{HC}$ from the baseline LES (B1-B-ESF-DD-lu19-8 and B2-B-ESF-DD-lu19-8) and the experiments for B1 (1st row) and B2 (2nd row) at $x/D = 1$, 3, 5, and 10. In both simulations the agreement of $\widetilde{Z}_{HC}$ on the fuel lean side 1 diameter above the nozzle is very good. This is still the case for flame B1 at $x/D = 3$, while there is a discrepancy for B2 with lower differential diffusion effects on the lean side. On the fuel rich side the picture
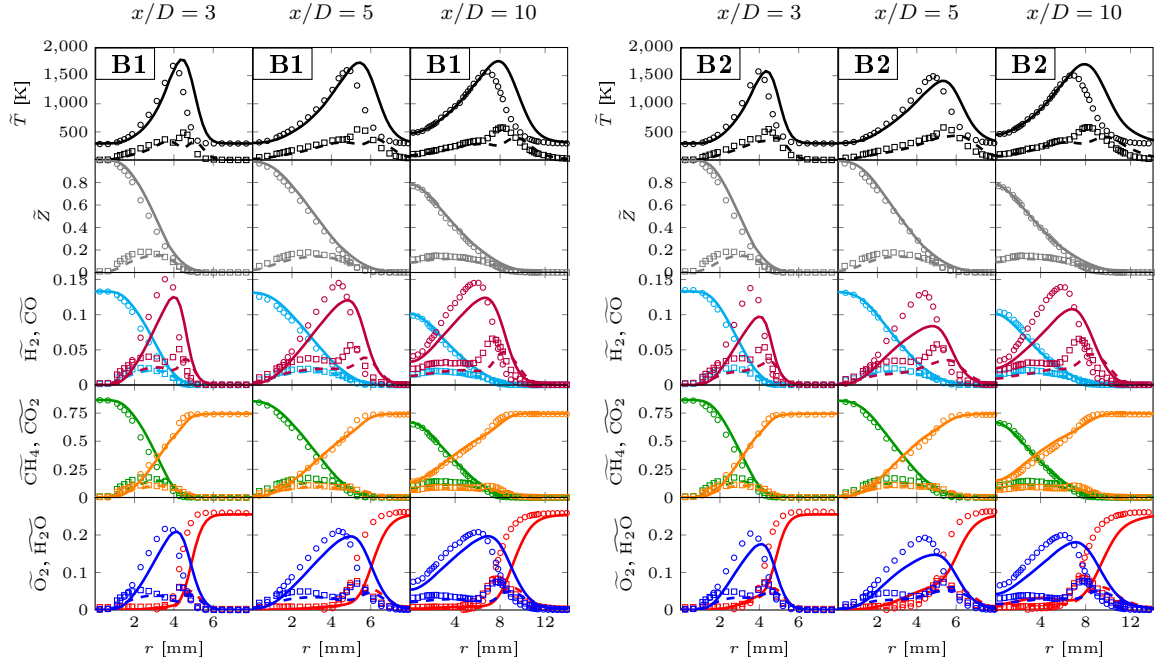
Figure 6.45: Radial distribution of mean and RMS temperature and species mass fractions for case B1 (left) and B2 (right). The color legend is: $\widetilde{Z}$——, $\widetilde{H_2}$——, $\widetilde{CO}$——, $\widetilde{CO_2}$——, $\widetilde{CH_4}$——, $\widetilde{O_2}$——, $\widetilde{H_2O}$——. LES mean is shown as solid line (——) and RMS as dashed line (- - -). Experimental mean is shown as solid with circles (∘) and RMS as squares (▫).

is different. While the experimental $\widetilde{Z}_{HC}$ exhibits an equal diffusivities behavior the LES weights the influence of differential diffusion more. Further downstream at $x/D = 5$ and $x/D = 10$ the effect of differential diffusion is getting 'washed out' by turbulent motion, however, the impact of turbulence is stronger in the LES.

The observations can be explained as follows: Close to the nozzle the reaction zone and coflow (fuel lean region) are mostly in laminarized state and differential diffusion effects do play a role. On the contrary, the cold fuel jet and the inner shear layer of the reaction zone is highly turbulent and mixing is controlled by turbulent transport. With increasing distance in downstream direction the laminar reaction zone and adjacent coflow are getting perturbed by turbulent eddies and differential diffusion loses its influence. The LES predicts very well the molecular diffusion in the fuel lean regions close to the nozzle. However, it does underestimate the turbulent transport inside the fuel jet, while it overestimates the turbulent transport in the laminar reaction zone further downstream. Apparently, this effect is more pronounced for higher Reynolds numbers (case B2) and could explain the increased localized extinction as seen in Figure 6.44.

Discrepancies can also be caused by numerical diffusion. Minor species (e.g. H, OH) may be formed in a thin layer within the combustion zone, which is not resolved by the ESF method. After all, the resolution of the individual stochastic fields is not finer than the filter width, as it has also been shown recently by Picciani et al. [208] in the context of a premixed flame front. Numerical diffusion thickens the thin reaction layers of minor species and zones of steep gradients in major species. Thereby, the diffusive scalar fluxes may be different.
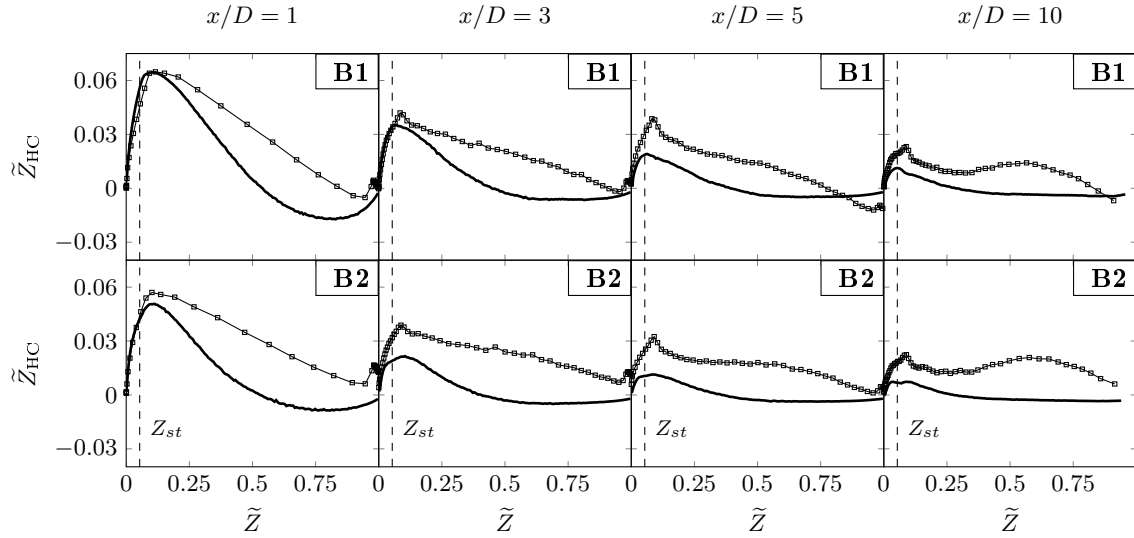
Figure 6.46: Differential diffusion parameter $\widetilde{Z}_{HC}$ plotted over the mixture fraction space $\widetilde{Z}$. The vertical dashed line marks the stoichiometric mixture fraction. The first row shows flame B1, the second row B2: —□—Exp., ——LES.

6.3.3.4 Effect of reaction mechanism, FPV combustion model, N_s stochastic fields, and computational mesh

In the following analysis only configuration B1 is considered. Different cases (see Tab. 6.11) are simulated with a variation of the combustion model, the chemical mechanism, and the computational mesh. The results are compared against the baseline simulation of case B1-B-ESF-DD-lu19-8.

Name	Flame	Mesh	TCI model	Chemistry	N_s	SGS model
B1-B-ESF-DD-lu13-8	B1	B	ESF-DD	Lu13	8	WALE
B1-B-FPV	B1	B	β-PDF	FPV	-	WALE
B1-B-LAM-DD-lu19	B1	B	-	Lu19	-	WALE
B1-M-ESF-DD-lu19-8	B1	M	ESF-DD	Lu19	8	WALE

Table 6.11: Variation of case setups for configuration B1.

For the FPV combustion model the species mass fraction of H_2O solely was used as progress variable, i.e. $PV = Y_{H_2O}/M_{H_2O}$ with the source term $\dot{\omega}_{PV} = \dot{\omega}_{H_2O}/M_{H_2O}$. The mass fraction of CO_2 had to be excluded as it is contained in the oxidizer stream. Using H_2O and CO for PV leads to multiple peaks in the source term manifold, therefore, this option was discarded. The manifold is constructed from non–premixed flamelets genereated with `FlameMaster` with the *unity Lewis number* assumption. Simulations with manifolds created from premixed flamelets were not successful and are not shown here. The boundary conditions and plots of the temperature and source term manifold can be found in the Appendix B.3.

Figure 6.47 compares the mixture fraction conditional temperature and species mass fractions, Figure 6.48 shows the radial distribution of mean and RMS values of the different cases. The simulation with the Lu13 mechanism (B1-B-ESF-DD-lu13-8) is in good agree-

Figure 6.47: Mean conditional temperature (i.e. $\langle \widetilde{T} | \widetilde{Z} \rangle$) and species mass fractions for case B1. The color legend is the same as in Fig. 6.42. Cases: ——B1-B-ESF-DD-lu19-8, - - - B1-B-ESF-DD-lu13-8, - - - B1-B-LAM-DD-lu19, - · · B1-M-ESF-DD-lu19-8, ······B1-B-FPV.

ment with the benchmark simulation close to the fuel inlet. At the beginning ($x/D = 5$) the results show deviations from the benchmark and experimental data with respect to the temperature and species distribution, both in mix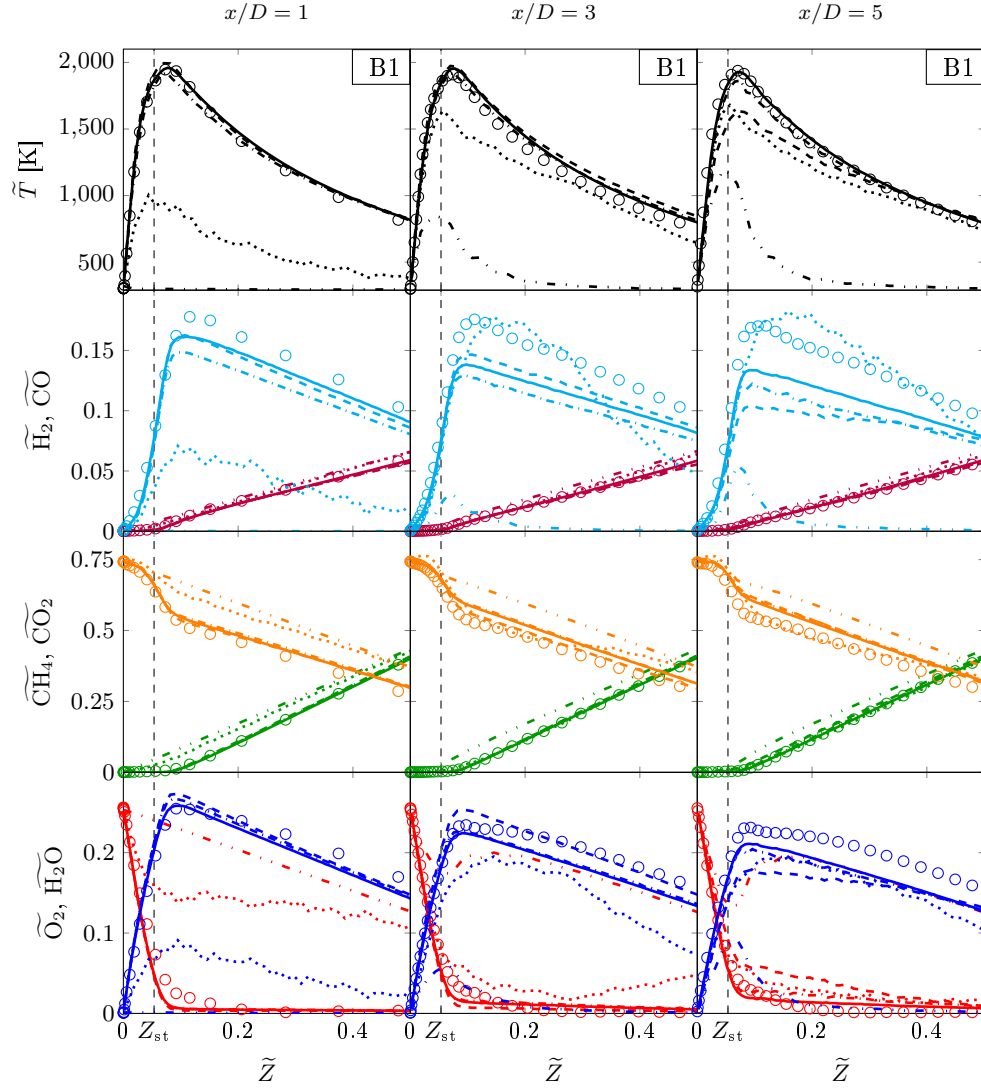ture fraction and radial space (Fig. 6.47 and Fig. 6.48 (a)). The simulation with the FPV combustion model shows increased extinction in the front part. This improves further downstream, as it can be seen in mixture fraction space (Fig. 6.47). However, in physical space the flame temperatures and species distributions are not in good agreement with the experimental data (Fig. 6.48 (b)). The simulation without TCI and laminar chemistry (B1-B-LAM-DD-lu19) is in very good agreement with the benchmark simulation. In mixture fraction space (Fig. 6.47) it performs only slightly worse than the benchmark, however, differences can be seen especially with the CO mass fractions. Although the *medium* mesh is not significantly more coarse than the *base* mesh, the simulations on this mesh were not successful (B1-M-ESF-DD-lu19-8). The flame is completely blown off in the front part and only starts to burn further downstream ($x/D > 10$). Because of this, temperatures are close to 300 K at $x/D = 3$ and the species and mixture fraction profiles are not comparable to the experimental data (Fig. 6.48 (d)). The flame itself is not depicted, as it looks similar to the temperature distribution of the Le $= 1$ simulation, shown in Fig. 6.40.

It is not clear why the simulation on the *medium* mesh is not successful. A possible explanation therefore could be the resolved H_2 flux $\widetilde{J}_{H_2}$. Figure 6.49 compares $\widetilde{J}_{H_2}$ on the *medium* (red) and *base* (black) mesh. The scalar fluxes are much higher on the *base* mesh, allowing H_2 to diffuse faster from the fuel stream into the oxidzer stream. This might contribute to the stabilization of the flame. The reason for this could be that filtered formulations tend to underestimate scalar property gradients, which leads to a lower scalar flux on more coarse meshes.

6.3.4 Summary

In this analysis two oxy–fuel flames (B1 & B2) from the series of [250] with the same H_2 content at different jet Reynolds numbers were simulated. It could be shown that differential diffusion is an essential mechanism for the stabilization of the flame, whereas with the *unity Lewis number* assumption flame B1 experienced heavy lift off and is completely blown out below $x/D = 10$. Therefore, the ESF-DD (4.31) method has been applied with the Lu19 mechanism for the baseline simulations on the *base* mesh. Localized extinction is predicted well for flame B1. However, the degree of extinction is overpredicted for flame B2 with higher jet Reynolds number. The flame structure in the reaction zone and the fuel lean regions are reproduced well, while some species mass fractions are mismatched on the fuel rich side. Similar observations have also been reported for flame B1 by Gierth et al. [79]. The CO mass fractions are underpredicted in both simulations with a decreasing tendency for case B2 at higher Reynolds number. It is speculated that a mismatch in localized extinction and the ratio of CO_2/O_2 mass fraction is responsible for this. Moreover, differential diffusion effects are captured well for both flames in the near nozzle region in terms of $\widetilde{Z}_{HC}$ and the peak temperature shift towards the fuel rich side. Further downstream these effects are canceled out by turbulent transport, however, too fast in the LES.

The configuration B1 was also investigated with different combustion models and setups. Using the FPV combustion model with a non–premixed manifold and the *unity Lewis number* assumption it was possible to simulate a burning, anchored flame. However, the results were not satisfying. The results with the Lu13 mechanism and the ESF method are
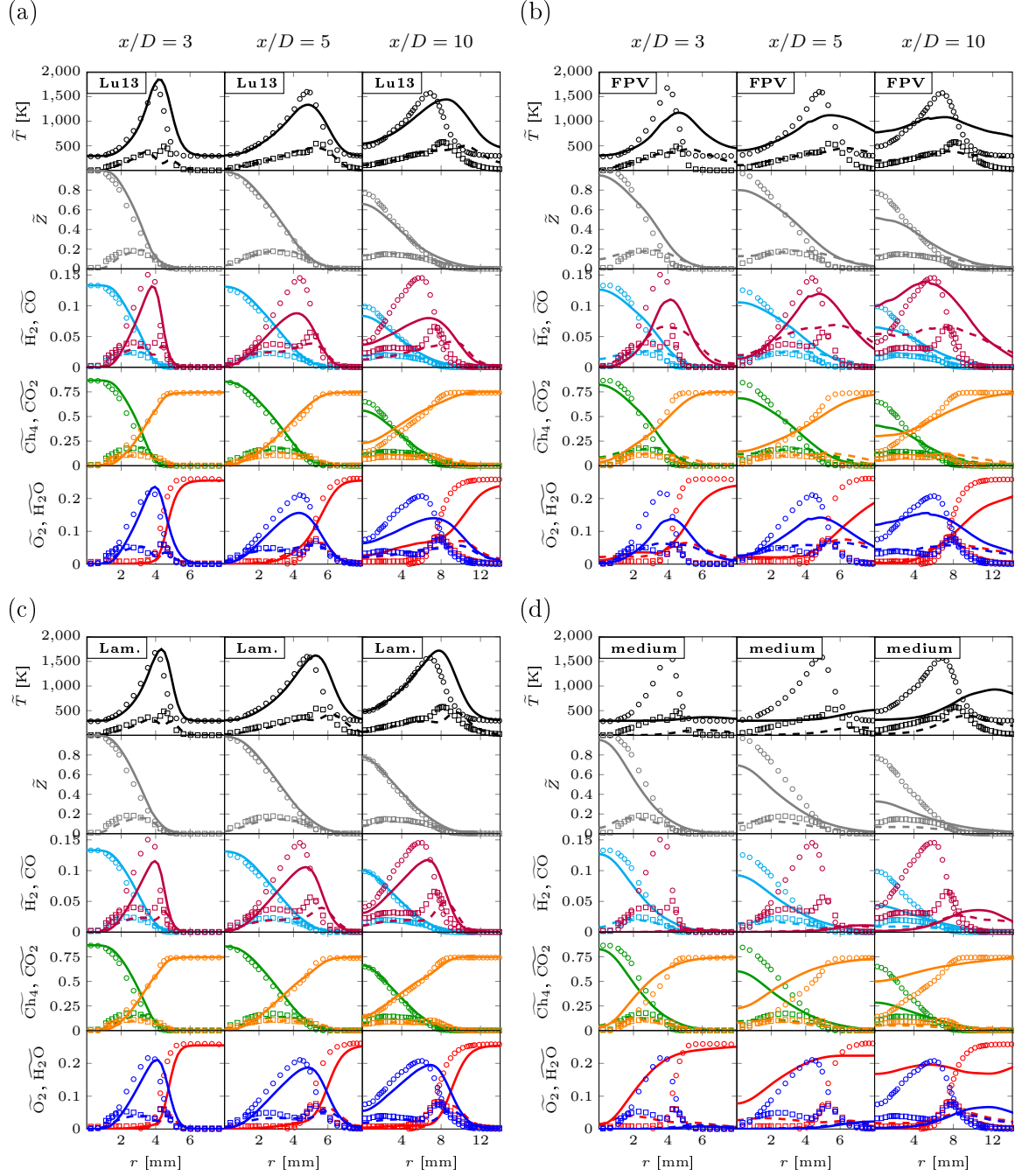
Figure 6.48: Radial distribution of mean and RMS temperature and species mass fractions for case B1-B-ESF-DD-lu13-8 (left) and B1-B-FPV (right). The color legend is the same as in Fig. 6.42. Cases: (a) B1-B-ESF-DD-lu13-8, (b) B1-B-FPV, (c) B1-B-LAM-DD-lu19, (d) B1-M-ESF-DD-lu19-8. LES mean is shown as solid line (——) and RMS as dashed line (- - -). Experimental mean is shown as solid with circles ∘ and RMS as squares ▫.
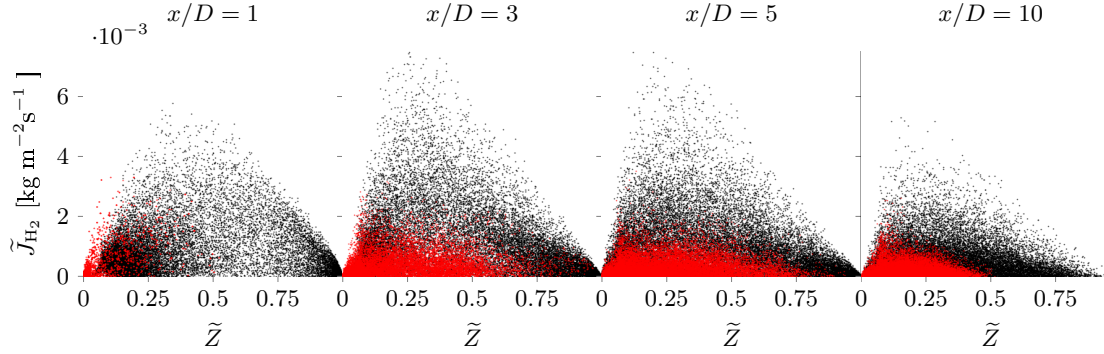
Figure 6.49: Comparison of the radial H_2 fluxes $\widetilde{J}_{H_2}$ on the *medium* (red) and *base* (black) mesh at different axial positions.

in reasonable agreement with the baseline simulation, although a higher degree of extinction can be observed at $x/D \geq 5$. Results where TCI is deliberately neglected and laminar finite rate chemistry is assumed are in very good agreement with the ESF benchmark simulation, only small deviations in mixture fraction space can be observed. Finally, the simulation on the slightly more coarse *medium* mesh shows a complete extinction of the flame up to $x/D = 10$. The reason for this is not fully understood. It is speculated that a considerable aspect is that filtered formulations tend to underestimate scalar property gradients, which generally leads to an underestimation of differential diffusion in relation to the numerical cell size. This speculation is underpinned by a comparison of the resolved H_2 scalar fluxes $\widetilde{J}_{H_2}$ which are considerably smaller on the *medium* mesh.

Chapter 7

Conclusion and outlook

The present study explores the capabilities of the Eulerian Stochastic Fields method and the flamelet/progress variable model in Large Eddy Simulation of partially premixed flames and aims to quantify differences in their predictive capabilities. Of particular interest were the questions, how does the choice of the chemical mechanism affect the results, which ESF formulation is more appropriate, how does the number of stochastic fields improve the results or is laminar finite rate chemistry also sufficient in LES, which FPV manifold is more suitable for partially premixed flames, a premixed or a non–premixe one? Finally the question, which combustion model is better and by how much? To this end three test cases with different flame structures and degrees of localized extinction have been selected and were simulated with the ESF method and the FPV model using identical numerical setups and computational meshes.

The first test case was the Sydney piloted methane/air flame FJ200-5GP-Lr75-57 with inhomogeneous inlet that exhibits a mixed combustion mode and transitions from a pre-mixed flame to a non–premixed flame. When the ESF method with an analytically reduced Lu19 chemical mechanism was used, the simulation results were in very good agreement with experimental and qDNS data in terms of temperature and species mass fractions. A statistical analysis of the probability of local extinction and the burning index also agree well with the reference data. A detailed study on the different ESF formulations and the number N_s of stochastic fields reveals that turbulence chemistry interaction may deliber-ately be neglected and laminar finite rate chemistry is sufficiently correct in LES for the studied cases (it has not been shown that this is always the case, e.g., at higher pressures). When different chemical mechanisms of lower quality were used the prediction quality of minor species deteriorated. Simulations with the FPV combustion model are found to be less accurate. However, using a premixed manifold shows an acceptable prediction of the temperature.

The second test case focused on the simulation of Sandia Flame F. It is the flame from the Sandia Flame series that shows the strongest degree of local extinction and is close to blow-off. A fine mesh and a very coarse mesh were used. The latter one was considered already too coarse to be suitable for a proper LES according to Pope's mesh resolution criteria. However, using the ESF method and the Lu19 mechanism it could be shown that the results are comparable. The baseline simulation on the fine mesh is in good agreement with the experiments. Although, local extinction in the front part of the flame was underpredicted. The effect of the stochastic fields method on the sub–grid scalar fluctuation of temperature and mixture fraction was investigated and it was shown that

the sub–grid contribution of these terms is significant when compared to the resolved terms of fluctuation. Nevertheless, no evidence was found that a higher number of stochastic fields would increase the prediction quality and laminar finite rate chemistry results were found equally accurate. It was shown that the magnitude of the mixing model term is very small compared to the stochastic velocity term explains that a variation of the IEM mixing model constant has no effect. There is also no significant difference between the Lu13 and Lu19 mechanism, whereas the JL-R mechanism was not found suitable, as the flame extinguishes. The results with the FPV combustion model are slightly worse than the ones obtained with the ESF method, especially with respect to minor species, but acceptable. However, the simulations with the premixed manifold showed a very good agreement with the local extinction observed in the front part of the flame.

The last setup that was simulated is an oxy–fuel hydrogen enriched jet flame that is burnt in an oxygen/carbon dioxide atmosphere. From this setup two configurations haven been considered at different jet Reynolds numbers with different degrees of local extinction. To account for the elevated hydrogen content an ESF formulation that incorporates differential diffusion has been devised (ESF-DD). It could be shown that differential diffusion is an essential mechanism for the stabilization process of the flame, whereas with the unity Lewis number assumption the flame is completely blown off close to the fuel inlet. With the ESF-DD method and the Lu19 mechanism localized extinction was predicted well for both flames. The flame structure in the reaction zone was also matched well, with the exception of CO where the mass fractions are underpredicted for both flames. In addition, the differential diffusion effects were investigated and the peak temperature shift towards the fuel rich side in mixture fraction space was reproduced well. Simulations with the Lu13 mechanism were also in good agreement, but slightly worse. Results where turbulence chemistry interaction is deliberately neglected are comparable to the benchmark simulation. Simulations with the FPV combustion model were only successful with a non–premixed manifold. However, the results were not satisfying. Finally, a simulation with the ESF-DD method on a slightly more coarse mesh showed a lifted flame. It was argued that an underestimation of scalar gradients in filtered simulations is the reason for a reduced hydrogen flux into the oxidizer stream, which leads to an extinction of the flame.

In summary, the ESF method in conjunction with the Lu19 mechanism proved to be a reliable and robust combustion model for the simulation of partially premixed flames with different degrees of local extinction. However, from the investigations no trace was found that the number of employed stochastic fields significantly improves the simulation accuracy. In fact, neglecting turbulence chemistry interaction and assuming laminar finite rate chemistry was sufficiently accurate in all three test cases. Also, no significant difference between the ESF-O and ESF formulation could be found. So far, these findings explicitly apply to time resolved LES of partially premixed piloted or jet flames. More research is needed, e.g. in the field of auto ignition or wall bounded flames with quenching, to be able to make a clearer statement if turbulence chemistry interaction (and thus the sub–grid PDF) may be neglected in general for LES of non–premixed and partially premixed flames when finite rate chemistry is employed. With LES as a design tool for combustion problems in the industry, the computational costs have to be considered. The integration of the chemical source terms with the Lu19 mechanism accounts for approximately 90% of the costs per computational time step when eight stochastic fields are used. Reducing the number of stochastic fields (and thus reducing the computationl costs) while maintaining

the same level of accuracy in the simulation results allows engineers and practitioners to further refine the computational mesh, employ more complex mechanisms, carry out more parametric studies, or simply advance their simulations.

With the FPV combustion model the costs can be lowered even more. This, however, comes at the price of accuracy. Even if the FPV model predicts the temperatures fairly well minor species and CO mass fractions are mostly mispredicted. Moreover, prior to the simulation it is not clear if a premixed or non–premixed manifold predicts more reliable simulation results.

Future research for partially premixed combustion should focus on substituting finite rate chemistry with advanced manifold reduction strategies or regression techniques, such as artificial neural networks, which have the ability to further cut the computational costs.

Appendix A

Wasserstein metric

The Wasserstein distance is a metric based on the theory of optimal transport. It gives a natural measure of the distance between two distributions with a wide range of applications. The following sections provide an overview on the computation of the Wasserstein W_2-metric. For a more detailed explanation the reader is referred to current research papers by [169, 192, 197, 206].

Optimal transport problem

The classical optimal transport problem formulated by Monge in 1781 concerns finding the optimal way via the minimization of a transportation cost required to move a pile of soil from one site to another. Let X and Y denote two probability spaces with measures μ and ν, respectively, and let $c(x,y)$ denote the transportation cost for moving one unit of mass from $x \in X$ to $y \in Y$. The OT problem seeks then to find a (measurable) transport map (matrix) $T : X \to Y$ that minimizes the total transportation cost $\int Xc(x,T(x))\mu(dx)$.

Wasserstein metric for discrete distributions

In 1942, Kantorovich proposed a relaxed formulation that transforms the Monge's nonlinear problem to a linear programming problem [270]. Based on the Kantorovich's formulation, the W_p-Wasserstein distance between μ and ν on R^d is defined as:

$$W_p(\mu,\nu) = \min \left(\int_{R^d \times R^d} ||x - y||^p d\pi(x,y) \right) . \tag{A.1}$$

Scattered thermo-chemical data from experiments and numerical simulations are usually not available as continuous distributions, but as set of discrete random samples. From these random values discrete distributions can be built and compared. For the discrete distributions, f, e.g. the scatter data from the experiments, and g, e.g. the scatter data from the simulation, the p-th Wasserstein metric can be obtained as:

$$W_p(f,g) = \min \left(\sum_{i=1}^{m} \sum_{i=1}^{n} \gamma_{i,j} |x_i - y_j|^p \right)^{1/p} , \tag{A.2}$$

subject to $\sum_{i=1}^{m} \gamma_{i,j} = f_i$, and $\sum_{i=1}^{n} \gamma_{i,j} = g_j$, $\gamma_{i,j} \geq 0$, where $\gamma_{i,j}$ represents the *amount* transported from x_i to y_j in the $n \times m$ transport matrix T.

Note that in this study only the W_2 Wasserstein metric is used, which is similar to the $L2$-loss and uses the squared Euclidean distance $c(x,y) = |x - y|^2$ in the cost function [169].

Calculation procedure

The procedure described in [115] is followed for the computation of the W_2-metric, using the successive shortest path linear programming algorithm according to [198]. The pseudo code of the corresponding algorithm is given in 1.

Algorithm 1 Pseudo code for evaluating the Wasserstein metric.

Data: Two sets of d-dimensional data representing empirical distribution functions: X, Y, with lengths n and m from scatter data. X and Y have to be normalized by standard deviation of one data set, σ_X

for $i = 1 : n$ **do**

    for $j = 1 : m$ **do**

        Evaluate pair-wise distance matrix $c_{i,j} = \sum_{k=1}^{d}(X_{k,i} - Y_{k,j})^2$

    end

end

Compute Wasserstein metric W_2 and transport matrix as solution to minimization problem of Eq. A.2 using the shortest path algorithm by [198] with input $c_{i,j}$.

Output: Wasserstein metric: W_2

It is important to mention that the input data sets to the Wasserstein metric are normalized to enable a direct comparison and enable a physical interpretation of the results. A natural choice is to normalize each sample-space variable by its respective standard deviation that is computed from the reference data set (in this case it is experimental or qDNS data). Suppose we have two sets of data with sample sizes of m and n, respectively. Each sample represents a point in the thermo-chemical space, e.g., $\mathbf{x} = [T, CO, CO_2, H_2, ...]$. A Python-based example of the post processing code can be found under:
`https://github.com/mhansinger/WasserSteinCombustion`.

Interpretation of W_2-metric

The Wasserstein metric enables the comparison between two multi-dimensional distributions via a single metric while taking into account all information presented by the distributions. The empirical distribution is obtained from a subset of the samples. The Wasserstein metric can then be computed following the definition in Eq. A.2, either for one quantity in the thermo-chemical space, e.g., only T, or in the form of a stacked metric, e.g., $[T, CO, CO_2, H_2]$. The latter one allows for a more holistic error analysis, as the contribution from each variable to the overall dissimilarity (between the data sets) becomes visible. In the case of one-dimensional distributions, the obtained value of the metric shares the same unit as the sample data. For instance, if two distributions of temperature are considered, the corresponding Wasserstein metric in units of Kelvin can be interpreted as the average difference between the values of temperature from the two distributions. In the case of multidimensional distributions, each dimension is normalized before pair-wise distances are calculated. The choice of the normalization method is application-specific. In the present study, the marginal standard deviation is chosen. The so obtained W_2 represents the averaged difference, which is proportional to the marginal standard deviations, between samples from the two distributions. As such, a value of $W_2 = 0.5$ can be interpreted as a difference between simulation and experimental data at the level of 0.5 standard deviation.

Appendix B

Additional simulation results

B.1 Piloted flame with inhomogeneous inlet

B.1.1 Non–reactive cases

Figure B.1 compares the instantaneous (a) and time averaged (b) axial velocity U_x of these two cases close to the jet inlet between $-1 < x/D < 10$ on the *very fine* mesh. The upper half shows the case with the hot pilot, the lower half the cold pilot, respectively. Figure B.2 shows the same situation for the instantaneous (a) and time averaged (b) mixture fraction.

The comparison of the instantaneous velocities shows that the velocity core of the cold case breaks up further upstream than in the case of a hot pilot. This is even more evident in the comparison of the time averaged velocity fields where the black lines depict the iso-contour of $\langle U_x \rangle = 65$ m/s ($\langle \cdot \rangle$ denotes temporal averaging). While the iso-contour of the mean velocity at 65 m/s of the hot case reaches up to $x/D \approx 9$ the iso-contour has its tip already at $x/D \approx 5$ in the cold pilot case. We attribute this to the adjustment of the cold pilot inlet velocity, which is with $U_{\mathrm{P}_{cold}} = 3.26$ m/s significantly lower than the hot pilot velocity at $U_{\mathrm{P}} = 26.6$ m/s. This leads to higher shear velocities between jet and pilot in the cold case and higher momentum transfer in radial direction, eventually leading to a shear layer breakup and turbulent dissipation of the jet's kinetic energy. The effect of the radial momentum transport can also be seen in the mixture fraction distribution. In the comparison of the time averaged mixture fraction (Fig. B.2 (b)) the iso–contour of $\langle Z \rangle = 0.5$ is depicted as a black line. In the hot case the tip of the iso–contour reaches up to $x/D \approx 6$ and surpasses the cold case by about $1\ D$.

B.1.2 Reactive cases

B.1.2.1 Comparison of turbulence models

Name	Mesh	TCI model	Chemistry	N_s	SGS model
CASE-C-ESF-lu19-8	C	ESF	Lu19	1	WALE
CASE-C-ESF-lu19-8-Smag	C	ESF	Lu19	8	Smagorinsky
CASE-C-ESF-lu19-8-Vre	C	ESF	Lu19	16	Vreman

Table B.1: Variation of the turbulence model for the piloted flame with inhomogeneous inlet.
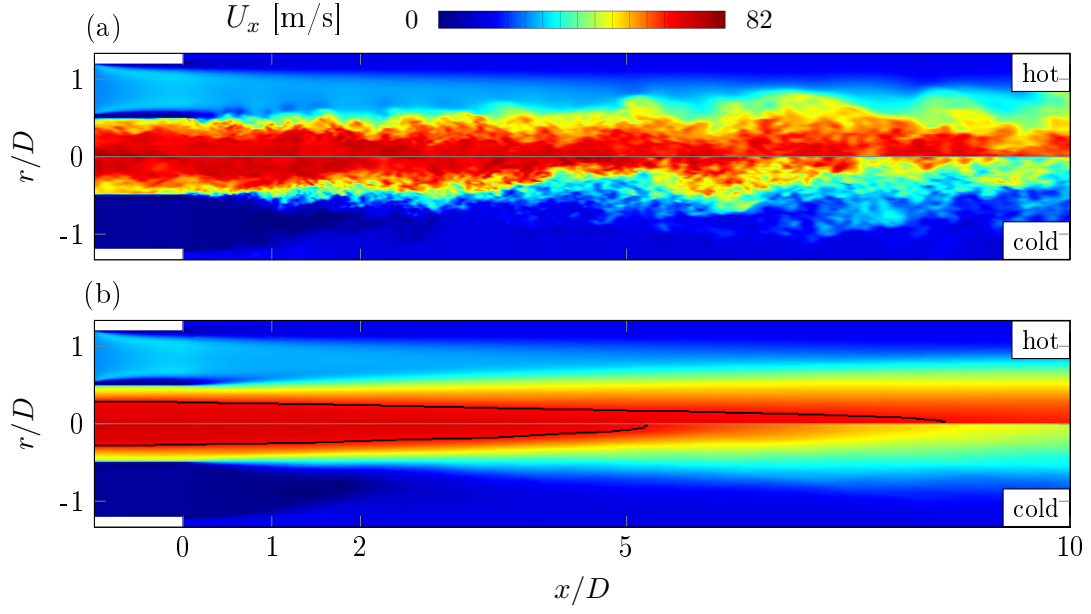
Figure B.1: Snapshot of instantaneous axial velocity U_x (a) and time averaged velocity field $\langle U_x \rangle$ (b) near the jet exit for the non–reactive cases on the *fine* mesh. Upper half shows the hot pilot, lower half the cold pilot case.
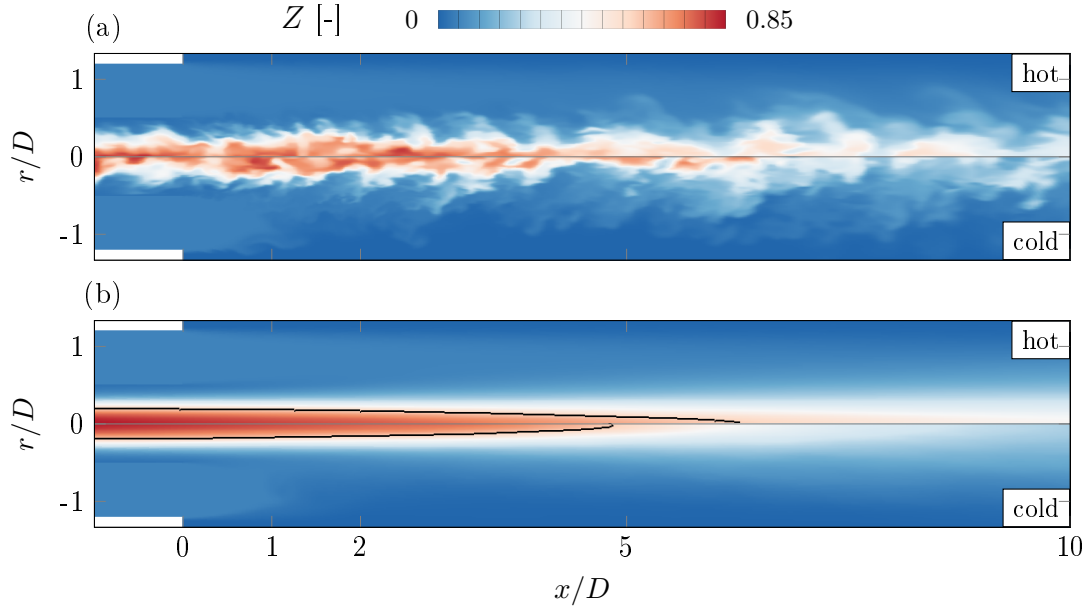
Figure B.2: Snapshot of instantaneous mixture fraction field Z (a) and time averaged mixture fraction field $\langle Z \rangle$ (b) near the jet exit for the non–reactive cases on the *fine* mesh. Upper half shows the hot pilot, lower half the cold pilot case.

B.2   Sandia Flame F

B.2.1   FPV manifolds

The non–premixed manifold was constructed from counterflow diffusion flamelets, which
have been created with `FlameMaster` using the GRI-3.0 mechanism. The premixed manifold
was generated from 150 laminar freely propagating flamelets between $0.1 \leq Z \leq 0.6$ with
CANTERA using the GRI-3.0 mechanism. Beyond the flammability limits the manifold
was interpolated linearly to the boundaries of the manifold at $Z = 0$ and $Z = 1$, where the
experimental boundary conditions (Sec. 6.2.1) were imposed with a temperature of $T = 294$
K at $Z = 1$ and $T = 291$ K at $Z = 0$.
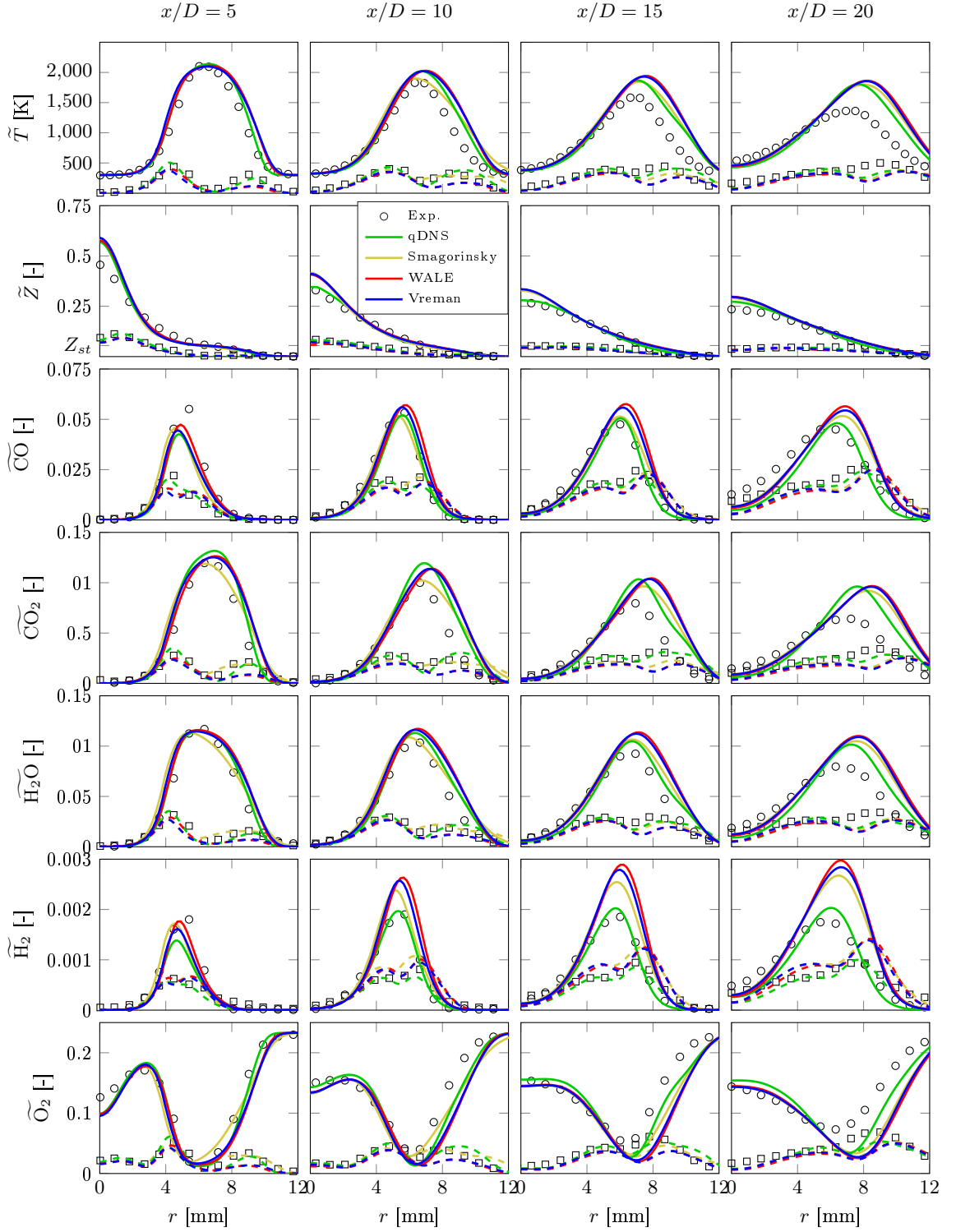
Figure B.3: Comparison of the effect of different turbulence models. All simulations were conducted on the *medium* mesh with $N_s = 8$ stochastic fields. Solid lines represent the mean value, dashed lines the RMS.
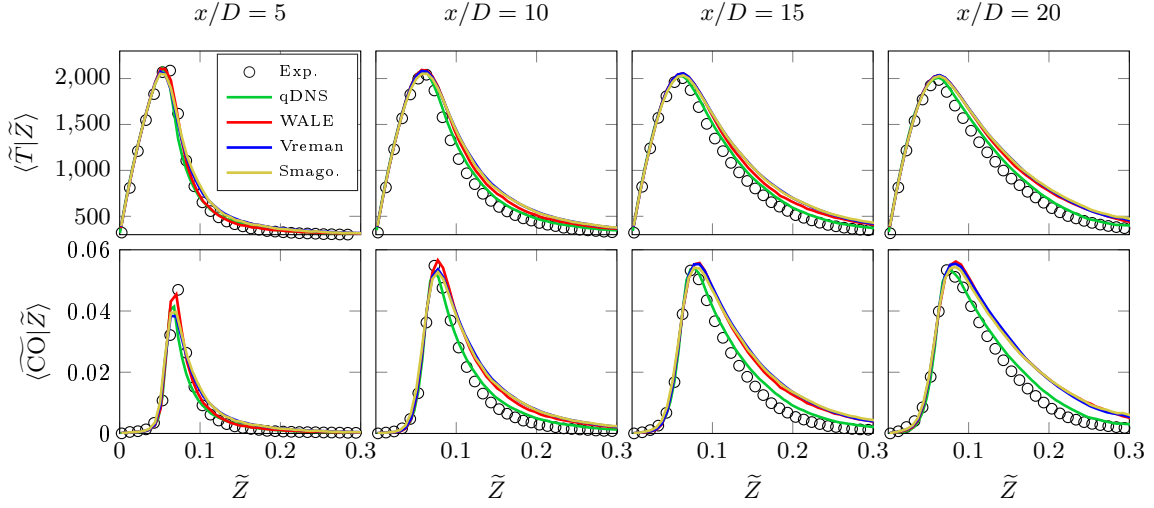
Figure B.4: Comparison of mixture fraction conditional mean values of temperature and CO mass fraction simulated on the *medium* mesh with $N_s = 8$ stochastic fields and different turbulence models.

(a) Temperature manifold

(b) Source term $\dot{\omega}_{PV}$ manifold

Figure B.5: Temperature T and source term $\dot{\omega}_{PV}$ manifold in Z and normalized PV space from non–premixed flamelets.

(a) Temperature manifold

(b) Source term $\dot{\omega}_{PV}$ manifold

Figure B.6: Temperature T and source term $\dot{\omega}_{PV}$ manifold in Z and normalized PV space from premixed flamelets.

B.2.2   Additional plots

Figure B.7 shows the temperature for Flame F, simulated with the ESF method an the JL-R mechanism. The flame gets blown off, as the scalar dissipation rates are too high.
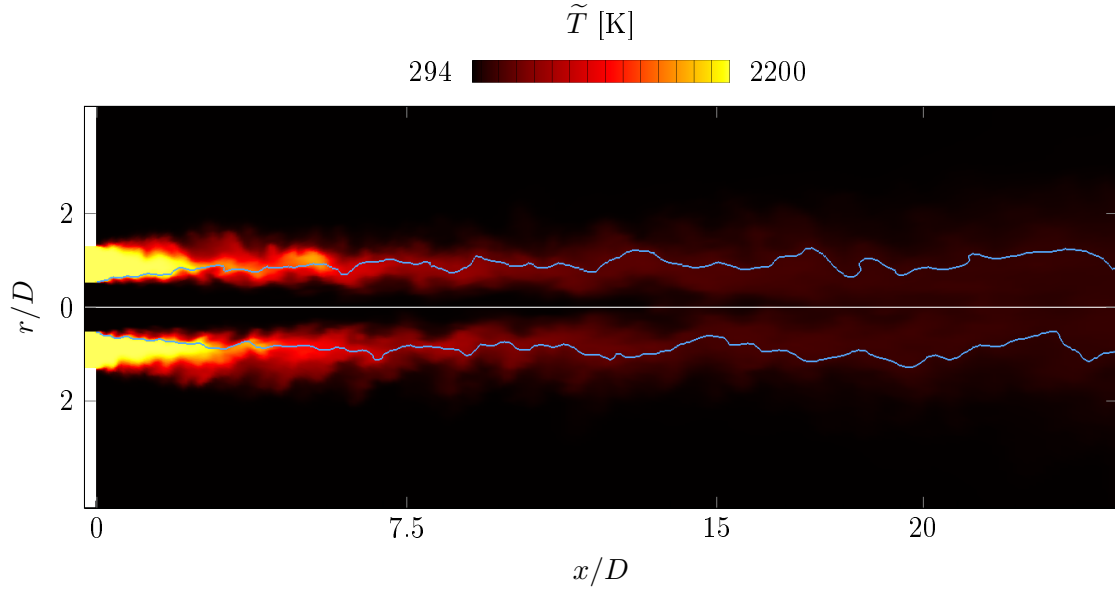
Figure B.7: Simulation of Flame F with the JL-R mechanism on the *very coarse* (VC) mesh.
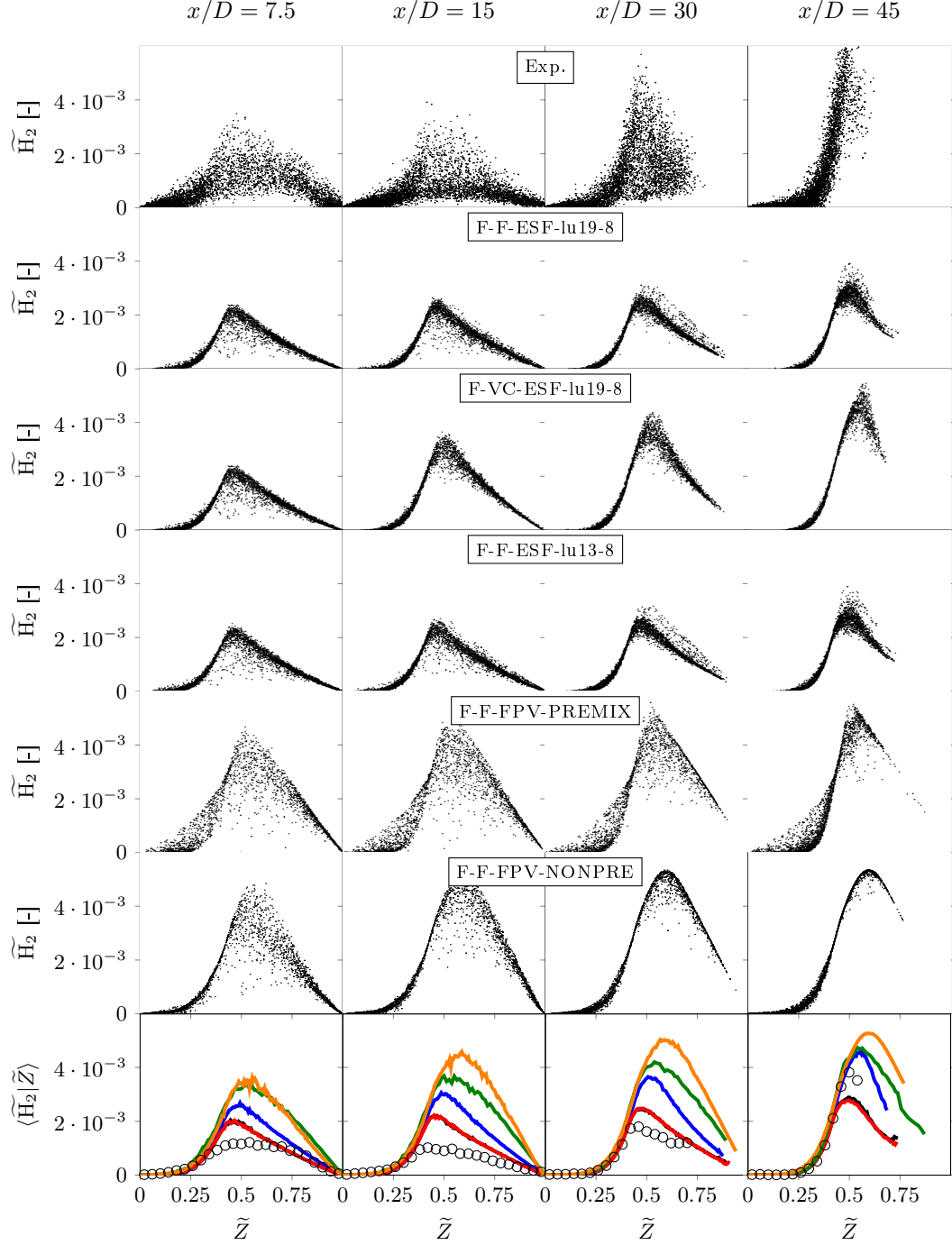
Figure B.8: Scatter plots of $\widetilde{H_2}$ and mixture fraction conditional temperature $\langle\widetilde{H_2}|\widetilde{Z}\rangle$ at different axial locations. The color legend is: ○ Experiment, ——F-F-ESF-lu19-8, ——F-VC-ESF-lu19-8, ——F-F-ESF-lu13-8, ——F-F-FPV-PREMIX, ——F-F-FPV-NONPRE.
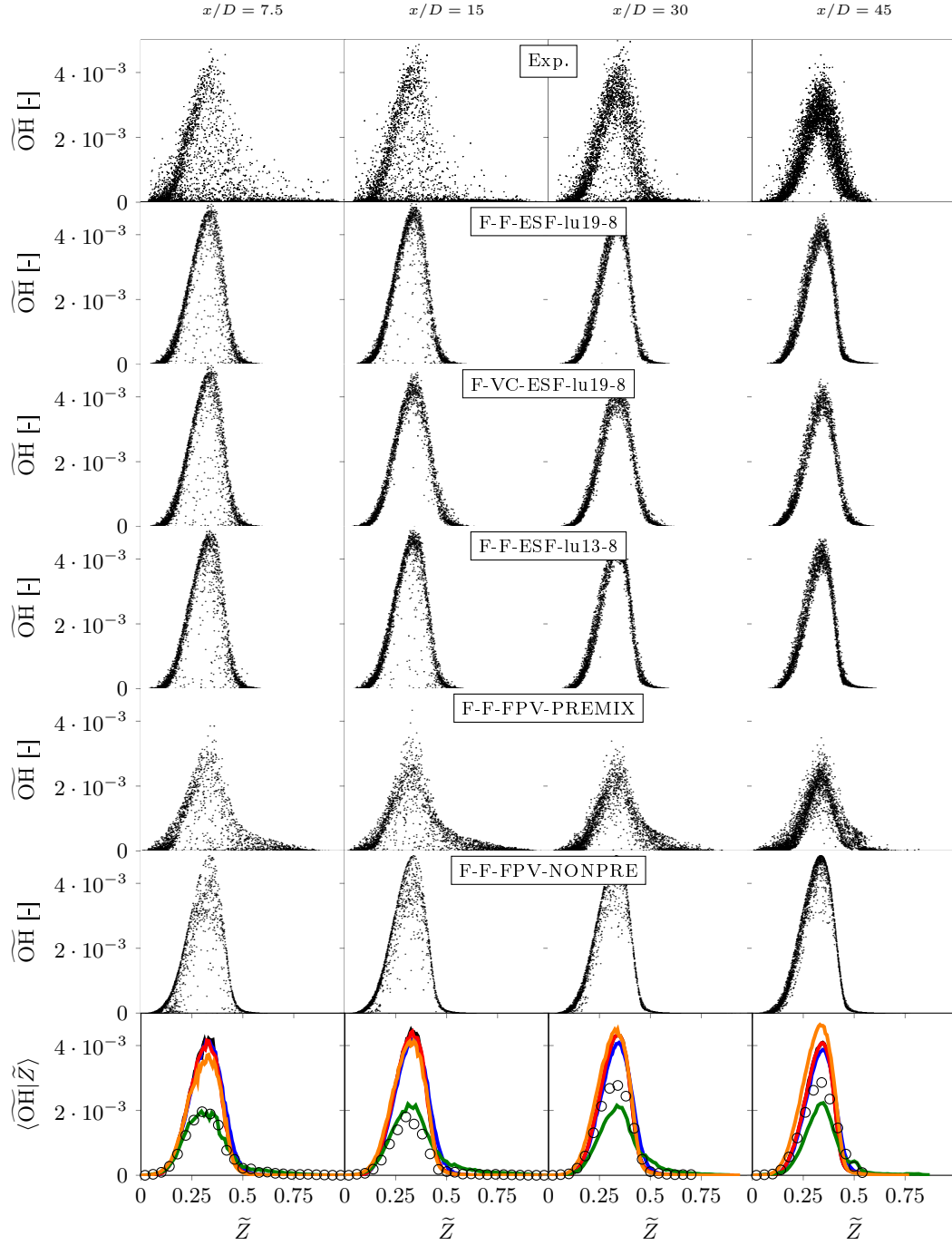
Figure B.9: Scatter plots of $\widetilde{OH}$ and mixture fraction conditional temperature $\langle \widetilde{OH} | \widetilde{Z} \rangle$ at different axial locations. The color legend is: ○ Experiment, ——F-F-ESF-lu19-8, —— F-VC-ESF-lu19-8, ——F-F-ESF-lu13-8, ——F-F-FPV-PREMIX, ——F-F-FPV-NONPRE.

B.3   Oxy–fuel flame

Figure B.10 shows the temperature and source term manifold for the oxy–fuel case. The
manifold was constructed from non–premixed flamelets generated with `FlameMaster`. No
differential diffusion effects were included, instead the *unity Lewis number* assumption was
used. The following boundary conditions have been applied (Tab. B.2):

	T [K]	CH_4	H_2	O_2	CO_2
$Z = 1$	294	0.867	0.133	0.0	0.0
$Z = 0$	294	0.0	0.0	0.255	0.745

Table B.2: Boundary conditions for oxy–fuel flamelets.

(a) Temperature manifold   (b) Source term $\dot{\omega}_{PV}$ manifold
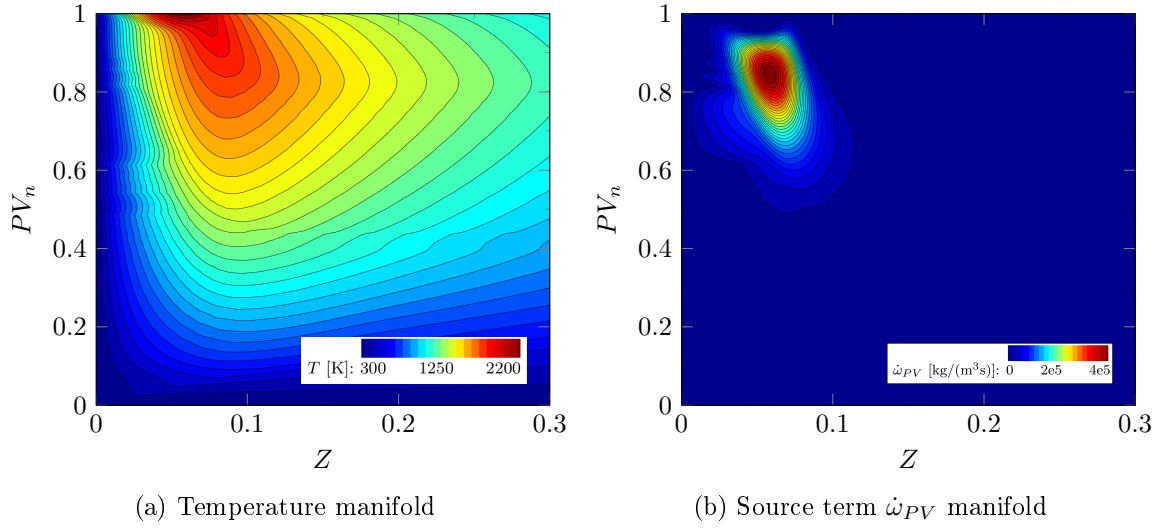
Figure B.10: Temperature T and source term $\dot{\omega}_{PV}$ manifold in Z and normalized PV space
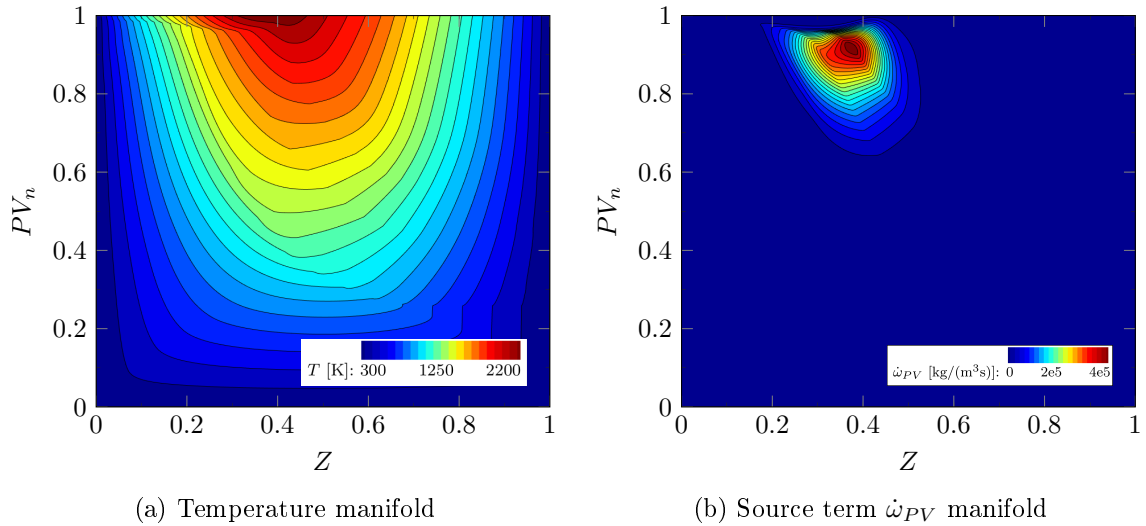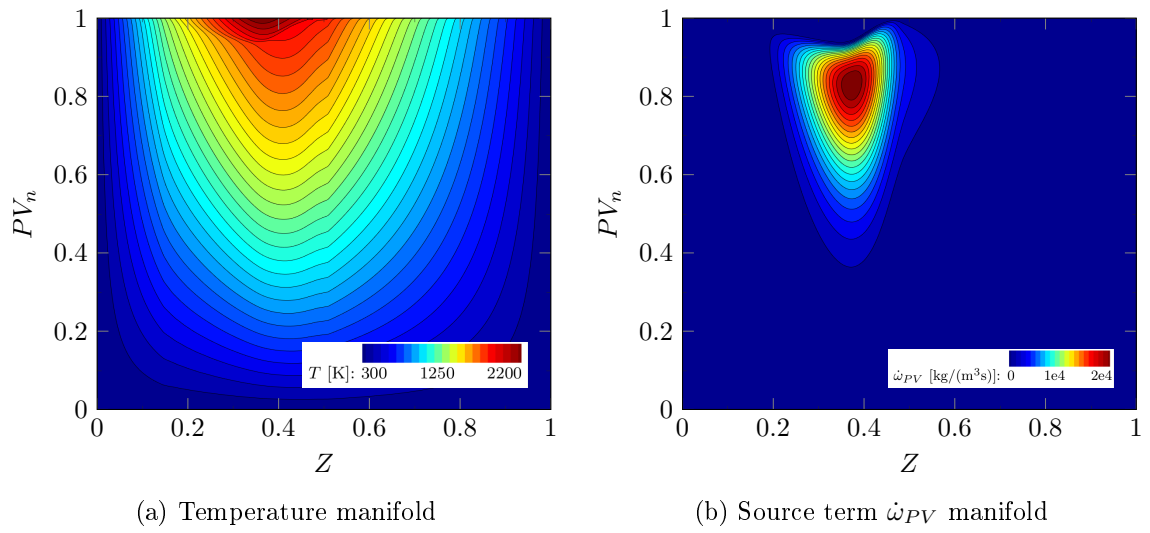from non–premixed flamelets.

Appendix C

The ESF method applied to high–pressure premixed combustion

C.1 Introduction

Transported probability density function (tPDF) methods have originally been developed in the RANS context [220] for non–premixed combustion and adopted for LES. There, the joint sub–grid PDF $\widetilde{\mathcal{P}}_{\text{sgs}}$ of the thermo–chemical state space Ψ is transported with the flow field.The ESF method has already been successfully applied in the field of non–premixed and partially-premixed combustion at ambient pressures [64, 94, 122]. It is also used in LES for premixed combustion in some works [4, 23, 100, 119]. However, Picciani, Richardson, and Navarro-Martinez [208] recently pointed out that the ESF method is highly sensitive to the mesh resolution when applied to premixed combustion and gives reasonable results only in the limit of resolved flame fronts. With typical flame thicknesses of $\delta_{th} < 0.1$ mm for premixed methane-air combustion at ambient pressures an appropriate resolution of the flame front becomes even more expensive at high pressures, as the flame thickness scales inversely proportional to the pressure $\delta_{th} \propto p^{-0.5}$. In order to verify the hypothesis of Picciani, Richardson, and Navarro-Martinez [208], LES of Kobayashi's premixed bunsen flames [136] were carried out at different pressures with the ESF method on different meshes. The results are qualitatively compared to with simulation that use the flame surface density model (FSD) [128].

C.2 Test case and numerical setup

The test cases are three turbulent premixed CH_4/air ($\phi = 0.9$) bunsen flame configurations according to Kobayashi et al. [136] at different pressure levels. Table C.1 gives an overview. The cylindrical computational domain has a diameter of 80 mm and a length of 120 mm

Case	p [MPa]	U_{bulk} [m/s]	u' [m/s]	δ_{th} [cm]
1 bar	0.1	2.36	0.46	0.045
5 bar	0.5	2.21	0.40	0.02
10 bar	1	3.57	0.85	0.014

Table C.1: Kobayashi test case overview.

143

and consists of 2.1 million cells, with a filter width of $\Delta = 0.25$ mm. For the LES the WALE turbulence model was used, the chemical reactions are described with the BFER mechanism [62]. The turbulent transient inflow boundary conditions were generated with the digital filter, proposed by Klein, Sadiki, and Janicka [131].

C.3   Results and conclusion

Figure C.1 shows results form the ESF simulations at 1, 5, and 10 bar. The firs column shows the time averaged temperature $\langle \widetilde{T} \rangle$ at each pressure level and compares it to simulation results with the FSD combustion model [128]. It can be clearly seen that the flame is too long, compared to the FSD reference solution. This indicates that the ESF model underpredicts the consumption rate at the sub–grid scale level. Column two to four show the instantaneous temperature of individual fields, the fourth column shows the filtered temperature field, the last column depicts the instantaneous sub–grid (SGS) temperature fluctuation resulting from the individual fields.

The individual fields, where each field constitutes an individual flame evolution, cause a flame thickening in the filtered temperature field without a 'sharp' interface between burnt and unburnt regions. This effect becomes more evident in Figure C.2, which shows an instantaneous temperature distribution along the x-axis center line ($y = z = 0$) for the 5 bar case. The black dashed lines are the temperatures of the individual fields. The flame fronts of the individual fields are shifted along the x-axis, as a result, the flame front of the filtered field $\widetilde{T}$ (red) (which is the mean from the individual fields) is less steep and thickened.

The findings underpin the hypothesis of Picciani, Richardson, and Navarro-Martinez [208] and show that the ESF method has no beneficial contribution towards the simulation of premixed combustion.
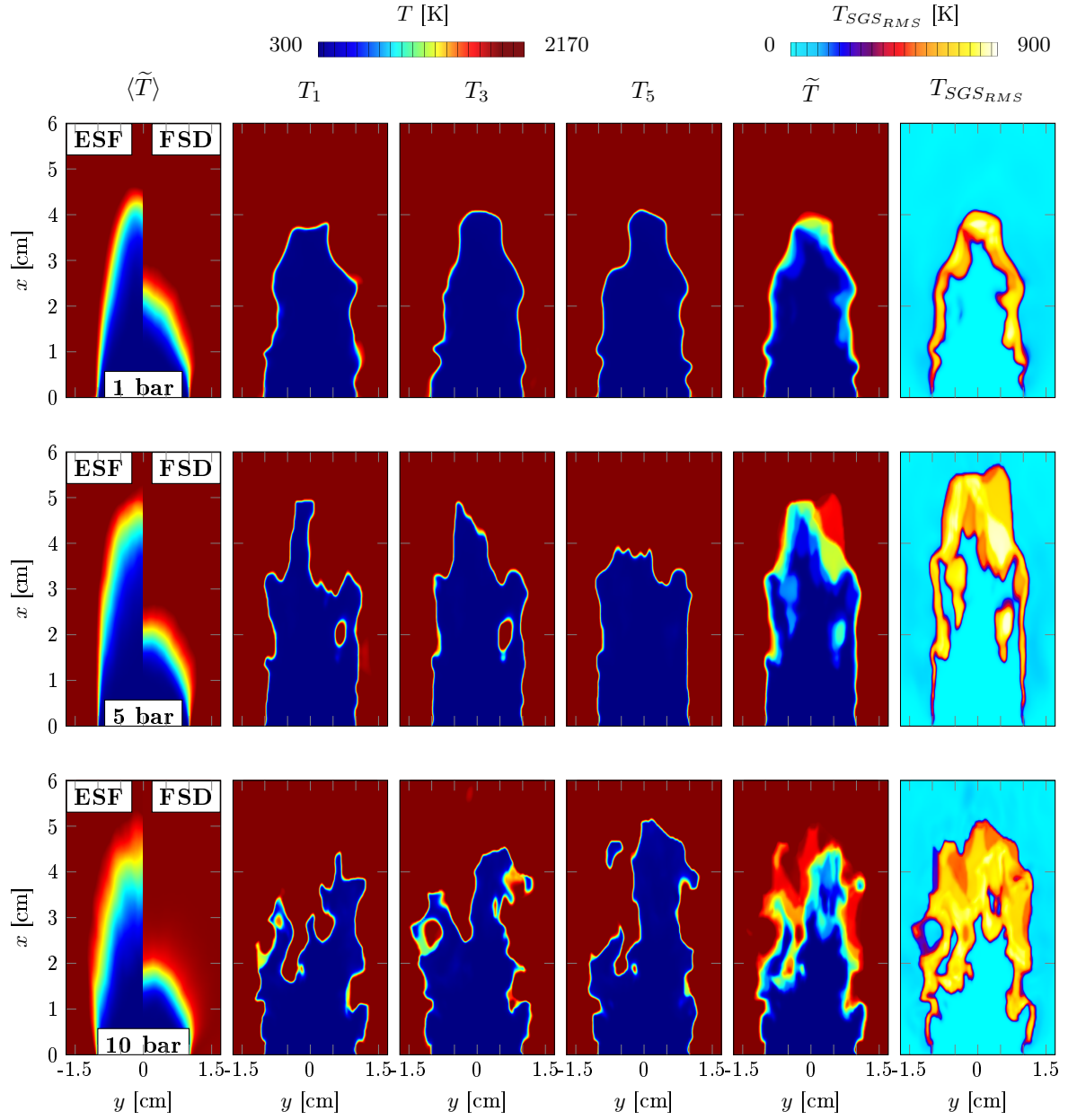
Figure C.1: ESF simulation results at 1, 5, and 10 bar: Time-averaged temperature $\langle \widetilde{T} \rangle$ compared against FSD solution, instantaneous temperature fields (T_1,T_3,T_5), filtered $\widetilde{T}$, and sub–grid scale (SGS) RMS $T_{SGS_{RMS}}$ in $x - y$ plane.
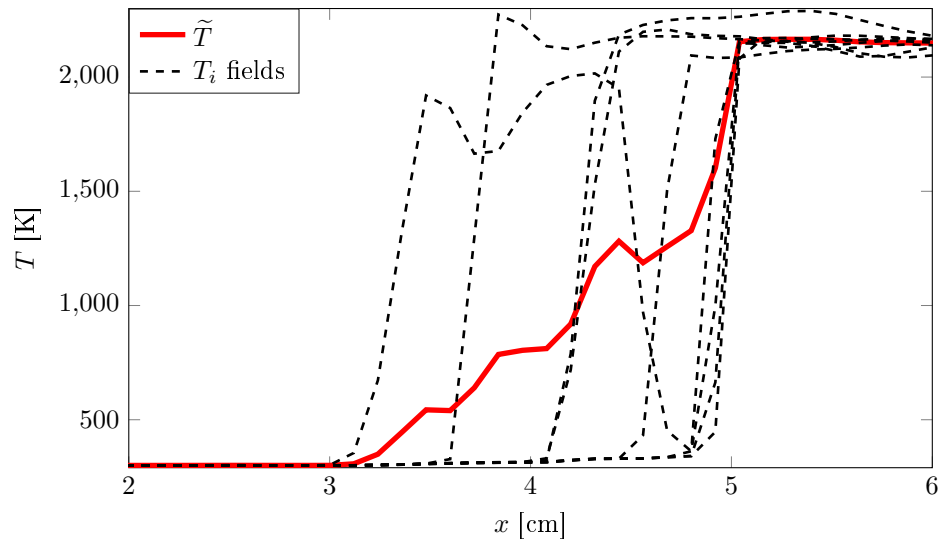
Figure C.2: Temperature distribution along the x–axis ($y = z = 0$) for the 5 bar case.

Bibliography

[1] Acampora, L., Marra, F. S., and Martelli, E. "Comparison of Different CH4-Air Combustion Mechanisms in a Perfectly Stirred Reactor with Oscillating Residence Times Close to Extinction". *Combustion Science and Technology* 188.4-5 (2016), pp. 707–718. DOI: 10.1080/00102202.2016.1138810.

[2] Almeida, Y. P. d. and Navarro-Martinez, S. "Large Eddy Simulation of a supersonic lifted flame using the Eulerian stochastic fields method". *Proceedings of the Combustion Institute* 37.3 (2019), pp. 3693–3701. DOI: 10.1016/j.proci.2018.08.040.

[3] Arrhenius, S. "Über die Reaktionsgeschwindigkeit bei der Inversion von Rohrzucker durch Säuren". *Zeitschrift für Physikalische Chemie* 4.1 (1889). DOI: 10.1515/zpch-1889-0416.

[4] Avdić, A., Kuenne, G., and Janicka, J. "Flow Physics of a Bluff-Body Swirl Stabilized Flame and their Prediction by Means of a Joint Eulerian Stochastic Field and Tabulated Chemistry Approach". *Flow, Turbulence and Combustion* 97.4 (2016), pp. 1185–1210. DOI: 10.1007/s10494-016-9781-y.

[5] Avdić, A., Kuenne, G., Mare, F. di, and Janicka, J. "LES combustion modeling using the Eulerian stochastic field method coupled with tabulated chemistry". *Combustion and Flame* 175 (2017), pp. 201–219. DOI: 10.1016/j.combustflame.2016.06.015.

[6] Barlow, R., Fiechtner, G., Carter, C., and Chen, J.-Y. "Experiments on the scalar structure of turbulent CO/H2/N2 jet flames". *Combustion and Flame* 120.4 (2000), pp. 549–569. DOI: 10.1016/S0010-2180(99)00126-1.

[7] Barlow, R. and Frank, J. "Effects of turbulence on species mass fractions in methane/air jet flames". *Symposium (International) on Combustion* 27.1 (1998), pp. 1087–1095. DOI: 10.1016/S0082-0784(98)80510-9.

[8] Barlow, R., Karpetis, A., Frank, J., and Chen, J.-Y. "Scalar profiles and NO formation in laminar opposed-flow partially premixed methane/air flames". *Combustion and Flame* 127.3 (2001), pp. 2102–2118. DOI: 10.1016/S0010-2180(01)00313-3.

[9] Barlow, R., Meares, S., Magnotti, G., Cutcher, H., and Masri, A. "Local extinction and near-field structure in piloted turbulent CH4/air jet flames with inhomogeneous inlets". *Combustion and Flame* 162.10 (2015), pp. 3516–3540. DOI: 10.1016/j.combustflame.2015.06.009.

[10] Barlow, R. S. and Karpetis, A. N. "Scalar length scales and spatial averaging effects in turbulent piloted methane/air jet flames". *Proceedings of the Combustion Institute* 30.1 (2005), pp. 673–680. DOI: 10.1016/j.proci.2004.08.139.

[11] Barlow, R. S., Magnotti, G., Cutcher, H. C., and Masri, A. R. "On defining progress variable for Raman/Rayleigh experiments in partially-premixed methane flames". *Combustion and Flame* 179 (2017), pp. 117–129. DOI: `10.1016/j.combustflame.2017.01.027`.

[12] Barlow, R. and Frank, J. *Piloted CH4/Air Flames C, D, E, and F – Release 2*. Tech. rep. Livermore: Sandia National Laboratories, 2007, p. 12.

[13] Batchelor, G. K. *An introduction to fluid dynamics*. 1. Cambridge mathematical ed., 14. print. Cambridge mathematical library. OCLC: 838184093. Cambridge: Cambridge Univ. Press, 2010.

[14] Ben-Nasr, O., Hadjadj, A., Chaudhuri, A., and Shadloo, M. "Assessment of subgrid-scale modeling for large-eddy simulation of a spatially-evolving compressible turbulent boundary layer". *Computers & Fluids* 151 (2017), pp. 144–158. DOI: `10.1016/j.compfluid.2016.07.004`.

[15] Bilger, R. W. "Conditional moment closure for turbulent reacting flow". *Physics of Fluids A: Fluid Dynamics* 5.2 (1993), pp. 436–444. DOI: `10.1063/1.858867`.

[16] Bilger, R., Pope, S., Bray, K., and Driscoll, J. "Paradigms in turbulent combustion research". *Proceedings of the Combustion Institute* 30.1 (2005), pp. 21–42. DOI: `10.1016/j.proci.2004.08.273`.

[17] Bilger, R., Stårner, S., and Kee, R. "On reduced mechanisms for methaneair combustion in nonpremixed flames". *Combustion and Flame* 80.2 (1990), pp. 135–149. DOI: `10.1016/0010-2180(90)90122-8`.

[18] Bird, R. B., Stewart, W. E., and Lightfoot, E. N. *Transport phenomena*. Rev. 2. ed. OCLC: 255914840. New York: Wiley, 2007.

[19] Boger, M., Veynante, D., Boughanem, H., and Trouvé, A. "Direct numerical simulation analysis of flame surface density concept for large eddy simulation of turbulent premixed combustion". *Symposium (International) on Combustion* 27.1 (1998), pp. 917–925. DOI: `10.1016/S0082-0784(98)80489-X`.

[20] Böhm, B., Frank, J., and Dreizler, A. "Temperature and mixing field measurements in stratified lean premixed turbulent flames". *Proceedings of the Combustion Institute* 33.1 (2011), pp. 1583–1590. DOI: `10.1016/j.proci.2010.06.139`.

[21] Boileau, M., Staffelbach, G., Cuenot, B., Poinsot, T., and Berat, C. "LES of an ignition sequence in a gas turbine engine". *Combustion and Flame* 154.1-2 (2008), pp. 2–22. DOI: `10.1016/j.combustflame.2008.02.006`.

[22] Borghi, R. "On the Structure and Morphology of Turbulent Premixed Flames". *Recent Advances in the Aerospace Sciences*. Ed. by C. Casci and C. Bruno. Boston, MA: Springer US, 1985, pp. 117–138. DOI: `10.1007/978-1-4684-4298-4_7`.

[23] Brauner, T., Jones, W. P., and Marquis, A. J. "LES of the Cambridge Stratified Swirl Burner using a Sub-grid pdf Approach". *Flow, Turbulence and Combustion* 96.4 (2016), pp. 965–985. DOI: `10.1007/s10494-016-9719-4`.

[24] Breda, P., Hansinger, M., and Pfitzner, M. "Low dimensional chemistry manifolds applied to premixed methane/air flames under atmospheric conditions". *9th European Combustion Meeting*. Lisbon, Portugal, 2019.

[25] Breda, P., Hansinger, M., and Pfitzner, M. "Chemistry computation without a sub-grid PDF model in LES of turbulent non-premixed flames showing moderate local extinction". *Proceedings of the Combustion Institute* (2020). DOI: `10.1016/j.proci.2020.06.161`.

[26] Breda, P., Yu, C., and Pfitzner, M. "Validation of an Eulerian Stochastic Fields solver coupled with reaction-diusion manifolds on LES of methane/air non-premixed ames". *Flow Turb Comb* under review (2020).

[27] British Petroleum. *BP Energy Outlook: 2019 edition*. Tech. rep. British Petroleum, 2019.

[28] British Petroleum. *Statistical Review of World Energy*. Tech. rep. British Petroleum, 2020.

[29] Bulat, G., Jones, W., and Marquis, A. "Large Eddy Simulation of an industrial gas-turbine combustion chamber using the sub-grid PDF method". *Proceedings of the Combustion Institute* 34.2 (2013), pp. 3155–3164. DOI: `10.1016/j.proci.2012.07.031`.

[30] Burcat, A. and Rusic, B. *Third Millennium Ideal Gas and Condensed Phase Thermochemical Database for Combustion with Updates from Active Thermochemical Tables*. Tech. rep. Argonne National Laboratory, 2005.

[31] Butler, T. and O'Rourke, P. "A numerical method for two dimensional unsteady reacting flows". *Symposium (International) on Combustion* 16.1 (1977), pp. 1503–1515. DOI: `10.1016/S0082-0784(77)80432-3`.

[32] Butz, D., Hartl, S., Popp, S., Walther, S., Barlow, R. S., Hasse, C., Dreizler, A., and Geyer, D. "Local flame structure analysis in turbulent CH4/air flames with multi-regime characteristics". *Combustion and Flame* 210 (2019), pp. 426–438. DOI: `10.1016/j.combustflame.2019.08.032`.

[33] Bykov, V. and Maas, U. "The extension of the ILDM concept to reaction–diffusion manifolds". *Combustion Theory and Modelling* 11.6 (2007), pp. 839–862. DOI: `10.1080/13647830701242531`.

[34] Cao, R. and Pope, S. "The influence of chemical mechanisms on PDF calculations of nonpremixed piloted jet flames". *Combustion and Flame* 143.4 (2005), pp. 450–470. DOI: `10.1016/j.combustflame.2005.08.018`.

[35] Cao, R. R., Pope, S. B., and Masri, A. R. "Turbulent lifted flames in a vitiated coflow investigated using joint PDF calculations". *Combustion and Flame* 142.4 (2005), pp. 438–453. DOI: `10.1016/j.combustflame.2005.04.005`.

[36] Cao, R. R., Wang, H., and Pope, S. B. "The effect of mixing models in PDF calculations of piloted jet flames". *Proceedings of the Combustion Institute* 31.1 (2007), pp. 1543–1550. DOI: `10.1016/j.proci.2006.08.052`.

[37] Celis, C. and Figueira da Silva, L. F. "Lagrangian Mixing Models for Turbulent Combustion: Review and Prospects". *Flow, Turbulence and Combustion* 94.3 (2015), pp. 643–689. DOI: `10.1007/s10494-015-9597-1`.

[38] Chen, Z. X., Doan, N. A. K., Ruan, S., Langella, I., and Swaminathan, N. "A-priori investigation of subgrid correlation of mixture fraction and progress variable in partially premixed flames". *Combustion Theory and Modelling* 22.5 (2018), pp. 862–882. DOI: `10.1080/13647830.2018.1459862`.

[39] Choi, H. and Moin, P. "Grid-point requirements for large eddy simulation: Chapman's estimates revisited". *Physics of Fluids* 24.1 (2012), p. 011702. DOI: `10.1063/1.3676783`.

[40] Cleary, M. J. and Klimenko, A. Y. "A Generalised Multiple Mapping Conditioning Approach for Turbulent Combustion". *Flow, Turbulence and Combustion* 82.4 (2009), pp. 477–491. DOI: `10.1007/s10494-008-9161-3`.

[41] Colin, O., Ducros, F., Veynante, D., and Poinsot, T. "A thickened flame model for large eddy simulations of turbulent premixed combustion". *Physics of Fluids* 12.7 (2000), pp. 1843–1863. DOI: `10.1063/1.870436`.

[42] Colucci, P. J., Jaberi, F. A., Givi, P., and Pope, S. B. "Filtered density function for large eddy simulation of turbulent reacting flows". *Physics of Fluids* 10.2 (1998), pp. 499–515. DOI: `10.1063/1.869537`.

[43] Cuenot, B. and Poinsot, T. "Effects of curvature and unsteadiness in diffusion flames. Implications for turbulent diffusion combustion". *Symposium (International) on Combustion* 25.1 (1994), pp. 1383–1390. DOI: `10.1016/S0082-0784(06)80781-2`.

[44] Demtröder, W. *Experimentalphysik. Bd. 3: Atome, Moleküle und Festkörper: mit 9 Farbtafeln, 48 Tabellen, zahlreichen durchgerechneten Beispielen und 151 Übungsaufgaben mit ausführlichen Lösungen*. 4., überarb. Aufl. Springer-Lehrbuch. OCLC: 845643265. Berlin: Springer, 2010.

[45] Ditaranto, M. and Hals, J. "Combustion instabilities in sudden expansion oxy–fuel flames". *Combustion and Flame* 146.3 (2006), pp. 493–512. DOI: `10.1016/j.combustflame.2006.04.015`.

[46] Donini, A., M. Bastiaans, R. J., Oijen, J. A. van, and H. de Goey, L. P. "A 5-D Implementation of FGM for the Large Eddy Simulation of a Stratified Swirled Flame with Heat Loss in a Gas Turbine Combustor". *Flow, Turbulence and Combustion* 98.3 (2017), pp. 887–922. DOI: `10.1007/s10494-016-9777-7`.

[47] Dopazo, C. "Relaxation of initial probability density functions in the turbulent convection of scalar fields". *Physics of Fluids* 22.1 (1979), p. 20. DOI: `10.1063/1.862431`.

[48] Dopazo, C. and O'Brien, E. E. "An approach to the autoignition of a turbulent mixture". *Acta Astronautica* 1.9-10 (1974), pp. 1239–1266. DOI: `10.1016/0094-5765(74)90050-2`.

[49] T. Echekki, ed. *Turbulent combustion modeling: advances, new trends and perspectives*. Fluid mechanics and its applications 95. OCLC: 838423788. Dordrecht: Springer, 2011.

[50] Felden, A. *CANTERA Hands on*. Tech. rep. 2015.

[51] Felden, A. "Development of Analytically Reduced Chemistries (ARC) and applications in Large Eddy Simulations (LES) of turbulent combustion". PhD Thesis. Toulouse: Institut National Polytechnique de Toulouse, 2017.

[52] Ferraro, F. "Hybrid LES/conditional RANS-PDF approach for turbulent non-premixed combustion". PhD Thesis. Bundeswehr University Munich, 2017.

[53]   Ferraro, F., Ge, Y., Pfitzner, M., and Cleary, M. J. "A Fully Consistent Hybrid
        Les/Rans Conditional Transported Pdf Method for Non-premixed Reacting Flows".
        Combustion Science and Technology (2019), pp. 1–40. DOI: 10.1080/00102202.
        2019.1657849.

[54]   Ferziger, J. H. and Perić, M. *Computational Methods for Fluid Dynamics*. OCLC:
        1053826523. 1996.

[55]   Fiorina, B., Gicquel, O., Vervisch, L., Carpentier, S., and Darabiha, N. "Premixed
        turbulent combustion modeling using tabulated detailed chemistry and PDF". *Pro-
        ceedings of the Combustion Institute* 30.1 (2005), pp. 867–874. DOI: 10.1016/j.
        proci.2004.08.062.

[56]   Fiorina, B., Vicquelin, R., Auzillon, P., Darabiha, N., Gicquel, O., and Veynante, D.
        "A filtered tabulated chemistry model for LES of premixed combustion". *Combustion
        and Flame* 157.3 (2010), pp. 465–475. DOI: 10.1016/j.combustflame.2009.09.015.

[57]   Fiorina, B., Baron, R., Gicquel, O., Thevenin, D., Carpentier, S., and Darabiha,
        N. "Modelling non-adiabatic partially premixed flames using flame-prolongation of
        ILDM". *Combustion Theory and Modelling* 7.3 (2003), pp. 449–470. DOI: 10.1088/
        1364-7830/7/3/301.

[58]   Fiorina, B., Veynante, D., and Candel, S. "Modeling Combustion Chemistry in
        Large Eddy Simulation of Turbulent Flames". *Flow, Turbulence and Combustion*
        94.1 (2015), pp. 3–42. DOI: 10.1007/s10494-014-9579-8.

[59]   Flemming, F., Sadiki, A., and Janicka, J. "LES using artificial neural networks for
        chemistry representation". *Progress in Computational Fluid Dynamics, an Interna-
        tional Journal* 5.7 (2005), pp. 375–385.

[60]   Frank, G. "Reaktive Kühlfilme und Flamme-Wand-Interaktionen inRaketenbrennkam-
        mern". PhD Thesis. Universität der Bundeswehr München, 2018.

[61]   Frank, J., Barlow, R., and Lundquist, C. "Radiation and nitric oxide formation in
        turbulent non-premixed jet flames". *Proceedings of the Combustion Institute* 28.1
        (2000), pp. 447–454. DOI: 10.1016/S0082-0784(00)80242-8.

[62]   Franzelli, B., Riber, E., Gicquel, L. Y., and Poinsot, T. "Large Eddy Simulation of
        combustion instabilities in a lean partially premixed swirled flame". *Combustion and
        Flame* 159.2 (2012), pp. 621–637. DOI: 10.1016/j.combustflame.2011.08.004.

[63]   Frassoldati, A., Cuoci, A., Faravelli, T., Ranzi, E., Candusso, C., and Tolazzi, D.
        "Simplified kinetic schemes for oxy-fuel combustion". 2009, p. 15.

[64]   Fredrich, D., Jones, W., and Marquis, A. J. "The stochastic fields method applied
        to a partially premixed swirl flame with wall heat transfer". *Combustion and Flame*
        205 (2019), pp. 446–456. DOI: 10.1016/j.combustflame.2019.04.012.

[65]   Fröhlich, J. *Large Eddy Simulation turbulenter Strömungen: mit 14 Tabellen*. 1. Aufl.
        Lehrbuch Maschinenbau. OCLC: 180044459. Wiesbaden: Teubner, 2006.

[66]   Galindo, S., Salehi, F., Cleary, M., and Masri, A. "MMC-LES simulations of turbulent
        piloted flames with varying levels of inlet inhomogeneity". *Proceedings of the Com-
        bustion Institute* 36.2 (2017), pp. 1759–1766. DOI: 10.1016/j.proci.2016.07.055.

[67]   Gao, F. and O'Brien, E. E. "A large-eddy simulation scheme for turbulent reacting flows". *Physics of Fluids A: Fluid Dynamics* 5.6 (1993), pp. 1282–1284. DOI: 10.1063/1.858617.

[68]   Gardiner, C. W. and Gardiner, C. W. *Stochastic methods: a handbook for the natural and social sciences*. 4th ed. Springer series in synergetics. Berlin: Springer, 2009.

[69]   Gardiner, W. C. *Combustion Chemistry*. OCLC: 851823729. New York, NY: Springer US, 1984.

[70]   Garmory, A. and Mastorakos, E. "Capturing localised extinction in Sandia Flame F with LES–CMC". *Proceedings of the Combustion Institute* 33.1 (2011), pp. 1673–1680. DOI: 10.1016/j.proci.2010.06.065.

[71]   Garmory, A. and Mastorakos, E. "Numerical simulation of oxy-fuel jet flames using unstructured LES–CMC". *Proceedings of the Combustion Institute* 35.2 (2015), pp. 1207–1214. DOI: 10.1016/j.proci.2014.05.032.

[72]   Garmory, A. "Micromixing effects in atmospheric reacting flows". PhD Thesis. University of Cambridge, 2008.

[73]   Ge, Y., Cleary, M., and Klimenko, A. "A comparative study of Sandia flame series (D–F) using sparse-Lagrangian MMC modelling". *Proceedings of the Combustion Institute* 34.1 (2013), pp. 1325–1332. DOI: 10.1016/j.proci.2012.06.059.

[74]   Ge, Y., Hansinger, M., Traxinger, C., and Pfitzner, M. "Deep residual learning applied to real-gas thermodynamics". *International Conference of Computational Methods in Sciences and Engineering 2018*. Thessaloniki, Greece, 2018, p. 150004. DOI: 10.1063/1.5079207.

[75]   Gerlinger, P. *Numerische Verbrennungssimulation*. Berlin, Heidelberg: Springer Berlin Heidelberg, 2005. DOI: 10.1007/3-540-27535-5.

[76]   Germano, M., Piomelli, U., Moin, P., and Cabot, W. H. "A dynamic subgrid-scale eddy viscosity model". *Physics of Fluids A: Fluid Dynamics* 3.7 (1991), pp. 1760–1765. DOI: 10.1063/1.857955.

[77]   Gicquel, L., Staffelbach, G., and Poinsot, T. "Large Eddy Simulations of gaseous flames in gas turbine combustion chambers". *Progress in Energy and Combustion Science* 38.6 (2012), pp. 782–817. DOI: 10.1016/j.pecs.2012.04.004.

[78]   Gicquel, O., Darabiha, N., and Thevenin, D. "Laminar premixed hydrogen/air counterflow flame simulations using flame prolongation of ILDM with differential diffusion". *Proceedings of the Combustion Institute* 28 (2000), pp. 1901–1908.

[79]   Gierth, S., Hunger, F., Popp, S., Wu, H., Ihme, M., and Hasse, C. "Assessment of differential diffusion effects in flamelet modeling of oxy-fuel flames". *Combustion and Flame* 197 (2018), pp. 134–144. DOI: 10.1016/j.combustflame.2018.07.023.

[80]   Givi, P. "Model-free simulations of turbulent reactive flows". *Progress in Energy and Combustion Science* 15.1 (1989), pp. 1–107. DOI: 10.1016/0360-1285(89)90006-3.

[81]   Glassman, I. and Yetter, R. A. *Combustion*. 4th ed. Amsterdam ; Boston: Academic Press, 2008.

[82]   Goodwin, D. G., Moffat, H. K., and Speth, R. L. *Cantera: An Object-Oriented Software Toolkit For Chemical Kinetics, Thermodynamics, And Transport Processes. Version 2.3.0*. 2017. DOI: 10.5281/zenodo.170284.

[83] Göttgens, J., Mauss, F., and Peters, N. "Analytic approximations of burning velocities and flame thicknesses of lean hydrogen, methane, ethylene, ethane, acetylene, and propane flames". *Symposium (International) on Combustion* 24.1 (1992), pp. 129–135. DOI: `10.1016/S0082-0784(06)80020-2`.

[84] Gottiparthi, K. C., Sankaran, R., Ruiz, A. M., Lacaze, G., and Oefelein, J. C. "Large Eddy Simulation of a Supercritical Fuel Jet in Cross Flow using GPU-Acceleration". *54th AIAA Aerospace Sciences Meeting*. San Diego, California, USA: American Institute of Aeronautics and Astronautics, 2016. DOI: `10.2514/6.2016-1939`.

[85] Greenshields, C. *OpenFOAM User Guide*. User Guide. OpenFOAM Foundation Ltd., 2020.

[86] Gu, X., Haq, M., Lawes, M., and Woolley, R. "Laminar burning velocity and Markstein lengths of methane–air mixtures". *Combustion and Flame* 121.1-2 (2000), pp. 41–58. DOI: `10.1016/S0010-2180(99)00142-X`.

[87] Han, W., Raman, V., and Chen, Z. "LES/PDF modeling of autoignition in a lifted turbulent flame: Analysis of flame sensitivity to differential diffusion and scalar mixing time-scale". *Combustion and Flame* 171 (2016), pp. 69–86. DOI: `10.1016/j.combustflame.2016.05.027`.

[88] Hansinger, M., Müller, H., and Pfitzner, M. "Comparison of Premixed and Non-Premixed Manifold Representations in the LES of a Piloted Jet Flame with Inhomogeneous Inlets". *8th European Combustion Meeting*. Dubrovnik, Croatia, 2017.

[89] Hansinger, M., Zips, J., and Pfitzner, M. "Eulerian Stochastic Fields method and model free finite rate chemistry applied to Sydney partially premixed flame". *9th European Combustion Meeting*. Lisbon, Portugal, 2019.

[90] Hansinger, M., Ge, Y., and Pfitzner, M. "Deep residual networks for flamelet/progress variable tabulation method in combustion LES". *29. Deutscher Flammentag*. Bochum, 2019.

[91] Hansinger, M., Ge, Y., and Pfitzner, M. "Deep residual networks for flamelet/progress variable tabulation with application to a piloted flame with inhomogeneous inlet". *Combustion Science and Technology* (2020). DOI: `10.1080/00102202.2020.1822826`.

[92] Hansinger, M., Pfitzner, M., and Klein, M. "Statistical Analysis and Verification of a New Premixed Combustion Model with DNS Data". *Combustion Science and Technology* (2020), pp. 1–22. DOI: `10.1080/00102202.2020.1781833`.

[93] Hansinger, M., Pfitzner, M., and Sabelnikov, V. "LES of oxy–fuel jet flames using the Eulerian Stochastic Fields method with differential diffusion". *Proceedings of the Combustion Institute* (2020). DOI: `10.1016/j.proci.2020.06.206`.

[94] Hansinger, M., Zirwes, T., Zips, J., Pfitzner, M., Zhang, F., Habisreuther, P., and Bockhorn, H. "The Eulerian Stochastic Fields Method Applied to Large Eddy Simulations of a Piloted Flame with Inhomogeneous Inlet". *Flow, Turbulence and Combustion* 105.3 (2020), pp. 837–867. DOI: `10.1007/s10494-020-00159-5`.

[95] Haworth, D. "Progress in probability density function methods for turbulent reacting flows". *Progress in Energy and Combustion Science* 36.2 (2010), pp. 168–259. DOI: `10.1016/j.pecs.2009.09.003`.

[96] He, K., Zhang, X., Ren, S., and Sun, J. "Deep Residual Learning for Image Recognition". *Proceedings of the IEEE Conference on Computer Vision and Pattern Recognition (CVPR)* (2016). arXiv: 1512.03385, pp. 770–778.

[97] Hegetschweiler, M., Zoller, B. T., and Jenny, P. "Reactive parametrized scalar profiles (R-PSP) mixing model for partially premixed combustion". *Combustion and Flame* 159.2 (2012), pp. 734–747. DOI: `10.1016/j.combustflame.2011.08.018`.

[98] Heil, P., Toporov, D., Förster, M., and Kneer, R. "Experimental investigation on the effect of O2 and CO2 on burning rates during oxyfuel combustion of methane". *Proceedings of the Combustion Institute* 33.2 (2011), pp. 3407–3413. DOI: `10.1016/j.proci.2010.05.047`.

[99] Hirschfelder, J. O., Curtiss, C. F., and Bird, R. B. *Molecular theory of gases and liquids*. Corr. print. with notes added. Structure of matter series. OCLC: 70387122. New York,NY: Wiley, 1964.

[100] Hodzic, E., Jangi, M., Szasz, R.-Z., and Bai, X.-S. "Large eddy simulation of bluff body flames close to blow-off using an Eulerian stochastic field method". *Combustion and Flame* 181 (2017), pp. 1–15. DOI: `10.1016/j.combustflame.2017.03.010`.

[101] IEA. *World Energy Outlook*. Tech. rep. Paris: International Energy Agency, 2019.

[102] Ihme, M., Cha, C. M., and Pitsch, H. "Prediction of local extinction and re-ignition effects in non-premixed turbulent combustion using a flamelet/progress variable approach". *Proceedings of the Combustion Institute* 30.1 (2005), pp. 793–800. DOI: `10.1016/j.proci.2004.08.260`.

[103] Ihme, M. and Pitsch, H. "Prediction of extinction and reignition in nonpremixed turbulent flames using a flamelet/progress variable model". *Combustion and Flame* 155.1-2 (2008), pp. 70–89. DOI: `10.1016/j.combustflame.2008.04.001`.

[104] Ihme, M. and Pitsch, H. "Prediction of extinction and reignition in nonpremixed turbulent flames using a flamelet/progress variable model.2. Application in LES of Sandia flames D and E". *Combustion and Flame* (2008), p. 18.

[105] Ihme, M., Schmitt, C., and Pitsch, H. "Optimal artificial neural networks and tabulation methods for chemistry representation in LES of a bluff-body swirl-stabilized flame". *Proceedings of the Combustion Institute* 32.1 (2009), pp. 1527–1535. DOI: `10.1016/j.proci.2008.06.100`.

[106] Ihme, M. and See, Y. C. "Prediction of autoignition in a lifted methane/air flame using an unsteady flamelet/progress variable model". *Combustion and Flame* 157.10 (2010), pp. 1850–1862. DOI: `10.1016/j.combustflame.2010.07.015`.

[107] Ihme, M., Shunn, L., and Zhang, J. "Regularization of reaction progress variable for application to flamelet-based combustion models". *Journal of Computational Physics* 231.23 (2012), pp. 7715–7721. DOI: `10.1016/j.jcp.2012.06.029`.

[108] IPCC. *Summary for Policymakers: Global Warming of 1.5°C. An IPCC Special Report on the impacts of global warming of 1.5°C above pre-industrial levels and related global greenhouse gas emission pathways, in the context of strengthening the global response to the threat of climate change, sustainable development, and efforts to eradicate poverty*. Tech. rep. Intergovernmental Panel on Climate Change, 2018.

[109]   Issa, R., Ahmadi-Befrui, B., Beshay, K., and Gosman, A. "Solution of the implicitly discretised reacting flow equations by operator-splitting". *Journal of Computational Physics* 93.2 (1991), pp. 388–410. DOI: 10.1016/0021-9991(91)90191-M.

[110]   Jaberi, F. A., Colucci, P. J., James, S., Givi, P., and Pope, S. B. "Filtered mass density function for large-eddy simulation of turbulent reacting flows". *Journal of Fluid Mechanics* 401 (1999), pp. 85–121.

[111]   James, S., Zhu, J., and Anand, M. "Large eddy simulations of turbulent flames using the filtered density function model". *Proceedings of the Combustion Institute* 31.2 (2007), pp. 1737–1745. DOI: 10.1016/j.proci.2006.07.160.

[112]   Janicka, J., Kolbe, W., and Kollmann, W. "Closure of the transport equation for the probability density function of turbulent scalar fields". *J. Non-Equilib. Thermodyn* 4 (1977), pp. 47–66.

[113]   Jasak, H. "Error Analysis and Estimation for the Finite Volume Method with Applications to Fluid Flows". PhD thesis. Imperial College London, 1996.

[114]   Jiménez, J., Liñán, A., Rogers, M. M., and Higuera, F. J. "A-priori testing of subgrid models for chemically reacting non-premixed turbulent shear flows". *Journal of Fluid Mechanics* 349 (1997), pp. 149–171. DOI: 10.1017/S0022112097006733.

[115]   Johnson, R., Wu, H., and Ihme, M. "A general probabilistic approach for the quantitative assessment of LES combustion models". *Combustion and Flame* 183 (2017), pp. 88–101. DOI: 10.1016/j.combustflame.2017.05.004.

[116]   Jones, E. "Combustion of Methane". *Nature* 178.4542 (1956), pp. 1112–1112. DOI: 10.1038/1781112a0.

[117]   Jones, W. and Kakhi, M. "Pdf Modeling of Finite-rate Chemistry Effects in Turbulent Nonpremixed Jet Flames". *Combustion and Flame* 115.1-2 (1998), pp. 210–229. DOI: 10.1016/S0010-2180(98)00002-9.

[118]   Jones, W. and Lindstedt, R. "Global reaction schemes for hydrocarbon combustion". *Combustion and Flame* 73.3 (1988), pp. 233–249. DOI: 10.1016/0010-2180(88)90021-1.

[119]   Jones, W., Marquis, A., and Prasad, V. "LES of a turbulent premixed swirl burner using the Eulerian stochastic field method". *Combustion and Flame* 159.10 (2012), pp. 3079–3095. DOI: 10.1016/j.combustflame.2012.04.008.

[120]   Jones, W. and Navarro-Martinez, S. "Study of hydrogen auto-ignition in a turbulent air co-flow using a Large Eddy Simulation approach". *Computers & Fluids* 37.7 (2008), pp. 802–808. DOI: 10.1016/j.compfluid.2007.02.015.

[121]   Jones, W., Navarro-Martinez, S., and Röhl, O. "Large eddy simulation of hydrogen auto-ignition with a probability density function method". *Proceedings of the Combustion Institute* 31.2 (2007), pp. 1765–1771. DOI: 10.1016/j.proci.2006.07.041.

[122]   Jones, W. and Prasad, V. "Large Eddy Simulation of the Sandia Flame Series (D–F) using the Eulerian stochastic field method". *Combustion and Flame* 157.9 (2010), pp. 1621–1636. DOI: 10.1016/j.combustflame.2010.05.010.

[123]   Jones, W. and Prasad, V. "LES-pdf simulation of a spark ignited turbulent methane jet". *Proceedings of the Combustion Institute* 33.1 (2011), pp. 1355–1363. DOI: 10.1016/j.proci.2010.06.076.

[124] Karpetis, A. and Barlow, R. "Measurements of scalar dissipation in a turbulent piloted methane/air jet flame". *Proceedings of the Combustion Institute* 29.2 (2002), pp. 1929–1936. DOI: 10.1016/S1540-7489(02)80234-6.

[125] Kee, R. J., Coltrin, M. E., and Glarborg, P. *Chemically reacting flow: theory and practice*. Hoboken, N.J: Wiley-Interscience, 2003.

[126] Kemenov, K. A., Wang, H., and Pope, S. B. "Modelling effects of subgrid-scale mixture fraction variance in LES of a piloted diffusion flame". *Combustion Theory and Modelling* 16.4 (2012), pp. 611–638. DOI: 10.1080/13647830.2011.645881.

[127] Keppeler, R. "Entwicklung und Evaluierung von Verbrennungsmodellen für die Large Eddy Simulation der Hochdruck-Vormischverbrennung". PhD Thesis. Universität der Bundeswehr München, 2013.

[128] Keppeler, R., Tangermann, E., Allaudin, U., and Pfitzner, M. "LES of Low to High Turbulent Combustion in an Elevated Pressure Environment". *Flow, Turbulence and Combustion* 92.3 (2014), pp. 767–802. DOI: 10.1007/s10494-013-9525-1.

[129] Kim, T. and Kim, Y. "Interactive transient flamelet modeling for soot formation and oxidation processes in laminar non-premixed jet flames". *Combustion and Flame* 162.5 (2015), pp. 1660–1678. DOI: 10.1016/j.combustflame.2014.11.029.

[130] Klein, M., Nachtigal, H., Hansinger, M., Pfitzner, M., and Chakraborty, N. "Flame Curvature Distribution in High Pressure Turbulent Bunsen Premixed Flames". *Flow, Turbulence and Combustion* 101.4 (2018), pp. 1173–1187. DOI: 10.1007/s10494-018-9951-1.

[131] Klein, M., Sadiki, A., and Janicka, J. "A digital filter based generation of inflow data for spatially developing direct numerical or large eddy simulations". *Journal of Computational Physics* 186.2 (2003), pp. 652–665. DOI: 10.1016/S0021-9991(03)00090-1.

[132] Kleinheinz, K., Kubis, T., Trisjono, P., Bode, M., and Pitsch, H. "Computational study of flame characteristics of a turbulent piloted jet burner with inhomogeneous inlets". *Proceedings of the Combustion Institute* 36.2 (2017), pp. 1747–1757. DOI: 10.1016/j.proci.2016.07.067.

[133] Klimenko, A. Y. and Bilger, R. W. "Conditional moment closure for turbulent combustion". *Progress in Energy and Combustion Science* (1999), p. 93.

[134] Klimenko, A. Y. "Multicomponent diffusion of various admixtures in turbulent flow". *Fluid Dynamics* 25.3 (1990), pp. 327–334. DOI: 10.1007/BF01049811.

[135] Knudsen, E., Richardson, E. S., Doran, E. M., Pitsch, H., and Chen, J. H. "Modeling scalar dissipation and scalar variance in large eddy simulation: Algebraic and transport equation closures". *Physics of Fluids* 24.5 (2012), p. 055103. DOI: 10.1063/1.4711369.

[136] Kobayashi, H., Tamura, T., Maruta, K., Niioka, T., and Williams, F. A. "Burning velocity of turbulent premixed flames in a high-pressure environment". *Symposium (International) on Combustion* 26.1 (1996), pp. 389–396. DOI: 10.1016/S0082-0784(96)80240-2.

[137] Kolmogorov, A. N. "The Local Structure of Turbulence in Incompressible Viscous Fluid for Very Large Reynolds Numbers". *Dokl. Akad. Nauk. SSSR* 30.4 (1941), pp. 299–303.

[138] Kronenburg, A. and Papoutsakis, A. "Conditional moment closure modeling of extinction and re-ignition in turbulent non-premixed flames". *Proceedings of the Combustion Institute* 30.1 (2005), pp. 759–766. DOI: 10.1016/j.proci.2004.08.235.

[139] Kronenburg, A. and Stein, O. T. "LES-CMC of a Partially Premixed, Turbulent Dimethyl Ether Jet Diffusion Flame". *Flow, Turbulence and Combustion* 98.3 (2017), pp. 803–816. DOI: 10.1007/s10494-016-9788-4.

[140] Kronenburg, A. and Kostka, M. "Modeling extinction and reignition in turbulent flames". *Combustion and Flame* 143.4 (2005), pp. 342–356. DOI: 10.1016/j.combustflame.2005.08.021.

[141] Kuenne, G., Ketelheun, A., and Janicka, J. "LES modeling of premixed combustion using a thickened flame approach coupled with FGM tabulated chemistry". *Combustion and Flame* 158.9 (2011), pp. 1750–1767. DOI: 10.1016/j.combustflame.2011.01.005.

[142] Kuenne, G., Seffrin, F., Fuest, F., Stahler, T., Ketelheun, A., Geyer, D., Janicka, J., and Dreizler, A. "Experimental and numerical analysis of a lean premixed stratified burner using 1D Raman/Rayleigh scattering and large eddy simulation". *Combustion and Flame* 159.8 (2012), pp. 2669–2689. DOI: 10.1016/j.combustflame.2012.02.010.

[143] Kuo, K. K. and Acharya, R. *Fundamentals of Turbulent and Multiphase Combustion: Kuo/Fundamentals of Turbulent Multi-Phase Combustion.* Hoboken, NJ, USA: John Wiley & Sons, Inc., 2012. DOI: 10.1002/9781118107683.

[144] Kuron, M., Ren, Z., Hawkes, E. R., Zhou, H., Kolla, H., Chen, J. H., and Lu, T. "A mixing timescale model for TPDF simulations of turbulent premixed flames". *Combustion and Flame* 177 (2017), pp. 171–183. DOI: 10.1016/j.combustflame.2016.12.011.

[145] Lamouroux, J., Ihme, M., Fiorina, B., and Gicquel, O. "Tabulated chemistry approach for diluted combustion regimes with internal recirculation and heat losses". *Combustion and Flame* 161.8 (2014), pp. 2120–2136. DOI: 10.1016/j.combustflame.2014.01.015.

[146] Lampmann, A., Hansinger, M., and Pfitzner, M. "Artificially thickened flame vs. Eulerian stochastic fields combustion models applied to a turbulent partially-premixed flame". *29. Deutscher Flammentag.* Bochum, 2019.

[147] Lampmann, A., Hansinger, M., and Pfitzner, M. "Comparison of LES combustion models for turbulent premixed flames at atmospheric pressures". *9th European Combustion Meeting.* Lisbon, Portugal, 2019.

[148] Law, C., Makino, A., and Lu, T. "On the off-stoichiometric peaking of adiabatic flame temperature". *Combustion and Flame* 145.4 (2006), pp. 808–819. DOI: 10.1016/j.combustflame.2006.01.009.

[149] Lawrence Livermore National Laboratory. *SUNDIALS: SUite of Nonlinear and DIfferential/ALgebraic Equation Solvers.* https://computing.llnl.gov/projects/sundials.

[150] Leer, B. van. "Towards the ultimate conservative difference scheme. II. Monotonicity and conservation combined in a second-order scheme". *Journal of Computational Physics* 14.4 (1974), pp. 361–370. DOI: 10.1016/0021-9991(74)90019-9.

[151]   Leonard, A. "Energy Cascade in Large-Eddy Simulations of Turbulent Fluid Flows". *Advances in Geophysics*. Vol. 18. Elsevier, 1975, pp. 237–248. DOI: 10.1016/S0065-2687(08)60464-1.

[152]   Lessani, B. and Papalexandris, M. V. "Time-accurate calculation of variable density flows with strong temperature gradients and combustion". *Journal of Computational Physics* 212.1 (2006), pp. 218–246. DOI: 10.1016/j.jcp.2005.07.001.

[153]   Li, S., Xu, Y., and Gao, Q. "Measurements and modelling of oxy-fuel coal combustion". *Proceedings of the Combustion Institute* 37.3 (2019), pp. 2643–2661. DOI: 10.1016/j.proci.2018.08.054.

[154]   Liang, Y., Pope, S. B., and Pepiot, P. "A pre-partitioned adaptive chemistry methodology for the efficient implementation of combustion chemistry in particle PDF methods". *Combustion and Flame* 162.9 (2015), pp. 3236–3253. DOI: 10.1016/j.combustflame.2015.05.012.

[155]   Lindstedt, R. and Vaos, E. "Transported PDF modeling of high-Reynolds-number premixed turbulent flames". *Combustion and Flame* 145.3 (2006), pp. 495–511. DOI: 10.1016/j.combustflame.2005.12.015.

[156]   Ling, J., Rossi, R., and Eaton, J. K. "Near wall modeling for trailing edge slot film cooling". *Journal of Fluids Engineering* 137.2 (2015), p. 021103.

[157]   Lipatnikov, A. N. "Stratified turbulent flames: Recent advances in understanding the influence of mixture inhomogeneities on premixed combustion and modeling challenges". *Progress in Energy and Combustion Science* 62 (2017), pp. 87–132. DOI: 10.1016/j.pecs.2017.05.001.

[158]   Lu, T., Ju, Y., and Law, C. K. "Complex CSP for chemistry reduction and analysis". *Combustion and Flame* 126.1 (2001), pp. 1445–1455.

[159]   Lu, T. and Law, C. K. "A criterion based on computational singular perturbation for the identification of quasi steady state species: A reduced mechanism for methane oxidation with NO chemistry". *Combustion and Flame* 154.4 (2008), pp. 761–774. DOI: 10.1016/j.combustflame.2008.04.025.

[160]   Lu, T. and Law, C. K. "A directed relation graph method for mechanism reduction". *Proceedings of the Combustion Institute* 30.1 (2005), pp. 1333–1341. DOI: 10.1016/j.proci.2004.08.145.

[161]   Lu, T. and Law, C. K. "Toward accommodating realistic fuel chemistry in large-scale computations". *Progress in Energy and Combustion Science* 35.2 (2009), pp. 192–215. DOI: 10.1016/j.pecs.2008.10.002.

[162]   Ma, P. C., Wu, H., Ihme, M., and Hickey, J.-P. "A Flamelet Model with Heat-Loss Effects for Predicting Wall-Heat Transfer in Rocket Engines". American Institute of Aeronautics and Astronautics, 2017. DOI: 10.2514/6.2017-4856.

[163]   Ma, P. C., Wu, H., Labahn, J. W., Jaravel, T., and Ihme, M. "Analysis of transient blow-out dynamics in a swirl-stabilized combustor using large-eddy simulations". *Proceedings of the Combustion Institute* 37.4 (2019), pp. 5073–5082. DOI: 10.1016/j.proci.2018.06.066.

[164]   Maas, U. and Pope, S. "Implementation of simplified chemical kinetics based on intrinsic low-dimensional manifolds". *Symposium (International) on Combustion* 24.1 (1992), pp. 103–112. DOI: 10.1016/S0082-0784(06)80017-2.

[165]   Maas, U. and Pope, S. B. "Simplifying chemical kinetics: intrinsic low-dimensional manifolds in composition space". *Combustion and flame* 88.3 (1992), pp. 239–264.

[166]   Mahmoud, R., Jangi, M., Fiorina, B., Pfitzner, M., and Sadiki, A. "Numerical Investigation of an Oxyfuel Non-Premixed Combustion Using a Hybrid Eulerian Stochastic Field/Flamelet Progress Variable Approach: Effects of H2/CO2 Enrichment and Reynolds Number". *Energies* 11.11 (2018), p. 3158. DOI: `10.3390/en11113158`.

[167]   Mahmoud, R., Jangi, M., Ries, F., Fiorina, B., Janicka, J., and Sadiki, A. "Combustion Characteristics of a Non-Premixed Oxy-Flame Applying a Hybrid Filtered Eulerian Stochastic Field/Flamelet Progress Variable Approach". *Applied Sciences* 9.7 (2019), p. 1320. DOI: `10.3390/app9071320`.

[168]   Maio, G., Cailler, M., Fiorina, B., Mercier, R., and Moureau, V. "LES modeling of piloted jet flames with inhomogeneous inlets using tabulated chemistry methods". American Institute of Aeronautics and Astronautics, 2017. DOI: `10.2514/6.2017-1471`.

[169]   Mallasto, A. and Feragen, A. "Learning from uncertain curves: The 2-Wasserstein metric for Gaussian processes". *31st Conference on Neural Information Processing Systems*. Long Beach, CA, USA, 2017.

[170]   Masri, A. "Partial premixing and stratification in turbulent flames". *Proceedings of the Combustion Institute* 35.2 (2015), pp. 1115–1136. DOI: `10.1016/j.proci.2014.08.032`.

[171]   Masri, A., Dibble, R., and Barlow, R. "The structure of turbulent nonpremixed flames revealed by Raman-Rayleigh-LIF measurements". *Progress in Energy and Combustion Science* 22.4 (1996), pp. 307–362. DOI: `10.1016/S0360-1285(96)00009-3`.

[172]   McDermott, R. and Pope, S. "A particle formulation for treating differential diffusion in filtered density function methods". *Journal of Computational Physics* 226.1 (2007), pp. 947–993. DOI: `10.1016/j.jcp.2007.05.006`.

[173]   Meares, S., Prasad, V., Magnotti, G., Barlow, R., and Masri, A. "Stabilization of piloted turbulent flames with inhomogeneous inlets". *Proceedings of the Combustion Institute* 35.2 (2015), pp. 1477–1484. DOI: `10.1016/j.proci.2014.05.071`.

[174]   Meares, S. and Masri, A. R. "A modified piloted burner for stabilizing turbulent flames of inhomogeneous mixtures". *Combustion and Flame* 161.2 (2014), pp. 484–495. DOI: `10.1016/j.combustflame.2013.09.016`.

[175]   Meier, W., Weigand, P., Duan, X., and Giezendannerthoben, R. "Detailed characterization of the dynamics of thermoacoustic pulsations in a lean premixed swirl flame". *Combustion and Flame* 150.1-2 (2007), pp. 2–26. DOI: `10.1016/j.combustflame.2007.04.002`.

[176]   Mercier, R., Auzillon, P., Moureau, V., Darabiha, N., Gicquel, O., Veynante, D., and Fiorina, B. "LES Modeling of the Impact of Heat Losses and Differential Diffusion on Turbulent Stratified Flame Propagation: Application to the TU Darmstadt Stratified Flame". *Flow, Turbulence and Combustion* 93.2 (2014), pp. 349–381. DOI: `10.1007/s10494-014-9550-8`.

[177]   Messig, D., Hunger, F., Keller, J., and Hasse, C. "Evaluation of radiation modeling approaches for non-premixed flamelets considering a laminar methane air flame". *Combustion and Flame* 160.2 (2013), pp. 251–264. DOI: 10.1016/j.combustflame. 2012.10.009.

[178]   Meyer, D. W. and Jenny, P. "A mixing model for turbulent flows based on parameterized scalar profiles". *Physics of Fluids* 18.3 (2006), p. 035105. DOI: 10.1063/1. 2182005.

[179]   Mitarai, S., Riley, J. J., and Kosály, G. "Testing of mixing models for Monte Carlo probability density function simulations". *Physics of Fluids* 17.4 (2005), p. 047101. DOI: 10.1063/1.1863319.

[180]   Mueller, M. E. and Pitsch, H. "LES model for sooting turbulent nonpremixed flames". *Combustion and Flame* 159.6 (2012), pp. 2166–2180. DOI: 10.1016/j.combustflame. 2012.02.001.

[181]   Müller, H. "Simulation turbulenter nicht-vorgemischterVerbrennung bei überkritischen Drücken". PhD Thesis. Universität der Bundeswehr München, 2016.

[182]   Müller, H., Hansinger, M., and Pfitzner, M. "Large Eddy Simulation einer turbulenten LOx/GCH 4 Flamme unter Verwendung der Eulerian Stochastic Fields Methode Large eddy simulation of a turbulent LOx/GCH 4 flame using the Eulerian stochastic field method". *28. Deutscher Flammentag*. Darmstadt, 2017.

[183]   Müller, H., Zips, J., Pfitzner, M., Maestro, D., Cuenot, B., Menon, S., Ranjan, R., Tudisco, P., and Selle, L. "Numerical Investigation of Flow and Combustion in a Single-Element GCH4/GOX Rocket Combustor: A comparative LES study". *52nd AIAA/SAE/ASEE Joint Propulsion Conference*. Salt Lake City, UT: American Institute of Aeronautics and Astronautics, 2016. DOI: 10.2514/6.2016-4997.

[184]   Munson, B. R., Young, D. F., and Okiishi, T. H. *Fundamentals of fluid mechanics*. 5th ed. Hoboken, NJ: J. Wiley & Sons, 2006.

[185]   Muradoglu, M. "PDF modeling of a bluff-body stabilized turbulent flame". *Combustion and Flame* 132.1-2 (2003), pp. 115–137. DOI: 10.1016/S0010-2180(02)00430-3.

[186]   Muradoglu, M., Pope, S. B., and Caughey, D. A. "The Hybrid Method for the PDF Equations of Turbulent Reactive Flows: Consistency Conditions and Correction Algorithms". *Journal of Computational Physics* 172.2 (2001), pp. 841–878. DOI: 10.1006/jcph.2001.6861.

[187]   Mustata, R., Valiño, L., Jiménez, C., Jones, W., and Bondi, S. "A probability density function Eulerian Monte Carlo field method for large eddy simulations: Application to a turbulent piloted methane/air diffusion flame (Sandia D)". *Combustion and Flame* 145.1-2 (2006), pp. 88–104. DOI: 10.1016/j.combustflame.2005.12.002.

[188]   Navarro-Martinez, S. and Kronenburg, A. "LES-CMC simulations of a turbulent bluff-body flame". *Proceedings of the Combustion Institute* 31.2 (2007), pp. 1721–1728. DOI: 10.1016/j.proci.2006.07.212.

[189]   Navarro-Martinez, S. and Kronenburg, A. "LES–CMC simulations of a lifted methane flame". *Proceedings of the Combustion Institute* 32.1 (2009), pp. 1509–1516. DOI: 10.1016/j.proci.2008.06.178.

[190] Navarro-Martinez, S., Kronenburg, A., and Mare, F. D. "Conditional Moment Closure for Large Eddy Simulations". *Flow, Turbulence and Combustion* 75.1-4 (2005), pp. 245–274. DOI: 10.1007/s10494-005-8580-7.

[191] Nicoud, F. and Ducros, F. "Subgrid-Scale Stress Modelling Based on the Square of the Velocity Gradient Tensor". *Flow turbulence and Combustion* 62 (1999), pp. 183–200.

[192] Oh, J. H., Pouryahya, M., Iyer, A., Apte, A. P., Tannenbaum, A., and Deasy, J. O. "Kernel Wasserstein Distance". *Computers in Biology and Medicine* 120 (2020). arXiv: 1905.09314, p. 103731. DOI: 10.1016/j.compbiomed.2020.103731.

[193] Oijen, J. V. and Goey, L. D. "Modelling of Premixed Laminar Flames using Flamelet-Generated Manifolds". *Combustion Science and Technology* 161.1 (2000), pp. 113–137. DOI: 10.1080/00102200008935814.

[194] Oijen, J. van, Donini, A., Bastiaans, R., Thije Boonkkamp, J. ten, and Goey, L. de. "State-of-the-art in premixed combustion modeling using flamelet generated manifolds". *Progress in Energy and Combustion Science* 57 (2016), pp. 30–74. DOI: 10.1016/j.pecs.2016.07.001.

[195] Ourliac, M., Sabel'nikov, V., and Soulard, O. "A hybrid conservative Eulerian (Field) Monte Carlo algorithm for the solving composition PDF transport equation in turbulent reacting flows". *ICHMT DIGITAL LIBRARY ONLINE*. Begel House Inc., 2009.

[196] R. K. Pachauri, L. Mayer, and I. P. on Climate Change, eds. *Climate change 2014: synthesis report*. OCLC: 914851124. Geneva, Switzerland: Intergovernmental Panel on Climate Change, 2015.

[197] Panaretos, V. M. and Zemel, Y. "Statistical Aspects of Wasserstein Distances". *Annu. Rev. Stat. Appl.* 6.1 (2019). arXiv: 1806.05500, pp. 405–431. DOI: 10.1146/annurev-statistics-030718-104938.

[198] Pele, O. and Werman, M. "Fast and robust Earth Mover's Distances". *2009 IEEE 12th International Conference on Computer Vision*. Kyoto: IEEE, 2009, pp. 460–467. DOI: 10.1109/ICCV.2009.5459199.

[199] Perry, B. A. and Mueller, M. E. "Effect of multiscalar subfilter PDF models in LES of turbulent flames with inhomogeneous inlets". *Proceedings of the Combustion Institute* 37.2 (2019), pp. 2287–2295. DOI: 10.1016/j.proci.2018.07.116.

[200] Perry, B. A., Mueller, M. E., and Masri, A. R. "A two mixture fraction flamelet model for large eddy simulation of turbulent flames with inhomogeneous inlets". *Proceedings of the Combustion Institute* 36.2 (2017), pp. 1767–1775. DOI: 10.1016/j.proci.2016.07.029.

[201] Peters, N. "Laminar diffusion flamelet models in non-premixed turbulent combustion". *Progress in Energy and Combustion Science* 10.3 (1984), pp. 319–339. DOI: 10.1016/0360-1285(84)90114-X.

[202] Peters, N. "Laminar flamelet concepts in turbulent combustion". *Symposium (International) on Combustion* 21.1 (1988), pp. 1231–1250. DOI: 10.1016/S0082-0784(88)80355-2.

[203] Peters, N. "Multiscale combustion and turbulence". *Proceedings of the Combustion Institute* 32.1 (2009), pp. 1–25. DOI: 10.1016/j.proci.2008.07.044.

[204] Peters, N. "The turbulent burning velocity for large-scale and small-scale turbulence". *Journal of Fluid Mechanics* 384 (1999), pp. 107–132. DOI: 10.1017/S0022112098004212.

[205] Peters, N. *Turbulent Combustion*. Cambridge University Press, 2000.

[206] Peyré, G. and Cuturi, M. "Computational Optimal Transport". *arXiv:1803.00567 [stat]* (2020). arXiv: 1803.00567.

[207] Picciani, M. A., Richardson, E. S., and Navarro-Martinez, S. "A Thickened Stochastic Fields Approach for Turbulent Combustion Simulation". *Flow, Turbulence and Combustion* 101.4 (2018), pp. 1119–1136. DOI: 10.1007/s10494-018-9954-y.

[208] Picciani, M. A., Richardson, E. S., and Navarro-Martinez, S. "Resolution Requirements in Stochastic Field Simulation of Turbulent Premixed Flames". *Flow, Turbulence and Combustion* (2018). DOI: 10.1007/s10494-018-9953-z.

[209] Pierce, C. D. and Moin, P. "Progress-variable approach for large-eddy simulation of non-premixed turbulent combustion". *Journal of Fluid Mechanics* 504 (2004), pp. 73–97. DOI: 10.1017/S0022112004008213.

[210] Pierce, C. D. "Progress-Variable Approach for Large Eddy Simulation of Turbulent Combustion". PhD Thesis. Stanford University, 2001.

[211] Piomelli, U. "Large-eddy simulation of turbulent flows". *Large Eddy Simulation: Theory and Simulations*. Rhode St. Genesius, Belgium: von Karman Institute for Fluid Dynamics, 2016.

[212] Pitsch, H. and Peters, N. "A Consistent Flamelet Formulation for Non-Premixed Combustion Considering Differential Diffusion Effects". *Combustion and Flame* 114.1-2 (1998), pp. 26–40. DOI: 10.1016/S0010-2180(97)00278-2.

[213] Pitsch, H. and Steiner, H. "Large-eddy simulation of a turbulent piloted methane/air diffusion flame (Sandia flame D)". *Physics of Fluids* 12.10 (2000), p. 2541. DOI: 10.1063/1.1288493.

[214] Pitsch, H. *FlameMaster*. https://www.itv.rwth-aachen.de/index.php?id=flamemaster.

[215] Pitsch, H. "Large-eddy simulation of turbulent combustion". *Annu. Rev. Fluid Mech.* 38 (2006), pp. 453–482.

[216] Pohl, S. "Numerische Untersuchung von Verbrennungsprozessen in Raketenbrennkammern und Gasturbinen". PhD Thesis. Universität der Bundeswehr München, 2016.

[217] Poinsot, T. and Veynante, D. *Theoretical and numerical combustion*. 2nd ed. Philadelphia: Edwards, 2005.

[218] Pope, S. B. "Computationally efcient implementation of combustion chemistry using in situ adaptive tabulation". *Combustion Theory and Modelling* 1 (1997), pp. 41–63.

[219] Pope, S. B. "Lagrangian PDF Methods for Turbulent Flows". *Annual Review of Fluid Mechanics* 26 (1994), pp. 23–63.

[220] Pope, S. B. "A Monte Carlo Method for the PDF Equations of Turbulent Reactive Flow". *Combustion Science and Technology* 25.5-6 (1981), pp. 159–174. DOI: 10.1080/00102208108547500.

[221] Pope, S. "PDF methods for turbulent reactive flows". *Progress in Energy and Combustion Science* 11.2 (1985), pp. 119–192. DOI: 10.1016/0360-1285(85)90002-4.

[222] Pope, S. "The probability approach to the modelling of turbulent reacting flows". *Combustion and Flame* 27 (1976), pp. 299–312. DOI: 10.1016/0010-2180(76)90035-3.

[223] Pope, S. B. "A model for turbulent mixing based on shadow-position conditioning". *Physics of Fluids* 25.11 (2013), p. 110803. DOI: 10.1063/1.4818981.

[224] Pope, S. B. "Computations of turbulent combustion: progress and challenges". *Proceedings of the Combustion Institute* 23 (1990), pp. 591–612.

[225] Pope, S. B. *Turbulent Flows*. 1st ed. Cambridge University Press, 2000. DOI: 10.1017/CBO9780511840531.

[226] Prandtl, L. "7. Bericht über Untersuchungen zur ausgebildeten Turbulenz". *ZAMM - Journal of Applied Mathematics and Mechanics / Zeitschrift für Angewandte Mathematik und Mechanik* 5.2 (1925), pp. 136–139. DOI: 10.1002/zamm.19250050212.

[227] Prasad, V. N., Luo, K. H., and Jones, W. P. "LES-PDF simulation of a highly sheared turbulent piloted premixed flame". *7th Mediterranean Combustion Symposium*. 2011, pp. 11–15.

[228] Prasad, V. N. "Large Eddy Simulation of Partially Premixed Turbulent Combustion". PhD Thesis. Imperial College London, 2011.

[229] Proch, F. and Kempf, A. "Modeling heat loss effects in the large eddy simulation of a model gas turbine combustor with premixed flamelet generated manifolds". *Proceedings of the Combustion Institute* 35.3 (2015), pp. 3337–3345. DOI: 10.1016/j.proci.2014.07.036.

[230] Ramaekers, W. "Development of flamelet generated manifolds for partially-premixed flame simulations". OCLC: 8087215237. PhD Thesis. Technische Universiteit Eindhoven, 2011.

[231] Raman, V., Pitsch, H., and Fox, R. "Hybrid large-eddy simulation/Lagrangian filtered-density-function approach for simulating turbulent combustion". *Combustion and Flame* 143.1-2 (2005), pp. 56–78. DOI: 10.1016/j.combustflame.2005.05.002.

[232] Raman, V., Fox, R. O., and Harvey, A. D. "Hybrid finite-volume/transported PDF simulations of a partially premixed methane–air flame". *Combustion and Flame* 136.3 (2004), pp. 327–350. DOI: 10.1016/j.combustflame.2003.10.012.

[233] Raman, V. and Pitsch, H. "A consistent LES/filtered-density function formulation for the simulation of turbulent flames with detailed chemistry". *Proceedings of the Combustion Institute* 31.2 (2007), pp. 1711–1719. DOI: 10.1016/j.proci.2006.07.152.

[234] Ranade, R., Li, G., Li, S., and Echekki, T. "An Efficient Machine-Learning Approach for PDF Tabulation in Turbulent Combustion Closure". *Combustion Science and Technology* (2019), pp. 1–20. DOI: 10.1080/00102202.2019.1686702.

[235] Ren, Z., Kuron, M., Zhao, X., Lu, T., Hawkes, E., Kolla, H., and Chen, J. H. "Micromixing Models for PDF Simulations of Turbulent Premixed Flames". *Combustion Science and Technology* 191.8 (2019), pp. 1430–1455. DOI: 10.1080/00102202.2018.1530667.

[236]   Reynolds, O. "An Experimental Investigation of the Circumstances Which Determine Whether the Motion of Water Shall Be Direct or Sinuous, and of the Law of Resistance in Parallel Channels". *Philosophical Transactions of the Royal Society of London* 17 (1883), pp. 935–982.

[237]   Reynolds, O. "On the Dynamical Theory of Incompressible Viscous Fluids and the Determination of the Criterion". *Philosophical Transactions of the Royal Society of London. A* 18 (1895), pp. 123–164.

[238]   Richardson, E. S. and Chen, J. H. "Application of PDF mixing models to premixed flames with differential diffusion". *Combustion and Flame* 159.7 (2012), pp. 2398–2414. DOI: 10.1016/j.combustflame.2012.02.026.

[239]   Richardson, L. F. *Weather Prediction by Numerical Process.* 2nd ed. Cambridge mathematical library. OCLC: ocn150337883. Cambridge: New York : Cambridge University Press, 1922.

[240]   Sabel'nikov, V. and Soulard, O. "Rapidly decorrelating velocity-field model as a tool for solving one-point Fokker-Planck equations for probability density functions of turbulent reactive scalars". *Physical Review E* 72.1 (2005). DOI: 10.1103/PhysRevE. 72.016301.

[241]   Sabel'nikov, V. and Soulard, O. "White in Time Scalar Advection Model as a Tool for Solving Joint Composition PDF Equations". *Flow, Turbulence and Combustion* 77.1-4 (2006), pp. 333–357. DOI: 10.1007/s10494-006-9049-z.

[242]   Sagaut, P. *Large eddy simulation for incompressible flows: an introduction.* 3rd ed. Scientific computation. Berlin ; New York: Springer, 2006.

[243]   Sankaran, R., Hawkes, E. R., Chen, J. H., Lu, T., and Law, C. K. "Structure of a spatially developing turbulent lean methane–air Bunsen flame". *Proceedings of the Combustion Institute* 31.1 (2007), pp. 1291–1298. DOI: 10.1016/j.proci.2006.08. 025.

[244]   Schlichting, H. *Boundary-layer theory.* New York, NY: Springer Berlin Heidelberg, 2016.

[245]   Schmidhuber, J. "Deep learning in neural networks: An overview". *Neural Networks* 61 (2015), pp. 85–117. DOI: 10.1016/j.neunet.2014.09.003.

[246]   Schneider, C., Dreizler, A., Janicka, J., and Hassel, E. "Flow field measurements of stable and locally extinguishing hydrocarbon-fuelled jet flames". *Combustion and Flame* 135.1-2 (2003), pp. 185–190. DOI: 10.1016/S0010-2180(03)00150-0.

[247]   Schumann, U. "Subgrid scale model for finite difference simulations of turbulent flows in plane channels and annuli". *Journal of Computational Physics* 18.4 (1975).

[248]   See, Y. C. and Ihme, M. "Large eddy simulation of a partially-premixed gas turbine model combustor". *Proceedings of the Combustion Institute* 35.2 (2015), pp. 1225–1234. DOI: 10.1016/j.proci.2014.08.006.

[249]   Seneviratne, S. I., Rogelj, J., Séférian, R., Wartenburger, R., Allen, M. R., Cain, M., Millar, R. J., Ebi, K. L., Ellis, N., Hoegh-Guldberg, O., Payne, A. J., Schleussner, C.-F., Tschakert, P., and Warren, R. F. "The many possible climates from the Paris Agreement's aim of 1.5 °C warming". *Nature* 558.7708 (2018), pp. 41–49. DOI: 10. 1038/s41586-018-0181-4.

[250] Sevault, A., Dunn, M., Barlow, R. S., and Ditaranto, M. "On the structure of the near field of oxy-fuel jet flames using Raman/Rayleigh laser diagnostics". *Combustion and Flame* 159.11 (2012), pp. 3342–3352. DOI: 10.1016/j.combustflame.2012.06.017.

[251] Sewerin, F. and Rigopoulos, S. "A methodology for the integration of stiff chemical kinetics on GPUs". *Combustion and Flame* 162.4 (2015), pp. 1375–1394. DOI: 10.1016/j.combustflame.2014.11.003.

[252] Sheikhi, M., Drozda, T., Givi, P., Jaberi, F., and Pope, S. "Large eddy simulation of a turbulent nonpremixed piloted methane jet flame (Sandia Flame D)". *Proceedings of the Combustion Institute* 30.1 (2005), pp. 549–556. DOI: 10.1016/j.proci.2004.08.028.

[253] Shi, Y., Green, W. H., Wong, H.-W., and Oluwole, O. O. "Accelerating multi-dimensional combustion simulations using GPU and hybrid explicit/implicit ODE integration". *Combustion and Flame* 159.7 (2012), pp. 2388–2397. DOI: 10.1016/j.combustflame.2012.02.016.

[254] Shunn, L. "Large-eddy simulation of combustion systems with convective heat-loss". PhD Thesis. Stanford: Stanford University, 2009.

[255] Smagorinsky, J. "General circulation experiments with the primitive equaitons: I. The basic experiment". *Monthly Weather Review* 91.3 (1963), pp. 99–164. DOI: 10.1175/1520-0493(1963)091<0099:GCEWTP>2.3.CO;2.

[256] Smith, G., Golden, D., Frenklach, M., Moriarty, N., and Eiteneer, B. *The GRI-3.0 chemical kinetic mechanism.* http://www.me.berkeley.edu/gri_mech/.

[257] Soulard, O. and Sabel'nikov, V. A. "Eulerian Monte Carlo method for the joint velocity and mass-fraction probability density function in turbulent reactive gas flows". *Combustion, Explosion, and Shock Waves* 42.6 (2006), pp. 753–762.

[258] Soulard, O. and Sabel'nikov, V. "Eulerian Monte Carlo methods for solving joint velocity-scalar PDF equations in turbulent reacting flows". *European Conference on Computational Fluid Dynamics, Delft, Netherlands.* 2006.

[259] Steinberg, A., Arndt, C., and Meier, W. "Parametric study of vortex structures and their dynamics in swirl-stabilized combustion". *Proceedings of the Combustion Institute* 34.2 (2013), pp. 3117–3125. DOI: 10.1016/j.proci.2012.05.015.

[260] Stöllinger, M. and Heinz, S. "PDF modeling and simulation of premixed turbulent combustion". *Monte Carlo Methods and Applications* 14.4 (2008). DOI: 10.1515/MCMA.2008.016.

[261] Straub, C., De, S., Kronenburg, A., and Vogiatzaki, K. "The effect of timescale variation in multiple mapping conditioning mixing of PDF calculations for Sandia Flame series D–F". *Combustion Theory and Modelling* 20.5 (2016), pp. 894–912. DOI: 10.1080/13647830.2016.1191677.

[262] Subramaniam, S. "A mixing model for turbulent reactive flows based on Euclidean minimum spanning trees". *Combustion and Flame* 115.4 (1998), pp. 487–514. DOI: 10.1016/S0010-2180(98)00023-6.

[263] Sutherland, W. "The viscosity of gases and molecular force". *The London, Edinburgh, and Dublin Philosophical Magazine and Journal of Science* 36.223 (1893), pp. 507–531. DOI: 10.1080/14786449308620508.

[264]   Tian, L. and Lindstedt, R. "Evaluation of reaction progress variable - mixture fraction statistics in partially premixed flames". *Proceedings of the Combustion Institute* (2018). DOI: 10.1016/j.proci.2018.06.129.

[265]   TNF. *International Workshop on Measurement and Computation of Turbulent Flames.* https://tnfworkshop.org, 2020.

[266]   Turkeri, H., Zhao, X., Pope, S. B., and Muradoglu, M. "Large eddy simulation/probability density function simulations of the Cambridge turbulent stratified flame series". *Combustion and Flame* 199 (2019), pp. 24–45. DOI: 10.1016/j.combustflame.2018.10.018.

[267]   Ukai, S., Kronenburg, A., and Stein, O. "Large eddy simulation of dilute acetone spray flames using CMC coupled with tabulated chemistry". *Proceedings of the Combustion Institute* 35.2 (2015), pp. 1667–1674. DOI: 10.1016/j.proci.2014.06.013.

[268]   Valiño, L. "A field Monte Carlo formulation for calculating the probability density function of a single scalar in a turbulent flow". *Flow, turbulence and combustion* 60.2 (1998), pp. 157–172.

[269]   Valiño, L., Mustata, R., and Letaief, K. B. "Consistent Behavior of Eulerian Monte Carlo fields at Low Reynolds Numbers". *Flow, Turbulence and Combustion* 96.2 (2016), pp. 503–512. DOI: 10.1007/s10494-015-9687-0.

[270]   Vershik, A. M. "Two Ways to Define Compatible Metrics on the Simplex of Measures". *Journal of Mathematical Sciences* 196.2 (2014), pp. 138–143. DOI: 10.1007/s10958-013-1645-6.

[271]   Veynante, D. and Vervisch, L. "Turbulent combustion modeling". *Progress in Energy and Combustion Science* (2002), p. 74.

[272]   Villermaux, J. and Devillon, J. "Representation de la Coalescence et de la Redispersion des Domaines de Segregation dans un Fluide par un Modele d'Interaction Phenomenologique". *2nd International Symposium on Chemical Reaction Engineering* (1972).

[273]   Vreman, A. W. "An eddy-viscosity subgrid-scale model for turbulent shear flow: Algebraic theory and applications". *Physics of fluids* 16.10 (2004), pp. 3670–3681.

[274]   Vreman, A. W., Oijen, J. A. van, Goey, L. P. H. de, and Bastiaans, R. J. M. "Subgrid Scale Modeling in Large-Eddy Simulation of Turbulent Combustion Using Premixed Flamelet Chemistry". *Flow, Turbulence and Combustion* 82.4 (2009), pp. 511–535. DOI: 10.1007/s10494-008-9159-x.

[275]   Vreman, A., Albrecht, B., Vanoijen, J., Degoey, L., and Bastiaans, R. "Premixed and nonpremixed generated manifolds in large-eddy simulation of Sandia flame D and F". *Combustion and Flame* 153.3 (2008), pp. 394–416. DOI: 10.1016/j.combustflame.2008.01.009.

[276]   Wang, H. and Pope, S. B. "Large eddy simulation/probability density function modeling of a turbulent CH4/H2/N2 jet flame". *Proceedings of the Combustion Institute* 33.1 (2011), pp. 1319–1330. DOI: 10.1016/j.proci.2010.08.004.

[277]   Wang, H. and Zhang, P. "A unified view of pilot stabilized turbulent jet flames for model assessment across different combustion regimes". *Proceedings of the Combustion Institute* 36.2 (2017), pp. 1693–1703. DOI: 10.1016/j.proci.2016.06.008.

[278] Wang, H., Zhang, P., and Pant, T. "Consistency and convergence of Eulerian Monte Carlo field method for solving transported probability density function equation in turbulence modeling". *Physics of Fluids* 30.11 (2018), p. 115106. DOI: `10.1063/1.5053098`.

[279] Warnatz, J., Maas, U., and Dibble, R. W. *Verbrennung*. Berlin, Heidelberg: Springer Berlin Heidelberg, 2001. DOI: `10.1007/978-3-642-56451-2`.

[280] Weise, S. and Hasse, C. "Reducing the memory footprint in Large Eddy Simulations of reactive flows". *Parallel Computing* 49 (2015), pp. 50–65. DOI: `10.1016/j.parco.2015.07.004`.

[281] Wen, X., Luo, Y., Wang, H., Luo, K., Jin, H., and Fan, J. "A three mixture fraction flamelet model for multi-stream laminar pulverized coal combustion". *Proceedings of the Combustion Institute* 37.3 (2019), pp. 2901–2910. DOI: `10.1016/j.proci.2018.05.147`.

[282] Westbrook, C. K. and Dryer, F. L. "Simplified Reaction Mechanisms for the Oxidation of Hydrocarbon Fuels in Flames". *Combustion Science and Technology* 27.1-2 (1981), pp. 31–43. DOI: `10.1080/00102208108946970`.

[283] WHO. "Ambient (outdoor) air pollution". *World Health Organization* (2018).

[284] Xu, J. and Pope, S. B. "PDF calculations of turbulent nonpremixed flames with local extinction". *Combustion and Flame* 123.3 (2000), pp. 281–307. DOI: `10.1016/S0010-2180(00)00155-3`.

[285] Yang, B. and Pope, S. "Treating chemistry in combustion with detailed mechanisms—In situ adaptive tabulation in principal directions—Premixed combustion". *Combustion and Flame* 112.1-2 (1998), pp. 85–112. DOI: `10.1016/S0010-2180(97)81759-2`.

[286] Yang, Y., Wang, H., Pope, S. B., and Chen, J. H. "Large-eddy simulation/probability density function modeling of a non-premixed CO/H2 temporally evolving jet flame". *Proceedings of the Combustion Institute* 34.1 (2013), pp. 1241–1249. DOI: `10.1016/j.proci.2012.08.015`.

[287] Yu, C., Breda, P., Pfitzner, M., and Maas, U. "Coupling of mixing models with manifold based simplified chemistry in PDF modeling of turbulent reacting flows". *Proceedings of the Combustion Institute* (2020). DOI: `10.1016/j.proci.2020.06.132`.

[288] Zhou, H., Yang, T., and Ren, Z. "Differential Diffusion Modeling in LES/FDF Simulations of Turbulent Flames". *AIAA Journal* 57.8 (2019), pp. 3206–3212. DOI: `10.2514/1.J058524`.

[289] Zips, J., Traxinger, C., Breda, P., and Pfitzner, M. "Assessment of Presumed/Transported Probability Density Function Methods for Rocket Combustion Simulations". *Journal of Propulsion and Power* 35.4 (2019), pp. 747–764. DOI: `10.2514/1.B37331`.

[290] Zips, J. "Simulation turbulenter Verbrennung von Methan und Sauerstoff in Raketenbrennkammern". PhD Thesis. Universität der Bundeswehr München, 2018.

[291] Zips, J., Müller, H., and Pfitzner, M. "Efficient Thermo-Chemistry Tabulation for Non-Premixed Combustion at High-Pressure Conditions". *Flow, Turbulence and Combustion* 101.3 (2018), pp. 821–850. DOI: `10.1007/s10494-018-9932-4`.

[292]   Zirwes, T., Zhang, F., Denev, J., Habisreuther, P., and Bockhorn, H. *High Performance Computing in Science and Engineering '17*. Ed. by W. Nagel, D. Kroener, and M. Resch. Berlin, Heidelberg: Springer, 2017.

[293]   Zirwes, T., Zhang, F., Habisreuther, P., Hansinger, M., Bockhorn, H., Pfitzner, M., and Trimis, D. "Quasi-DNS Dataset of a Piloted Flame with Inhomogeneous Inlet Conditions". *Flow, Turbulence and Combustion* 104.4 (2020), pp. 997–1027. DOI: 10.1007/s10494-019-00081-5.